
Onset of Global Instabilities in the Plane Channel Flow between Compliant Walls

Waleed A. A. Ali

Cardiff University

School of Mathematics

Submitted September 20, 2016

A thesis presented for the degree of

Doctor of Philosophy



بِسْمِ اللَّهِ الرَّحْمَنِ الرَّحِيمِ

131. ١٤٢٠ هـ

Abstract

The development of disturbances in plane channel flow between compliant walls is studied. It is well known that compliant walls have the ability to stabilise the *Tollmien-Schlichting* instability arising from the flow. However, given the wave-bearing nature of compliant walls, wall-based instabilities can be generated. In the absence of any modal interactions, the predominant wall-based instabilities are those known as *divergence* and *travelling wave flutter* which have their origins in the free-waves that can propagate in either direction along a compliant wall in the absence of any fluid.

The treatment of the problem at hand is mainly numerical, in particular two numerical approaches are used. The first involves solving the coupled fluid flow/compliant wall system of stability equations for disturbances with a normal mode form and the second is through direct numerical simulations for a finite compliant wall.

The results presented here show that the normal mode solutions of the governing equations can provide excellent predictions for the wavenumbers that characterise the compliant wall displacements for the wall-based modes that arise in the simulations. This documents the onset of the wall-based instabilities using the current simulation method and this has not been systematically studied before. Additionally, and perhaps most interestingly, they can also predict some aspects of the contribution from end effects for finite wall simulations *even though* the numerical procedure used to obtain said solutions has been designed for an infinite compliant wall.

Finally, cases which display different types of instability in action and the range of possibilities for the spatial and temporal evolution are presented. Modal interactions between wall-based modes and those that can persist in a rigid channel are discussed and used to analyse the onset of global and absolute instability. These instabilities are studied from three different points of view: normal mode solutions of the fluid flow/compliant wall system, two-dimensional global mode computations and the direct numerical simulations.

Declaration

This work has not been submitted in substance for any other degree or award at this or any other university or place of learning, nor is being submitted concurrently in candidature for any degree or other award.

Signed Date

Statement 1

This thesis is being submitted in partial fulfilment of the requirements for the degree of PhD.

Signed Date

Statement 2

This thesis is the result of my own independent work/investigation, except where otherwise stated, and the thesis has not been edited by a third party beyond what is permitted by Cardiff Universitys Policy on the Use of Third Party Editors by Research Degree Students. Other sources are acknowledged by explicit references. The views expressed are my own.

Signed Date

Statement 3

I hereby give consent for my thesis, if accepted, to be available online in the Universitys Open Access repository and for inter-library loan, and for the title and summary to be made available to outside organisations.

Signed Date

Statement 4: Previously Approved Bar on Access

I hereby give consent for my thesis, if accepted, to be available online in the Universitys Open Access repository and for inter-library loans after expiry of a bar on access previously approved by the Academic Standards & Quality Committee.

Signed Date

Acknowledgements

First and foremost, I would like to express my greatest and utmost gratitude to my supervisor Dr. Christopher Davies whose endless guidance and unlimited patience has made this thesis possible.

A special thanks goes to Dr. Maurice J. Blount for his commentary and guidance through parts of this work, especially in providing the two-dimensional global mode computations for verifying some of the results obtained.

On a more personal note, I would like to thank my parents who have been a source of great inspiration and motivation throughout life, especially during my time in education and research. They have always aimed for making me achieve the best that I possibly could and I hope I have not disappointed.

For their many years of friendship and constant support, my best friends James Evans and Sally Hill deserve a very special thanks. I would also like to thank Xander Ramage and Scott Morgan for being very helpful colleagues. And for their endless source of joy, amusement and company, my utmost gratitude goes to Danny Groves, Joe Bishop and Matthew Lewis as well as my office mates Alex Safar, Asyl Hawa and Nikoleta Glenatsi.

Finally, I recognize that this research would not have been possible without the financial assistance of EPSRC and I express my gratitude to this agency.

Contents

1	Introduction	1
1.1	History	1
1.2	Use of Compliant Walls	4
1.2.1	Practicality	4
1.2.2	Applications	4
1.3	Classification of Instabilities	6
1.3.1	Wall/Flow Based Classification	7
1.3.2	Energy-Based Classification	8
1.3.3	Propagation-Based Classification	9
1.4	Effect of Wall Compliance on Instabilities	11
1.5	Flow Configuration	11
1.5.1	Basic Flow Profile: The Plane Channel Flow	12
1.5.2	Wall Model	13
1.5.3	The Spring-Backed Plate Model	15

1.5.4	The Dolphin Skin	17
1.6	Methodology & Assumptions	18
1.7	Thesis Layout	19
2	Governing Equations of the Fluid Flow/Compliant Wall System	21
2.1	Flow Equations	22
2.1.1	Normal Mode Decomposition	25
2.1.2	Squire’s Theorem	28
2.1.3	Pressure Integral	29
2.2	Boundary Conditions	30
2.2.1	Rigid Walls	30
2.2.2	Compliant Walls	31
2.3	Previous Analytic Work	35
2.3.1	Dispersion Relation	35
2.4	Numerical Examples: Eigenvalues & Neutral Stability Curves	38
2.4.1	Temporal Stability	39
2.4.2	Spatial Stability	41
2.5	Stabilisation of Tollmien-Schlichting Waves by using Compliant Walls	43
3	Numerical Solution of the Orr-Sommerfeld Equation	47

3.1	Chebyshev Collocation Method	48
3.2	Discretising the Functions of the System	48
3.3	Discretising the Differential Operators	50
3.3.1	Phase Speed c -Eigenvalue Problem	50
3.3.2	Wavenumber α -Eigenvalue Problem	51
3.4	Incorporating the Boundary Conditions	52
3.4.1	Rigid Wall Boundary Conditions	53
3.4.2	Compliant Wall Boundary Conditions	54
3.5	Plotting Neutral Stability Curves	58
3.6	Some Numerical Examples	61
3.7	Merged Neutral Curves	67
3.7.1	Curves of c Against Re	69
3.7.2	Curves of c Against α	73
4	Numerical Simulation Method	77
4.1	Introduction	78
4.2	Flow Set-up	79
4.2.1	Flow Configuration	79
4.2.2	Disturbing the Basic Flow	80
4.3	Establishing the Governing Equations	82

4.3.1	Velocity-Vorticity Formulation	82
4.3.2	Governing Equations	83
4.3.3	Fluid Motion	84
4.3.4	Pressure Integral	88
4.3.5	Wall Motion	88
4.3.6	Boundary Conditions	90
4.3.7	Inflow & Outflow Conditions	90
4.3.8	Join Condition Between the Rigid & Compliant Walls . .	92
4.4	Numerical Discretisation Procedure	93
4.5	Discretisation in the y -Direction	95
4.5.1	General Form of the Discretised Functions	96
4.5.2	Governing Equations	98
4.5.3	Pressure Integral	102
4.5.4	Boundary Conditions	102
4.6	Discretisation in the x & t -Directions	103
4.7	The Numerical Procedure	105
4.7.1	Vorticity Predication	105
4.7.2	Velocity Iteration	106
4.7.3	Vorticity Correction	110
4.8	Summary	111

5	Simulation of Disturbance Development for Various Instabilities	113
5.1	Introduction	113
5.2	Least Squares Fitting	117
5.3	TSM: Tollmien-Schlichting Mode	119
5.3.1	Choice of Flow Parameters	120
5.3.2	Vorticity Time-History	122
5.3.3	Frequency	124
5.3.4	Approximating the Wall Displacement	125
5.3.5	Wall Velocity	128
5.3.6	Incorporating the Time-Dependence	129
5.3.7	Remarks on TSM	130
5.4	TSS: Tollmien-Schlichting Stabilisation	131
5.4.1	Choice of Flow Parameters	132
5.4.2	Wall Displacement Decomposition	136
5.4.3	Tollmien-Schlichting Stabilisation	137
5.4.4	Remarks on TSS	138
5.5	TWF: Travelling Wave Flutter	140
5.5.1	Flow Parameter Choices	141
5.5.2	DNS	143

5.5.3	Wall Displacement Decomposition	146
5.6	DivEnd: Divergence & End Effects	147
5.6.1	Choice of Flow Parameters	148
5.6.2	DNS	150
5.6.3	End Effects	155
5.6.4	Remarks for DivEnd	160
5.7	Summary	162
6	Absolute Instability	163
6.1	Introduction	163
6.1.1	Wall Parameters	164
6.2	STG: Spatio-Temporal Growth	167
6.2.1	STG1	167
6.2.2	STG2	184
6.2.3	Summary of STG	190
6.3	TG: Temporal Growth	192
6.3.1	TG	193
6.4	Modifications to TG	201
6.4.1	TGE: End Conditions	201
6.4.2	TGL: Compliant Wall Length	202

6.4.3	TGR: Reynolds Number	205
6.4.4	TGC: A Combination of Factors	206
6.4.5	TGM: Wall Mass	207
6.4.6	TGD: Damping Coefficient	208
6.5	Two-Dimensional Global Mode Computations	209
6.5.1	Compliant Wall Length	210
6.5.2	Wall Mass & Damping	212
6.5.3	Remarks on the Two-Dimensional Global Mode Computations	213
6.6	Wall Energy Balances	214
6.7	Summary	234
7	Conclusions	235
7.1	Conclusion of the Thesis	235
7.2	Future Work	237
A	Inviscid Solutions	239
B	Chebyshev Polynomials	243
C	Plotting Eigenfunctions	247
D	Reformulation of the Discretisation in Terms of α & ω	249

E Full Forms of M_3 & M_5	253
F The Tau Method	257
G Thomas Algorithm (TDMA)	261
H Identification of Absolute Instabilities via Briggs' Method	269

Chapter 1

Introduction

1.1 History

In 1936, a British zoologist by the name of Sir James Gray proposed a paradox pertaining to the elaborate swimming of dolphins [58]. This paradox, later termed *Gray's Paradox*, was posed to question how dolphins can attain high swimming speeds and accelerations with what seems to be insufficient muscle mass capable of overcoming the hydrodynamics drag forces. In light of his work regarding their muscular physiology, he concluded that the dolphins had to possess skins with the capacity to reduce drag.

Gray employed a rigid-body hydrodynamic model in order to determine the drag forces on dolphins at high swimming speeds. Gray's conclusion was phrased thusly: "*If the resistance of an actively swimming dolphin is equal to that of a rigid model towed at the same speed, the muscles must be capable of generating energy at a rate at least seven times greater than that of other types of mammalian muscle.*"

The paradox was posed largely due to a flawed assumption by Gray which stated that the swimmer had to expend muscle energy in order to overcome the drag forces in the direction of swimming. This statement was later revised from a mathematical, rather than an experimental, point of view by Bale *et al.* [4]. They showed that undulatory swimmers (like most sea dwelling cetaceans as depicted in Figure 1.1) use their muscle power in order to undulate the body which results in both drag and thrust simultaneously. Therefore, the power generated by the muscles should be equated to the power needed in order to deform the body and not to the drag forces.



Figure 1.1: Schematic representation of the undulatory motion of cetaceans (side view).

Many decades after the initial proposal of Gray's Paradox, Fish [40] [41] [43] [45], Fish & Rohr [42] and Fish & Hui [44] set out to investigate this paradox experimentally and test whether there actually is any skin-based trickery employed by the dolphin. They used particle image-velocometry to show that dolphins could in fact exert 10 to 20 times the burst forces predicted by Gray [58]. From their work, it seemed that the basic assertion of the paradox was flawed due to estimation errors in measuring the dolphin's swimming performance and the data extracted from the muscles. This accumulation of research into the subject area dispelled Gray's paradox and the dolphin skin did not seem to be the only contributing factor in the high swimming speeds.

One of the very first experimentalists in the field was a German aeronautical engineer, Max Otto Kramer. He approached the problem from a more experimental point of view and published a pioneering series of papers outlining his analysis and experiments [75] [76] [77] [78]. The results claimed that for a compliant wall of his own making (which is known as the *Kramer Coating*), the hydrodynamic drag could be reduced by as much as 30% due to boundary layer stabilisation. This raised great interest within the fluid dynamics community since the results seemed very optimistic. The experiments conducted by Kramer were performed in Long Beach Harbour, California which was not ideal since this made his experiments difficult to reproduce under more controlled laboratory conditions. Even when the experiments could be duplicated, the results were very modest and did not match Kramer's apparently overly optimistic original findings.

In the years that followed the "*Kramer Controversy*", many authors like Benjamin [5] [6] [7] and Landahl [81] took it in their stride to study the matter further. Their analysis did indeed find that flexible walls were capable of delaying the transition to turbulence and with time, some of Kramer's claims were substantiated by further research into the topic. Carpenter & Garrad [21] [22] later extended the analysis further by studying the different instabilities that arise in fluid flows with compliant boundaries. They compared the properties of different wall models and their respective advantages and disadvantages, they also investigated the nature and growth (or suppression thereof) of the different instabilities in compliant wall bound flows. This was later followed by carefully conducted experiments which support some of Kramer's findings (accounts of these works are outlined in Gad-el-Hak [48], Gaster [55] and Fisher *et al.* [82]).

1.2 Use of Compliant Walls

1.2.1 Practicality

The use of compliant walls for boundary layer manipulation is quite advantageous from both financial and technological points of view. The alternative is to use *active* compliant walls which respond actively to instabilities as they develop. This requires the use of elaborate equipment such as sensors, pressure pads and actuators which are not necessarily the most economical choice. *Passive* compliant walls, on the other hand, can be relatively inexpensive to manufacture and do not require such luxuries.

1.2.2 Applications

Underwater Travel

The study of dolphin skins was the main motivation for flows with compliant boundaries so it only stands to reason that applications in underwater travel would be a natural extension. Some of this research gained momentum during the height of the Cold War in order to develop faster submarines, torpedoes and ships [41] [43] [46].

Artificial compliant skins can also be used for manufacturing swimsuits for enhanced swimming; wetsuits made of thick rubberised materials (over 5mm in thickness) with small fins have been suggested to improve swimming speeds and allow a “better grip on the water” while swimming. These uniforms have been deemed very effective, however they were once banned by the International Triathlon Union since they are considered as being “*outside the spirit of fair play in wetsuit design*” [35].

Engineering

Though compliant walls can be used to improve swimming speeds in water, the same cannot be said for air-borne applications. In theory, compliant coatings can suppress certain instabilities for use in aeronautical applications but in practice, the balance between the different wall parameters would result in a very delicate compliant wall which would be far too impractical to achieve any desirable effects (according to Carpenter [19]).

Additionally, the design and manufacture of compliant walls is not without its difficulties. When it comes to large-scale applications, if a surface is to be rigid, then its stiffness can be scaled up for reasons pertaining to “health & safety” without any consequences to the final design. However when manufacturing flexible surfaces, the wall properties have to be reproduced exactly as the theory states lest the results would not be as promising.

Anatomy & Physiology

The study of compliant walls can help in modelling certain physiological phenomena such as blood flow through vessels and wheezing in asthmatics. The human trachea (windpipe) and blood vessels can be modelled as flexible tubes so studying the effect of wall flexibility on fluid flows through said pipes can shed light on the mechanisms that affect the tubes’ collapse, for example.

The study of compliant walls in human anatomy has been studied extensively from a firm mathematical grounding by many authors. The studies focussed mainly on flows in flexible pipes and their applications in blood and air flow and the conditions that lead to the pipe’s collapse. Some of this analysis is presented in several publications including, but not limited to, Gavriely *et al.* [57], Grotberg & Davies [60], Grotberg [61], Grotberg & Shee [63] and

Moriarty & Grotberg [101]. A general overview of the whole area was also given in Grotberg & Jensen [62].

Ecology

In the natural world, modelling of compliant walls can help investigate how fluid flows erode and alter the state of riverbeds. One of these studies was conducted by Vignaga *et al.* [126] where they considered a bacterial bio-film covering a riverbed which acted as a compliant surface for the river to flow over. According to experimental evidence, the bio-film can break for river flow speeds higher than a particular threshold due to the instabilities arising from the wall's flexibility. Thus, this breakage can expose the riverbed and potentially accelerating the rate of riverbed erosion.

1.3 Classification of Instabilities

In the study of hydrodynamic instabilities over compliant walls, there are different types of instabilities which fall under three classifications: wall/flow based, energy based and propagation based. The first is with regards to the coupled fluid/compliant wall system which divides the instabilities to those which arise due to the fluid flow and those arising from the compliant wall itself. The second and third classifications pertain to hydrodynamic instabilities in general, the former considers the irreversible energy exchange into and out of the flow while the latter describes the direction in which the instability travels. It should be noted that these classifications aim to distinguish between the different mechanisms at play for the instabilities that arise in the coupled fluid/compliant wall system.

1.3.1 Wall/Flow Based Classification

This classification was investigated at great lengths initially by Carpenter & Garrad [21] [22] where the instabilities were divided according to where they proliferate, in the flow or on the wall itself. Since both the wall and the flow are wave bearing media, the instabilities that arise from the flow have to be coupled with those arising from the wall itself.

Flow-Based Instabilities

These instabilities, which are referred to as *Tollmien-Schlichting* waves/instabilities (hereafter denoted TS), arise due to the fluid flow even over rigid walls. This type of instability is one of the more common ways in which a laminar boundary layer becomes turbulent. The effect of wall compliance on the growth and decay of TS^I instabilities was addressed in great detail by Carpenter & Garrad [21], Davies [28] and Davies & Carpenter [31].

Wall-Based Instabilities/Flow Induced Surface Instabilities

Since the compliant wall is a wave bearing medium, it has the ability to carry a wave known as the *free-wave*, even in the absence of fluid flow. Carpenter & Garrad [21] [22] studied the wall-based modes (also known as *flow-induced surface instabilities* and denoted *FISI*) extensively and found two most prominent modes:

- * Travelling Wave Flutter (hereafter TWF): This instability only exists when there is a shear in the flow and travels downstream with a speed similar to that of the free-wave.

^IWhen the wall is compliant, the TS instability should technically be referred to as a *modified flow-based mode* but it will be referred to as TS instead.

* Divergence (Hydroelastic) Instability: This wall-based instability sets in at very small phase speeds and can also occur when the boundary layer is turbulent (as suggested by Carpenter *et al.* [19]). Therefore, the divergence mode can be described as an instability that arises when the restorative elastic forces are overwhelmed by the destabilising hydrodynamic forces. Thus, the divergence instability is notorious for being a dangerous mode and can cause physical damage to the compliant walls [47].

1.3.2 Energy-Based Classification

For the study of flows with compliant boundaries, Benjamin [5] [6] and Landahl [81] classified instabilities according to the irreversible energy transfer that takes place between the compliant wall and the flow. These were referred to by three different classes: *Class A* (negative energy waves), *B* (positive energy waves) and *C*. These have also been referred to differently by Sen & Arora [116] as *Class TS* (Tollmien-Schlichting), *Class R* (resonant) and *Class KH* (Kelvin-Helmholtz). This classification was introduced initially by Benjamin [5] after having been inspired by Kramer's results [75] and it was believed that recognising these three distinct forms of instability provides a complete interpretation of all the possibilities that could arise in this context. A brief description is presented here but more details are given in Benjamin [5] [6], Landahl [81] and Sen & Arora [116].

Class A or Class TS

This type of wave is slightly counter intuitive since it is stabilised by an irreversible energy transfer into the flow. Therefore, this class of wall instabilities can be stabilised by high wall flexibility but destabilised by wall damping.

Class B or Class R

This type of wave is the opposite of Class A where the wall instability is destabilised by an irreversible energy transfer into the flow. It should be noted that flows between compliant walls are notorious for having a very rich and complicated behaviour which can sometimes be counter intuitive.

Class C or Class KH

Class C instabilities are indifferent to irreversible energy transfer between the flow and the wall however, they can manifest if the wall is too flexible.

1.3.3 Propagation-Based Classification

This classification of instabilities is to demonstrate how the modes discussed grow in the flow. When a disturbance is excited, an instability could either travel downstream (*convective instability*) or it could grow in both the upstream and downstream directions (*absolute instability*). Davies [29] and Yeo *et al.* [132] [133] investigated these different types of instabilities for flows with compliant walls.

Absolute Instability

An instability is absolute if at least one of the modes has a zero group velocity at onset hence causing the instability to grow both upstream and downstream. Therefore for any point in the flow, the disturbance will be experienced at some point in time and will persist for all future times. Note, however, that having a zero group velocity is a necessary but not a sufficient condition for absolute instability (i.e. if the flow is absolutely unstable, then there has to be a mode with a zero group velocity but the opposite is not necessarily true). A depiction of the absolute growth of a disturbance is shown

in Figure 1.2(a) where the disturbance grows upstream and downstream from the point of excitation.

Convective Instabilities

An instability is convective when the disturbance travels downstream from the point of excitation therefore for any point in the downstream direction, the instability is experienced for a period of time then it will convect away, leaving the points in its wake to return to their undisturbed states (as shown in Figure 1.2(b)).

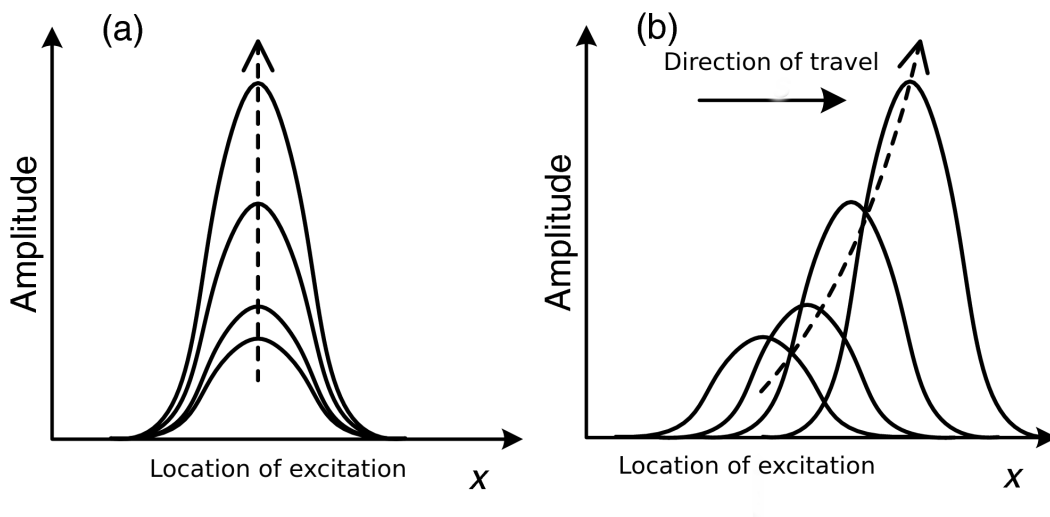


Figure 1.2: Depiction of (a) absolute and (b) convective instabilities. The arrows denote the direction of growth.

Different instabilities can interact and coalesce to form new modes that can be even more effective at destabilising flows than the individual modes that make them up (see for example [23] [82] [116]). For instance, TS and TWF can coalesce to give rise to a *transitional instability*, this arises as a result of using excessive damping for controlling some of the instabilities. Another interaction can happen between TWF and divergence to form a powerful *flutter-type instability*.

In terms of the energy transfer between the wall and the flow, the “optimal” compliant wall has to be of high flexibility and low damping in order to suppress the growth of Class A instabilities. On the other hand, the damping has to be high enough to suppress Class B modes while the flexibility has to be low enough to suppress Class B and C instabilities.

1.4 Effect of Wall Compliance on Instabilities

It has been documented that compliant walls can stabilise the TS instability very effectively given the appropriate choice of wall parameters (see for example [5] [6] [7] [21] [22] [81]) but as mentioned earlier, both the wall and the flow can carry waves independently. In this case, suppressing the flow-based TS mode by using a compliant wall can also risk introducing more instabilities in the process (namely the wall-based modes). However, the compliant wall parameters can be modified appropriately in order to delay the onset of wall-based modes and avoid any interaction between them while still stabilising TS (at least within a particular region of the parameter space). This gives greater flexibility when choosing the wall parameters since they can be modified appropriately to achieve “optimal” suppression of the flow-based modes while still controlling the wall-based ones.

1.5 Flow Configuration

Several rigid/compliant wall configurations were considered over the years. For instance, Carpenter & Garrad [21] [22], Green & Ellen [59] and Benjamin [5] [6] [7] considered compliant walls that extend infinitely while others like Burke [12], Wiplier & Ehrenstein [131] and Davies & Carpenter [31] only took

a finite compliant wall section inserted between two rigid walls.

In Carpenter [15] [17], a compliant wall each assembled out of several compliant panels, each of these sections has wall parameters to suit their local flow environments. According to numerical results, compliant walls as short as a single TS wavelength can be very effective at suppressing the growth of (or even stabilise) the flow-based instability, therefore having a succession of compliant wall sections each with different wall properties could, at least in theory, delay the transition to turbulence indefinitely.

1.5.1 Basic Flow Profile: The Plane Channel Flow

For the work presented here, the basic flow configuration is the plane channel flow (or *Poiseuille flow*), i.e. a fluid flowing between two parallel walls (be they rigid or compliant) extending infinitely in the streamwise and spanwise directions, therefore the undisturbed velocity profile is parabolic. In order to simplify the problem further, the flow can be assumed to be gravity-driven rather than having a mean pressure gradient driving the flow, in other words, the channel can be assumed to be vertical so the fluid flow is driven by gravity. Initially, a plane channel flow between two infinite compliant walls is considered however in Chapter 4, direct numerical simulations will only be conducted for a finite compliant wall section.

The plane channel flow provides a relatively simpler problem compared to the flow over a flat plate (*Blasius boundary layer*) since the flow profile is exactly parallel and no further assumptions need to be imposed on the basic state. Also, the presence of a wall-bound shear flow results in the growth of TS instabilities which eventually leads to turbulence. Flows over a flat compliant plate were studied by authors such as Carpenter [17], Landahl [81], Lee *et al.*

[82], Sen & Arora [116] and Wang *et al.* [127].

Other basic flow profiles were considered by several studies in order to model different phenomena, for instance flexible tubes were studied by Gavriely *et al.* [57], Grotberg [61], Grotberg & Jansen [62] and Moriarty & Grotberg [101].

The plane channel flow itself has had its fair share of modifications, for instance, Gajjar & Sibanda [50] considered a flow between two parallel walls where one of the walls is compliant while the other is rigid. Pedley & Luo [94] [95] [96] [107] also considered channels with one rigid boundary but the other wall had a finite compliant wall section (rather than being infinite). Vignaga *et al.* [126] considered the plane channel flow where one wall is compliant while the other boundary is free (exposed to the atmosphere). Other, more complicated, plane channel flows were also considered by Guaus & Bottaro [64] where the plane channel flow, with both walls compliant, was curved rather than being straight.

1.5.2 Wall Model

Over the years, many different compliant wall models have been used to illustrate the workings of a flexible surface. Some of these models are shown in Figure 1.3.

In this thesis, the spring-backed plate model (Figure 1.3(b)) is used to model the compliant wall. The wall consists of a set of springs held perpendicularly on a rigid wall and are attached to a thin flexible membrane with a substrate filling the central cavity. Carpenter & Garrad [21] [22] discussed the different materials that can occupy the region between the thin plate and rigid wall, namely, the substrate material. This can either be a soft solid or

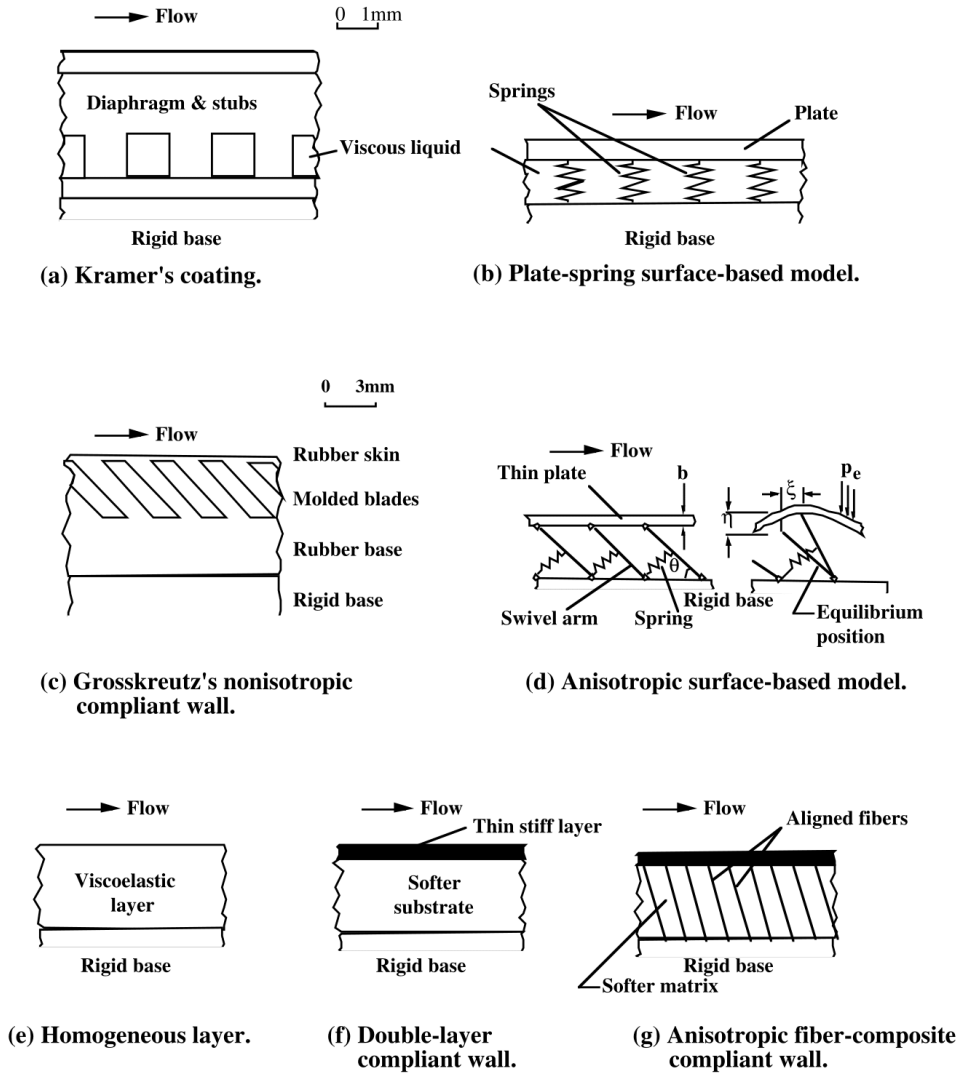


Figure 1.3: Different compliant wall models (taken from Gad-el-Hak [47]).

a fluid is inviscid, viscous or viscoelastic and usually has a different viscosity and density compared to the fluid in the flow. According to their findings, an inviscid fluid substrate will stabilise the flow but for a viscous or viscoelastic fluid substrate, the flow could be destabilised. (It should be noted that it will be assumed that the motion of the springs has negligible effect on the movement of the fluid substrate.) More details about the wall model will be provided in Chapter 2.

The Kramer coating (Figure 1.3(a)) was devised and studied by its proposer

Max O. Kramer, the investigations he carried on this particular wall model are given in his works [75] [76] [77] [78]. Further studies were conducted by Carpenter & Garrad [21] [22] for a Blasius flow over a Kramer-type surface while Wiplier & Ehrenstein [131] considered the same case but with finite compliant wall panels instead.

Another very popular wall model is the rigid wall with a viscoelastic layer on top (Figure 1.3(e)), this was studied by many authors such as Lee *et al.* [82], Lucey & Carpenter [91], Wang *et al.* [127] and Yeo *et al.* [132] and were mainly used to study the effect of using a compliant wall in the Blasius boundary layer.

All the models described so far (as well as the double-layer compliant wall in Figure 1.3(f)) are *isotropic*, meaning that the wall will behave in exactly the same way regardless of the direction of flow. These different models can be modified to have a wall that is *anisotropic* (or *non-isotropic*), in other words, the wall will behave differently depending on the direction of flow, examples of these are shown in Figures 1.3(c), (d) and (g). (Flows over these types of walls were studied by Carpenter & Gajjar [20] and Carpenter & Morris [23].) An example of using anisotropic compliant walls was outlined by Pavlov [106] who suggested that the morphology of the dolphin skin allows the fluid/surface interface to behave as if though the skin is anisotropic in the regions of favourable or adverse pressure gradients.

1.5.3 The Spring-Backed Plate Model

For the spring-backed plate model, there are five wall parameters to consider which dictate the wall motion (the governing equations for the wall are given in Chapter 2). The wall parameters are:

*** m : Mass Per Unit Area**

This can be considered as the inertial term that characterises the compliant wall's mass. It has been shown by Carpenter & Garrad [21] that increasing the plate mass has a stabilising effect on the flow over a flexible surface. Davies & Carpenter [30] also showed that the onset of TWF and the flutter-type instability can be greatly influenced by the wall's mass but the divergence onset is indifferent.

*** B : Flexural Rigidity**

This term refers to the flexural rigidity (or bending stiffness) of the compliant wall which describes the force couple required to bend the wall and an increase in its value would result in a stabilisation of the flow.

*** T : Tension Per Unit Length**

This term represents the tension on the thin membrane per unit length. Usually, the value of T is taken to be zero since according to Carpenter & Garrad [22], the other wall parameters can be modified in order to set $T = 0$ while still retaining the same effect on the flow. This can be attributed to an effective stiffness parameter which behaves as $\sqrt{2\sqrt{BK} + T}$, further details of this are given in Davies & Carpenter [30] and are also elaborated upon further in Chapter 2.

*** K : Spring Stiffness**

The compliant wall model involves the use of springs between the rigid wall base and the thin flexible membrane. The springs are attached perpendicularly to both and are sitting in the substrate material. It is assumed that the motion of the spring acting on the thin membrane can be modelled by an elastic foundation and spring motion does not affect the movement of the fluid substrate.

* ***d*: Damping**

The final term in the wall model is the damping coefficient of the wall. This can be introduced as a property of the material making up the wall itself or as a modification to the wall model by having dampeners alongside the springs (as used by Burke *et al.* [12]).

1.5.4 The Dolphin Skin

With regards to the dolphin skin, many of the previous studies such as those conducted by Bale *et al.* [4], Fish and others in [40] [41] [42] [44] [45], and Gray [58] looked at the stabilisation properties of the dolphin skin from an experimental point of view. Kramer [75] [76] [77] [78] studied the dolphin skin by modelling it using the wall model shown in Figure 1.3(a) while Pavlov [106] used an anisotropic wall model for modelling the dolphin skin. A number of review papers have been published on the subject collating the information with regards to the suppression capabilities of dolphin skins as in Carpenter *et al.* [19], Fish & Hui [44], Gad-el-Hak [49], Gaster [55], Ridgway & Carder [110].

The spring-backed plate model used here cannot be readily extended to capture all the effects of the dolphin skin since even some of the simplest dolphin skin models used in the aforementioned works are more complicated and intricate compared to the spring-backed plate. One of the reasons is that a true depiction of the dolphin skin would require an element of active control by the nervous system in different parts of the dolphin's body (as suggested by Ridgway [110]). The dolphin skin has been a motivator for the study of stabilising flows by using flexible walls from the time Gray first proposed his paradox but now, compliant walls are of interest in their own right and

the growth of the wall-based instabilities can shed light not only on the way in which dolphin skins behave, but on the mechanisms that can lead to instability when using compliant walls.

1.6 Methodology & Assumptions

Some previous studies, such as Landahl [81], assumed a potential flow over a compliant surface. However some of the predictions made did not match the experimental results like those conducted by Riley *et al.* [111]. The potential theory predicted an early onset of the divergence instability therefore when experiments were conducted, the existing theory suggested the use of compliant walls which were far stiffer than necessary hence affecting the TS suppression. This presented a limitation when using potential theory to predict the onset of divergence (similarly for inviscid shear layer theory). Therefore, alternative approaches were later undertaken, mainly in the form of asymptotic analysis. In this thesis, most of the work presented will be from a numerical standpoint, although it will still be interlaced with some previously conducted analysis.

The main assumptions for the present work are two-fold. First, the disturbance amplitude will be sufficiently small to allow linear theory to hold and the second is to take a relatively large value of the Reynolds number.

The first assumption is imposed to predict the onset and behaviour of instabilities when the background disturbance is of a low amplitude. Moreover, small amplitude disturbances avoid non-linearity.

The assumption of having a large yet finite Reynolds number helps simplify some of the equations by allowing some terms to be negligible in size. It should be noted that for the TS mode that appears when the Reynolds number is quite large (5772.2 for the rigid wall plane channel flow), therefore for the purposes

of studying the effect of using compliant walls on the TS mode, the Reynolds number can be assumed to be large. The extreme case of having an inviscid fluid flowing over a compliant wall was studied by Burke *et al.* [12] and Lucey & Carpenter [89].

1.7 Thesis Layout

This work will be laid out in several chapters as follows:

- * **Chapter 2:** The equations of the system are set up (from earlier works). First, the equation that governs the stability of parallel flows, namely the *Orr-Sommerfeld equation*, and the assumptions imposed on it are discussed. Then, the rigid and compliant wall boundary conditions are formulated. Some preliminary numerical results are presented which illustrate the compliant wall's TS suppression capabilities and an account of previous analytic work done by Davies & Carpenter [30] is discussed briefly.
- * **Chapter 3:** The equations of the system determined in Chapter 2 are discretised using a *Chebyshev collocation method* in order to solve the fluid flow/compliant wall system of equations numerically (note that the compliant wall in this case will be infinite). Some interesting numerical observations regarding the different instabilities and their prevalence within the flow parameter space are then presented.
- * **Chapter 4:** The procedure for the *direct numerical simulation* of flows over finite compliant wall sections is discussed. This previously devised method is adopted from Davies [28] and Davies & Carpenter [31] and is deployed for the following chapters. The explanation of this method is

included here in an attempt to present it in a more concise way (since it was a collection of different works by different studies).

- * **Chapter 5:** In this chapter, some examples of flow simulations are presented where the effect of different instabilities, wall-based and flow-based, are studied. The results obtained from Chapter 4 are compared to the solution of the coupled system of equations from Chapter 3. This is done in order to demonstrate whether the numerical solution to the global problem can be used to predict which modes would proliferate when a simulation is performed and whether the flow parameters can be predicted effectively. The wall-based modes are also investigated using the method described in Chapter 4, the results obtained have not been documented before and this will be a part of the original content of this thesis.
- * **Chapter 6:** In this chapter, *absolute* and *global instabilities* arising in the flow are discussed. Different triggers are used to excite the flow and the growth of the *global instabilities* is investigated from three different points of view: the solution of the coupled system of equations, direct numerical simulations and two-dimensional global mode computations. The effect of using different compliant wall parameters and flow configurations on the growth of the absolute instability are also discussed. The onset of absolute instability within this context has not been documented before and this will also be a part of the original content of this thesis.
- * **Chapter 7:** The final chapter outlines the conclusions of the work as well as some limitations and further work.

Chapter 2

Governing Equations of the Fluid Flow/Compliant Wall System

In this chapter, the governing equations that dictate the flow configuration are set up. Establishing these equations constitutes of two parts: the equations that govern the fluid flow and those that govern the motion of the compliant wall. First, the perturbed form of the Navier-Stokes equations is used to obtain expressions that dictate the stability of the plane channel flow as well as expressions for the pressure field. Then, the equations that dictate the motion of the wall are established and used to obtain appropriate compliant wall boundary conditions. These two sets of equations can then be coupled through the dispersion relation which governs the fluid flow/compliant wall system.

Some preliminary illustrative numerical examples will be presented after the equations of the system have been obtained. From now on, the following

notation will be adopted:

x – streamwise direction

y – direction normal to the wall

z – spanwise direction

t – time

u – streamwise velocity component

v – normal velocity component

w – spanwise velocity component

p – pressure.

It should be noted that even though the equations derived here are already well-established in the literature, their derivation is outlined since some of the intermediate equations are used later.

2.1 Flow Equations

Consider a fluid flowing between two rigid parallel walls of distance $2h$ apart which extend infinitely in both the streamwise and spanwise directions, a schematic representation of the flow configuration is shown in Figure 2.1. The flow in this case is two-dimensional, therefore there is no variation in the z -direction and there is no spanwise velocity component either, i.e.

$$w = 0 \quad \text{and} \quad \frac{\partial f}{\partial z} = 0 \quad \text{for} \quad f = u, v, p.$$

In the current work, only the two-dimensional development of instabilities in the plane channel flow are considered as a consequence of Squire's theorem

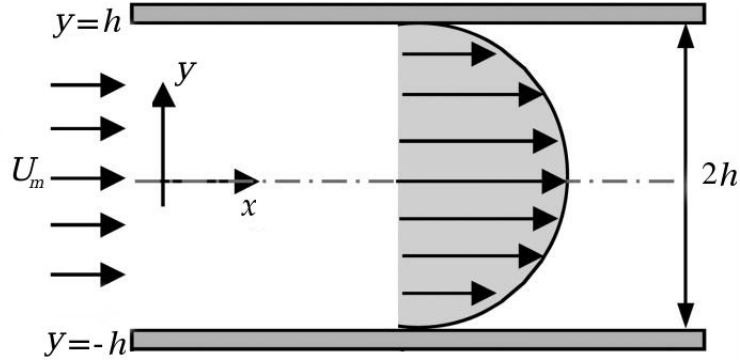


Figure 2.1: Flow configuration for the plane channel flow.

which will be stated formally in §2.1.2^I.

The fluid in question has density ρ , dynamic viscosity ν and a centreline (mean) velocity U_m . The variables of the system can be non-dimensionalised by using:

$$x = \frac{x^*}{h}, \quad y = \frac{y^*}{h}, \quad t = \frac{t^* U_m}{h}, \quad \hat{u} = \frac{u^*}{U_m}, \quad \hat{v} = \frac{v^*}{U_m}, \quad \hat{p} = \frac{p^*}{\rho U_m^2} \quad (2.1)$$

and the Reynolds number of the system is given by $\text{Re} = \frac{U_m h \rho}{\nu}$.

Terms with an asterisk (\square^*) are *dimensional* quantities and the terms with a caret/hat ($\hat{\square}$) are *disturbed* quantities^{II}.

In vector form, the two-dimensional non-dimensionalised Navier-Stokes equations are:

$$\text{Momentum equations:} \quad \frac{\partial \hat{\mathbf{u}}}{\partial t} + (\hat{\mathbf{u}} \cdot \nabla) \hat{\mathbf{u}} = -\nabla \hat{p} + \frac{1}{\text{Re}} \nabla^2 \hat{\mathbf{u}} + \mathbf{F}$$

$$\text{Conservation of mass:} \quad \nabla \cdot \hat{\mathbf{u}} = 0$$

^IThe three-dimensional development of instabilities in boundary layer flows over compliant walls was investigated by authors as Carpenter & Gajjar [14]. They compared their theory to that of Benjamin [5] [6] [7] with regards to the stabilisation of Class B TWF.

^{II}Note that this non-dimensionalisation only holds for the plane channel flow and cannot be extended to other flow configurations such as the semi-infinite Blasius boundary layer flow. This is mainly due to the fact that the plane channel flow has an inherent length-scale built into it, namely the channel half-width, unlike the Blasius case.

$$\text{where } \hat{\mathbf{u}} = (\hat{u}, \hat{v}) \quad \text{and} \quad \nabla = \left(\frac{\partial}{\partial x}, \frac{\partial}{\partial y} \right).$$

In the case considered here, the body force \mathbf{F} includes the effect of gravity only. Since the flow can be assumed to be flowing vertically downwards (i.e. the flow is gravity-driven), this term can be neglected. The Navier-Stokes equations can now be written in their full form as:

$$x\text{-momentum equation: } \hat{u}_t + \hat{u}\hat{u}_x + \hat{v}\hat{u}_y = -\hat{p}_x + \frac{1}{\text{Re}} (\hat{u}_{xx} + \hat{u}_{yy}) \quad (2.2a)$$

$$y\text{-momentum equation: } \hat{v}_t + \hat{u}\hat{v}_x + \hat{v}\hat{v}_y = -\hat{p}_y + \frac{1}{\text{Re}} (\hat{v}_{xx} + \hat{v}_{yy}) \quad (2.2b)$$

$$\text{Conservation of mass } \hat{u}_x + \hat{v}_y = 0. \quad (2.2c)$$

Note that the subscripts here denote differentiation (for instance for a function f , f_x denotes $\frac{\partial f}{\partial x}$, f_{xx} denotes $\frac{\partial^2 f}{\partial x^2}$ etc.).

If only two-dimensional disturbances are considered, then for a small parameter $\varepsilon > 0$, the disturbed quantities \hat{u} , \hat{v} and \hat{p} can be expressed as:

$$\begin{aligned} \hat{u}(x, y, t) &= U(x, y, t) + \varepsilon \tilde{u}(x, y, t) \\ \hat{v}(x, y, t) &= V(x, y, t) + \varepsilon \tilde{v}(x, y, t) \\ \hat{p}(x, y, t) &= P(x, y, t) + \varepsilon \tilde{p}(x, y, t). \end{aligned} \quad (2.3)$$

The terms with a tilde ($\tilde{\square}$) denote *perturbation* quantities and U, V and P are the *basic* (undisturbed) velocity and pressure profiles. In the current work, only the first order approximation is used since the investigation is carried out on the linear theory only. For the undisturbed plane channel flow, the streamwise basic velocity profile is parabolic and there is no normal velocity

component, i.e.

$$U(x, y, t) = U(y) = 1 - y^2 \quad \text{and} \quad V(x, y, t) = 0.$$

The perturbation terms appear as $\mathcal{O}(\varepsilon)$ terms which are

$$\tilde{u}_t + U\tilde{u}_x + U_y\tilde{v} = -\tilde{p}_x + \frac{1}{\text{Re}}(\tilde{u}_{xx} + \tilde{u}_{yy}) \quad (2.4a)$$

$$\tilde{v}_t + U\tilde{v}_x = -\tilde{p}_y + \frac{1}{\text{Re}}(\tilde{v}_{xx} + \tilde{v}_{yy}) \quad (2.4b)$$

$$\tilde{u}_x + \tilde{v}_y = 0. \quad (2.4c)$$

Since the flow is two-dimensional, a streamfunction $\psi = \psi(x, y, t)$ can be introduced which satisfies

$$\tilde{u} = \frac{\partial\psi}{\partial y} \quad \text{and} \quad \tilde{v} = -\frac{\partial\psi}{\partial x}.$$

This allows the incompressibility condition (2.4c) to be satisfied identically. In order to tackle the resulting set of equations, a *normal mode decomposition* is employed.

2.1.1 Normal Mode Decomposition

The normal mode decomposition is a result of a Fourier-type analysis which assumes that the streamfunction ψ takes the form of a wave that evolves periodically in x and t with an amplitude function $\varphi = \varphi(y)$ as

$$\psi(x, y, t) = \varphi(y)e^{i(\alpha x - \omega t)}.$$

The function φ represents the *disturbance velocity profile*, $\omega \in \mathbb{C}$ is the *temporal frequency* and $\alpha \in \mathbb{C}$ is the *spatial wavenumber*. (Note that if α is real, it takes the form $\alpha = \frac{2\pi}{\lambda}$ where λ is the disturbance wavelength.) With the normal mode decomposition in mind, the stability characteristics of the flow can be classified depending on whether the imaginary parts of α and ω are positive or negative as shown in Table 2.1 (note that $\Re(z)$ and $\Im(z)$ denote the real and imaginary parts of a complex number z respectively).

	$\Im(\alpha) < 0$	$\Im(\alpha) = 0$	$\Im(\alpha) > 0$
$\Im(\omega) < 0$	Spatio-temporal	Temporally stable	Spatio-temporal
$\Im(\omega) = 0$	Spatially unstable	Neutrally stable	Spatially stable
$\Im(\omega) > 0$	Spatio-temporal	Temporally unstable	Spatio-temporal

Table 2.1: Different stability characteristics of the flow depending on the signs of $\Im(\omega)$ and $\Im(\alpha)$.

Applying the normal mode decomposition to the perturbation quantities \tilde{u} , \tilde{v} and \tilde{p} gives expressions in terms of the flow parameters α, ω and φ as

$$\begin{aligned}
 \tilde{u}(x, y, t) &= \varphi'(y)e^{i(\alpha x - \omega t)} \\
 \tilde{v}(x, y, t) &= -i\alpha\varphi(y)e^{i(\alpha x - \omega t)} \\
 \tilde{p}(x, y, t) &= p(y)e^{i(\alpha x - \omega t)}.
 \end{aligned} \tag{2.5}$$

The primes (\square') here represent differentiation with respect to y and p is a function arising due to the normal mode decomposition being applied to \tilde{p} . Using this approximation on the flow variables implies that differentiating with respect to x is equivalent to multiplying by $i\alpha$ while differentiating with

respect to t is equivalent to multiplying by $-i\omega$, i.e.

$$\frac{\partial \tilde{f}}{\partial x} \equiv i\alpha f \quad \text{and} \quad \frac{\partial \tilde{f}}{\partial t} \equiv -i\omega f \quad \text{for} \quad f = u, v, p.$$

When these decompositions are used in the momentum equations (2.2a) and (2.2b), the set of equations can be written in terms of the *phase speed* $c = \frac{\omega}{\alpha}$ as

$$(U - c)\varphi' - U'\varphi = -p + \frac{1}{i\alpha\text{Re}}(\varphi''' - \alpha^2\varphi') \quad (2.6a)$$

$$\alpha^2(U - c)\varphi = -p' - \frac{i\alpha}{\text{Re}}(\varphi'' - \alpha^2\varphi). \quad (2.6b)$$

The phase speed c of the wave is the rate at which the phase travels through space. If $\Im(c) > 0$ for at least one disturbance mode, then the flow is deemed unstable but if $\Im(c) < 0$ for all disturbance modes, then the flow is stable.

The pressure term p can be eliminated from (2.6) to give the well-known *Orr-Sommerfeld equation*

$$(U - c)(\varphi'' - \alpha^2\varphi) - U''\varphi = \frac{1}{i\alpha\text{Re}}(\varphi'''' - 2\alpha^2\varphi'' + \alpha^4\varphi). \quad (2.7)$$

This is a fourth order ordinary differential equation in the disturbance profile φ which dictates the stability of parallel viscous flows.

For a parallel *inviscid* flow, the disturbances are governed by the *Rayleigh equation*

$$(U - c)(\varphi'' - \alpha^2\varphi) - U''\varphi = 0. \quad (2.8)$$

This can be derived in the same way from the Euler equations and is equivalent to the Orr-Sommerfeld equation after formally passing the limit $\text{Re} \rightarrow \infty$.

This second order ordinary differential equation has two linearly independent solutions which were first derived by Heisenberg [70]^{III}. In his solution, φ was expanded asymptotically in powers of α^2 which resulted in two decoupled solutions, one of which is symmetric/even about the channel centreline ($\varphi(-y) = \varphi(y)$ for all $y \in [-1, 1]$) while the other is antisymmetric/odd^{IV} ($\varphi(-y) = -\varphi(y)$ for all $y \in [-1, 1]$). A brief description of his solution is outlined in Appendix A.

For the rigid wall plane channel flow, the TS instability is dictated by the symmetric modes therefore for the purposes of TS suppression, the symmetric form of φ is considered. It is possible that there may be cases where an antisymmetric counterpart to the TS wave is more effective at destabilising the flow in the compliant wall case but these are not studied here. Later in §2.4, the consequences of considering a symmetric form of φ is illustrated by numerical examples.

Due to the symmetry of φ , only one half of the channel needs to be considered since the other is the same because of symmetry. For the sake of convenience, the upper half channel $y \in [0, 1]$ is considered. Note that \tilde{v} will be even while \tilde{u} and \tilde{p} will be odd if φ is assumed to be even (from equations (2.5)).

2.1.2 Squire's Theorem

Only two-dimensional disturbances are considered here as a consequence of the following theorem:

^{III}Werner Heisenberg derived these solutions in 1924 in his earlier work on hydrodynamic stability theory with his Doctoral advisor Arnold Sommerfeld before embarking on quantum mechanics.

^{IV}The terms “even” and “symmetric” in the context of functions will be used interchangeably, similarly for “odd” and “antisymmetric”.

Squire's Theorem. [24] Consider a three-dimensional unstable mode with flow parameters $(\alpha_x, \alpha_z, \omega)$ where α_x and α_z are the streamwise and spanwise wavenumbers respectively while ω is the temporal frequency with a growth rate $\omega_i = \Im(\omega)$. For this particular mode, there exists an associated two-dimensional mode $(\tilde{\alpha}, \tilde{\omega})$ with a temporal growth rate

$$\tilde{\omega}_i = \Im(\tilde{\omega}) = \frac{\sqrt{\alpha_x^2 + \alpha_z^2}}{\alpha_x} \omega_i$$

which is more unstable than its three-dimensional counterpart since $\tilde{\omega}_i > \omega_i$.

This theorem holds for the rigid wall case however the extension to the compliant wall is only possible for a particular non-dimensionalisation of the wall parameters.

2.1.3 Pressure Integral

The Orr-Sommerfeld equation in its form given in (2.7) does not take pressure into account. So in order to obtain an expression for the pressure p , consider the y -momentum equation (2.6b)

$$p'(y) = -\alpha^2(U - c)\varphi + \frac{i\alpha^3}{\text{Re}}\varphi - \frac{i\alpha}{\text{Re}}\varphi''.$$

Integrating across the channel half-width $y \in [0, 1]$ and using the fact that $\varphi'(0) = p(0) = 0$ (since they are both odd), the y -momentum equation then gives a condition for the pressure at the upper wall, namely

$$p(1) = -\alpha^2 \int_0^1 \left[(U - c)\varphi - \underbrace{\frac{i\alpha}{\text{Re}}\varphi}_{\text{(I)}} \right] dy - \underbrace{\frac{i\alpha}{\text{Re}}\varphi}_{\text{(II)}}. \quad (2.9)$$

The magnitude of the term labelled (II) is, in fact, half of the normal viscous stress acting on the wall. It can be assumed that the fluid stresses driving the wall motion can be approximated using the pressure only and to this end, the term (II) can be dispensed with, similarly for the term labelled (I) (further details of these assumptions are given in Davies & Carpenter [30]). Therefore, the terms involving $\frac{\alpha}{\text{Re}}$ can be neglected and the pressure at the upper wall can be expressed as

$$p(1) = -\alpha^2 \int_0^1 (U - c)\varphi \, dy. \quad (2.10)$$

This form of the pressure will prove useful in the numerical treatment of the system of equations.

2.2 Boundary Conditions

2.2.1 Rigid Walls

The Orr-Sommerfeld equation is a fourth order ordinary differential equation and would therefore require four boundary conditions. For the rigid wall plane channel flow, these are simply the no penetration and no slip at the walls, namely

$$\varphi(\pm 1) = \varphi'(\pm 1) = 0. \quad (2.11)$$

As for the Rayleigh equation, the only conditions that need to be imposed are the no penetration conditions at the walls, i.e. $\varphi(\pm 1) = 0$.

As mentioned earlier, since the stability of the rigid walled plane channel flow is dictated by the even modes, then two boundary conditions would suffice and these are imposed at the upper wall $y = 1$. Therefore the Orr-Sommerfeld equation only requires two boundary conditions $\varphi(1) = \varphi'(1) = 0$. Similarly,

the Rayleigh equation requires one boundary condition $\varphi(1) = 0$.

2.2.2 Compliant Walls

For the spring-backed plate model, the pressure driven wall equation at the upper wall (in its dimensional form) is given by

$$p^*(x^*, h, t^*) = \left(m^* \frac{\partial^2}{\partial t^{*2}} + d^* \frac{\partial}{\partial t^*} + B^* \frac{\partial^4}{\partial x^{*4}} - T^* \frac{\partial^2}{\partial x^{*2}} + K^* \right) \eta^*(x^*, t^*) \quad (2.12)$$

where η^* is the vertical displacement of the upper wall from equilibrium and the terms with an asterisk (\square^*) denote dimensional quantities^V. The flow parameters are non-dimensionalised using (2.1) while the wall parameters can be non-dimensionalised by using

$$m = \frac{m^*}{\rho h}, \quad \frac{d}{\text{Re}} = \frac{d^*}{\rho U_m}, \quad \frac{B}{\text{Re}^2} = \frac{B^*}{\rho h^3 U_m^2}, \quad \frac{T}{\text{Re}^2} = \frac{T^*}{\rho h U_m^2}, \quad \frac{K}{\text{Re}^2} = \frac{K^* h}{\rho U_m^2}, \quad \hat{\eta} = \frac{\tilde{\eta}}{h}. \quad (2.13)$$

This particular form of the non-dimensionalisation is chosen since there is no explicit mention of the centreline velocity U_m , therefore the Reynolds number Re can be varied by changing U_m hence keeping the flow terms h and ν fixed and consequently, the wall parameters m, B, T, K and d will also remain fixed as well^{VI}. The pressure at the upper wall given in (2.12) then becomes

$$\tilde{p}(x, 1, t) = \left(m \frac{\partial^2}{\partial t^2} + \frac{d}{\text{Re}} \frac{\partial}{\partial t} + \frac{1}{\text{Re}^2} \left[B \frac{\partial^4}{\partial x^4} + T \frac{\partial^2}{\partial x^2} + K \right] \right) \tilde{\eta}(x, t) \quad (2.14)$$

where the wall parameters are now non-dimensional.

^VFurther details of the spring-backed compliant wall model are given in Carpenter & Garrad [21] [22].

^{VI}Note that, once again, this non-dimensionalisation only holds for the plane channel flow and cannot be readily extended to other flow configurations where there is only a locally defined measure of the boundary layer thickness such as the Blasius flow.

In this context, the spring-backed plate model consists of a thin flexible membrane of mass m with a damping coefficient d and flexural rigidity B . The plate is pulled taut with tension per unit length T and is attached perpendicularly to a series of springs. These springs have a spring stiffness K and are held perpendicularly to a rigid base. For the sake of simplicity, the flexible membrane is restricted to move in the vertical direction only. A schematic representation of the wall model is shown in Figure 2.2 (further descriptions of each of the individual wall terms was given in §1.5.3).

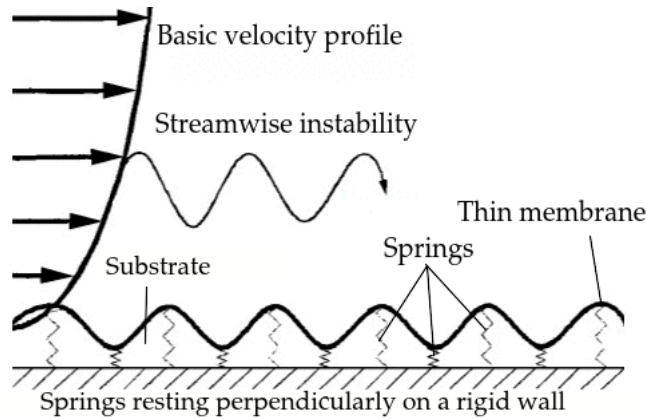


Figure 2.2: The spring-backed plate model for half the channel.

The disturbance profile φ was assumed to be symmetric and therefore, this requires that the vertical displacement of the compliant wall from its equilibrium position η has to also be symmetric. This means that both the upper and lower walls will move away or towards the channel centreline simultaneously as opposed to moving in the same direction, this is best observed diagrammatically as shown in Figure 2.3.

When the normal mode decomposition is used on both \tilde{p} and $\tilde{\eta}$ in equation (2.14), i.e.

$$\tilde{p}(x, y, t) = p(y)e^{i(\alpha x - \omega t)} \quad \text{and} \quad \tilde{\eta}(x, t) = \eta e^{i(\alpha x - \omega t)},$$

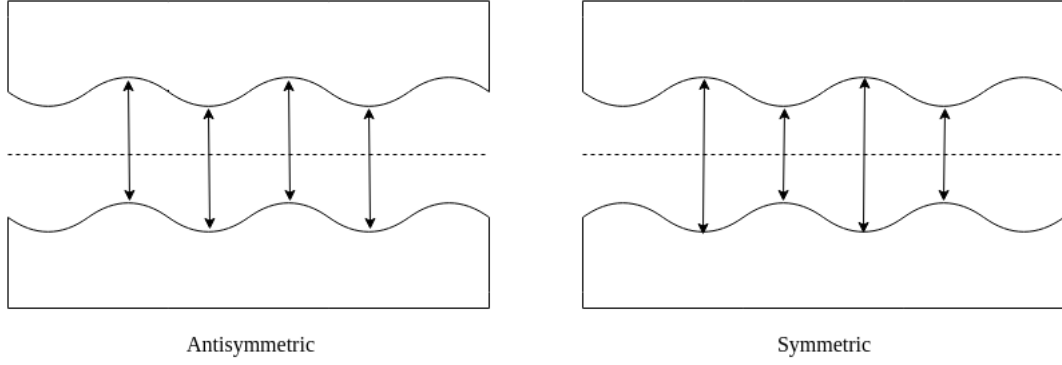


Figure 2.3: Difference between choosing symmetric and antisymmetric disturbance profiles, the dotted line represents the channel centreline.

the result gives an expression for the pressure at the upper wall as

$$p(1) = \left(-m\omega^2 - \frac{id\omega}{\text{Re}} + \frac{1}{\text{Re}^2} [B\alpha^4 + T\alpha^2 + K] \right) \eta. \quad (2.15)$$

The compliant wall properties are subsequently characterised by two quantities:

- * The *stiffness coefficient* \mathcal{S} which takes the form:

$$\mathcal{S}(\alpha, c) = -mc^2 - \frac{idc}{\alpha \text{Re}} + \frac{1}{\text{Re}^2} \left[B\alpha^2 + T + \frac{K}{\alpha^2} \right]. \quad (2.16)$$

Thus the pressure in equation (2.15) can be written as

$$p(1) = \alpha^2 \mathcal{S}(\alpha, \omega) \eta.$$

- * The *effective stiffness* σ which takes the form:

$$\sigma(\alpha) = B\alpha^4 + T\alpha^2 + K. \quad (2.17)$$

Therefore (2.15) can be written as

$$p(1) = \left(-m\omega^2 - \frac{id\omega}{\text{Re}} + \frac{1}{\text{Re}^2} \sigma(\alpha) \right) \eta.$$

Since the wall is flexible, the movement of the fluid near the wall has to be coupled with the movement of the wall itself. Therefore matching the horizontal and vertical velocity components at the upper wall will give the linearised boundary conditions:

$$\varphi(1) = c\eta \tag{2.18a}$$

$$\varphi'(1) = -U'(1)\eta. \tag{2.18b}$$

(See for example, Carpenter & Garrad [21].)

Another form of the boundary conditions that involves the wall parameters may be obtained by first eliminating η from (2.18) to give

$$U'(1)\varphi(1) + c\varphi'(1) = 0. \tag{2.19}$$

Eliminating η from (2.18b) and (2.15) (and using (2.16)) gives

$$p(1)c - \varphi(1)\mathcal{S}(\alpha, c) = 0. \tag{2.20}$$

The two equations (2.19) and (2.20) provide another form of the boundary conditions that depend on the wall's stiffness coefficient \mathcal{S} rather than its vertical displacement from equilibrium η . This alternative formulation is helpful when it comes to discretising the boundary conditions when solving the Orr-Sommerfeld equation numerically as will be described in Chapter 3. (Notice that if the wall is made stiffer, i.e. $\mathcal{S}(\alpha, \omega) \rightarrow \infty$ or $\eta \rightarrow 0$, then the rigid wall boundary conditions can be recovered.)

2.3 Previous Analytic Work

For the current problem, a major analytic treatment was conducted by Davies [28] and Davies & Carpenter [30] amongst others (these two are mentioned here since they are the most relevant to the current study). They obtained analytic approximations to the dispersion relation, onset flow speeds of the different instabilities and analytic approximations to neutral stability curves (subject to certain assumptions). Here, a selection of these analytic results are mentioned since they are used in Chapter 6.

2.3.1 Dispersion Relation

The Orr-Sommerfeld equation and its boundary conditions form a relationship that takes the form

$$\mathcal{D}(\alpha, \omega; \text{Re}) = 0.$$

This is known as the *dispersion relation* which relates the wall and flow parameters for the current flow configuration. In the absence of the fluid flow, the wall itself can carry a wave with a speed c_0 , this is known as the *free-wave speed* and takes the form

$$c_0 = \frac{1}{\text{Re}} \sqrt{\frac{1}{m\alpha^2} \sigma(\alpha)}.$$

Using this, the wall's stiffness coefficient (2.16) can be rearranged to give an expression of the dispersion relation which relates the flow and wall parameters as

$$m(c^2 - c_0^2) + \mathcal{S}(\alpha, c) + \frac{idc}{\alpha \text{Re}} = 0. \quad (2.21)$$

In the inviscid case, the free-wave speed c_0 cannot be expressed in terms of the Reynolds number, indeed, it will be expressed in terms of the channel centreline velocity U_m . In order to do so, let

$$\bar{f} = \frac{U_m^2}{\text{Re}^2} f \quad \text{for } f = B, T, K \quad (2.22)$$

and these now have the same dimension as the square of the velocity. The free-wave speed c_0 (which is still dimensionless) can now be written as

$$c_0 = \frac{1}{U_m} \sqrt{\frac{1}{m\alpha^2} \bar{\sigma}(\alpha)}. \quad (2.23)$$

In order to obtain expressions for the onset flow speeds of the different instabilities, suppose that the minimum dimensional free wave speed that the compliant wall can attain is given by U_0 , i.e.

$$U_0 = \min_{\alpha} \left(\sqrt{\frac{\bar{\sigma}(\alpha)}{\alpha^2}} \right).$$

Therefore

$$U_0 \leq \sqrt{\frac{\bar{\sigma}(\alpha)}{\alpha^2}} = U_m c_0 \sqrt{m} \quad \text{by using (2.23).}$$

The minimum value U_0 is attained when the wavenumber α takes a critical value α_c where

$$\alpha_c = \sqrt[4]{\frac{\bar{K}}{\bar{B}}} \quad (2.24)$$

The critical wavenumber α_c can also be written differently using (2.22) as

$$\alpha_c = \sqrt[4]{\frac{K}{B}}.$$

This can give an explicit expansion for U_0 as

$$U_0 = \sqrt{2\sqrt{\bar{B}\bar{K}} + \bar{T}} = \frac{U_m}{\text{Re}} \sqrt{2\sqrt{BK} + T}. \quad (2.25)$$

By imposing a long wave approximation ($\alpha \sim 0$), Davies & Carpenter [30] obtained expressions for the critical flow speeds which cause the onset of certain instabilities. First, they assumed that the wavenumber is small, in particular $\alpha^2 \sim 0$, and obtained an approximation to the wall stiffness. The dispersion relation (2.21) was then used to show that the *flutter-type instability* (which arises due to a interaction between divergence and TWF) has the onset flow speed

$$U_F = U_0 \frac{3}{2} \sqrt{\frac{5m+5}{6m+1}}. \quad (2.26)$$

If the damping is assumed to be quite small (particularly $d^2 \sim 0$), then the divergence onset flow speed can be obtained by setting $c = 0$ (since this is the onset phase speed for divergence) to give

$$U_d = U_0 \sqrt{\frac{15}{8}}. \quad (2.27)$$

Finally, in the absence of damping ($d = 0$) and at $c = 1$ (onset phase speed of the TWF instability), the dispersion relation yields an approximation for the TWF onset flow speed as

$$U_{TWF} = U_0 \sqrt{\frac{5}{5m+1}}. \quad (2.28)$$

The onset flow speeds in equations (2.26), (2.27) and (2.28) provide expressions for the onset Reynolds numbers by using (2.25). Note that if the wall mass

$m > \frac{1}{3}$, then

$$U_{TWF} < U_d < U_F$$

but if $0 < m < \frac{1}{3}$, then

$$U_d < U_{TWF} < U_F.$$

From these approximations, it can be seen that the wall mass affects the onset flow speed of TWF and can push it above or below that of divergence (whose onset is unaffected by the change in mass). However, note the coalescence between these two, the flutter-type instability, always sets at a flow speed beyond either TWF or divergence.

All these derivations are discussed at length in Davies & Carpenter [30] to which reference should be made for further details, they are mentioned here since they are used later in Chapter 6.

2.4 Numerical Examples: Eigenvalues & Neutral Stability Curves

In this section, preliminary numerical examples are presented which reproduce well-known results for the rigid wall case and some comparisons with the compliant wall case as well.

For a fixed value of Re , the Orr-Sommerfeld equation and its boundary conditions form an eigenvalue problem for the eigenfunction φ and eigenvalues α , c or ω (depending on how the problem is formulated). Details regarding the formulation of the eigenvalue problems is presented in Chapter 3 but in this section, only a preliminary account of some results is given.

The results shown here are already very well-known, they are presented mainly to show eigenvalues and neutral stability curves as well as the consequences of choosing an even disturbance profile φ . Some examples of eigenvalues on the complex α and ω planes and neutral stability curves are also shown.

2.4.1 Temporal Stability

The Orr-Sommerfeld equation and its boundary conditions can be written in the form a *temporal eigenvalue problem* where the complex eigenvalues ω are to be determined for fixed Re and $\alpha \in \mathbb{R}$. When $\Im(\omega) > 0$, the flow is termed *temporally unstable* but if $\Im(\omega) < 0$, then it is *temporally stable*.

Figure 2.4 shows the ω eigenvalues on the complex ω -plane for the rigid wall plane channel flow with $Re = 10000$ and $\alpha = 1$. In general for a real value of α , the eigenvalues accumulate around three branches: the *A branch* (where $\Re(\frac{\omega}{\alpha}) \rightarrow 0$), *P branch* (where $\Re(\frac{\omega}{\alpha}) \rightarrow 1$) and *S branch* (where $\Re(\frac{\omega}{\alpha}) \approx \frac{2}{3}$ according to Schmid & Henningson [115]). The figure shows the eigenvalues that result from taking even (red) and odd (blue) modes separately, this is possible since both solutions are uncoupled (as shown by Heisenberg [70] and outlined in Appendix A). The only temporally unstable eigenvalue with $\Im(\omega) > 0$ (circled) corresponds to the flow-based TS instability which belongs to the set of eigenvalues obtained from assuming that φ is even.

Figure 2.5 shows a curve on the α - Re plane which separates the region of the parameter space where the flow is temporally stable ($\Im(\omega) < 0$) and temporally unstable ($\Im(\omega) > 0$). This curve is known as the *neutral stability curve* and represents the locations where $\Im(\omega) = 0 = \Im(\alpha) = 0$. The critical Reynolds number is located at $Re_c = 5772.2$, this means that if $Re < Re_c$,

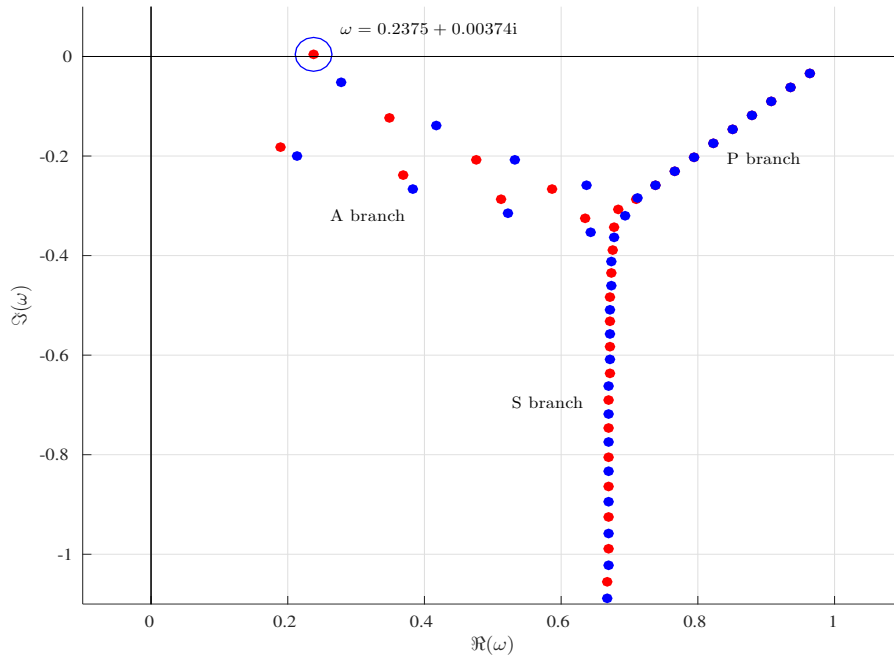


Figure 2.4: ω eigenvalues of the Orr-Sommerfeld equation with rigid wall boundary conditions at $\text{Re} = 10000$ and $\alpha = 1$, the A , P and S branches are labelled accordingly. The red/blue points denote the eigenvalues corresponding to the case when φ is even/odd. The only temporally unstable eigenvalue is circled and belongs to the set of values obtained by assuming that φ is even.

then the flow is temporally stable for all values of α but if $\text{Re} > \text{Re}_c$, then the flow is stable for some values of α (this is denoted by a vertical dashed line).

According to Cowley & Wu [25], the upper and lower branches of the neutral stability curve represent different underlying structures and reflect different physical balances at play, in fact, each branch represents a distinguished asymptotic scaling. Analytically, these scalings are obtained from the maximal interactions between the competing processes and the major difficulty comes about when attempting to identify these appropriate scalings.

In order to have a more complete picture of what happens in the α - Re plane, *curves of constant growth rate* can be plotted, these lines represent locations where $\Im(\omega)$ take fixed values. Figure 2.6 shows the growth and decay contours

for the rigid walled plane channel flow, the growth contours are those with $\Im(\omega) > 0$ and decay contours with $\Im(\omega) < 0$. These curves can provide a good indication of the general stability characteristics of the flow in the α -Re- $\Im(\omega)$ space as a whole (this is discussed later in Chapter 3).

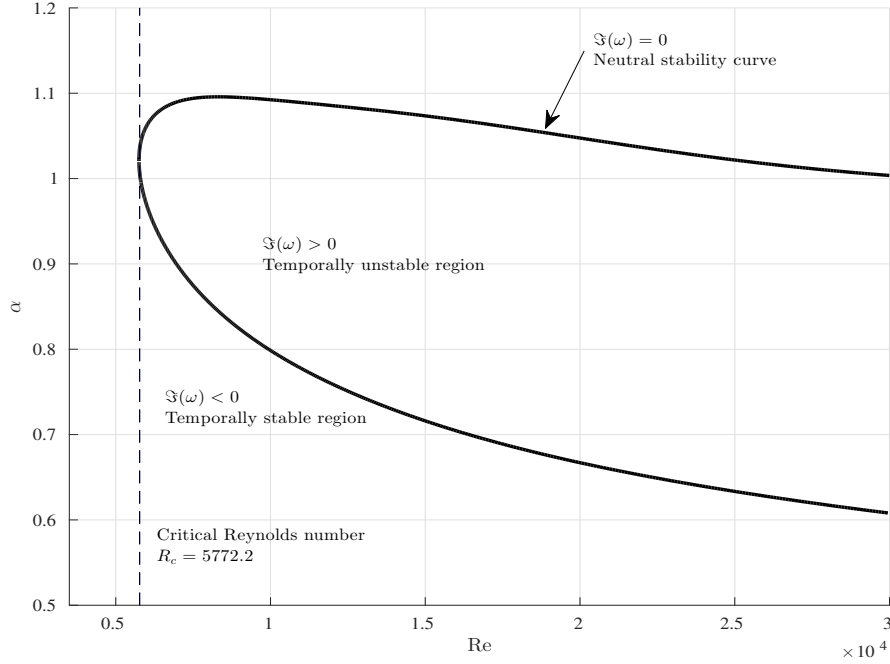


Figure 2.5: Neutral stability curve on the α -Re plane for the rigid wall plane channel flow. The neutral curve separates the temporally stable and unstable regions of the α -Re plane. The critical Reynolds number $Re_c = 5772.2$ is denoted by a vertical dashed line.

2.4.2 Spatial Stability

The Orr-Sommerfeld equation (2.7) can be reformulated to form a *spatial eigenvalue problem* as

$$\left[\frac{1}{iR} \varphi \right] \alpha^4 + \left[(U-c)\varphi \right] \alpha^3 + \left[-\frac{2}{iR} \varphi'' \right] \alpha^2 + \left[-(U-c)\varphi'' + U''\varphi \right] \alpha + \left[\frac{1}{iR} \varphi'''' \right] = 0.$$

In this case, the complex eigenvalues $\alpha \in \mathbb{C}$ are to be determined for fixed Re and $\omega \in \mathbb{R}$. When $\Im(\alpha) < 0$, the flow is termed *spatially unstable* but if

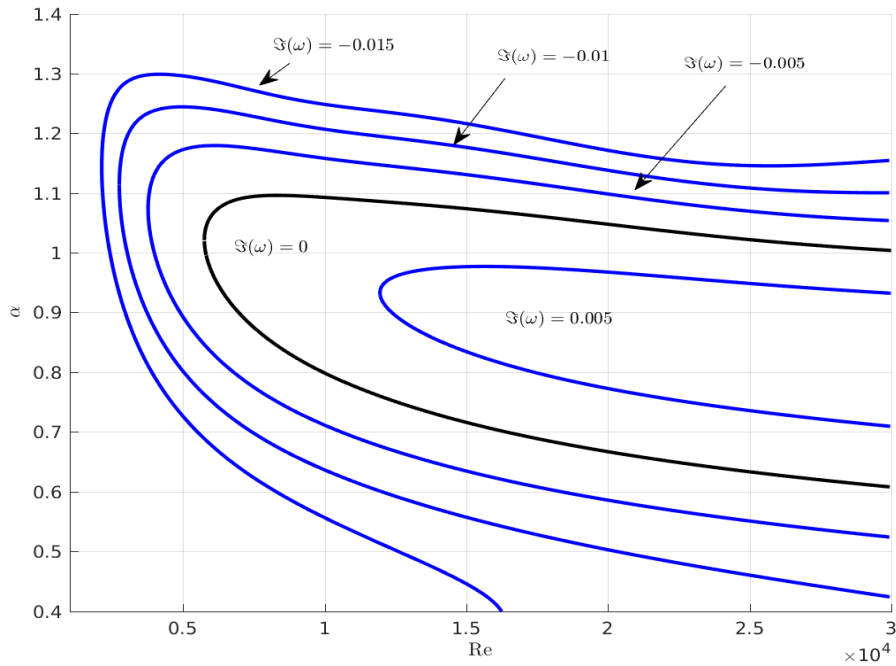


Figure 2.6: Curves of constant growth/decay rate. The curves of constant growth rate are given by the curves when of $\Im(\omega) > 0$ while the curves of constant decay rate are given by $\Im(\omega) < 0$.

$\Im(\alpha) > 0$, then it is *spatially stable*.

Figure 2.7 shows the α -eigenvalues for the rigid wall plane channel flow with $\text{Re} = 10000$ and $\omega = 0.2375$. Just as before, the eigenvalues shown are those which result from taking even (red) and odd (blue) modes separately. The only spatially unstable eigenvalue with $\Im(\alpha) < 0$ (circled) is a result of assuming that φ is symmetric.

From Figures 2.4 and 2.7, it can be seen that the assumption of a symmetric form of φ would suffice for dictating the stability of the flow for the rigid wall plane channel flow, corroborating the assumptions made earlier. This assumption also simplifies the analysis substantially as will become apparent in the subsequent chapters.

These numerical results only illustrate the fact that the most unstable mode

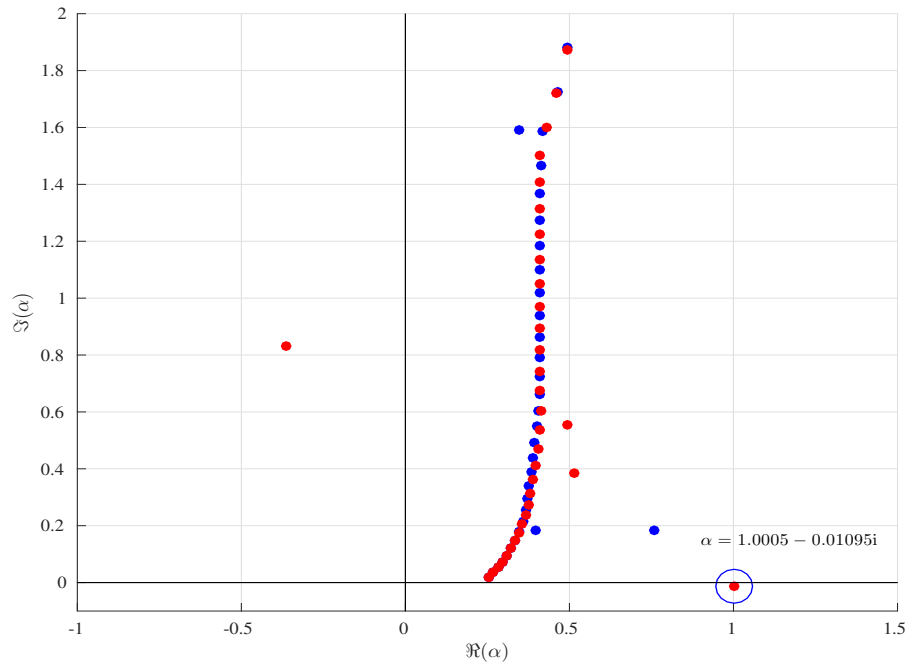


Figure 2.7: α eigenvalues of the Orr-Sommerfeld equation with rigid boundaries at $R = 10000$ and $\omega = 0.2375$. The red/blue points denote the eigenvalues corresponding to the case when φ is even/odd. The only spatially unstable mode is given by the circled eigenvalue and belongs to the set of values obtained by assuming that φ is even.

in the rigid wall case, being the TS mode, is governed by the even modes of the Orr-Sommerfeld equation. Therefore restriction to the even modes aids in the investigation of TS stabilisation as well as the interaction between the different modes under this assumption. Moreover, this condition is also instrumental because of the analogy with the semi-infinite flows such as the Blasius case (although this investigation is not carried out here).

2.5 Stabilisation of Tollmien-Schlichting Waves by using Compliant Walls

From the rigid wall plane channel flow, the most unstable mode is that belonging to the TS mode. When the wall is compliant, however, the TS

mode is altered and new modes corresponding to the wall-based instabilities will be present on the complex ω and α -planes. This change in boundary conditions modifies the shape of the neutral stability curve for TS instability and introduce new curves which correspond to the wall-based modes as well.

An example of this is given in Figure 2.8 which shows the neutral stability curves on the α -Re plane for the rigid wall (black) compared to three different compliant walls with parameters:

$$m = 2, \quad B = 4K, \quad T = 0, \quad d = 0 \quad \text{with} \quad K = 10^7, 2 \times 10^7, 6 \times 10^7.$$

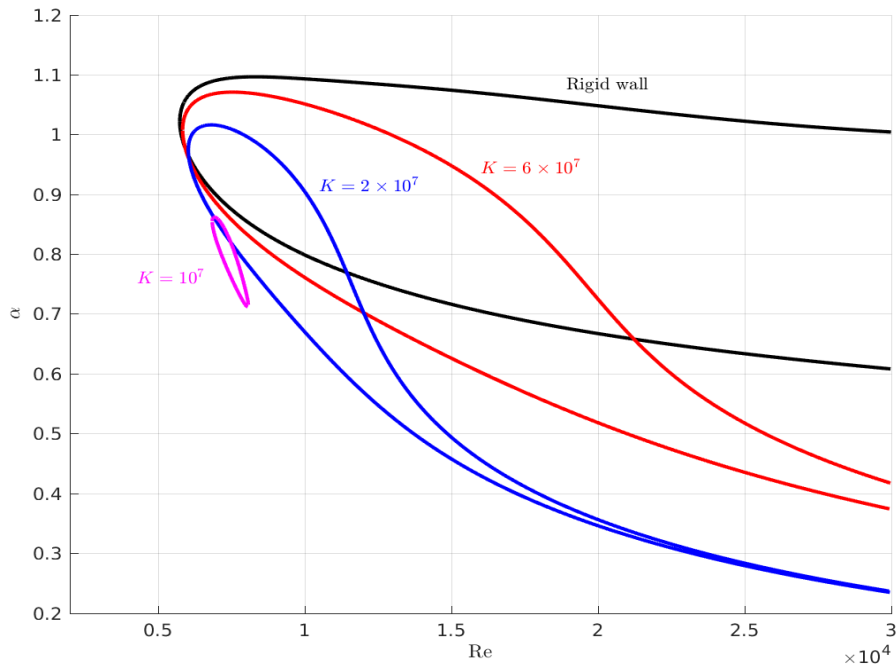


Figure 2.8: Neutral stability curves for the flow-based TS mode on the α -Re plane for the rigid wall (black) and the compliant walls with the parameters $m = 2, B = 4K, T = 0, d = 0$ with $K = 10^7, 2 \times 10^7, 6 \times 10^7$ (labelled accordingly).

(Note that the results shown here are reproduced from Davies & Carpenter [30] and are included here for illustration purposes.) As the wall is made softer by decreasing the value of K (and B accordingly), the neutral stability curve

shrinks down to a small loop, this implies that this set of wall parameters causes the unstable region of the parameter space to shrink down leading to the stabilisation of the TS instability.

Figure 2.9 shows the neutral stability curve for the TWF mode. As the wall is made softer, the wall-based mode starts to occupy a larger region of the α -Re plane even though the TS mode has been significantly stabilised. This demonstrates the fact that since the wall can carry a wave independently of the fluid, the wall flexibility results in wall-based instabilities that can be more effective at destabilising the flow at an even wider range of flow parameters.

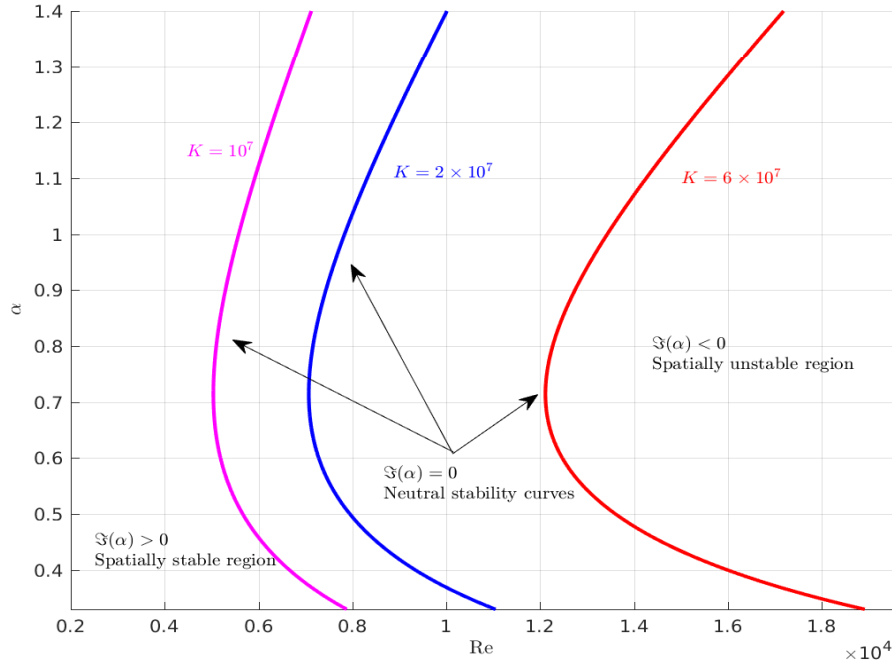


Figure 2.9: Neutral stability curves for the wall-based insatiability on the α -Re plane for the compliant walls with parameters $m = 2$, $B = 4K$, $T = 0$, $d = 0$ with $K = 10^7, 2 \times 10^7, 6 \times 10^7$ (labelled accordingly).

Instead of studying the neutral stability curves on the α -Re plane, an alternative is to consider the ω -Re plane. In this case, the neutral curve separates the parameter space into regions where the flow is spatially stable/unstable. Figure 2.10 shows the neutral curve for the rigid wall (black) and compliant

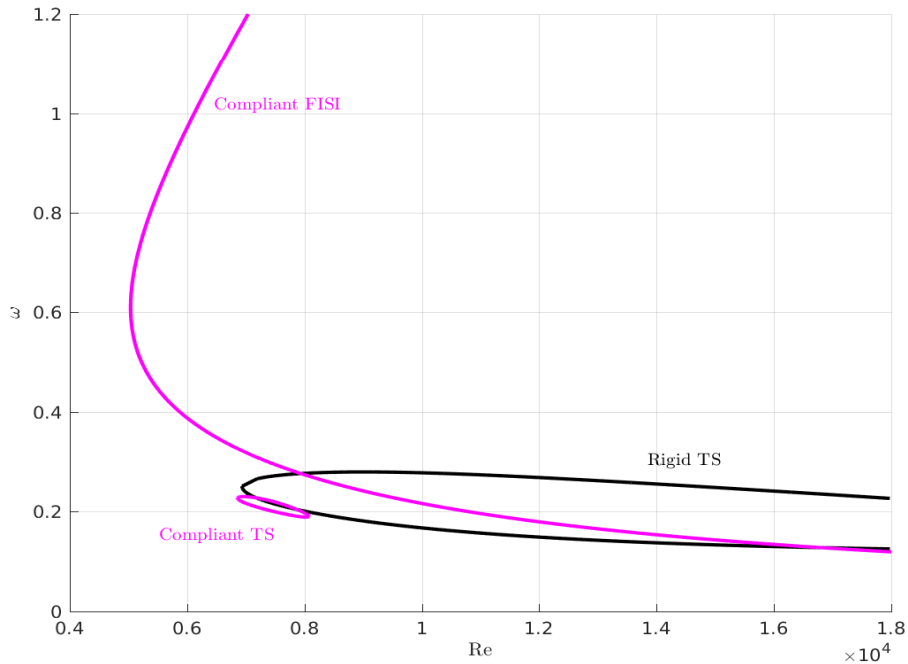


Figure 2.10: Neutral stability curves on the ω -Re plane for the rigid wall (black) and the compliant wall (magenta) with parameters $m = 2$, $B = 4 \times 10^7$, $T = 0$, $K = 10^7$, $d = 0$.

wall with $K = 10^7$ (magenta). The curve corresponding to the rigid wall TS mode occupies a region for relatively small values of the frequency ω . However when the wall is compliant, the TS neutral curve shrinks down to a small loop but as a consequence of stabilising the TS instability, the wall's flexibility introduces another instability occupying a large portion of the parameter space, this is the TWF wall-based mode and is labelled as FIS I (*flow-induced surface instability*).

From these preliminary numerical results, it can be seen that even though the compliant wall may stabilise the flow-based TS mode, it can still introduce wall-based modes that pose a problem to the stability of the flow as a whole. The way in which these numerical results were obtained is elaborated upon in the following chapter.

Chapter 3

Numerical Solution of the Orr-Sommerfeld Equation

In this chapter, the numerical method used to solve the eigenvalue problem consisting of the Orr-Sommerfeld equation and its boundary conditions are discussed. The numerical scheme used here involves discretising the disturbance and basic velocity profiles in the y -direction using the *Chebyshev collocation method*. This converts the differential form of the Orr-Sommerfeld equation into a matrix eigenvalue problem, the boundary conditions are then discretised and incorporated into said matrices appropriately. Finally, the resulting matrix system of equations can then be solved numerically on MATLAB to obtain the eigenvalues. A description of the procedure used to plot the neutral stability curves is also presented in the later part of this chapter.

After the numerical procedures have been established, some examples of their application are presented. These include neutral stability curves, curves of constant growth rate and eigenvalues on the complex c -plane. Some interesting features of the neutral curves are also be discussed.

3.1 Chebyshev Collocation Method

For problems in hydrodynamic stability theory, a widely used approach in discretising equations is the *Chebyshev collocation method*. This involves representing the functions of the system as a finite linear combination of Chebyshev polynomials.

The Chebyshev collocation method has a number of practical advantages over other numerical methods such as finite elements. Firstly, this method possesses spectral accuracy, in other words, the error decreases more rapidly than any power of $\frac{1}{N}$ as $N \rightarrow \infty$ where N is the truncation order. On the other hand, finite element methods have an accuracy of finite order, i.e. the error behaves as h^p as the grid scale $h \rightarrow 0$ for $p < \infty$. Using a Chebyshev collocation method also achieves high accuracy with little extra computational effort (see for example Orszag [104]). Moreover, using Chebyshev polynomials as a polynomial basis helps determine coefficients very efficiently compared to other polynomial bases such as Legendre polynomials (see for example Orszag [105]). Other benefits of using Chebyshev polynomials and comparisons with other polynomial bases are discussed by Orszag [104] and Peyret [108] to which reference should be made for further details.

3.2 Discretising the Functions of the System

The first step in the discretisation is to represent the functions of the system φ and U as linear combinations of Chebyshev polynomials. First, the disturbance profile φ is written as a linear combination of the first $N + 1$ Chebyshev

polynomials^I as

$$\varphi(y) = \sum_{n=0}^N a_n T_n(y) \quad (3.1)$$

Since U is a quadratic function, it can be represented as a linear combination of Chebyshev polynomials as

$$U(y) = 1 - y^2 = \frac{1}{2} \left(T_0(y) - T_2(y) \right). \quad (3.2)$$

The function T_n is the n^{th} Chebyshev polynomial of the first kind and is given by

$$T_n(y) = \cos \left(n \cos^{-1}(y) \right) \quad \text{for } n \in \mathbb{N}_0 \quad \text{and } y \in [-1, 1].$$

For this Chebyshev expansion, if the series is truncated at the term T_N , then the residual error is close to a multiple of T_{N+1} (provided the approximated function would possess a rapidly converging power series according to Peyret [108]).

The collocation points used here are the extrema of the N^{th} Chebyshev polynomial, these are known as the *Gauss-Lobatto points* and are given by

$$y_j = \cos \left(\frac{\pi j}{N} \right) \quad \text{for } j = 0, 1, \dots, N. \quad (3.3)$$

This set of points allows a clustering of collocation values near the boundaries $y = \pm 1$ which helps capture the more interesting behaviours that occur near the walls. Another advantage of using Chebyshev polynomials is that they

^IThe number of Chebyshev polynomials chosen for the truncation N has to be large enough to determine the eigenvalues accurately but should not be too large. If the value of N was taken to be excessively large, then the accuracy in determining the eigenvalues would be reduced as found by McBain *et al.* [99].

also possess a relatively simple multiplication formula, namely

$$2T_m(y)T_n(y) = T_{m+n}(y) + T_{|m-n|}(y) \quad \text{for any } m, n \in \mathbb{N}_0.$$

Other properties of Chebyshev polynomials, along with differentiation and integration recipes, are given in Appendix B. The formulae presented there will prove very useful in discretising the Orr-Sommerfeld equation and the boundary conditions.

3.3 Discretising the Differential Operators

The expressions for φ and U in (3.1) and (3.2) can be used to write the Orr-Sommerfeld equation as an eigenvalue problem for either finding the eigenvalues ω or c (corresponding to the temporal case) or α (spatial case).

3.3.1 Phase Speed c -Eigenvalue Problem

Consider the Orr-Sommerfeld equation in its differential form

$$(U - c)(\varphi'' - \alpha^2\varphi) - U''\varphi = \frac{1}{i\alpha\text{Re}}(\varphi'''' - 2\alpha^2\varphi'' + \alpha^4\varphi).$$

Collecting the terms involving c gives

$$\left[\varphi'' - \alpha^2\varphi \right] c + \left[\frac{1}{i\alpha\text{Re}}\varphi'''' - \left(\frac{2\alpha^2}{i\alpha\text{Re}} + U \right) \varphi'' + \left(\frac{\alpha^4}{i\alpha\text{Re}} + \alpha^2U + U'' \right) \varphi \right] = 0. \quad (3.4)$$

Let $\mathbf{a} = (a_0, a_1, \dots, a_N)^T$ be the vector of coefficients of φ in (3.1) (where the superscript T denotes transposition) and let D_n be the matrix representation of the n^{th} derivative for any $n \in \mathbb{N}_0$ (i.e. $\frac{d^n\varphi}{dy^n} \equiv D_n\mathbf{a}$). The differentiation

matrix D_n is of size $(N + 1) \times (N + 1)$ whose expression can be obtained from the differentiation formulae given in Appendix B. The basic velocity profile U is discretised by an $(N + 1) \times (N + 1)$ matrix whose j^{th} column is $1 - y_j^2$ where y_j are the Gauss-Lobatto points given in (3.3).

Define the matrix differential operators A_0 and A_1 of size $(N + 1) \times (N + 1)$ as

$$A_0 = \frac{1}{i\alpha\text{Re}}D_4 - \left(\frac{2\alpha^2}{i\alpha\text{Re}} + U\right)D_2 + \left(\frac{1}{i\alpha\text{Re}}\alpha^4 + \alpha^2U + U''\right)D_0 \quad (3.5)$$

and $A_1 = D_2 - \alpha^2D_0$.

Therefore Orr-Sommerfeld equation can now be written in matrix form as

$$(A_1c + A_0)\mathbf{a} = \mathbf{0}. \quad (3.6)$$

This is a generalised eigenvalue problem with the eigenvalue c and its corresponding eigenvector \mathbf{a} . Since the boundary conditions have not yet appeared anywhere, solving this eigenvalue problem will not yield a valid solution. The discretisation of the boundary conditions and their incorporation into the system will be addressed later in §3.4 but before that, the spatial eigenvalue problem is formulated.

3.3.2 Wavenumber α -Eigenvalue Problem

If the Orr-Sommerfeld equation is written differently as a polynomial in α instead of c , then the result is

$$\left[\frac{1}{iR}\varphi\right]\alpha^4 + \left[(U - c)\varphi\right]\alpha^3 + \left[-\frac{2}{iR}\varphi''\right]\alpha^2 + \left[-(U - c)\varphi'' + U''\varphi\right]\alpha + \left[\frac{1}{iR}\varphi''''\right] = 0. \quad (3.7)$$

Define the matrix differential operators C_0, C_1, C_2, C_3 and C_4 (of size $(N + 1) \times (N + 1)$) in terms of the differentiation matrices D_n as

$$C_0 = \frac{1}{iR}D_4, \quad C_1 = -(U - c)D_2 + U''D_0, \quad C_2 = -\frac{2}{iR}D_2, \quad (3.8)$$

$$C_3 = (U - c)D_0 \quad \text{and} \quad C_4 = \frac{1}{iR}D_0.$$

In this case, the Orr-Sommerfeld equation can be written as

$$(C_4\alpha^4 + C_3\alpha^3 + C_2\alpha^2 + C_1\alpha + C_0)\mathbf{a} = \mathbf{0} \quad (3.9)$$

which is a generalised eigenvalue problem with eigenvalues α and their corresponding eigenvector \mathbf{a} .

The discretised differential forms of the Orr-Sommerfeld equation given in (3.6) and (3.9) are used to obtain the eigenvalues and eigenfunctions of the system after the boundary conditions have been incorporated appropriately.

3.4 Incorporating the Boundary Conditions

For the two eigenvalue problems given in (3.6) and (3.9), there has been no mention of boundary conditions yet and these need to be incorporated into the problem to obtain valid solutions. In order to do so, the discretised forms of the boundary conditions need to be incorporated into the matrices $A_0, A_1, C_0, C_1, C_2, C_3$ and C_4 appropriately^{II}. Simply concatenating the boundary conditions into the matrix problems will lead to an overdetermined system of equations. In order to remedy this problem, some of the rows from the matrix equations need to be eliminated and replaced with the boundary con-

^{II}Note that from now on, the rows and columns of these matrices which are of size $(N + 1) \times (N + 1)$ will be labelled from 0 to N .

ditions hence giving a fully determined system of equations that can then be solved numerically.

In the case of the Orr-Sommerfeld equation with four boundary conditions, the first and last two rows of the matrices are replaced with the discretised form of the four boundary conditions. Since φ is assumed to be symmetric then only two boundary conditions are needed and these replace the last two rows only. In fact, *any* four rows can be replaced by the boundary conditions and the results are unchanged, the first and last two are chosen for convenience.

3.4.1 Rigid Wall Boundary Conditions

When the wall is rigid, the boundary conditions are the no penetration and no slip at the wall, namely $\varphi(\pm 1) = \varphi'(\pm 1) = 0$. These boundary conditions can be discretised by using the differentiation recipes given in Appendix B as

$$\varphi(\pm 1) \equiv \sum_{n=0}^N (\pm 1)^n a_n = 0 \quad \text{and} \quad \varphi'(\pm 1) \equiv \sum_{n=0}^N (\pm 1)^{n+1} n^2 a_n = 0.$$

Since both of these boundary conditions are independent of α and c , they are incorporated into the matrix coefficients of α^0 and c^0 , namely the matrices C_0 and A_0 respectively. In other words, all matrices of the system are determined from their respective forms given in (3.5) and (3.8) then the first and last two rows are set to zero apart from A_0 and C_0 which will be replaced by the discretised forms of the rigid wall boundary conditions. These are given by vectors of size $N + 1$ which take the following form:

$$\begin{aligned} \text{row } 0: & \quad \varphi(1) \equiv (1, \quad 1, \quad 1, \quad 1, \quad \dots \quad 1 \quad) \\ \text{row } 1: & \quad \varphi(-1) \equiv (1, \quad -1, \quad 1, \quad -1, \quad \dots \quad (-1)^N \quad) \\ \text{row } N - 1: & \quad \varphi'(1) \equiv (0, \quad 1, \quad 4, \quad 9, \quad \dots \quad N^2 \quad) \\ \text{row } N: & \quad \varphi'(-1) \equiv (0, \quad 1, \quad -4, \quad 9, \quad \dots \quad (-1)^N N^2 \quad). \end{aligned}$$

3.4.2 Compliant Wall Boundary Conditions

For the compliant wall case, since φ is assumed to be even, its Chebyshev expansion takes the form

$$\varphi(y) = \sum_{n=0}^M a_{2n} T_{2n}(y) \quad (3.10)$$

where $M = \frac{1}{2}N$. The odd rows and columns of the matrices $A_0, A_1, C_0, C_1, C_2, C_3$ and C_4 can be eliminated to give a matrix representation of the eigenvalue problems with the assumption that φ is even and the a_{2n} are relabelled a_n for the sake of convenience. In this case, only two boundary conditions are needed and they were mentioned in Chapter 2 and were expressed in terms of the wall stiffness coefficient \mathcal{S} as:

$$U'(1)\varphi(1) + c\varphi'(1) = 0 \quad (3.11)$$

$$p(1)c - \varphi(1)\mathcal{S}(\alpha, c) = 0 \quad (3.12)$$

$$\text{where } \mathcal{S}(\alpha, c) = -mc^2 - \frac{idc}{\alpha \text{Re}} + \frac{1}{\text{Re}^2} \left[B\alpha^2 + T + \frac{K}{\alpha^2} \right].$$

The integral expression of the pressure at the upper wall is given in equation (2.10), this is used in the second boundary condition (3.12) to give

$$\frac{1}{\alpha^2} \mathcal{S}(\alpha, c)\varphi(1) + c \int_0^1 (U - c)\varphi \, dy = 0. \quad (3.13)$$

In assuming that φ is even, the boundary conditions (3.11) and (3.13) can be discretised, respectively, as

$$2c \sum_{n=0}^M n^2 a_n - \sum_{n=0}^M a_n = 0 \quad (3.14)$$

$$\begin{aligned}
 \text{and } & \left[-m\alpha^2 c^2 - \frac{id\alpha c}{\text{Re}} + \frac{1}{\text{Re}^2} (B\alpha^4 + T\alpha^2 + K) \right] \sum_{n=0}^M a_n \\
 & + \sum_{n=0}^M \frac{6\alpha^2 c}{(2n+1)(2n-1)(2n+3)(2n-3)} a_n + \sum_{n=0}^M \frac{\alpha^2 c^2}{(2n+1)(2n-1)} a_n = 0.
 \end{aligned} \tag{3.15}$$

These discretised forms of the boundary conditions have to be incorporated into the matrices of the system. Equation (3.14) replaces row $M - 1$ while (3.15) replaces row M (once again, the two last rows are chosen as a matter of convenience, but any two rows work equally well). If the boundary conditions are written as polynomials in α , then the resulting coefficients are incorporated into the last two rows of the matrices C_0, C_1, C_2, C_3 and C_4 as follows:

$$\begin{aligned}
 \text{Row } M - 1: & \quad \underbrace{2c \sum_{n=0}^M n^2 a_n - \sum_{n=0}^M a_n}_{\rightarrow C_0} = 0 \\
 \text{Row } M: & \quad \underbrace{\left[\frac{B}{R^2} \sum_{n=0}^M a_n \right]}_{\rightarrow C_4} \alpha^4 \\
 & + \underbrace{\left[\left(-mc^2 + \frac{T}{R^2} \right) \sum_{n=0}^M a_n + \sum_{n=0}^M \frac{c^2}{4n^2 - 1} a_n + \sum_{n=0}^M \frac{6c}{(4n^2 - 1)(4n^2 - 9)} a_n \right]}_{\rightarrow C_2} \alpha^2 \\
 & + \underbrace{\left[-\frac{idc}{R} \sum_{n=0}^M a_n \right]}_{\rightarrow C_1} \alpha + \underbrace{\left[\frac{K}{R^2} \sum_{n=0}^M a_n \right]}_{\rightarrow C_0} = 0
 \end{aligned}$$

Similarly, if the boundary conditions were to be rewritten as polynomials in c instead, then the resulting coefficients are to be incorporated into the matrices A_0 and A_1 . Notice, however, that there is an extra c^2 term appearing in the boundary conditions so an additional matrix A_2 has to be introduced which is a matrix of zeros with the boundary conditions in the last two rows.

In summary, the generalised eigenvalue problems are

$$\begin{aligned} \text{Temporal: } & (A_2c^2 + A_1c + A_0)\mathbf{a} = \mathbf{0}, \\ \text{Spatial: } & (C_4\alpha^4 + C_3\alpha^3 + C_2\alpha^2 + C_1\alpha + C_0)\mathbf{a} = \mathbf{0}. \end{aligned} \quad (3.16)$$

The matrices $A_0, A_1, A_2, C_0, C_1, C_2, C_3$ and C_4 (which now include the boundary conditions) can be written as:

$$\begin{aligned} A_0 &= \begin{pmatrix} \left[\begin{array}{c} \frac{1}{i\alpha\text{Re}}D_4 - \left(\frac{2\alpha^2}{i\alpha\text{Re}} + U\right)D_2 \\ + \left(\frac{1}{i\alpha\text{Re}}\alpha^4 + \alpha^2U + U''\right)D_0 \end{array} \right] & & & & \\ -1 & -1 & -1 & \dots & -1 \\ \frac{B\alpha^4+T\alpha^2+K}{\text{Re}^2} & \frac{B\alpha^4+T\alpha^2+K}{\text{Re}^2} & \frac{B\alpha^4+T\alpha^2+K}{\text{Re}^2} & \dots & \frac{B\alpha^4+T\alpha^2+K}{\text{Re}^2} \end{pmatrix} \\ A_1 &= \begin{pmatrix} & & [[D_2 - \alpha^2D_0]] & & \\ 0 & 2 & 8 & \dots & 2M^2 \\ \frac{2}{3}\alpha^2 - \frac{id\alpha}{\text{Re}} & -\frac{2}{5}\alpha^2 - \frac{id\alpha}{\text{Re}} & \frac{2}{35}\alpha^2 - \frac{id\alpha}{\text{Re}} & \dots & \frac{6\alpha^2}{(4M^2-1)(4M^2-9)} - \frac{id\alpha}{\text{Re}} \end{pmatrix} \\ A_2 &= \begin{pmatrix} & & \left[\begin{array}{c} \text{Zero matrix of size} \\ (M-1) \times (M+1) \end{array} \right] & & \\ 0 & 0 & 0 & \dots & 0 \\ -(1+m)\alpha^2 & \left(\frac{1}{3}-m\right)\alpha^2 & \left(\frac{1}{15}-m\right)\alpha^2 & \dots & \left(\frac{1}{4M^2-1}-m\right)\alpha^2 \end{pmatrix} \\ C_0 &= \begin{pmatrix} & & \left[\frac{1}{iR}D_4 \right] & & \\ -1 & 2c-1 & 8c-1 & \dots & 2M^2c-1 \\ \frac{K}{\text{Re}^2} & \frac{K}{\text{Re}^2} & \frac{K}{\text{Re}^2} & \dots & \frac{K}{\text{Re}^2} \end{pmatrix} \\ C_1 &= \begin{pmatrix} & & [[-(U+c)D_2 + U''D_0]] & & \\ 0 & 0 & 0 & \dots & 0 \\ -\frac{idc}{\text{Re}} & -\frac{idc}{\text{Re}} & -\frac{idc}{\text{Re}} & \dots & -\frac{idc}{\text{Re}} \end{pmatrix} \end{aligned}$$

$$\begin{aligned}
 C_2 &= \begin{pmatrix} & & [[-\frac{2}{i\text{Re}}D_2]] & & \\ & 0 & 0 & \dots & 0 \\ \frac{2}{3}c - \frac{T}{\text{Re}^2} & -\frac{2}{5}c - \frac{T}{\text{Re}^2} & \frac{2}{35}c - \frac{T}{\text{Re}^2} & \dots & \frac{6c}{(4M^2-1)(4M^2-9)} - \frac{T}{\text{Re}^2} \\ -(1+m)c^2 & +(\frac{1}{3}-m)c^2 & +(\frac{1}{15}-m)c^2 & \dots & +(\frac{1}{4M^2-1}-m)c^2 \end{pmatrix} \\
 C_3 &= \begin{pmatrix} & & [[(U-c)D_0]] & & \\ 0 & 0 & 0 & \dots & 0 \\ 0 & 0 & 0 & \dots & 0 \end{pmatrix} \\
 C_4 &= \begin{pmatrix} & & [[\frac{1}{iR}D_0]] & & \\ 0 & 0 & 0 & \dots & 0 \\ \frac{B}{\text{Re}^2} & \frac{B}{\text{Re}^2} & \frac{B}{\text{Re}^2} & \dots & \frac{B}{\text{Re}^2} \end{pmatrix}.
 \end{aligned}$$

The terms in the double square brackets ($[[\square]]$) are block matrices of size $(M-1) \times (M+1)$, these are determined from their respective forms given in (3.5) and (3.8), the odd rows and columns are then eliminated and the last two rows removed in order to incorporate the boundary conditions.

After the generalised eigenvalue problems have been formulated along with the boundary conditions as in equations (3.16), they can be solved numerically to find the eigenvalues α or c and the eigenvector \mathbf{a} . This is done numerically by employing the `polyeig` command on MATLAB which uses a QZ-factorisation in order to find intermediate results in the computation of the generalised eigenvalues [1]. The eigenfunction φ can then be determined by a simple matrix multiplication procedure which is described briefly in Appendix C.

The eigenvalue problems explained so far were formulated in such a way that α and c are the eigenvalues. These equations can be reformulated to have ω as the eigenvalue instead of c and this is very helpful in plotting the curves

of neutral stability (which is discussed in the next section). The eigenvalue problems in that case are

$$(Z_4\alpha^4 + Z_3\alpha^3 + Z_2\alpha^2 + Z_1\alpha + Z_0)\mathbf{a} = \mathbf{0} \quad \text{and} \quad (\tilde{A}_2\omega^2 + \tilde{A}_1\omega + \tilde{A}_0)\mathbf{a} = \mathbf{0}.$$

The details of the matrices $\tilde{A}_0, \tilde{A}_1, \tilde{A}_2, Z_0, Z_1, Z_2, Z_3$ and Z_4 are given in Appendix D and also include the incorporated boundary conditions.

3.5 Plotting Neutral Stability Curves

In order to plot the neutral stability curves, an iterative procedure used by Bridges & Morris [10] is employed. Here, it is more convenient if the system was to be written as a polynomial eigenvalue problem in ω instead of c , thus giving the generalised eigenvalue problem

$$(Z_4\alpha^4 + Z_3\alpha^3 + Z_2\alpha^2 + Z_1\alpha + Z_0)\mathbf{a} = \mathbf{0}. \quad (3.17)$$

The explicit expressions for the matrices Z_0, Z_1, Z_2, Z_3 and Z_4 are given in Appendix D where the boundary conditions were incorporated appropriately.

In order to start the iterative procedure, very good initial estimates for the flow parameters α, Re and ω are needed for a given set of wall parameters at some point on the neutral stability curve. These values can be found by solving the eigenvalue problem (3.17) globally for a fixed value of $\alpha = \alpha_0$ and changing the Reynolds number incrementally until an eigenvalue ω is reached with $\Im(\omega) = 0$. This gives the first three ingredients for the plotting procedure: the temporal frequency $\omega \in \mathbb{R}$ (since it is on the neutral curve), Reynolds number Re and the spatial wavenumber α (which could be complex in general).

The wavenumber α needs to be “corrected” using a matrix form of an iterative procedure by Lancaster [79]. This method is cubically convergent and takes the root α back to the $\Re(\alpha)$ -Re plane (this method is, in fact, a modification of *Halley’s root finding algorithm*). The iterative procedure is as follows^{III}: starting with $k = 0$,

- 1) $D^k := Z_4\alpha_k^4 + Z_3\alpha_k^3 + Z_2\alpha_k^2 + Z_1\alpha_k + Z_0$
- 2)
$$\varepsilon_k := -\frac{2\mathcal{T}\left[(D^k)^{-1}\frac{\partial D^k}{\partial\alpha_k}\right]}{\left(\mathcal{T}\left[(D^k)^{-1}\frac{\partial D^k}{\partial\alpha_k}\right]\right)^2 - \mathcal{T}\left[\left((D^k)^{-1}\frac{\partial^2 D^k}{\partial\alpha_k^2}\right) - \left((D^k)^{-1}\frac{\partial D^k}{\partial\alpha_k}\right)^2\right]}$$
- 3) $\alpha_{k+1} = \alpha_k + \varepsilon_k.$

This iterative procedure starts with the initial guess for α being equal to α_0 while the values of ω and Re obtained earlier are used in determining the coefficient matrices Z_0, Z_1, Z_2, Z_3 and Z_4 . This iterative procedure is repeated until the error ε_k is below a given tolerance (which is 10^{-8} here) and the final value of $\alpha_k \in \mathbb{R}$ is as the “corrected” value of the wavenumber.

For the value of the wavenumber α , a corresponding matrix polynomial D is defined as

$$D = Z_4\alpha^4 + Z_3\alpha^3 + Z_2\alpha^2 + Z_1\alpha + Z_0.$$

Left and right eigenvectors of this matrix D, labelled \mathbf{v}^l and \mathbf{v}^r respectively, need to be determined by using the iteration^{IV}:

$$\mathbf{v}_{k+1}^l = \frac{(D^{-1})^*\mathbf{v}_k^l}{\|(D^{-1})^*\mathbf{v}_k^l\|_2}, \quad \mathbf{v}_{k+1}^r = \frac{D^{-1}\mathbf{v}_k^r}{\|D^{-1}\mathbf{v}_k^r\|_2}.$$

^{III}The operation \mathcal{T} here denotes the trace of a matrix

^{IV}The matrices with an asterisk denote the complex conjugate transposed

The initial values of the eigenvectors for starting the iterative procedure are

$$\mathbf{v}_0^l = \mathbf{v}_0^r = (1, 1, \dots, 1).$$

The iteration converges quite rapidly (usually, in less than 10 iterations) to obtain the left and right eigenvectors \mathbf{v}^l and \mathbf{v}^r .

Now that the corrected wavenumber α , its corresponding matrix polynomial D , Reynolds number Re , temporal frequency ω and the left and right eigenvectors \mathbf{v}^l and \mathbf{v}^r are obtained, the iterative procedure for plotting the neutral stability curve can begin. For a subsequent value of Re ($\text{Re} \leftarrow \text{Re} + \delta\text{Re}$ for some small enough increment $|\delta\text{Re}|$), let

$$\frac{\partial\alpha}{\partial\omega} := -\frac{(\mathbf{v}^l)^* \frac{\partial D}{\partial\omega} \mathbf{v}^r}{(\mathbf{v}^l)^* \frac{\partial D}{\partial\alpha} \mathbf{v}^r} \quad \text{and} \quad \Delta\omega := -\frac{\Im(\alpha)}{\Im\left(\frac{\partial\alpha}{\partial\omega}\right)}.$$

The values of ω and α need to be redefined as follows:

$$\begin{aligned} \omega &\leftarrow \omega + \Delta\omega \\ \Re(\alpha) &\leftarrow \Re(\alpha) + \Re\left(\frac{\partial\alpha}{\partial\omega}\right) \Delta\omega \\ \alpha &\leftarrow \Re(\alpha). \end{aligned}$$

This iterative procedure will find $\alpha \in \mathbb{R}$ and $\omega \in \mathbb{R}$ for the new value of Re to give the next point on the neutral stability curve. This process can be continued for subsequent values of Re to form the neutral stability curve.

Note that the Reynolds number increment $|\delta\text{Re}|$ has to be sufficiently small in order to capture all the interesting and fine behaviour that the neutral curve displays. If $|\delta\text{Re}|$ is too large, then either the iteration may not converge or the more interesting details of the neutral stability curve may not be captured.

The whole process of establishing the coefficient matrices, incorporating boundary conditions, correcting the value of α , forming the matrix polynomial D for the new value of Re , establishing the left and right eigenvectors \mathbf{v}^l and \mathbf{v}^r then finally obtaining new values of α and ω will have to be repeated for every subsequent values of Re . This plots the neutral stability curve on the α - Re plane which separates the temporally stable and unstable regions of the parameter space. A similar procedure to the one described here can be employed to plot the neutral curves on the ω - Re plane as well.

Bridges & Morris [10] and Davies [28] used a form of the Orr-Sommerfeld equation that involved the use of integral operators as opposed to differential ones used here and incorporated the boundary conditions using the Chebyshev-Tau method due to Lanczos [80]. An advantage of using this alternative form is that some of the matrices do not have to be recalculated at every step, however it has been found that the computational time saved is not substantial compared to the differentiated form is used instead. Details of this alternative formulation for the rigid walled plane channel flow is given in Bridges & Morris [10] and the compliant wall given in Davies [28]. In the next chapter, this will be discussed further since the integrated form is more convenient for the purposes of the simulations.

3.6 Some Numerical Examples

A selection of illustrative numerical results are now presented, in particular, neutral stability curves and some c -eigenvalues for certain choices of α and Re . All the cases presented here already been documented (see for example Davies & Carpenter [30]) but they are shown here in order to illustrate how these will be used in the chapters to follow. For the cases shown, three wall parameters

choices are considered which are

$$m = 2, \quad B = 4K, \quad T = 0, \quad d = 0 \quad \text{for} \quad K = 10^7, 2 \times 10^7, 6 \times 10^7.$$

This set of wall parameters is chosen so that the ratio of B and K remains constant thus keeping the critical wavenumber α_c (in equation (2.24) in Chapter 2) constant as well, taking the value

$$\alpha_c = \sqrt[4]{\frac{K}{B}} = \frac{\sqrt{2}}{2} \approx 0.7071.$$

For the three different values of K , the approximations for the onset Reynolds numbers for divergence and TWF (in equations (2.27) and (2.28)) are given in Table 3.1. This particular set of wall parameters was considered by Davies & Carpenter [30] and some of the results are reproduced here in order to show some of the eigenvalues and neutral curves.

K	10^7	2×10^7	6×10^7
Re_{TWF}	4264	6030	10445
Re_d	8660	12247	21213

Table 3.1: Onset Reynolds numbers for TWF (Re_{TWF}) and the divergence (Re_d) instabilities for the different choices of K .

$K=2 \times 10^7$

Figure 3.1 shows the neutral stability curves when $K = 2 \times 10^7$, one curve represents the modified flow-based TS mode (labelled TS) and the other represents the wall-based mode (labelled FISI denoting flow-induced surface instabilities). The wall-based mode in this case can be identified as the TWF instability and this can be verified by checking its growth rates. Also, the

analytic approximation for the onset Reynolds number of the TWF instability (which is 6030) compares quite well with this curve. (Note that according to Davies & Carpenter [30], as the value of the critical wavenumber α_c increases, the approximation for the onset Reynolds numbers become less accurate, hence the discrepancy.)

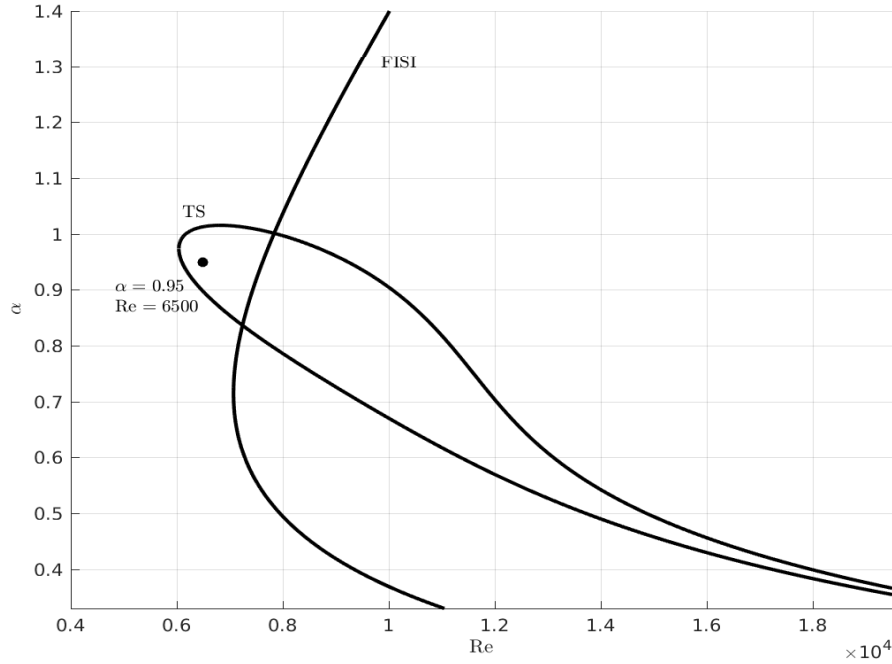


Figure 3.1: Neutral stability curves for the wall parameters $m = 2$, $B = 8 \times 10^7$, $T = 0$, $K = 2 \times 10^7$, $d = 0$. The curves represent the TS and FISI modes (which are labelled accordingly). The dot denotes the point where $\alpha = 0.95$ and $Re = 6500$ where the flow is destabilised by TS only, this is illustrated by the c eigenvalues shown in Figure 3.2.

In order to see an example of the temporal stability properties of different parts of the α - Re plane, a particular choice of flow parameters is chosen to see where the eigenvalues lie on the complex c -plane. To this end, choose the flow parameters $\alpha = 0.95$ and $Re = 6500$ (denoted by a dot in Figure 3.1), according to the neutral curves, the flow possessing these flow parameters is destabilised by the TS mode. This can be seen from the c -eigenvalues obtained by solving the eigenvalue problem numerically for the chosen wall and flow parameters,

as presented in Figure 3.2.

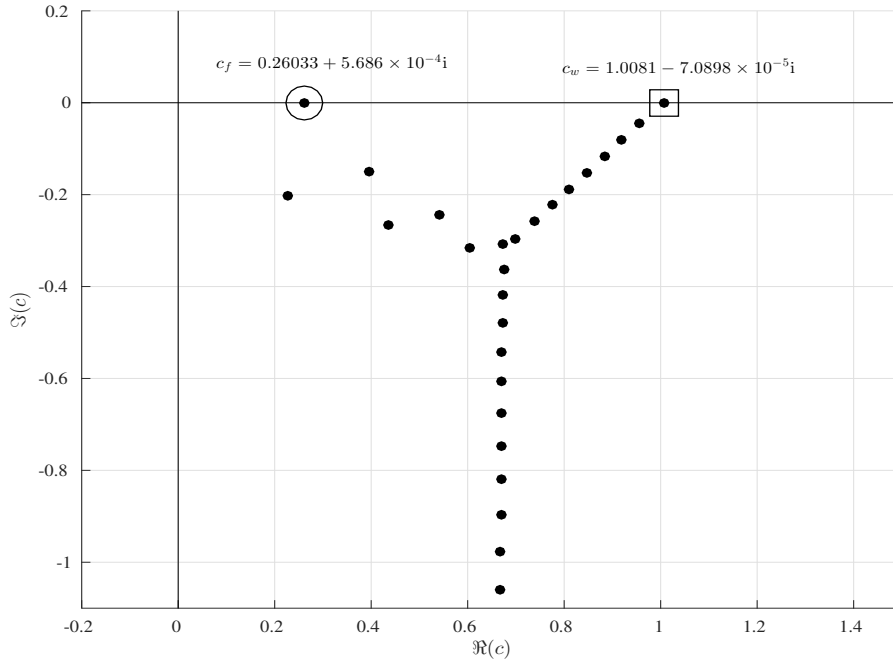


Figure 3.2: Complex c -eigenvalues for the same wall parameters as in Figure 3.1 with $\alpha = 0.95$ and $R = 6500$. The unstable TS mode is labelled c_f and the stable FISI is labelled c_w .

There are now two modes that are the least stable/unstable. The TS mode, labelled c_f , is temporally unstable (since $\Im(c_f) > 0$) while the FISI, c_w , is temporally stable (since $\Im(c_w) < 0$). This combination of wall parameters allows the TS instability to have a slightly lower onset Reynolds number compared to the FISI.

$K=10^7$

When the wall is made softer by reducing K to 10^7 (and changing B accordingly), the neutral stability curve in Figure 3.3 representing the TS instability shrinks down considerably to a small loop implying that it has been effectively stabilised by the compliant wall but in doing so, the FISI starts to occupy a large portion of the α -Re plane.

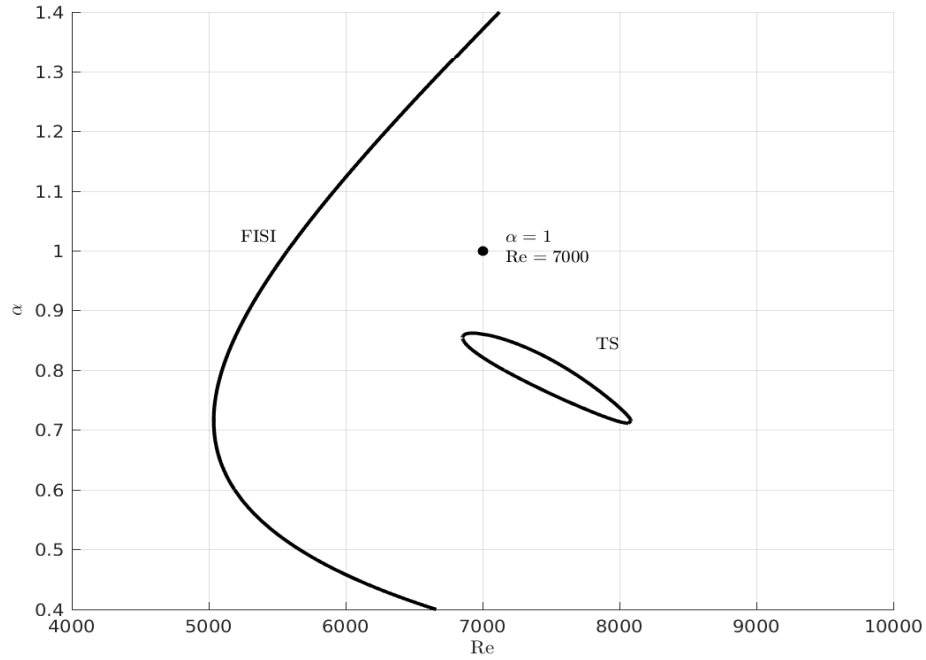


Figure 3.3: Neutral stability curves for the wall parameters $m = 2$, $B = 4 \times 10^7$, $T = 0$, $K = 10^7$, $d = 0$. The curves represent the TS and FISI modes (which are labelled accordingly). The dot denotes the point when $\alpha = 1$ and $\text{Re} = 7000$ where the flow is destabilised by the FISI only, this is illustrated by the c -eigenvalues shown in Figure 3.4.

A choice of flow parameters can be taken to see which eigenvalues play a part in destabilising the flow. Consider the case when $\alpha = 1$ and $\text{Re} = 7000$ (represented by the dot in Figure 3.3), the c eigenvalues for this choice of flow parameters is shown in Figure 3.4. In this case, the flow is destabilised by the TWF (labelled c_w) therefore even though the TS instability (c_f) has been stabilised by the compliant wall, its flexibility has resulted in the TWF mode to destabilise the flow instead.

$K=6 \times 10^7$

When the wall is made stiffer by increasing the value of K to 6×10^7 (and changing B accordingly), the TWF onset Reynolds number is pushed to higher values (as shown by the analytic approximation in Table 3.1). However, the compliant wall still allows the TS mode to be unstable for lower values of R .

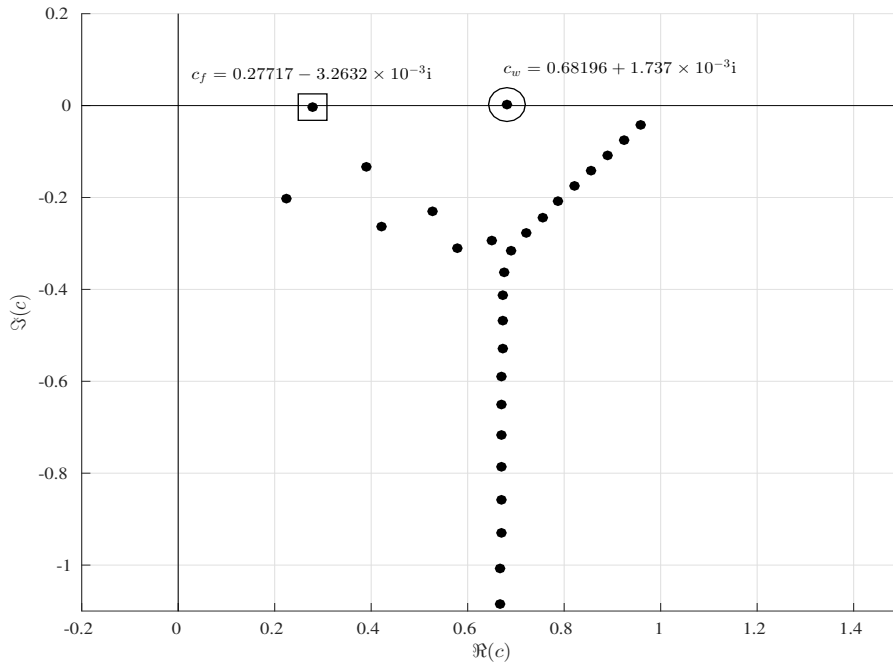


Figure 3.4: Complex c -eigenvalues for the same wall parameters as in Figure 3.3 with $\alpha = 1$ and $\text{Re} = 7000$. The unstable FISI mode is labelled c_w and the stable TS mode is labelled c_f .

This is seen from the neutral stability curves on the α - Re plane given in Figure 3.5.

Consider the choice of flow parameters $\alpha = 0.9$ and $\text{Re} = 14000$, the eigenvalues that result show two unstable modes (since their imaginary parts are positive) as shown on the complex c -plane in Figure 3.6. The two eigenvalues correspond to different instabilities, the wall-based TWF mode (labelled c_w) and the TS mode (labelled c_f).

From these preliminary results, it can be seen that the choice of wall parameters can influence the stability of the flow greatly. Even though only two wall parameters were varied here (in order to keep their ratio fixed), the results shown demonstrate the rich behaviour of flows over compliant walls. In Chapters 5 and 6, other wall parameters are varied and their effect on the different modes will be investigated.

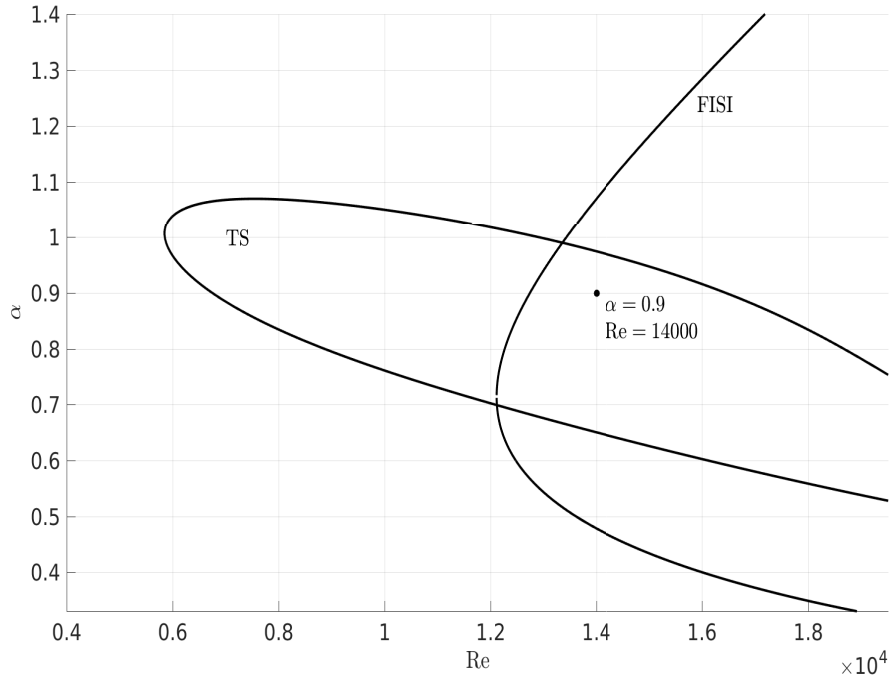


Figure 3.5: Neutral stability curves for the wall parameters $m = 2$, $B = 24 \times 10^7$, $T = 0$, $K = 6 \times 10^7$, $d = 0$. The curves represent the TS and FISI modes (which are labelled accordingly). The dot denotes the point when $\alpha = 0.9$ and $\text{Re} = 14000$ where the flow is destabilised by both TSI and FISI, this is illustrated by the c -eigenvalues in Figure 3.6.

3.7 Merged Neutral Curves

In the examples presented so far, the neutral curves representing TS and FISI can be considered as being distinct. In other words, the two modes are represented by two overlapping, yet separate, neutral curves. However in some cases, the TS and FISI modes can merge together giving rise to a single neutral curve that encompasses both of them. For example consider a compliant wall with parameters

$$m = \frac{1}{3}, \quad B = 1.28 \times 10^9, \quad T = 0, \quad K = 312500, \quad d = 200.$$

Figure 3.7 shows the rigid (black) and compliant wall (red) neutral curves for this set of wall parameters and in this case, the neutral stability curve

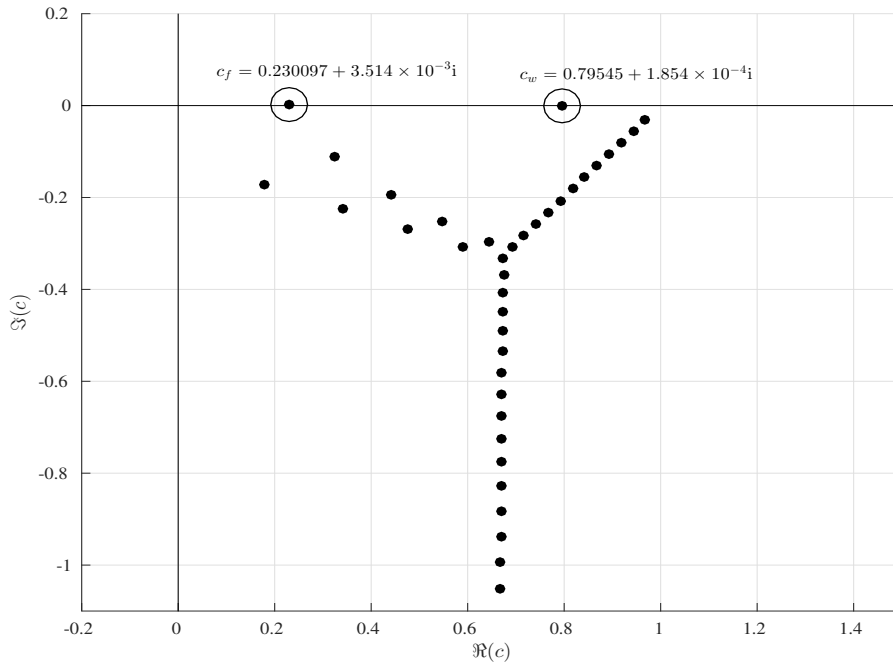


Figure 3.6: Complex c eigenvalues for the same wall parameters as in Figure 3.5 with $\alpha = 0.9$ and $Re = 14000$. The two unstable modes are TS, labelled c_w , and the FISI, labelled c_f .

representing the compliant wall consists of the TS and the wall-based flow induced surface instability (hereafter labelled FISI) regions, both of these parts are now joined together and represented by a single curve. It can be made certain that the neutral curves are merged rather than overlapping due to their associated curves of constant growth rate as in Figures 3.8 and 3.9.

Figure 3.8 shows the growth/decay rates starting from $\Im(\omega) = -0.005$ and increasing incrementally to $\Im(\omega) = 0.005$ in steps of 0.001, the neutral curve is when $\Im(\omega) = 0$ (recall that the growth rates are given by the curves when $\Im(\omega) > 0$ and the decay rates when $\Im(\omega) < 0$).

At $\Im(\omega) = 0.002$, the curves representing the TS and divergence modes start to separate into two distinct curves but as $\Im(\omega)$ is increased further, the TS curve shrinks considerably while divergence remains largely unchanged.

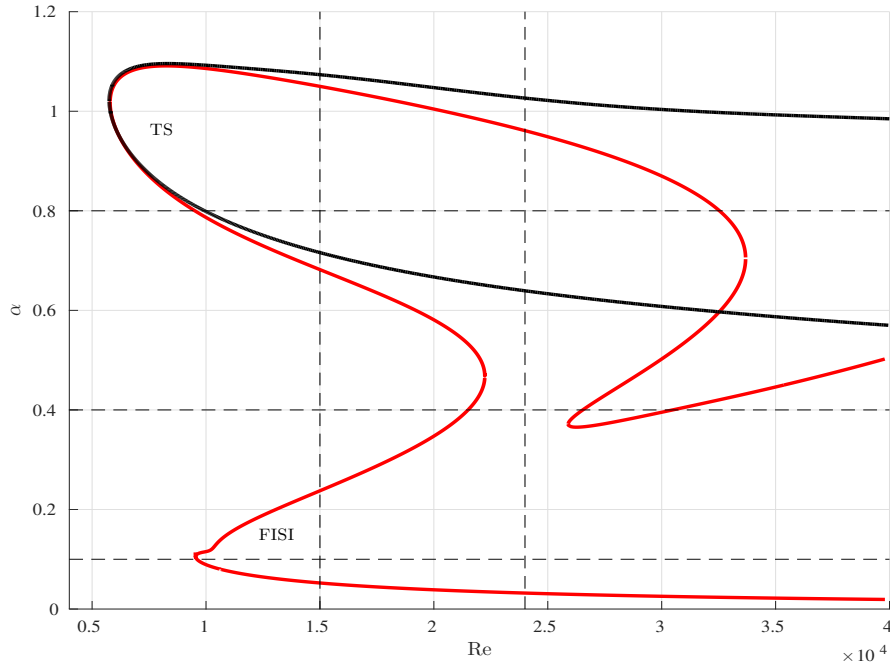


Figure 3.7: Neutral stability curves for a rigid (black) and a compliant wall (red) with $m = \frac{1}{3}$, $B = 1.28 \times 10^9$, $T = 0$, $K = 312500$, $d = 200$. The sections of the neutral curves that represent the TS and FISI modes are labelled accordingly. The vertical dashed lines denote fixed values of Re equal to 15000 and 24000 while the horizontal dashed lined denote the fixed values of α equal to 0.1, 0.4 and 0.8.

Similarly, Figure 3.9 shows growth rates from $\Im(\omega) = 0.01$ up to 0.09 in increments of 0.01. This reinforces the fact that the TS mode is far weaker (has a smaller growth rate) than the divergence instability which has a substantially heightened growth rate.

The growth rates of the different instabilities can be studied from two different points of view by taking cross sections across the stability curves diagrams for fixed values of α or Re .

3.7.1 Curves of c Against Re

In order to observe the variation of the phase speed c for a fixed value of the wavenumber α while changing Re , a “cross section” of the stability diagram

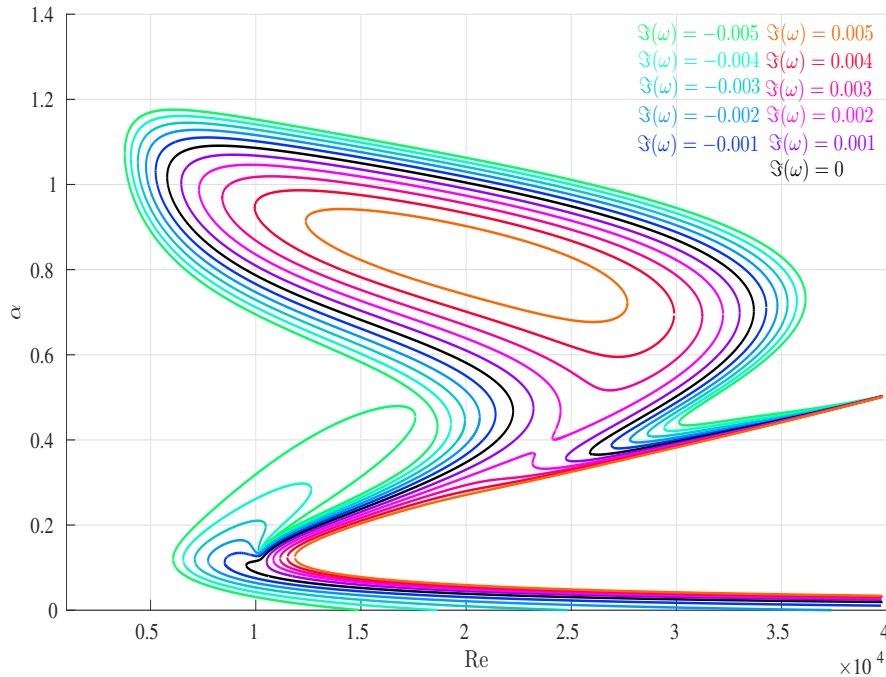


Figure 3.8: Curves of constant growth and decay rates for the same wall parameters as in Figure 3.7. The outermost plot is when $\Im(\omega) = -0.005$ while the innermost has $\Im(\omega) = 0.005$ and the lines are plotted in increments of 0.001 (the colours are labelled accordingly).

can to be taken at said value of α (these are represented by the horizontal lines in Figure 3.7). This provides valuable information to see how the real and imaginary parts of the phase speed belonging to different instabilities behave by changing Re . Consider, for example, the variation of c against Re for a fixed wavenumber $\alpha = 0.8$ (as shown by the horizontal line at $\alpha = 0.8$ in Figure 3.7). From the neutral curves in Figure 3.7, it can be seen that the TS onset for both the rigid and compliant walls is almost the same but at large enough Re , the compliant wall restores stability. Figure 3.10 shows the real and imaginary parts of the phase speed c plotted against the Reynolds number Re for the fixed wavenumber $\alpha = 0.8$. This way of presenting the information is useful when comparing growth rates of the different modes. Note that the instability that arises here is the TS and has a growth rate that barely reaches 0.01. This growth rate is typical of the TS instability since it is destabilised

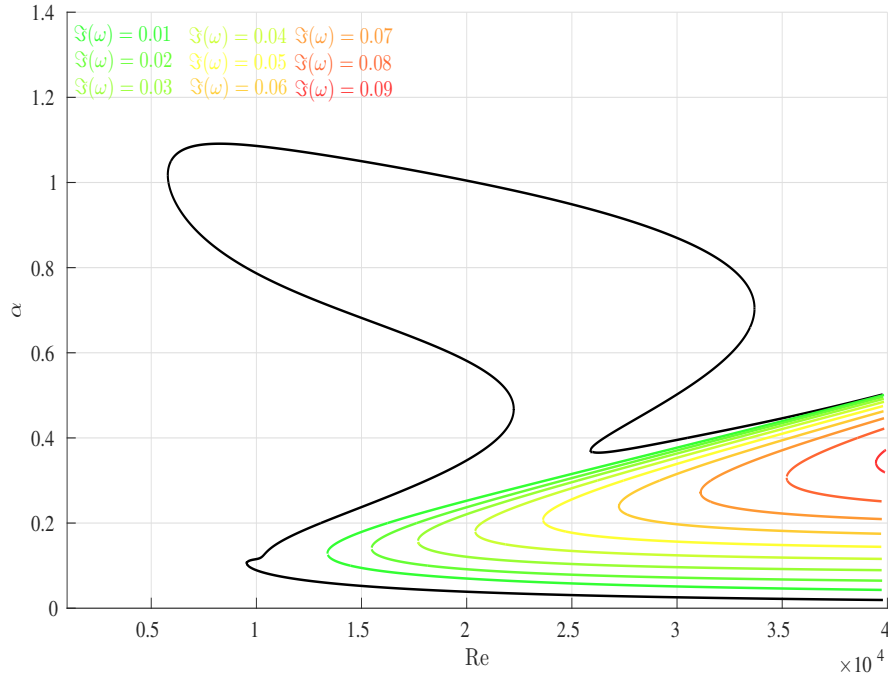


Figure 3.9: Curves of constant growth rate for the same wall parameters as in Figure 3.7. The outermost plot is the neutral curve with $\Im(\omega) = 0$ while the innermost has a growth rate of $\Im(\omega) = 0.09$, the graphs are plotted in increments of 0.01.

by a weak viscous mechanism (unless highly modified by the compliant wall).

Now consider the variation of c against Re for a smaller value of α , in particular $\alpha = 0.1$. Figure 3.11 shows the curves of c against Re for the FISI, this mode is unstable for all the values of Re greater than $\text{Re} \approx 9350$. The growth rate (given by the imaginary part) is at least an order of magnitude greater than the TS mode seen in Figure 3.10. Notice, also, that both the real and imaginary parts cross $c = 0$ at approximately the same value of Re , this implies that the instability takes the form of a standing wave at onset (as seen in Figure 3.11 at $\text{Re} \approx 9350$). This behaviour is highly distinctive of the *divergence instability* (see for example Davies & Carpenter [30]).

Perhaps the most intriguing part of the neutral curve is the region where the two modes appear to merge into one another at around $\alpha = 0.4$. The

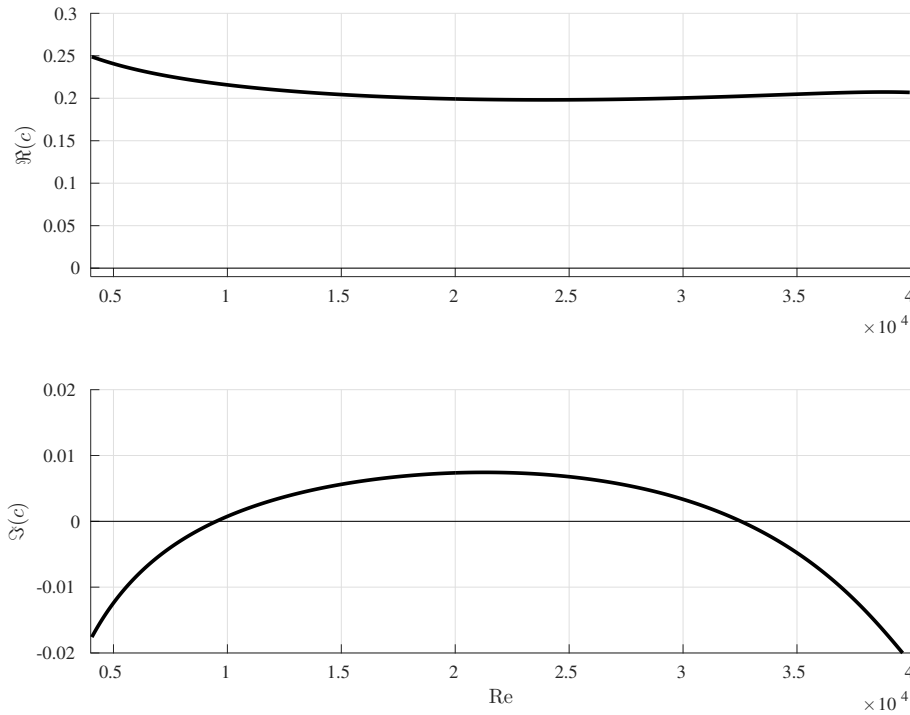


Figure 3.10: Real and imaginary parts of c against Re for a fixed $\alpha = 0.8$ and the same wall parameters as in Figure 3.7.

variation of c against Re at this value of α reveals three coexisting modes, two of which are stable for all values of Re as shown in Figure 3.12. These three can be identified as the TS (black), divergence (red) and TWF (blue) modes and these can be identified from the solutions of the Orr-Sommerfeld equation. The flow is stable up to $\text{Re} \approx 21000$ at which point the TS mode starts to set in but the flow returns to a stable state after $\text{Re} \approx 26000$. At even higher Reynolds numbers, the TWF mode undergoes a very strong stabilisation while the TS growth rate increases drastically causing the flow to be unstable for all subsequent values of Re .

The interaction between the divergence and TWF modes can be predicted by a low wavenumber asymptotic theory (see for example Lucey [87] and Gad-el-Hak [47]). It can be seen that the TS and TWF modes strongly interact, leading to a dramatic increase in the TS growth rates with a correspondingly

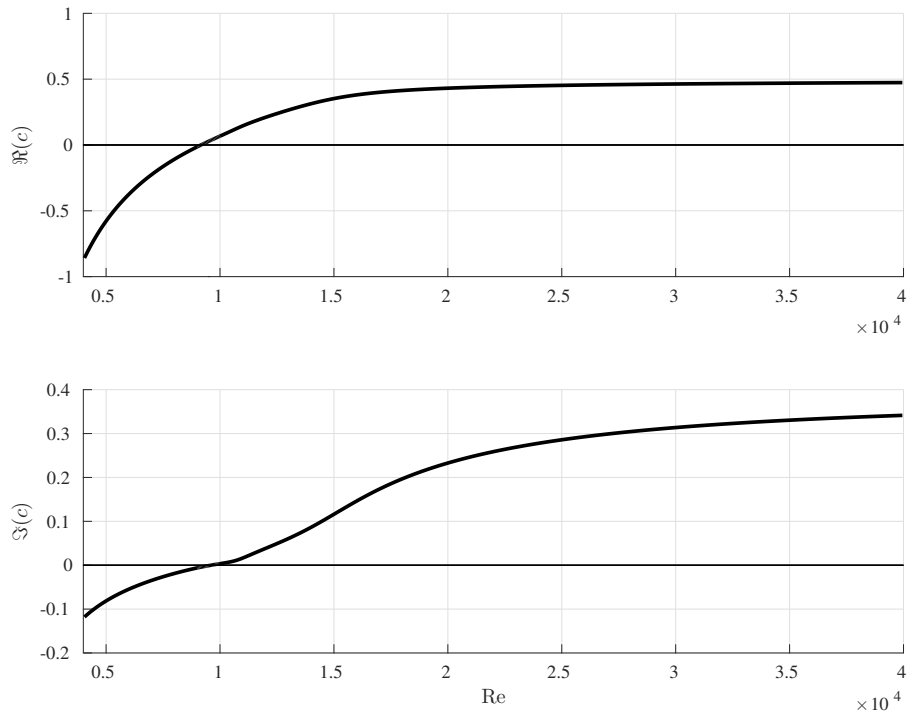


Figure 3.11: Real and imaginary parts of c against Re for a fixed $\alpha = 0.1$ and the same wall parameters as in Figure 3.7. Both the real and imaginary parts of c cross $c = 0$ at approximately the same value of Re suggesting that this behaviour is highly reminiscent of the divergence instability.

drastic stabilisation of the TWF mode.

3.7.2 Curves of c Against α

Another way of comparing instabilities is to consider the variation of c against α for a fixed value of Re (represented by the vertical lines in Figure 3.7). At $\text{Re} = 15000$, the neutral curve shows that the flow will be destabilised at two separate ranges of α by two different modes. Figure 3.13 shows the variation of the real and imaginary parts of c against α for this value of Re and indeed, the flow destabilised at two separate regions by the TS mode and FIS1 (the range of wavenumbers at which the instabilities act are labelled accordingly). The TS instability can be identified as such due to its correspondence with TS mode

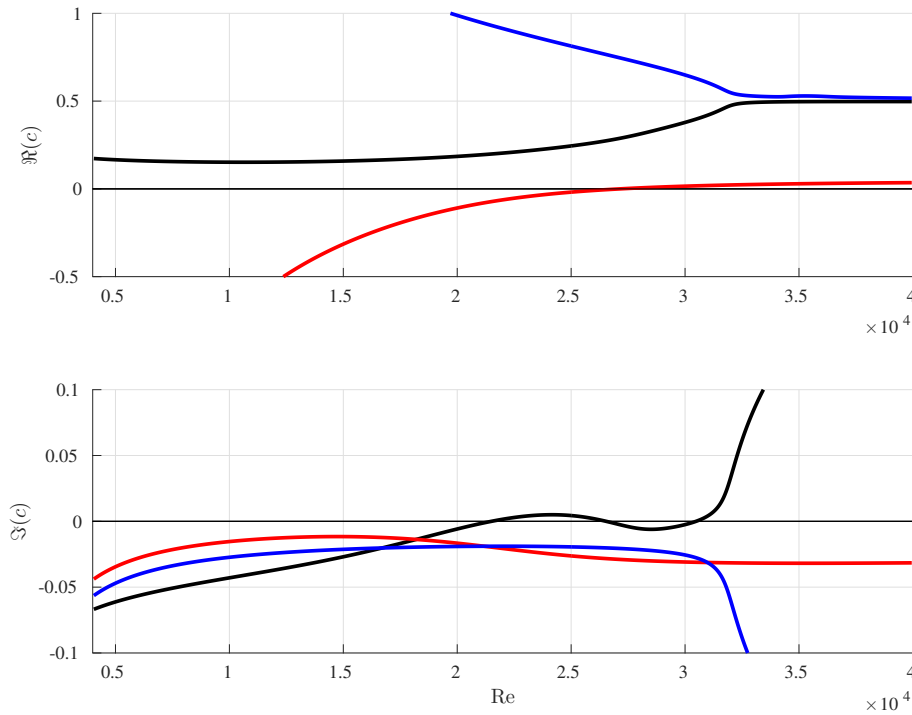


Figure 3.12: Real and imaginary parts of c plotted against Re for a fixed $\alpha = 0.4$ and the same wall parameters as in Figure 3.7. The three lines represent the divergence (red), TWF (blue) and TS (black) modes.

for the rigid wall (plotted in black). On the other hand, the FISI is stationary at onset and has a growth rate that is at least 20 times greater than that of TS implying that the wall-based mode is the divergence instability.

Increasing the Reynolds number to 24000 shows three modes as in Figure 3.14, one is unstable between $\alpha = 0.032$ and 0.962 (red) while other two are stable throughout (blue and green). The mode that is responsible for destabilising the flow (red) is due to an interaction between divergence and TS. This particular interaction between the instabilities and its implications for the disturbance behaviour as a whole is discussed in more detail in Chapter 6.

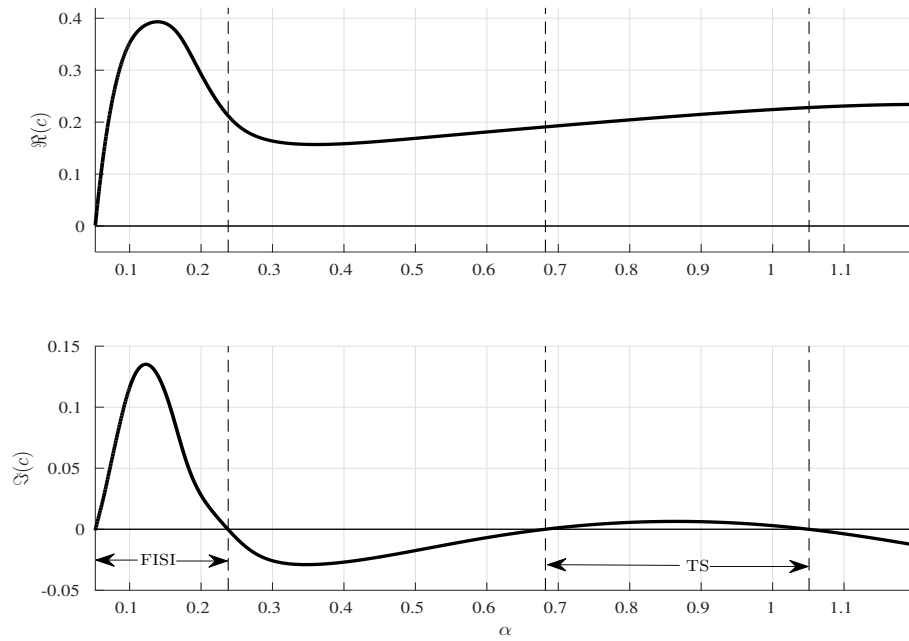


Figure 3.13: Real and imaginary parts of c plotted against α for a fixed $\text{Re} = 15000$ and the same wall parameters as in Figure 3.7. The vertical dashed lines show the regions where the TS and FISI (particularly the divergence mode) are unstable since the imaginary part is positive.

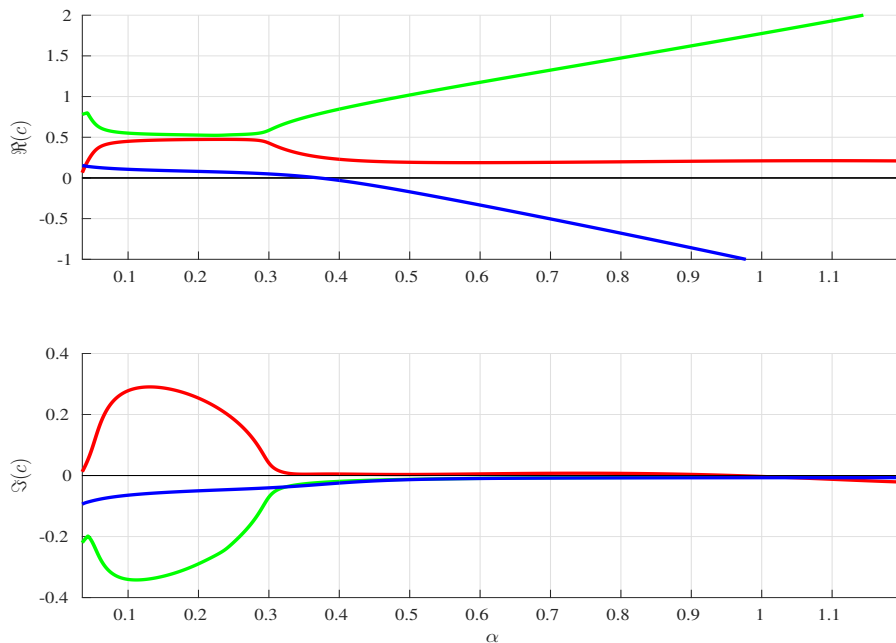


Figure 3.14: Real and imaginary parts of c plotted against α for a fixed $\text{Re} = 24000$ and the same wall parameters as in Figure 3.7. The instability in red destabilises the flow at values of α between 0.032 and 0.962, the others, however, are stable.

Chapter 4

Numerical Simulation Method

This section describes the method employed to conduct the linear direct numerical simulations^I (denoted DNS) which are then used extensively in Chapters 5 and 6. The procedure described here was initially developed by Davies [28] and Davies & Carpenter [31] having been inspired by the works of Fasel [36] [37] and Fasel & Konzelmann [38] [39]. This method was intended to investigate the evolution of Tollmien-Schlichting waves (be it growth or decay) as they propagate over a compliant wall section of finite length. However in the current investigation, the behaviour of the wall-based modes and their possible interactions (perhaps leading to absolute instabilities) are of greatest interest.

In Chapter 5, the linear DNS method described here are used to perform numerical experiments and the extracted results will be compared to the solutions of the Orr-Sommerfeld equation obtained from Chapter 3. Later on, in Chapter 6, *absolute instabilities* are presented and compared to a saddle point analysis due to Briggs and two-dimensional global mode computations^{II}.

^IIn the current work, only *linear* direct numerical simulations are performed since turbulence will not be accounted for

^{II}When the term “DNS results” is used, it refers to information extracted from the DNS which include wavenumbers, phase speeds, frequencies, growth/decay rates and time periods.

4.1 Introduction

The study of boundary layer transition by means of direct numerical simulations was first conducted by Fasel [36] [37] using a finite difference model. At the time, Fasel and co-workers were limited to studies of two-dimensional disturbances mainly due to the lack of computational power. However the processing power available now makes it possible to simulate the transition to turbulence for a fully developed three-dimensional flow (subject to certain domain restrictions). For the current purposes, *Squire's theorem* is evoked (as was remarked for the rigid wall in Chapter 2) and therefore only two-dimensional disturbances with small amplitudes are considered.

For a flow bound by compliant walls, any disturbance to the flow results in pressure changes which generate forces that deform the wall from its equilibrium position. This wall deflection modifies the motion of the fluid flowing over it which, in turn, alters the wall's deflection even further. This feedback loop results in the decay of the TS instability but in doing so, it can also be responsible for generating wall-based modes as well. These instabilities can have a detrimental effect on the stability of the flow, even more so than the TS mode can exhibit by itself.

In order to capture the interesting interactive behaviour between the wall and the flow, a highly efficient scheme was developed by Davies [28] to resolve the more prominent features of the flow to achieve stable converged solutions. This scheme involves using a hybrid between two numerical methods: a finite difference method for streamwise and time discretisations and a Chebyshev spectral method for the direction normal to the wall. The governing equations of the system are based on the velocity-vorticity formulation which gives a very

efficient and stable diagonal scheme when integration is performed.

In the previous chapters, the compliant wall was assumed to be of infinite extent in both the streamwise and spanwise directions but here, a wall of finite length is considered. The flow configuration consists of a compliant wall section attached to two rigid wall sections in the upstream and downstream locations by hinging or clamping. The flow is disturbed by either introducing an inflow profile or by means of a localised impulsive forcing.

After the DNS method is described, examples of its application will be shown in Chapters 5 and 6. First, the behaviour of the TS instability over compliant walls is studied, though this is reproduced from earlier works, these cases are still presented to show the way in which the method works. Then, the wall-based instabilities are studied and the DNS results are compared to those obtained from the solutions of the Orr-Sommerfeld equation. The proliferation of the wall-based modes has not been documented before in the literature using the current DNS scheme and this is where the original content of the thesis begins. In Chapter 6, the growth of absolute and global instabilities is investigated using this linear DNS method, Briggs' method and two-dimensional global mode computations.

4.2 Flow Set-up

4.2.1 Flow Configuration

Figure 4.1 shows a schematic representation of the flow configuration. The computational domain extends from $x = 0$ to $x = L$ which is where inflow and outflow conditions are imposed respectively. Both walls are rigid except in the

region $x \in [L_1, L_2]$ where a compliant section is inserted ($0 < L_1 < L_2 < L$). The joint conditions (be they hinging or clamping) are imposed at $x = L_1$ and $x = L_2$. Only the half channel $y \in [0, 1]$ is considered due to the assumed symmetry of φ .

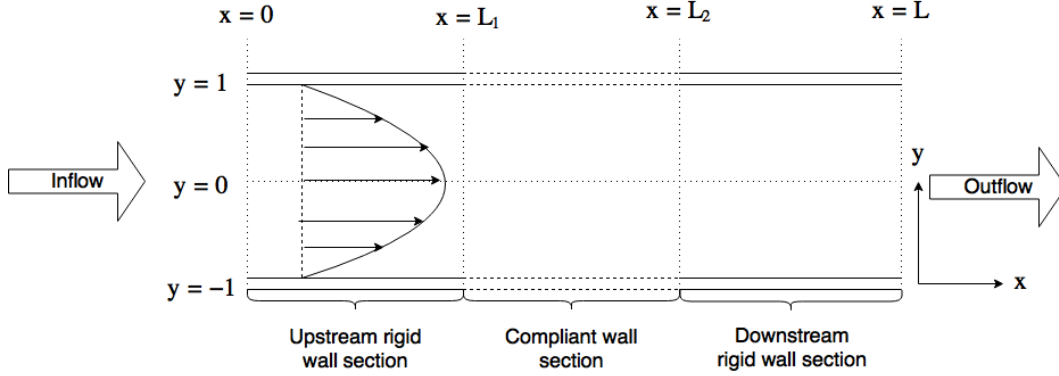


Figure 4.1: Schematic representation of the flow configuration used for the DNS.

It should be noted that the location of the start of the compliant wall L_1 should be sufficiently downstream of $x = 0$ in order to ensure that no upstream propagating effects reach location of the inflow. Otherwise, the solution near $x = 0$ could be contaminated by these spurious effects. Similarly, L_2 has to be sufficiently upstream of $x = L$ in order to apply a rigid wall outflow condition without risk of having any effects from the compliant wall.

4.2.2 Disturbing the Basic Flow

There are two ways in which the flow is disturbed, either by using an inflow profile or a localised impulsive excitation.

Inflow Profile

Since the wall is rigid at the inflow $x = 0$, a disturbance streamfunction corresponding to the rigid TS mode can be used as an inflow condition. This

allows the TS wave to enter the computational domain onto the rigid wall and as it travels over the compliant wall, it acts as a continuous source of excitation for the wall-based modes. In this case, there has to be an inherent inflow frequency associated with the disturbance profile and this is denoted β . The advantage of using a TS inflow profile to disturb the flow is that there will be no near-field effects associated with this disturbance as opposed to using other methods of excitation such a localised impulse, bump on the rigid wall section or vibrating ribbon for example.

Localised Impulsive Forcing

Another way in which the flow can be disturbed is through a localised impulsive forcing which takes the form

$$e^{-\sigma^2 t^2} \left(1 - e^{-\sigma^2 t^2}\right) e^{-(x-\bar{L})^2}.$$

The term σ defines a timescale for the forcing where this timescale behaves as $\frac{1}{\sigma}$ for the impulse (in all the cases presented here, σ is taken to be 1). The impulsive excitation is imposed at the location \bar{L} which is usually taken to be the middle of the compliant wall section (note that any other suitable location can be taken for \bar{L} but the middle is chosen here). This form gives the compliant wall an initial disturbed form that can then excite the flow without having to impose an inflow frequency to the system. The localised impulse is used mostly for the cases in Chapter 6 that show absolute and global instabilities.

4.3 Establishing the Governing Equations

4.3.1 Velocity-Vorticity Formulation

In the past, the Navier-Stokes equations have been formulated differently, these include forms such as the *Primitive Variable*, *Streamfunction-Vorticity*, *Streamfunction*, *Three-Field* and *Velocity-Vorticity* formulations. For the work presented here, the *Velocity-Vorticity* formulation of the Navier-Stokes equations is used, this is given by the set of equations:

$$\begin{aligned}\frac{\partial \omega}{\partial t} + \mathbf{u} \cdot \nabla \omega &= \frac{1}{\text{Re}} \nabla^2 \omega \\ \omega &= \frac{\partial u}{\partial y} - \frac{\partial v}{\partial x} \\ \nabla \cdot \mathbf{u} &= 0.\end{aligned}$$

This particular form is used as opposed to its equivalent counterparts since, first of all, it eliminates the need for determining the pressure p explicitly (as in the Primitive Variable and Three-Field formulations). Moreover, it also allows the boundary conditions to be imposed on the velocity components as opposed to the streamfunction (as in Streamfunction-Velocity and Streamfunction formulations). A more detailed account of the relative advantages of the Velocity-Vorticity formulation is given in Fasel [37] and Gatski [56]^{III}.

In this section, the simulation method used for the DNS from Davies [28] and Davies & Carpenter [31] is described. In the sections that follow, ω will be used to represent the vorticity while β will represent the frequency.

^{III}It should also be noted that Davies & Carpenter [32] have obtained a *novel velocity-vorticity* formulation of the Navier-Stokes equations along with applications to different problems in hydrodynamic stability theory such as flows over compliant surfaces and over rotating discs.

4.3.2 Governing Equations

The governing equations of the system in terms of the disturbance velocities and pressure (derived from the Navier-Stokes equations as shown earlier in equation (2.4), Chapter 2) are:

$$\begin{aligned} x\text{-momentum equation: } \frac{\partial u}{\partial t} + U \frac{\partial u}{\partial x} + \frac{dU}{dy} v &= - \frac{\partial p}{\partial x} + \frac{1}{\text{Re}} \left(\frac{\partial^2 u}{\partial x^2} + \frac{\partial^2 u}{\partial y^2} \right) \end{aligned} \quad (4.1a)$$

$$\begin{aligned} y\text{-momentum equation: } \frac{\partial v}{\partial t} + U \frac{\partial v}{\partial x} &= - \frac{\partial p}{\partial y} + \frac{1}{\text{Re}} \left(\frac{\partial^2 v}{\partial x^2} + \frac{\partial^2 v}{\partial y^2} \right) \end{aligned} \quad (4.1b)$$

$$\text{Conservation of mass: } \frac{\partial u}{\partial x} + \frac{\partial v}{\partial y} = 0 \quad (4.1c)$$

$$\text{Vorticity: } \frac{\partial u}{\partial y} - \frac{\partial v}{\partial x} = \omega. \quad (4.1d)$$

First, the equations that govern the fluid motion are derived from (4.1). These equations, which are in their differential form, are then converted to integral equations since this facilitates the discretisation of the governing equations and boundary conditions in the y -direction by means of a Chebyshev-Tau method.

In the sections that follow, the equations of the system will be discussed in this order:

1. Governing equations
2. Integral forms of the governing equations
3. Pressure integral
4. Pressure driven wall equation
5. Boundary conditions
6. Inflow and Outflow conditions
7. Join conditions.

These equations are then discretised in the y -direction by means of a Chebyshev-Tau method and then in the x and t -directions by using a finite difference method.

Before continuing, it should be made very clear that the equations and the method presented in this chapter have already been well-established, the main application of this method was in Davies [28] which was a collection of previous works as well as novel ones. This chapter only aims to collect these different ideas and present them for the sake of completeness.

4.3.3 Fluid Motion

Vorticity Transport Equation

To obtain the equation that dictates the evolution of the vorticity, differentiate (4.1a) with respect to y and subtract (4.1b) differentiated with respect x to give

$$\frac{\partial \omega}{\partial t} + U \frac{\partial \omega}{\partial x} + U''v = \frac{1}{\text{Re}} \nabla^2 \omega. \quad (4.2)$$

(The dashes here represent differentiation with respect to y .) Equation (4.2) is known as the *vorticity transport equation* and is the first of the two governing equations of the flow.

Even Forms of the Functions

Since both φ and U are symmetric, the normal velocity v has to also be symmetric according to the vorticity transport equation (4.2). With this assumption in mind, the streamwise disturbance velocity u and the pressure p have to be antisymmetric according to (4.1), hence $u(0) = p(0) = 0$. Therefore all in all, the functions v, ω and U are symmetric while u and p are antisymmetric.

Notice that the streamwise velocity component u does not appear explicitly in the vorticity transport equation (4.2), this could suggest that the evolution of the vorticity may be independent of the streamwise velocity but this is of course invalid. This problem can be resolved by an integral constraint on u which is obtained by imposing the no slip condition at the wall. Integrating the vorticity (4.1d) with respect to y gives an expression for the streamwise velocity u in terms of v and ω as

$$u(y) = \int_0^y \left(\omega + \frac{\partial v}{\partial x} \right) dy. \quad (4.3)$$

Evaluating at $y = 1$ gives the boundary condition on u

$$u_w = \int_0^1 \left(\omega + \frac{\partial v}{\partial x} \right) dy. \quad (4.4)$$

From now on, the terms with a subscript w (\square_w) represent functions evaluated at the upper wall, i.e.

$$f_w = f_w(x, t) = f(x, 1, t) \quad \text{for some function } f.$$

Poisson Equation

The vorticity transport equation (4.2) is the first of two governing equations of the system, the second is the Poisson equation

$$\nabla^2 v = -\frac{\partial \omega}{\partial x}. \quad (4.5)$$

This Poisson equation ensures that the conservation of mass $\nabla \cdot \mathbf{u} = 0$ is satisfied, indeed,

$$\begin{aligned}
 \nabla \cdot \mathbf{u} &= \frac{\partial u}{\partial x} + \frac{\partial v}{\partial y} \\
 &= \frac{\partial}{\partial x} \left[\int_0^y \omega \, dy + \frac{\partial}{\partial x} \int_0^y v \, dy \right] + \frac{\partial v}{\partial y} && \text{from (4.3)} \\
 &= \int_0^y \frac{\partial \omega}{\partial x} \, dy + \int_0^y \frac{\partial^2 v}{\partial x^2} \, dy + \int_0^y \frac{\partial^2 v}{\partial y^2} \, dy \\
 &= \int_0^y \left(\frac{\partial \omega}{\partial x} + \nabla^2 v \right) \, dy = 0 && \text{from (4.5).}
 \end{aligned}$$

Therefore, the two governing equations of the system are:

$$\text{Vorticity transport equation: } \frac{\partial \omega}{\partial t} + U \frac{\partial \omega}{\partial x} + U'' v = \frac{1}{\text{Re}} \left(\frac{\partial^2 \omega}{\partial x^2} + \frac{\partial^2 \omega}{\partial y^2} \right) \tag{4.6a}$$

$$\text{Poisson equation: } \frac{\partial^2 v}{\partial x^2} + \frac{\partial^2 v}{\partial y^2} = -\frac{\partial \omega}{\partial x}. \tag{4.6b}$$

According to Bridges & Morris [10], in order to discretise the governing equations in the y -direction, it is convenient if they were to be converted to equations that involve integral operators. In their work, they solved the Orr-Sommerfeld equation by integrating four times to obtain its corresponding integrated form^{IV}. This idea of integrating the governing equations (4.6a) and (4.6b) was used by Davies [28] and Davies & Carpenter [31] in order to facilitate the discretisation of the governing equations by using the Chebyshev-Tau method. An advantage of casting the problem into a form that involves integral operators is that the system can be written as a set of banded matrices

^{IV}The phrase “integral form” or “integrated form” used here denote the form of the equations which involve the use of integral operators rather than differential ones.

(diagonal, tridiagonal, pentadiagonal, etc.). In this case, a modified form of the *Thomas Algorithm* can be used for solving the equations numerically (this algorithm is discussed in some detail in Appendix G and Davies [28]).

Integral Operators

In its differential form, the vorticity transport equation (4.6a) can be written as

$$\frac{\partial \omega}{\partial t} + \frac{\partial}{\partial x}(U\omega) + U''v = \frac{1}{\text{Re}} \left(\frac{\partial^2 \omega}{\partial x^2} + \frac{\partial^2 \omega}{\partial y^2} \right).$$

Integrating with respect to y twice gives

$$\frac{\partial}{\partial t} \iint \omega + \frac{\partial}{\partial x} \iint U\omega + \iint U''v = \frac{1}{\text{Re}} \frac{\partial^2}{\partial x^2} \iint \omega + \frac{1}{\text{Re}} \omega + A_1(x, t)y + A_0(x, t) \quad (4.7)$$

where $A_0(x, t)$ and $A_1(x, t)$ are functions of integration. Here, the double integrals are a notational abbreviation denoting

$$\iint f = \int_0^y \int_0^{y_2} f(y_1) dy_1 dy_2 \quad \text{for some function } f.$$

Doing the same with the Poisson equation (4.6b), namely

$$\frac{\partial^2 v}{\partial x^2} + \frac{\partial^2 v}{\partial y^2} = -\frac{\partial \omega}{\partial x},$$

gives its corresponding integrated form

$$v + \frac{\partial^2}{\partial x^2} \iint v = -\frac{\partial}{\partial x} \iint \omega + B_1(x, t)y + B_0(x, t) \quad (4.8)$$

where $B_0(x, t)$ and $B_1(x, t)$ are functions of integration. Since v , ω and U are all symmetric, the functions $A_1(x, t)$ and $B_1(x, t)$ can both be taken as 0 since there are no other odd terms present. Therefore the integrated forms of the

governing equations are:

$$\frac{\partial}{\partial t} \iint \omega + \frac{\partial}{\partial x} \iint U\omega + \iint U''v = \frac{1}{\text{Re}} \frac{\partial^2}{\partial x^2} \iint \omega + \frac{1}{\text{Re}} \omega + A_0(x, t) \quad (4.9a)$$

$$v + \frac{\partial^2}{\partial x^2} \iint v = -\frac{\partial}{\partial x} \iint \omega + B_0(x, t). \quad (4.9b)$$

4.3.4 Pressure Integral

So far, the governing equations have not referred to the pressure term p is needed since the pressure at the wall p_w needs to be calculated in order to determine the interactively coupled wall motion. Consider the y -momentum equation (4.1b)

$$\frac{\partial v}{\partial t} + U \frac{\partial v}{\partial x} = -\frac{\partial p}{\partial y} + \frac{1}{\text{Re}} \left(\frac{\partial^2 v}{\partial x^2} + \frac{\partial^2 v}{\partial y^2} \right).$$

Integrating with respect to y and using the fact that $p(0) = 0$ gives

$$p(y) = \int_0^y \left[-\frac{\partial v}{\partial t} - U \frac{\partial v}{\partial x} + \frac{1}{\text{Re}} \nabla^2 v \right] dy.$$

Evaluating this expression at the upper wall $y = 1$ and using the Poisson relation (4.6b) gives an expression of the fluid pressure at the upper wall

$$p_w = - \int_0^1 \left[\frac{\partial v}{\partial t} + U \frac{\partial v}{\partial x} + \frac{1}{\text{Re}} \frac{\partial \omega}{\partial x} \right] dy. \quad (4.10)$$

4.3.5 Wall Motion

In order to couple the fluid and wall motions, the pressure at the wall needs to be obtained from the pressure driven wall equation. For the spring-backed

plate model, the pressure driven wall equation is

$$p^*(h) = \left(m^* \frac{\partial^2}{\partial t^{*2}} + d^* \frac{\partial}{\partial t^*} + B^* \frac{\partial^4}{\partial x^{*4}} - T^* \frac{\partial^2}{\partial x^{*2}} + K^* \right) \eta^*$$

where the terms with an asterisk (\square^*) are dimensional quantities. Previously in Chapter 2, the system was non-dimensionalised using the mean centreline velocity U_m , channel half-width h , fluid density ρ and kinematic viscosity ν as:

$$x = \frac{x^*}{h}, \quad \eta = \frac{\eta^*}{h}, \quad t = \frac{t^* U_m}{h}, \quad p = \frac{p^*}{\rho U_m^2}$$

$$m = \frac{m^*}{\rho h}, \quad \frac{d}{\text{Re}} = \frac{d^*}{\rho U_m}, \quad \frac{B}{\text{Re}^2} = \frac{B^*}{\rho h^3 U_m^2}, \quad \frac{T}{\text{Re}^2} = \frac{T^*}{\rho h U_m^2}, \quad \frac{K}{\text{Re}^2} = \frac{K^* h}{\rho U_m^2}$$

$$\text{and the Reynolds number is } \text{Re} = \frac{U_m h}{\nu}.$$

If the Reynolds number is thought of as being varied by only changing the centreline velocity, then the non-dimensional wall parameters will also be altered accordingly. However, in order to keep the wall parameters fixed with this respect to this change, an alternative non-dimensionalisation can be employed for the wall parameters, particularly,

$$m = \frac{m^*}{\rho h}, \quad d = \frac{d^* \rho}{\nu}, \quad B = \frac{B^*}{\rho h \nu^2}, \quad T = \frac{T^* h}{\nu^2 \rho}, \quad K = \frac{K^* h^3}{\rho \nu^2}.$$

This uses the kinematic viscosity ν as a reference scale for the wall parameters and therefore if the Reynolds number is changed (by changing U_m), then the non-dimensional wall parameters (m, B, T, K and d) and the flow's physical configuration (ν and h) will remain unchanged. Using this alternative non-dimensionalisation will give an expression for p_w (which is the same as (2.14))

in Chapter 2) as

$$p_w = \left(m \frac{\partial^2}{\partial t^2} + \frac{d}{R} \frac{\partial}{\partial t} + \frac{1}{R^2} \left[B \frac{\partial^4}{\partial x^4} - T \frac{\partial^2}{\partial x^2} + K \right] \right) \eta. \quad (4.11)$$

4.3.6 Boundary Conditions

Two different sets of boundary conditions need to be imposed to the problem, one for the rigid sections and the other for the compliant wall section. At the rigid walls, the no slip and no penetration conditions are imposed, i.e.

$$u_w(x, t) = v_w(x, t) = 0 \quad \text{for } x \in [0, L_1] \cup (L_2, L].$$

Along the length of the compliant wall, components of the velocity and stress have to be continuous between the fluid and the compliant wall hence giving two boundary conditions, one on u and the other on v . (Note that the boundary condition on u needs to be determined from the interactive coupling of the wall and fluid motions.) Therefore, the boundary conditions on u and v can be obtained by evaluating (4.3) and v at the upper wall $y = 1$ to give

$$u_w = \int_0^1 \left(\omega + \frac{\partial v}{\partial x} \right) dy \quad \text{and} \quad v_w = v(x, 1, t) \quad \text{for } x \in [L_1, L_2].$$

4.3.7 Inflow & Outflow Conditions

Inflow Condition at $x = 0$

For the the current investigation, there are two ways in which the flow can excited, either by introducing an inflow profile φ or by using a localised impulsive forcing in the middle of the compliant wall (the form of the impulse

forcing was mentioned earlier in §4.2.2). If an inflow profile is introduced, then u , v and ω have to be prescribed at $x = 0$ and $y \in [0, 1]$. All these can be determined from the solutions of the Orr-Sommerfeld equation with a symmetric eigenfunction φ corresponding to the TS wavenumber for the rigid wall (since the wall is rigid at the inflow). Therefore at $x = 0$, the flow variables take the form

$$f(0, y, t) = \Re \left(f_{OS}(y) e^{-i\beta t} \left[1 - e^{-\frac{\beta t}{P}} \right] \right) \quad \text{where } f = v, \omega$$

The forcing frequency of the inflow is β and the subscript OS refers to the Orr-Sommerfeld solutions for the rigid wall. The term in the square brackets ($[\square]$) is a ramping up term which allows the disturbance to grow from zero and P refers to a delay parameter (i.e. the higher the value of P , the longer it will take for the ramping up to reach full amplitude), for all the cases presented, $P = 4\pi^2$.

The terms with a subscript OS are given in terms of the inflow disturbance profile φ as

$$v_{OS}(y) = -i\alpha\varphi \quad \text{and} \quad \omega_{OS}(y) = \varphi'' - \alpha^2\varphi.$$

No inflow condition on u is necessary since it does not appear explicitly in the vorticity transport equation, moreover if both v and ω are known, then u can be determined from (4.3) if so desired.

If the flow is disturbed by a localised impulsive forcing, then the inflow profile φ can be set to zero and therefore $u, v, \omega = 0$ at $x = 0$ and $y \in [0, 1]$. Care needs to be taken in monitoring the progression of the excited disturbances in order to ensure that no artificial effects appear from reflections at the inflow boundary.

Outflow Condition at $x = L$

At the outflow, it can be assumed that the flow variables are wavelike (as was suggested by Fasel [36]), this means that they take the form $f \sim e^{i\alpha x}$ where α is complex in general. Therefore the flow variables u, v and ω satisfy the differential equation

$$\frac{\partial^2 f}{\partial x^2} + 2\Im(\alpha)\frac{\partial f}{\partial x} + |\alpha|^2 f = 0.$$

This outflow condition allows small amplitude TS waves to pass out of the computational domain smoothly without causing unphysical reflections from the end of the computational boundary. Imposing this condition requires an approximate value of the wavenumber α to be prescribed at the outflow and this can be obtained from the solution of the Orr-Sommerfeld equation for the rigid wall as well. It should be noted that the outflow condition is relatively insensitive of the exact value of the wavenumber α provided that the distance between the downstream end of the compliant wall ($x = L_2$) and the outflow ($x = L$) is sufficiently long.

4.3.8 Join Condition Between the Rigid & Compliant Walls

At the compliant wall ends ($x = L_1, L_2$), either hinging or clamping conditions can be imposed in order to attach the rigid and compliant wall sections. The hinged conditions are:

- * $\eta = 0$: The edges of the compliant wall section do not deflect from their equilibrium positions
- * $\frac{\partial^2 \eta}{\partial x^2} = 0$: The edges of the compliant wall section are free to rotate but

do not experience any torque.

On the other hand, the clamped conditions are:

- * $\eta = 0$: Same interpretation as the hinged case
- * $\frac{\partial \eta}{\partial x} = 0$: The compliant wall is horizontal at the edges.

Previous accounts on the join conditions (see for instance Davies & Carpenter [31]) reported that changes at the leading and trailing edge were less drastic when the clamped condition was imposed since clamping the wall effectively increases the wall stiffness, but otherwise the flow dynamics were largely similar. For the current purposes, the hinged conditions will be used unless otherwise stated.

4.4 Numerical Discretisation Procedure

The numerical scheme used here employs a hybrid approach combining a Chebyshev-Tau spectral method for discretising the flow variables in the y -direction and a second order finite differencing in the x and t -directions. In the following sections, the equations obtained earlier are discretised spatially and temporally, the system of equations then forms a banded system of matrices that can then be solved by using the modified Thomas Algorithm. These equations and boundary conditions are restated here for ease of reference:

- Governing equations which involve integral operators:
 - * Vorticity transport equation:

$$\iint \left[\frac{\partial \omega}{\partial t} + \frac{\partial}{\partial x}(U\omega) + U''v \right] = \frac{1}{\text{Re}} \frac{\partial^2}{\partial x^2} \iint \omega + \frac{1}{\text{Re}} \omega + A_0(x, t). \quad (4.12)$$

* Poisson equation:

$$v + \frac{\partial^2}{\partial x^2} \iint v = -\frac{\partial}{\partial x} \iint \omega + B_0(x, t). \quad (4.13)$$

– Pressure integral:

$$p_w(x, t) = - \int_0^1 \left(\frac{\partial v}{\partial t} + U \frac{\partial v}{\partial x} + \frac{1}{\text{Re}} \frac{\partial \omega}{\partial x} \right) dy. \quad (4.14)$$

– Pressure driven wall equation:

$$p_w(x, t) = \left(m \frac{\partial^2}{\partial t^2} + \frac{d}{\text{Re}} \frac{\partial}{\partial t} + \frac{1}{\text{Re}^2} \left[B \frac{\partial^4}{\partial x^4} - T \frac{\partial^2}{\partial x^2} + K \right] \right) \eta. \quad (4.15)$$

– Boundary conditions:

* Rigid wall $x \in (0, L_1) \cup (L_2, L)$:

$$u_w(x, t) = v_w(x, t) = 0. \quad (4.16)$$

* Compliant wall $x \in (L_1, L_2)$:

$$u_w(x, t) = \int_0^1 \left(\omega + \frac{\partial v}{\partial x} \right) dy, \quad v_w(x, t) = v(x, 1, t). \quad (4.17)$$

– Inflow conditions:

* Inflow profile φ :

$$f(0, y, t) = \Re (f_{OS}(y) e^{-i\beta t}) \quad \text{for } f = v, \omega \quad (4.18)$$

$$\text{where } v_{OS}(y) = -i\alpha\varphi, \quad \omega_{OS} = \varphi'' - \alpha^2\varphi.$$

The function φ is the disturbance streamfunction which is obtained from

the solution of the Orr-Sommerfeld equation for the TS mode over a rigid wall.

* Impulsive excitation: $\varphi \equiv 0$

– Outflow condition:

$$\frac{\partial^2 f}{\partial x^2} + 2\Im(\alpha)\frac{\partial f}{\partial x} + |\alpha|^2 f = 0 \quad \text{for } f = u, v, \omega. \quad (4.19)$$

– Join conditions at $x = L_1, L_2$:

* Clamped:

$$\eta = \frac{\partial \eta}{\partial x} = 0 \quad (4.20)$$

* Hinged:

$$\eta = \frac{\partial^2 \eta}{\partial x^2} = 0. \quad (4.21)$$

Once again, it should be made very clear that all the details of the discretisation have been taken from elsewhere, particularly Davies [28] and Davies & Carpenter [31]. However, detailed accounts of this method have not been previously given in the literature in a fully collated form.

4.5 Discretisation in the y -Direction

First, the Chebyshev-Tau method is used to discretise the disturbances in the y -direction, this involves representing the functions of the system as a linear combination of Chebyshev polynomials. Since v and ω are symmetric, they can be represented as a linear combination of even Chebyshev polynomials. The function u , on the other hand, is odd and can be represented as a linear combination of odd Chebyshev polynomials, alternatively, if v and ω

are known, then u can be determined from (4.3).

The Chebyshev-Tau method was used by Bridges & Morris [10] in order to discretise the Orr-Sommerfeld equation by first converting it into an equation with integral operators rather than differential ones. The boundary conditions for the rigid wall plane channel flow were then incorporated by using the Tau method in order to have a fully determined set of equations (this is due to Lanczos [80] and is described in Appendix F). The details for the y -discretisation of the Orr-Sommerfeld equation for the rigid wall plane channel flow is given in their appendix while that of the compliant wall is given in Davies [28].

4.5.1 General Form of the Discretised Functions

For an arbitrary even function $f = f(x, y, t)$, the general form for the y -discretisation and the corresponding matrix form of f , $\iint f$ and $\iint Uf$ need to be established.

First, since f is even, it can be represented as a linear combination of even Chebyshev polynomials as

$$f(x, y, t) = \frac{1}{2}f_1(x, t)T_0(y) + \sum_{k=2}^N f_k(x, t)T_{2(k-1)}(y)$$

for some functions f_1, f_2, \dots, f_N to be determined^V. Alternatively, f can be written as

$$f(x, y, t) = \sum_{k=1}^N r_k f_k(x, t) T_{2(k-1)}(y) \quad (4.22)$$

$$\text{where } r_k = \begin{cases} \frac{1}{2} & k = 1 \\ 1 & k = 2, 3, \dots, N. \end{cases} \quad (4.23)$$

^VBridges and Morris [10] used this expansion with the first term being $\frac{1}{2}$ rather than 1 for convenience when it comes to deriving the discretisation of the Orr-Sommerfeld equation.

A diagonal matrix M_1 (of size $N \times N$) can be used to represent this expansion and is given by

$$M_1 = \begin{pmatrix} \frac{1}{2} & & & & \\ & 1 & & & \\ & & \ddots & & \\ & & & 1 & \\ & & & & 1 \end{pmatrix}. \quad (4.24)$$

In the current scheme, the first row of the matrices is replaced with one of the boundary condition giving a matrix that will be denoted \tilde{M}_1 (therefore having the first term being $\frac{1}{2}$ is not pertinent any more). Additionally, dispensing with the first row is a feasible step since the first equation only serves the purpose of determining the functions of integration A_0 and B_0 (further details are given in the next section). The discretisation of the boundary conditions and their incorporation is discussed later in §4.5.4.

When the Chebyshev representation (4.22) is used to discretise $\iint f$, an extra equation would result equating the coefficients of the polynomial T_{2N} (since the integration increases the order of the polynomials). The matrix representation of $\iint f$, denoted M_3 , will therefore be of size $N \times (N + 1)$. Just as before, the first row is replaced by the boundary condition while the last row (equating the coefficients of T_{2N}) is dispensed with as a consequence of the Tau method, this new matrix is now denoted \tilde{M}_3 . The full form of the y -discretisation of $\iint f$ as well as its full matrix form M_3 is given in Appendix E. After the rows have been removed and the boundary conditions have been incorporated appropriately, the matrix \tilde{M}_3 will in fact be a tridiagonal matrix with a full first row (hence the subscript 3).

Finally, the discretisation of $\iint Uf$ is required. The basic velocity profile

U can be represented as linear combination of Chebyshev polynomials as

$$U(y) = 1 - y^2 = \frac{1}{2} [T_0(y) - T_2(y)] \quad \text{for } y \in [0, 1].$$

The corresponding matrix representation of $\iint Uf$ is denoted M_5 and its full form, along with the y -discretisation is given in Appendix E. The discretised form of $\iint Uf$ introduces *two* extra polynomials T_{2N} and T_{2N+2} , their corresponding equations are dispensed with as a consequence of the Tau method and the first row is replaced with the boundary condition (just as before). This modified matrix will be denoted by \tilde{M}_5 and is a pentadiagonal matrix with a full first row.

The banded matrices that are formed here can then be solved using the modified Thomas Algorithm, this method eliminates terms from the first row of the matrices during the backwards sweep. The Thomas algorithm for tridiagonal, pentadiagonal and pentadiagonal with a full first row is described in Appendix G.

Now that the general forms of the y -discretisations of f , $\iint f$ and $\iint Uf$ have been obtained for an arbitrary even function f , they will now be used to obtain the discretised forms of the governing equations.

4.5.2 Governing Equations

Poisson Equation

Since v and ω are symmetric, they can be expanded in the form given in (4.22). The y -discretisation of $\iint f$ can be used in the Poisson equation (4.13), namely,

$$\iint \left(\frac{\partial^2 v}{\partial x^2} + \frac{\partial \omega}{\partial x} \right) + v = B_0$$

with

$$f = \frac{\partial^2 v}{\partial x^2} + \frac{\partial \omega}{\partial x}$$

since f is even. The result is a set of $N+1$ equations (equating the coefficients of T_0, T_2, \dots, T_{2N}) in N unknown functions (v_1, v_2, \dots, v_N). As discussed earlier, the boundary condition replaces the first row and the last row is dispensed. This leaves a set of $N-1$ equations in N unknown functions which can be written as:

$$\sum_{k=1}^N \left[\delta_{jk} v_k + I_{jk} \left(\frac{\partial^2 v_k}{\partial x^2} + \frac{\partial \omega_k}{\partial x} \right) \right] = 0 \quad \text{for } j = 2, 3, \dots, N. \quad (4.25)$$

The term I_{jk} represents the matrix operator of $\iint f$ obtained from the full expression given in equation (E.1) in Appendix E and can be written as

$$I_{jk} f_k = \frac{\delta_{jk}}{4} \left(\frac{f_{k-1}}{(2k-2)(2k-3)} - \frac{2f_k}{(2k-1)(2k-3)} + \frac{f_{k+1}}{(2k-1)(2k-2)} \right) \quad (4.26)$$

where δ_{jk} is the Kronecker delta function

$$\delta_{jk} = \begin{cases} 1 & j = k \\ 0 & j \neq k. \end{cases} \quad (4.27)$$

The resulting set of $N-1$ equations can be written in a tridiagonal matrix form by using the matrices \tilde{M}_1 and \tilde{M}_3 (which are the matrices M_1 and M_3 with their first row replaced with the boundary condition and the last row of M_3 removed). Suppose that a caret over a vector ($\hat{\square}$) is the same vector with

its first term removed only, i.e.

$$\text{if } \mathbf{w} = \begin{pmatrix} w_1 \\ w_2 \\ \vdots \\ w_n \end{pmatrix}, \quad \text{then } \hat{\mathbf{w}} = \begin{pmatrix} w_2 \\ \vdots \\ w_n \end{pmatrix}.$$

The remaining set of equations can then be written as a tridiagonal matrix system of equations with a full first row as:

$$\left(\begin{array}{cccccccc} \bullet & \bullet & \bullet & \bullet & \cdots & \bullet & \bullet & \\ & \bullet & \bullet & \bullet & & & & \\ & & \bullet & \bullet & \bullet & & & \\ & & & \ddots & \ddots & \ddots & & \\ & & & & \bullet & \bullet & \bullet & \\ & & & & & \bullet & \bullet & \bullet \\ & & & & & & \bullet & \bullet \end{array} \right) \left. \begin{array}{l} \leftarrow \text{Boundary condition} \\ \text{These terms are obtained} \\ \text{from equation (4.25) as} \\ \tilde{M}_1 \hat{\mathbf{v}} + \tilde{M}_3 \hat{\mathbf{f}} = \mathbf{0} \\ \text{where} \\ \hat{\mathbf{f}} = \frac{\partial^2 \hat{\mathbf{v}}}{\partial x^2} + \frac{\partial \hat{\boldsymbol{\omega}}}{\partial x}. \end{array} \right\}$$

This set of equations can then be tackled by the modified Thomas algorithm (as explained in Appendix G).

Vorticity Transport Equation

The second governing equation of the fluid flow is given by the vorticity transport equation (4.12), namely

$$-\frac{1}{\text{Re}} \omega + \iint \left(\frac{\partial \omega}{\partial t} + U''v - \frac{1}{\text{Re}} \frac{\partial^2 \omega}{\partial x^2} \right) + \iint \left(U \frac{\partial \omega}{\partial x} \right) = A_0.$$

This is discretised in the same way as the Poisson equation using the y -discretisations of $\iint f$ and $\iint Uf$. Therefore the remaining set of equations

can be written as

$$-\frac{1}{\text{Re}} \sum_{k=1}^N \left[\delta_{jk} \omega_k + I_{jk} \left(\frac{\partial \omega_k}{\partial t} + U'' v_k - \frac{1}{\text{Re}} \frac{\partial^2 \omega_k}{\partial x^2} \right) + U_{jk} \frac{\partial \omega_k}{\partial x} \right] = 0$$

for $j = 2, 3, \dots, N$. (4.28)

The term U_{jk} represents the matrix operator of $\iint Uf$ obtained from the full expression given in equation (E.2) Appendix E. The operator $U_{jk}f$ is equivalent to writing $I_{jk}(Uf)$ where

$$Uf = \frac{f_1 - f_2}{2} - \sum_{k=2}^{N-1} \frac{f_{k+1} - 2f_k + f_{k-1}}{4} T_{2(k-1)}(y) + \frac{2f_N - f_{N-1}}{4}. \quad (4.29)$$

The resulting set of equations can be written in a pentadiagonal matrix form by using the matrices \tilde{M}_1, \tilde{M}_3 and \tilde{M}_5 with a full first row as:

$$\left(\begin{array}{cccccccc} \bullet & \bullet & \bullet & \bullet & \bullet & \bullet & \dots & \bullet & \bullet \\ \bullet & \bullet & \bullet & \bullet & & & & & \\ \bullet & \bullet & \bullet & \bullet & \bullet & & & & \\ & \bullet & \bullet & \bullet & \bullet & \bullet & & & \\ & & \dots & \dots & \dots & \dots & \dots & & \\ & & & \bullet & \bullet & \bullet & \bullet & \bullet & \\ & & & & \bullet & \bullet & \bullet & \bullet & \bullet \\ & & & & & \bullet & \bullet & \bullet & \bullet \\ & & & & & & \bullet & \bullet & \bullet \\ & & & & & & & \bullet & \bullet & \bullet \end{array} \right) \left. \begin{array}{l} \leftarrow \text{Boundary condition} \\ \\ \text{These terms are obtained} \\ \text{from equation (4.28) as} \\ -\frac{1}{\text{Re}} \tilde{M}_1 \hat{\omega} + \tilde{M}_3 \hat{\mathbf{g}} + \tilde{M}_5 \hat{\mathbf{h}} = \mathbf{0} \\ \\ \text{where} \\ \hat{\mathbf{g}} = \frac{\partial \hat{\omega}}{\partial t} + U'' \hat{\mathbf{v}} - \frac{1}{\text{Re}} \frac{\partial^2 \hat{\omega}}{\partial x^2} \\ \\ \text{and} \\ \hat{\mathbf{h}} = \frac{\partial \hat{\omega}}{\partial x}. \end{array} \right\}$$

4.5.3 Pressure Integral

The fluid pressure at the upper wall is given in equation (4.14) as

$$p_w = - \int_0^1 \left[\left(\frac{\partial v}{\partial t} + \frac{1}{\text{Re}} \frac{\partial \omega}{\partial x} \right) + U \frac{\partial v}{\partial x} \right] dy.$$

When the y -discretisation is imposed on v and ω , the pressure can be written as

$$p_w = - \sum_{k=1}^N \left[q_k \left(\frac{\partial v_k}{\partial t} + \frac{1}{\text{Re}} \frac{\partial \omega_k}{\partial x} \right) + s_k \frac{\partial v_k}{\partial x} \right]. \quad (4.30)$$

The term q_k represents the coefficients of the Chebyshev expansion when integrated with respect to y across the half-channel and s_k represents the coefficients of the Chebyshev expansion multiplied by the basic velocity profile U and then integrated on $y \in [0, 1]$, in other words

$$q_k = \int_0^1 T_{2k}(y) dy = \begin{cases} \frac{1}{2} & k = 1 \\ -\frac{1}{4k^2-1} & k = 2, 3, \dots, N \end{cases} \quad (4.31)$$

$$\text{and } s_k = \int_0^1 U(y) T_{2k}(y) dy = \begin{cases} \frac{1}{3} & k = 1 \\ \frac{6}{(4k^2-1)(4k^2-9)} & k = 2, 3, \dots, N. \end{cases} \quad (4.32)$$

The pressure term found here aids in updating the wall heights since the wall motion is assumed to be pressure driven.

4.5.4 Boundary Conditions

Over the rigid wall sections, the boundary conditions are simply zero, i.e.

$$u_w = v_w = 0.$$

Over the compliant wall insert, the two boundary conditions are

$$u_w = \int_0^1 \left(\omega + \frac{\partial v}{\partial x} \right) dy \quad (4.33a)$$

$$v_w = v(x, 1, t). \quad (4.33b)$$

Using the assumed expansion for v and ω given in (4.22) and the integration recipes in Appendix B, the compliant wall boundary conditions can be discretised, respectively, as

$$u_w = \sum_{k=1}^N q_k \left(\omega_k + \frac{\partial v_k}{\partial x} \right) \quad (4.34a)$$

$$v_w = \sum_{k=1}^N r_k v_k. \quad (4.34b)$$

The term r_k represents the coefficients of the Chebyshev expansion (4.22) (as given in equation (4.23)) while q_k represents the coefficients of the Chebyshev expansion when integrated on $y \in [0, 1]$ (as in (4.31)).

4.6 Discretisation in the x & t -Directions

The governing equations, boundary conditions and pressure integral have all been discretised in the y -direction by using a Chebyshev discretisation and the Tau method. Now, they shall be discretised in x and t using a finite differencing scheme.

For the current investigation, a second order finite differencing scheme is used in order to discretise the equations in x and t . For a function f , let

$$f_{k,n}^l \quad \text{denote} \quad f_k(x_n, t_l)$$

where $k \in \{1, 2, \dots, N\}$, $n \in \{0, 1, \dots, n_e\}$ and $l \in \mathbb{N}$.

The indices of $f_{k,n}^l$ are interpreted as follows:

- * k denotes the coefficient of the Chebyshev polynomial $T_{2(k-1)}$ as given in (4.22), namely the underlined terms below:

$$f(x, y, t) = \sum_{k=1}^N r_k \underline{f_k(x, t)} T_{2(k-1)}(y).$$

- * n denotes the discretised streamwise location where $x_n = n\Delta x$ for the streamwise increment Δx . This means that the inflow is at $n = 0$ (i.e. $x_0 = 0$), the outflow is at $n = n_e$ ($x_{n_e} = L$) and the compliant wall extends from $n = n_1$ ($x_{n_1} = L_1$) to $n = n_2$ ($x_{n_2} = L_2$).
- * l denotes the discretised time where $t_l = l\Delta t$ for the time increment Δt .

For the x -discretisation, a second order centred finite differencing approximation is taken, the expressions for the first four derivatives with respect to x are given as the following:

$$\begin{aligned} * \quad \frac{\partial f_{k,n}^l}{\partial x} &= \frac{1}{2\Delta x} (f_{k,n+1}^l - f_{k,n-1}^l) \\ * \quad \frac{\partial^2 f_{k,n}^l}{\partial x^2} &= \frac{1}{(\Delta x)^2} (f_{k,n+1}^l - 2f_{k,n}^l + f_{k,n-1}^l) \\ * \quad \frac{\partial^3 f_{k,n}^l}{\partial x^3} &= \frac{1}{2(\Delta x)^3} (f_{k,n+2}^l - 2f_{k,n+1}^l + 2f_{k,n-1}^l - f_{k,n-2}^l) \\ * \quad \frac{\partial^4 f_{k,n}^l}{\partial x^4} &= \frac{1}{(\Delta x)^4} (f_{k,n+2}^l - 4f_{k,n+1}^l + 6f_{k,n}^l - 4f_{k,n-1}^l + f_{k,n-2}^l). \end{aligned} \quad (4.35)$$

For the t -discretisation, a three-point backward differencing method is used, particularly,

$$\frac{\partial f_{k,n}^l}{\partial t} = \frac{1}{2\Delta t} (3f_{k,n}^l - 4f_{k,n}^{l-1} + f_{k,n}^{l-2}). \quad (4.36)$$

4.7 The Numerical Procedure

The numerical procedure employed here come in three steps, first, the vorticity ω is predicted from the vorticity equation using the values of v and ω from the previous time steps. Second, the velocity v is solved for iteratively by using the Poisson equation and finally, the vorticity ω is corrected using the vorticity equation. The vorticity predictor-corrector stage of the current method was used by previous authors such as Davies [28], Davies & Carpenter [32], Heaney [69] and Togneri [122].

4.7.1 Vorticity Predication

Consider the vorticity equation (4.2),

$$\frac{\partial\omega}{\partial t} + U\frac{\partial\omega}{\partial x} + U''v = \frac{1}{\text{Re}} \left(\frac{\partial^2\omega}{\partial x^2} + \frac{\partial^2\omega}{\partial y^2} \right).$$

This can be rewritten as

$$\frac{\partial\omega}{\partial t} = E + \frac{\partial^2\omega}{\partial y^2} \quad \text{where} \quad E = -U\frac{\partial\omega}{\partial x} - U''v + \frac{1}{\text{Re}} \frac{\partial^2\omega}{\partial x^2}. \quad (4.37)$$

The term E can be treated explicitly while the term $\frac{\partial^2\omega}{\partial y^2}$ is treated implicitly.

The predicted value of E , denoted \bar{E} , can be obtained from values of v and ω from the previous times as

$$\bar{E} = 2E^{l-1} - E^{l-2} = 2E(\omega^{l-1}, v^{l-1}) - E(\omega^{l-2}, v^{l-2}). \quad (4.38)$$

This can be used to predict the value of the vorticity ω at the timestep l and this shall be denoted $\bar{\omega}^l$. Using the time discretisation (4.36) and equation

(4.38), the vorticity transport equation (4.37) can be written as

$$\left(\frac{3}{2\Delta t} - \frac{1}{\text{Re}} \frac{\partial^2}{\partial y^2} \right) \bar{\omega}^l = [2E^{l-2} - E^{l-1}] + \frac{2}{\Delta t} \omega^{l-1} - \frac{1}{2\Delta t} \omega^{l-2}. \quad (4.39)$$

This is solved to find the predicted vorticity $\bar{\omega}^l$ subject to the integral condition

$$\int \bar{\omega}^l = \int (2\omega^{l-1} - \omega^{l-2}). \quad (4.40)$$

An equivalent form of this condition can be obtained by using the constraint on u given in equation (4.4) and the linearised boundary conditions on u , namely

$$u_w = \int_0^1 \left(\omega + \frac{\partial v}{\partial x} \right) dy \quad \text{and} \quad u_w = -U'(1)\eta. \quad (4.41)$$

The integral condition on ω given in equation (4.40) now becomes

$$\int \bar{\omega}^l = -U'(1) (2\eta^{l-1} - \eta^{l-2}) - \frac{\partial}{\partial x} \int (2v^{l-1} - v^{l-2}).$$

Notice that solving for the predicted vorticity $\bar{\omega}^l$ under this restriction is independent of the streamwise location.

4.7.2 Velocity Iteration

Now that the vorticity $\bar{\omega}^l$ has been predicted, the Poisson equation can be used to obtain an expression for the velocity field v^l (and hence the wall displacement η^l). Consider the Poisson equation (4.5), namely

$$\frac{\partial^2 v}{\partial x^2} + \frac{\partial^2 v}{\partial y^2} = -\frac{\partial \bar{\omega}}{\partial x}. \quad (4.42)$$

The right hand side of this equation is fixed after having been determined from the vorticity prediction stage. The Poisson relation needs to be solved iteratively in order to determine the velocity v^l . However, a problem arises since attempting to solve the system of equations for the fluid and wall motions independently will most likely incur numerical instabilities. Further details of this issue were addressed in Lucey & Carpenter [89] where they suggested that the wall and hydrodynamic inertias should be coupled otherwise if treated separately, one of the terms may dominate and the method fails to converge.

Flow Inertia

According to Lucey & Carpenter [89], the fluid and wall motions across the compliant wall section can be coupled by using the *total normal momentum of the channel* μ which consists of the wall and hydrodynamic inertial terms as

$$\mu(x, t) = \underbrace{mv_w}_{\text{wall inertia}} + \underbrace{\int_0^1 v \, dy}_{\text{hydrodynamic inertia}} \quad (4.43)$$

where m is the mass of the wall. This equation provides a condition when determining v from the Poisson equation over the compliant wall. As for the rigid sections, the condition on v is

$$v_w = 0. \quad (4.44)$$

The Poisson equation has to be solved for v iteratively subject to the conditions (4.43) and (4.44). After v is determined, the wall displacement η can be obtained by using the linearised boundary condition

$$v_w = \frac{\partial \eta}{\partial t}. \quad (4.45)$$

Using the time discretisation (4.36), equation (4.45) can be written in a form that would determine η at the current timestep l by using the determined value v^l as well as the values of η and the two previous timestep as

$$\eta^l = \frac{2\Delta t}{3} \left[\frac{2}{\Delta t} \eta^{l-1} - \frac{1}{2\Delta t} \eta^{l-2} + (v_w)^l \right]. \quad (4.46)$$

As yet, the newly introduced total normal momentum μ has not been used. This term comes into play when coupling the fluid and wall motions.

Total Normal Momentum

Consider the expressions for the pressure at $y = 1$ in equations (4.14) and (4.15):

$$* \quad p_w = \left(m \frac{\partial^2}{\partial t^2} + \frac{d}{\text{Re}} \frac{\partial}{\partial t} + \frac{B}{\text{Re}^2} \frac{\partial^4}{\partial x^4} - \frac{T}{\text{Re}^2} \frac{\partial^2}{\partial x^2} + \frac{K}{\text{Re}^2} \right) \eta \quad (4.47)$$

$$* \quad p_w = - \int_0^1 \left[\frac{\partial v}{\partial t} + U \frac{\partial v}{\partial x} + \frac{1}{\text{Re}} \frac{\partial \omega}{\partial x} \right] dy. \quad (4.48)$$

Equating both these expressions and using the linearised boundary condition $v_w = \frac{\partial \eta}{\partial t}$ gives

$$\frac{\partial \mu}{\partial t} + \frac{d}{\text{Re}} v_w + \mathcal{L} \eta = - \frac{\partial}{\partial x} \int_0^1 \left[U v + \frac{1}{\text{Re}} \omega \right] dy \quad (4.49)$$

where \mathcal{L} is a linear differential operator defined as

$$\mathcal{L} \equiv \frac{1}{\text{Re}^2} \left(B \frac{\partial^4}{\partial x^4} - T \frac{\partial^2}{\partial x^2} + K \right).$$

For an arbitrary function f , the operator \mathcal{L} acting on f at a point $x = x_n$ can be discretised using the x -discretisations in (4.35) as

$$\begin{aligned} \mathcal{L}f_n = \frac{1}{\text{Re}^2} & \left(\frac{B}{(\Delta x)^4} (f_{n+2} + f_{n-2}) - \frac{1}{(\Delta x)^2} \left[\frac{4B}{(\Delta x)^2} + T \right] (f_{n+1} + f_{n-1}) \right. \\ & \left. + \left[\frac{6B}{(\Delta x)^4} + \frac{2T}{(\Delta x)^2} + K \right] f_n \right). \end{aligned}$$

Using the t -discretisation (4.36), equation (4.49) can be used to determine μ at the current timestep by using the predicted vorticity $\bar{\omega}^l$ and the velocity v^l as

$$\begin{aligned} \mu^l = \frac{1}{3} [4\mu^{l-1} - \mu^{l-2}] - \frac{2\Delta t}{9} \mathcal{L} [4\eta^{l-1} - \eta^{l-2}] \\ - \frac{2\Delta t}{3} \left[\frac{d}{\text{Re}} + \frac{2\Delta t}{3} \mathcal{L} \right] v_w^l - \frac{2\Delta t}{3} \frac{\partial}{\partial x} \int_0^1 \left[Uv^l + \frac{1}{\text{Re}} \bar{\omega}^l \right] dy. \end{aligned} \quad (4.50)$$

Using the expression for μ given in (4.43), equation (4.50) can be expressed in terms of v and η as

$$\begin{aligned} mv_w^l + \int_0^1 v^l dy = \frac{1}{3} \left[m (4v_w^{l-1} - v_w^{l-2}) + \left(4 \int_0^1 v^{l-1} dy - \int_0^1 v^{l-2} dy \right) \right] \\ - \frac{2\Delta t}{9} \mathcal{L} [4\eta^{l-1} - \eta^{l-2}] - \frac{2\Delta t}{3} \left[\frac{d}{\text{Re}} + \frac{2\Delta t}{3} \mathcal{L} \right] v_w^l - \frac{2\Delta t}{3} \frac{\partial}{\partial x} \int_0^1 \left[Uv^l + \frac{1}{\text{Re}} \bar{\omega}^l \right] dy. \end{aligned} \quad (4.51)$$

According to Davies & Carpenter [31], equation (4.51) can be used to couple the fluid and wall motions effectively via the total inertia μ . Therefore the boundary condition (4.34b),

$$v_w = \sum_{k=2}^N r_k v_k,$$

can then be modified to include the wall terms as

$$\tilde{v}_w = \sum_{k=2}^N \tilde{r}_k v_k$$

$$\text{where } \tilde{r}_k = m + \frac{2d\Delta t}{3\text{Re}} + \frac{4(\Delta t)^2}{9\text{Re}^2} \left[\frac{6B}{(\Delta x)^4} + \frac{2T}{(\Delta x)^2} + K \right] + q_k$$

and q_k is given in (4.34a). The modified term \tilde{r}_k here can be regarded as being an *effective wall stiffness*.

Returning to the Velocity Iteration

Now that the predicted vorticity $\bar{\omega}$ has been obtained and fluid/wall motions have been coupled appropriately, the Poisson equation can be solved iteratively to obtain v^l (and hence v_w^l) subject to the boundary conditions:

$$\begin{aligned} v_w^l &= 0 && \text{on the rigid sections} \\ \mu^l &= m v_w^l + \int_0^1 v^l dy && \text{on the compliant section.} \end{aligned}$$

The wall displacement η^l can now be determined by using the discretised form of the linearised boundary condition $v_w = \frac{\partial \eta}{\partial t}$ as given in equation (4.46).

4.7.3 Vorticity Correction

The final stage is to correct the vorticity using its predicted value $\bar{\omega}^l$ and the velocity v^l . The vorticity transport equation is used just as in equation (4.39) but with a slight modification, particularly

$$\left(\frac{3}{2\Delta t} - \frac{1}{\text{Re}} \frac{\partial^2}{\partial y^2} \right) \omega^l = \bar{E}^l + \frac{2}{\Delta t} \omega^{l-1} - \frac{1}{2\Delta t} \omega^{l-2} \quad \text{where } \bar{E}^l = E(\bar{\omega}^l, v^l). \quad (4.52)$$

This equation is solved subject to a similar integral constraint as before, namely

$$\int \omega^l = -U'(1)\eta^l - \frac{\partial}{\partial x} \int v^l.$$

4.8 Summary

The velocity-vorticity formulation is used as a basis for the numerical procedure described here and consists of two equations, the vorticity transport equation and the Poisson equation. The Chebyshev-Tau method is used to discretise the equations in the y -direction then a second order finite differencing scheme is used for the x and t -discretisations. This forms a set of banded matrices with a full first row (representing the boundary conditions) which are then be tackled by using a modified form of the Thomas Algorithm. The numerical procedure is conducted in three steps as follows:

1. The vorticity is predicted from the vorticity transport equation using the values of v and ω from the previous time steps subject to an integral constraint on the vorticity.
2. The Poisson equations is solved iteratively in order to obtain the new velocity v subject to the local boundary conditions. The fluid and wall motions had to be coupled through a total momentum term to ensure that the method converges. The value of the wall displacement can also be obtained simultaneously alongside the velocity v during this iteration step.
3. The vorticity is corrected using the predicted vorticity and the newly obtained velocity field.

All the details of this method have been presented previously in different studies, particularly in Davies [28], Davies & Carpenter [30] [32], Fasel [36] [37] and Fasel & Konzelmann [38] [39]. However, its inclusion here serves the purpose of collating some of their different ideas and schemes.

In the two chapters that follow, this procedure is implemented for different cases. In Chapter 5, the results obtained from this numerical simulation are compared to the solutions of the Orr-Sommerfeld equation obtained from Chapter 3 to show how these solutions can be used to predict the behaviour of the waves appearing in the DNS.

In Chapter 6, the simulations are conducted to investigate the prospect of *absolute* and *global instabilities* in some flow scenarios. The Orr-Sommerfeld equation are used to locate regions in the parameter space where absolute growth may be expected then the DNS can be used to corroborate these claims.

Chapter 5

Simulation of Disturbance Development for Various Instabilities

5.1 Introduction

In this chapter, *direct numerical simulations* (DNS) are performed for specifically chosen wall and flow parameters in order to investigate the spatial development of the different instabilities, particularly, the effect of each of these instabilities/modes on the wall's displacement, velocity and vorticity are investigated. The solution of the Orr-Sommerfeld equation (described in Chapter 3) is used to obtain predictions for the wavenumbers that would be expected to arise from the DNS and the results will be compared.

The DNS method described in Chapter 4 was initially developed by Davies [28] in order to study the effect of wall compliance on the evolution of the TS instability. Here, this is extended to study the effects of wall compliance on the

wall-based instabilities as well and this has not been documented previously. In the next chapter, this method will be taken even further to investigate absolute and global instabilities.

Four different investigations are carried out in this chapter and these different cases are labelled in bold letters as follows:

- * **TSM**: This is a corroborative test showing a pure TS wave passing over the rigid and compliant wall sections. A particular set of wall parameters is chosen to demonstrate the spatial behaviour of the TS wave across the whole domain. Though this particular example has been documented previously, it is repeated here simply to set a theme for the rest of the cases and to show the workings of the DNS and how the Orr-Sommerfeld solutions can be used to predict the arising modes.
- * **TSS**: This case illustrates the compliant wall's TS stabilisation capabilities. An unstable TS wave is introduced at the inflow and the effect of the compliant wall on this wave is assessed. Once again, this case has been investigated before, particularly by Davies & Carpenter [31] but is reproduced here to show the original intention of the DNS method.
- * **TWF**: This case considers an interaction between different modes where the wall displacement takes the form of an amplitude modulated wave. This form is a result of a superposition of two modes travelling in different directions, one can be attributed to the TWF mode while the other is due to a reflection from the downstream boundary. This is the first documented evidence of using the current DNS method to show the spatial development of the TWF mode and the fact that the Orr-Sommerfeld solutions can predict the arising wavenumbers very effectively.

* **DivEnd**: The final case to consider is perhaps the most interesting. The wave that results is a combination of *five* modes, each playing a different role in forming the wall displacement. These modes arise as a result of the wall-based modes due to the choice of flow parameters, particularly the divergence instability. In this case, the solutions of the Orr-Sommerfeld equation can effectively predict the behaviour of the wall displacement in the central region of the compliant wall *and* the end effects as well (hence the name, **Div** for the divergence and **End** for the end effects). This is a peculiar phenomenon since the Orr-Sommerfeld equation solved in Chapter 3 assumes that the wall is infinitely long, even with this in mind, it can still predict the end effects that arise from the DNS when the wall is finite.

The cases labelled **TSM** and **TSS** are corroborative tests to demonstrate the way in which the DNS method works. **TWF** and **DivEnd**, on the other hand, are cases when the method is pushed to flow regimes that it was not initially intended to tackle. These two new cases show the TWF and divergence modes at play and these have not been observed before.

In the cases presented here, a set of wall parameters is chosen after being motivated by the neutral stability curves on the α -Re and β -Re planes (recall that β is the frequency here and ω is the vorticity). This is used to find regions of the flow parameter space which are of the greatest interest (this will be dealt with in a case by case basis). A DNS is then performed for the wall and flow parameters and the solution of the Orr-Sommerfeld equation is used to predict the arising wavenumbers.

The wavenumbers from the DNS can be isolated by using a *Fast Fourier Transform* (FFT) and these can be compared to those obtained from the solu-

tions of the Orr-Sommerfeld equation. The wall displacement profiles can then be reconstructed from a superposition of these different modes. The reason for doing this is that isolating the different wavenumbers will show how every mode affects the overall development of the wave¹ as it travels along the length of the compliant wall section.

In order to reconstruct the individual modes by superposition, a *least squares fitting* is employed to obtain the amplitudes of the different modes (this procedure is discussed in §5.2). At the start of the simulation, the wall and the flow responds to the initial wavepacket due to the starting up procedure (be it an inflow profile or a localised impulsive forcing). The transient waves that result due to this sudden change have to be filtered out of the computational domain before the fitting procedure is performed to avoid contaminating the results. Therefore, the wave fitting is only done after at time t^* when the wall displacement shows a time-periodic form, i.e. $\eta(t + \tau) = \eta(t)$ for a time-period τ and any time $t > t^*$.

For all the cases shown here, the flow is disturbed by means of an inflow profile, not by a localised impulse. The reason for this is that the inflow provides a constant source of excitation while the impulse does not. Having an impulse only allows the wall to respond to the initial excitation after which the disturbance starts to decay, returning the wall and the flow to their initially undisturbed states. Additionally, imposing an inflow profile avoids any near-field effects arising due to the impulse.

¹The term “wave” is used to refer to the wall displacement/velocity profile.

5.2 Least Squares Fitting

The least squares fitting procedure is performed on the wall displacement and velocity obtained from the DNS data in order to obtain the amplitudes and wavenumbers of the different modes. These can then be used to reconstruct the waves by superposition in order to see the role played by each of the individual modes/wavenumbers.

Consider two given vectors \mathbf{x} and \mathbf{y} of length k . The vector \mathbf{x} represents the streamwise positions and \mathbf{y} represents a function y evaluated at said locations, this function could be displacement, velocity, etc.. In other words,

$$\mathbf{x} = (x_1, x_2, \dots, x_k)$$

$$\text{and } \mathbf{y} = (y_1, y_2, \dots, y_k) \quad \text{where } y_m = y(x_m) \quad \text{for } m = 1, 2, \dots, k.$$

Since the arising modes were assumed to evolve spatially as $\sim e^{i\alpha x}$ (according to the normal mode decomposition), the function y can be approximated by a function f which is a linear combination of N modes, each taking the same form. The value of N is the number of the most unstable and/or least stable wavenumbers. In other words, y_m takes the approximate complex form

$$y_m \approx f(x_m) = A_1 e^{i\alpha_1 x_m} + A_2 e^{i\alpha_2 x_m} + \dots + A_N e^{i\alpha_N x_m} \quad \text{for } m = 1, 2, \dots, k. \quad (5.1)$$

The set of equations (5.1) can be rewritten in matrix form as $\mathbf{y} \approx \mathbf{E}\mathbf{A}$ where

$$\mathbf{y} = \begin{pmatrix} y_1 \\ y_2 \\ \vdots \\ y_k \end{pmatrix}, \quad \mathbf{A} = \begin{pmatrix} A_1 \\ A_2 \\ \vdots \\ A_N \end{pmatrix}$$

$$\text{and } \mathbf{E} = \begin{pmatrix} e_{11} & e_{12} & \dots & e_{1N} \\ e_{21} & e_{22} & \dots & e_{2N} \\ \vdots & \vdots & \ddots & \vdots \\ e_{k1} & e_{k2} & \dots & e_{kN} \end{pmatrix} \quad \text{where } e_{mn} = e^{i\alpha_n x_m} \quad \text{for } \begin{matrix} n \in \{1, 2, \dots, N\} \\ m \in \{1, 2, \dots, k\}. \end{matrix}$$

The fitting procedure requires initial estimates for the values of the wavenumbers α_n and amplitudes A_n , these values are then iteratively refined. The initial guess for the wavenumbers is taken from the solution of the Orr-Sommerfeld equation but the initial estimates for the amplitudes have to be taken from the DNS. Several choices for the initial amplitude were tested but the one that gave the most consistent results was taking wall's maximum height from the DNS as the starting value for the amplitude.

The temporal variation of these modes is $\sim e^{-i\beta t}$ (where β is the frequency at the inflow), this can be incorporated into the solution after the wavenumbers and amplitudes have been obtained.

This fitting procedure needs to be carried out on a central portion of the compliant wall section in order to avoid contamination due to edge effects. Doing this gives a more accurate reflection as to what would be expected to happen if the compliant wall was of infinite length. The size of the wall portioning is chosen visually to avoid the end effects.

The inbuilt MATLAB operation `lsqcurvefit` is used to determine the values of the amplitudes A_n and wavenumbers α_n for the assumed form of the solution given in (5.1) and the initial estimates provided for the wavenumbers and amplitudes. This command uses the Levenberg-Marquardt algorithm to obtain a non-linear least squares fit. This is quite robust and the wavenumbers and amplitudes always converge, even for relatively inaccurate initial values.

If the initial guess for a wavenumber is chosen very far away from the true solution, then the iterative procedure refines the wavenumber and could cause it to converge to another wavenumber but with a zero (or at least comparatively negligible) amplitude. This indicates that either the chosen wavenumber plays no part or that a more accurate initial estimate is needed.

The fitting procedure is usually quite accurate but in order to quantify the difference between the DNS and the fitted data, the following measure of the approximation error is used:

$$\text{error} = \frac{\|\mathbf{f} - \tilde{\mathbf{f}}\|_2}{\|\mathbf{f}\|_2} \times 100\%$$

where \mathbf{f} is the initial vector of information from the DNS and $\tilde{\mathbf{f}}$ is the approximated vector.

5.3 TSM: Tollmien-Schlichting Mode

First, an example of a well-established case is investigated, namely the excitation of the TS mode. This case gives a general overview of how the rest of the cases in this chapter are tackled.

For this investigation, the set of wall parameters are chosen to be:

$$m = 2, \quad B = 8 \times 10^7, \quad T = 0, \quad K = 2 \times 10^7, \quad d = 0.$$

(This particular set of parameters was also considered by Davies & Carpenter [30].)

5.3.1 Choice of Flow Parameters

Figures 5.1 and 5.2 show the neutral curves on the α -Re and β -Re planes restrictively, for the compliant (black) and the rigid (red) walls. The wall-based mode (labelled FISl) can be identified as the TWF instability due to the growth rates obtained from the solution of the Orr-Sommerfeld equation.

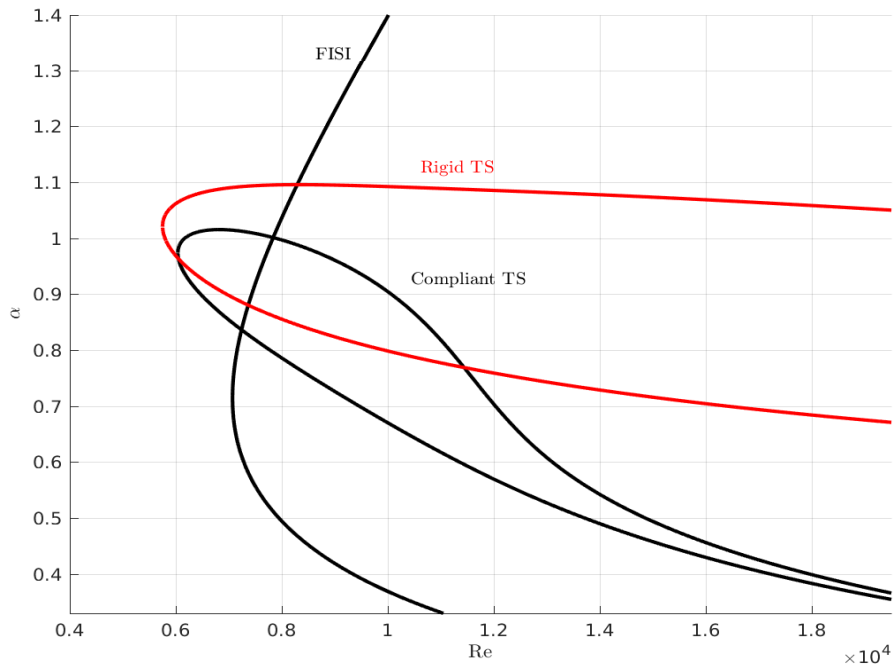


Figure 5.1: Neutral stability curves on the α -Re plane for the rigid (red) and compliant (black) wall with $m = 2$, $B = 8 \times 10^7$, $T = 0$, $K = 2 \times 10^7$, $d = 0$. The curves representing the wall-based (FISI) and the TS modes are labelled accordingly.

If the inflow frequency $\beta = 0.25$ and the Reynolds number $Re = 7000$, then this set of flow parameters falls within the unstable region for both the rigid and compliant walls. Indeed, Figure 5.3 shows a section of the β -Re plane showing this choice of flow parameters.

Over the rigid wall, these flow parameters correspond to the spatially un-

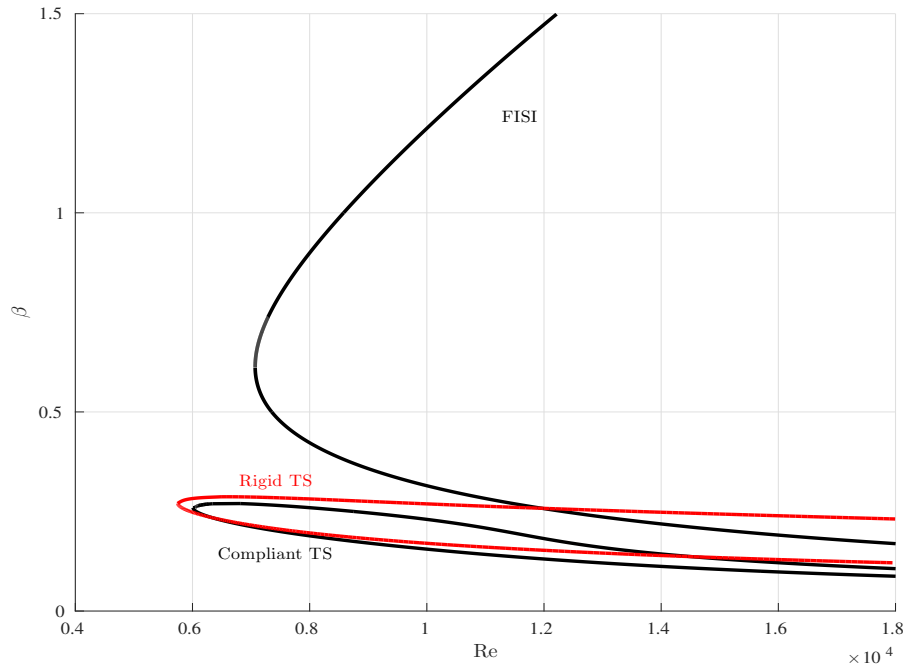


Figure 5.2: Neutral stability curves on the β -Re plane for the rigid (red) and compliant (black) wall with $m = 2$, $B = 8 \times 10^7$, $T = 0$, $K = 2 \times 10^7$, $d = 0$. The curves representing the FISI and the TS modes are labelled accordingly.

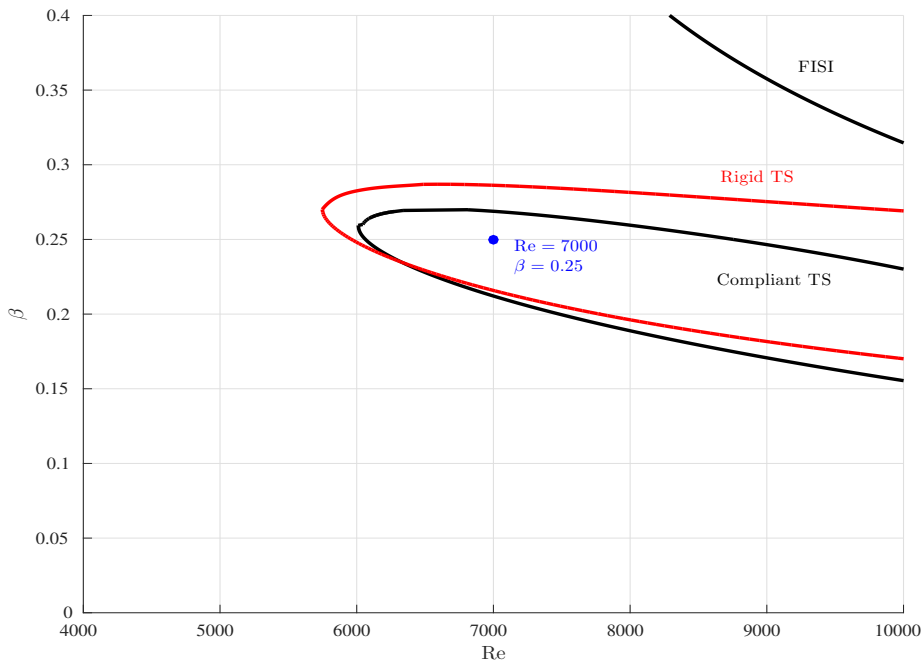


Figure 5.3: Neutral stability curve just as in Figure 5.2 but zoomed in on the TS section. The dot represents the flow parameters chosen for **TSM**.

stable TS wavenumber

$$\alpha^r = 0.992 - 4.67 \times 10^{-3}i.$$

On the other hand, over the compliant wall, the wavenumber is

$$\alpha^c = 0.962 - 2.60 \times 10^{-3}i.$$

Both these wavenumbers are obtained from the solutions of the Orr-Sommerfeld equation (as described in Chapter 3).

For the DNS, a domain of length 500 is chosen where the compliant wall extends from $x = 50$ to 450 and is hinged to the upstream and downstream rigid walls (i.e. $L_1 = 50, L_2 = 450, L = 500$). A DNS is performed for this wall configuration and wall displacement will be approximated using the wavenumber α^c . First of all, the time t^* after which the flow displays a time-periodic behaviour needs to be found.

5.3.2 Vorticity Time-History

The vorticity time-history shows the value that the vorticity takes at a given location during the whole simulation time. Figure 5.4 shows the vorticity time-history at the wall position $x = 250$. From this, it can be seen that after about $t = 1500$, the vorticity becomes sinusoidal and the amplitude reaches a fixed value. This implies that after such time, the flow has reached a time-periodic state and therefore, the flow variables can be approximated without risk of contamination from transient effects. In this case, the value t^* is taken to be 1500 meaning that for $t > t^*$, there are no transient effects that could contaminate the observations. The value of t^* is dictated by two factors:

1. The ramping up of the periodic forcing from zero
2. The time it takes for the disturbance to reach the chosen location.

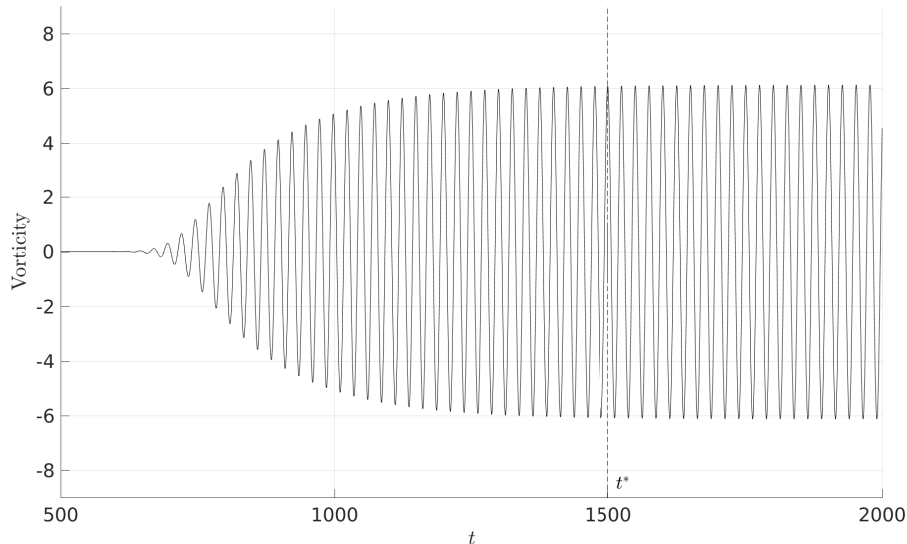


Figure 5.4: Plot of the vorticity time-history at the wall position $x = 250$. The wall response starts to take a time-periodic state after about $t = 1500$.

The vorticity time-history for other locations in the flow has been plotted but the results are slightly shifted to higher times^{II}. The wavenumber approximation procedure was performed at $t = 5000$ to ensure that all the transient effects have been filtered out of the domain. The vorticity time-history is used to determine the time t^* in all the subsequent cases but the details are not presented, only the value of t^* would be given.

Now that the appropriate time for the approximation has been obtained, the frequency of the system also needs to be determined. Even though the frequency of the system is known (being the forcing frequency $\beta = 0.25$), this is still carried out to illustrate that indeed, the most dominant frequency of the system is the inflow forcing frequency.

^{II}Perhaps it is more appropriate if the vorticity time-history was taken near the end of the compliant wall section but in that case, the results may display some effects that arise from the compliant wall ends, the qualitative behaviour is nonetheless the same.

5.3.3 Frequency

Since the flow is excited by means of an inflow disturbance profile, the frequency should be that of the inflow forcing, namely 0.25. Indeed, Figure 5.5 shows a plot of the FFT applied to the vorticity time-histories at evenly spaced wall positions from $x = 60$ to $x = 450$. The sharp peak is located at the frequency 0.25 which is exactly the inflow frequency (unsurprisingly).

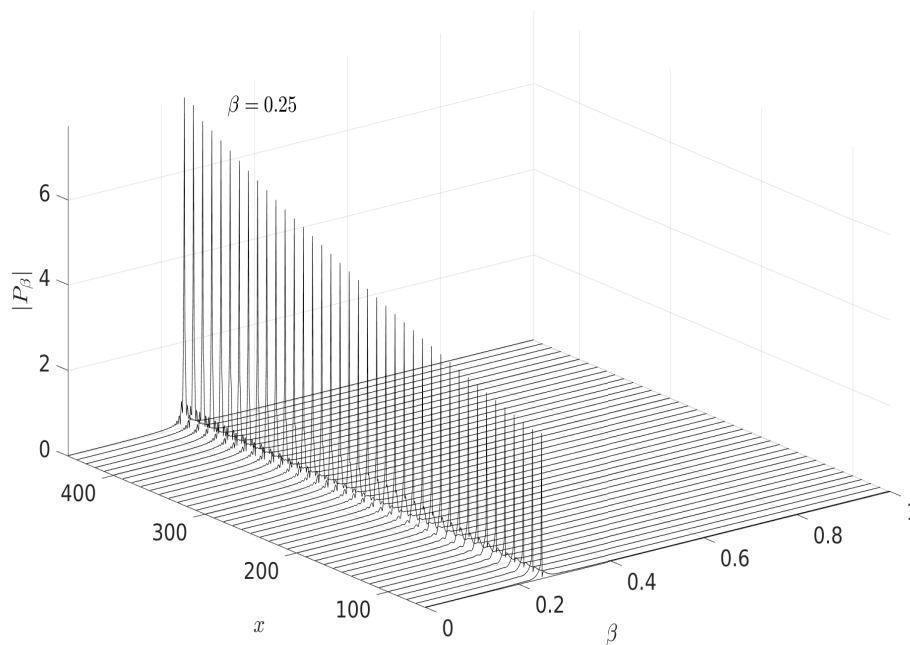


Figure 5.5: Plot of the FFT of the vorticity time-history along the compliant wall section from $x = 60$ to $x = 450$. This is done in order to determine the most dominant frequency in the system which in this case, is the inflow frequency $\beta = 0.25$.

The vorticity time-history and the FFT for obtaining the frequency are done for all the cases presented in this chapter but they are not discussed in detail, only the most relevant information is given.

5.3.4 Approximating the Wall Displacement

After the DNS is performed for the proposed flow configuration, the wall displacement takes the form shown in Figure 5.6 where the wall displacement forms a spatially growing wave along the length of the compliant wall. The wall displacement can now be approximated to see how the arising DNS wavenumber compares to the predicted wavenumber α^c .

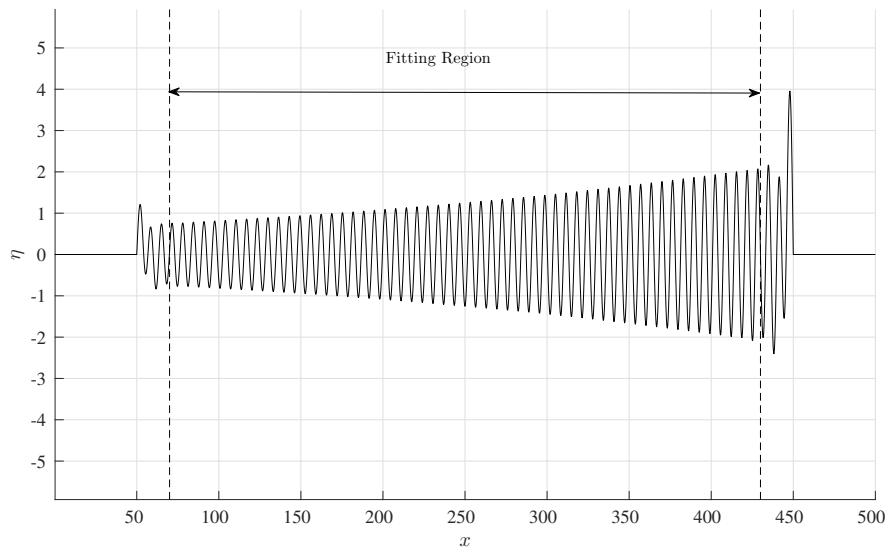


Figure 5.6: Wall displacement taken from the DNS. The fitting region is chosen in such a way that the end effects are not captured.

The approximation has to be done in a central portion of the compliant wall in order to avoid end effects. Seeing as that these effects are not very prominent (as seen visually), the fitting region can be taken to be reasonably large and is represented by the dashed lines in Figure 5.6. In other cases, the wall end effects can be relatively more noticeable and the region in which the wall displacement is approximated has to be made smaller.

Figure 5.7(a) shows the DNS wall displacement η taken from the DNS within the fitting region given in Figure 5.6. Figure 5.7(b) shows two plots,

the DNS wall displacement (black) and the approximated wall displacement $\tilde{\eta}$ (red). It can be seen that the two plots are virtually indistinguishable from one another and the fitting error is less than 0.5%. The difference between these two plots is made clearer when considering the relative error between them as shown in Figure 5.7(c). The ends effects play a minor role as seen by the increased error near the ends but nevertheless, the approximation is quite accurate giving a very small value of the error.

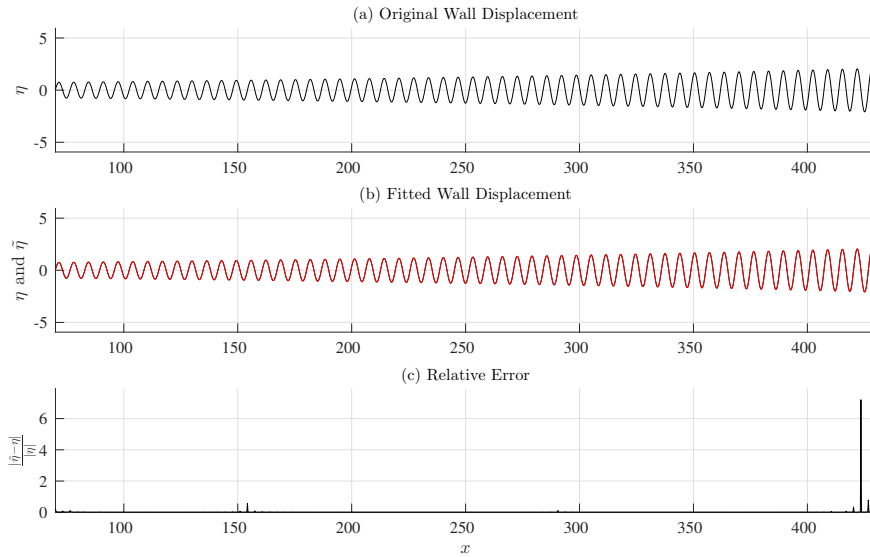


Figure 5.7: (a) DNS wall displacement η in the fitting region shown in Figure 5.6. (b) DNS wall displacement η (black) and the approximated wall displacement $\tilde{\eta}$ (red). (c) Relative error between η and $\tilde{\eta}$.

The least squares fitting gives an approximation to the wall displacement $\tilde{\eta}$ as

$$\tilde{\eta}(x) = A_1 e^{i\alpha_1 x} + A_2 e^{i\alpha_2 x}$$

$$\begin{aligned} \text{where } A_1 &= 0.305 - 4.66 \times 10^{-2}i, & \alpha_1 &= 0.968 - 2.85 \times 10^{-3}i, \\ A_2 &= 0.305 + 4.66 \times 10^{-2}i, & \alpha_2 &= -0.968 - 2.85 \times 10^{-3}i. \end{aligned}$$

This can be rewritten as

$$\tilde{\eta}(x) = Ae^{i\tilde{\alpha}^c x} + \text{c.c.}$$

$$\text{where } A = 0.305 - 4.66 \times 10^{-2}i \quad \text{and} \quad \tilde{\alpha}^c = 0.968 - 2.85 \times 10^{-3}i \quad (5.2)$$

and c.c. represents the complex conjugate of all the previous terms. The value of the amplitude A is not significant here since this is to test the efficacy of the Orr-Sommerfeld solutions in predicting the wavenumbers that arise in the DNS, *not* the amplitudes.

The approximated wavenumber $\tilde{\alpha}^c$ is very close to the predicted wavenumber from the Orr-Sommerfeld equation, namely

$$\alpha^c = 0.962 - 2.60 \times 10^{-3}i.$$

Therefore in this case, the Orr-Sommerfeld equation has effectively predicted the arising wavenumber obtained from the DNS which corresponds to a spatially growing TS wave^{III}. It can be seen that the Orr-Sommerfeld equations provides an excellent prediction for the wavenumber that dictates the wall displacement. The same can now be done to the wall velocity to see how this predictions fairs. Even though the predicted wavenumber is still expected to be a very good approximation to that of the DNS, the wall velocity approximation will nonetheless be undertaken to show the time dependence and the incorporation of the forcing frequency into the general form of $\tilde{\eta}$.

^{III}Note that the agreement between the wavenumber extracted from the simulation and the one predicted by the Orr-Sommerfeld equation can be improved by either increasing the resolution in the simulations or increasing the number of iterations in the fitting procedure.

5.3.5 Wall Velocity

The wall velocity is now approximated in exactly the same way as the wall displacement. Figure 5.8(a) shows the DNS wall velocity $\frac{\partial \eta}{\partial t}$ in the fitting region given in Figure 5.6, Figure 5.8(b) shows two plots, the DNS wall velocity $\frac{\partial \eta}{\partial t}$ (black) and the approximated wall velocity $\frac{\partial \tilde{\eta}}{\partial t}$ (red). Once again, it can be seen that the two plots are virtually indistinguishable from one another with a fitting error of less than 2.5%. The difference between these two plots is made clearer in Figure 5.8(c) showing the relative error between them.

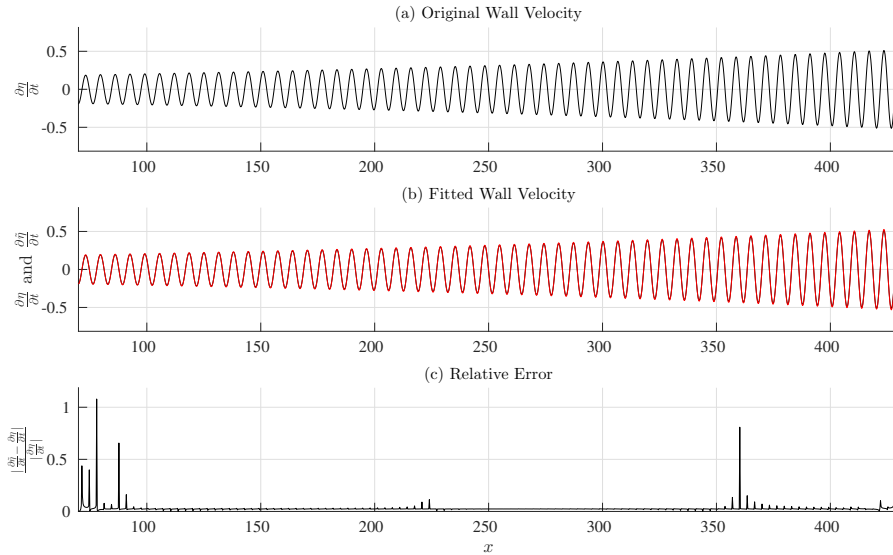


Figure 5.8: (a) DNS wall velocity $\frac{\partial \eta}{\partial t}$ in the fitting region shown in Figure 5.6. (b) DNS wall velocity $\frac{\partial \eta}{\partial t}$ (black) and the approximated wall velocity $\frac{\partial \tilde{\eta}}{\partial t}$ (red). (c) Relative error between $\frac{\partial \eta}{\partial t}$ and $\frac{\partial \tilde{\eta}}{\partial t}$.

The approximate complex form of the wall velocity obtained from the fitting can be written as

$$\frac{\partial \tilde{\eta}}{\partial t}(x) = B e^{i\tilde{\alpha}^c x} + \text{c.c.} \quad (5.3)$$

$$\text{where } B = -1.21 \times 10^{-2} - 7.79 \times 10^{-2}i$$

and the wavenumber $\tilde{\alpha}^c$ is the same as the one obtained in (5.2).

The wavenumber obtained from approximating the wall displacement and the velocity are the same *even though* they have both been obtained independently of one another (i.e. the approximations were carried out separately yet yielded the same result). The fact that the Orr-Sommerfeld equation managed to predict the wavenumber with considerable accuracy can be an indication that this can be extended to other, more complicated cases, when more than one mode is affecting the flow.

5.3.6 Incorporating the Time-Dependence

The approximated forms of the wall displacement $\tilde{\eta}$ and velocity $\frac{\partial \tilde{\eta}}{\partial t}$ have to include a time dependent element of the form $\sim e^{-i\beta t}$. This can be incorporated by simply multiplying $\tilde{\eta}$ by $e^{-i\beta t}$ without the need for an additional amplitude term coming from the forcing, therefore the wall displacement can be given by

$$\hat{\eta}(x, t) = e^{-i\beta t} \tilde{\eta}(x, t) = Ae^{i(\tilde{\alpha}^c x - \beta t)} + \text{c.c.} \quad (5.4)$$

where A and $\tilde{\alpha}$ are given in (5.2) and $\beta = 0.25$. This can be done since if $\hat{\eta}$ is differentiated with respect to t , then

$$\frac{\partial \hat{\eta}}{\partial t}(x, t) = -i\beta Ae^{i(\tilde{\alpha}^c x - \beta t)} + \text{c.c.}$$

For the given values of A and β , the coefficient of $e^{i(\tilde{\alpha}^c x - \beta t)}$ is

$$-i\beta A = -1.17 \times 10^{-2} - 7.63 \times 10^{-2}i \approx B.$$

This reinforces the fact that the approximation for the wall displacement is valid and the temporal contribution takes the form $e^{-i\beta t}$ (which is unsurprising

given the normal mode form of the terms). The incorporation of the time dependence is shown here for completeness, the wall velocities are not shown in any of the cases presented later since the intricate details are not necessary, only the final form of $\hat{\eta}$.

5.3.7 Remarks on TSM

In Figures 5.7 and 5.8, it can be seen that the errors near the start and/or end of the fitting region are greater than the central portion, this is because near the ends, edge effects become more noticeable. The ends will certainly affect the approximation however the fit is still quite accurate nonetheless. Later in the case **DivEnd**, the end effects become very apparent and therefore the fitting region has to be made smaller in order to avoid contamination due to end effects.

For this preliminary **TSM** case, a lot of detail is presented but this is simply to show the extent of the analysis that could be undertaken. However in the following cases where behaviour is more complicated, only the most relevant results are presented. For instance, since the amplitudes cannot be predicted from the solutions of the Orr-Sommerfeld equation, they are not mentioned from this point forward but they were included in this first case to show that amplitudes can be obtained and the waves can be superimposed effectively to reconstruct the waves, even in the presence of more than one mode. Moreover, the vorticity time-histories and the application of the FFT in order to determine the time t^* and most dominant frequency are not presented unless necessary. And finally, the wall velocity is not considered again since in all the remaining cases, the results are exactly as expected. It was only included here to illustrate that the approximated wall velocity can be recovered from

the wall displacement and the inflow frequency.

This preliminary case is presented as a test for the performance of the numerical simulation and the fitting procedure. The DNS results were validated against the Orr-Sommerfeld solutions in the case when there is no wall-based mode, this only increases confidence in the effectiveness of the simulation, fitting procedure and the numerical solution of the Orr-Sommerfeld equation. Additionally, the end effects observed here are localised. In some of the cases to follow, more complicated flow behaviours will be investigated (particularly **TWF** and **DivEnd**) which show a more significant contribution from the wall-based modes as well as the end effects. This will test the efficacy of the current DNS method to investigate cases that have not been documented previously.

5.4 TSS: Tollmien-Schlichting Stabilisation

In the previous case **TSM**, a spatially unstable TS mode was excited but as it travelled over the compliant wall section, its growth rate was only reduced. In the case presented here, a TS wave is introduced and then *stabilised* as it travels over the compliant wall section. Unlike **TSM**, there is more than just the TS mode, two other modes are also provoked and their effects on the wall displacement and vorticity are studied. This **TSS** case is, once again, a corroborative test and is presented here to illustrate the compliant wall's TS stabilisation capabilities. (Note that this case, along with **TSM**, were documented by Davies [28] and Davies & Carpenter [30].)

For this case, the same wall parameters as **TSM** are, namely,

$$m = 2, \quad B = 8 \times 10^7, \quad T = 0, \quad K = 2 \times 10^7, \quad d = 0.$$

5.4.1 Choice of Flow Parameters

In order to choose the appropriate flow parameters to illustrate the compliant wall's suppression capabilities, the neutral stability curves on the β -Re plane has to be investigated. Figure 5.9 shows the neutral stability curves on the β -Re plane exactly as in Figure 5.3, the flow parameters are chosen in such a way that the flow is spatially unstable over the rigid wall but stable over the compliant wall. Therefore an appropriate set of flow parameters can be

$$\text{Re} = 10000 \quad \text{and} \quad \beta = 0.2375.$$

This choice of parameters is labelled accordingly in Figure 5.9.

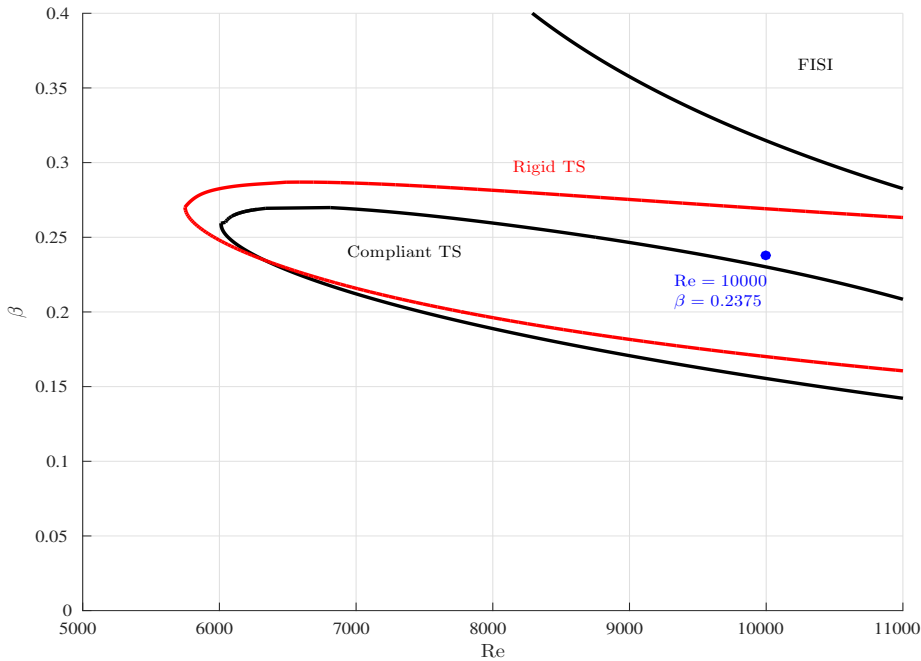


Figure 5.9: Neutral stability curves just as in Figure 5.2 but zoomed in on the TS section. The dot represents the flow parameters chosen for **TSS**.

According to the solutions of the Orr-Sommerfeld equation, the most unstable wavenumber over the rigid wall section can be identified as the spatially

unstable TS mode with the wavenumber

$$\alpha^r = 1 - 1.10 \times 10^{-2}i. \quad (5.5)$$

However over the compliant wall, there are *three* wavenumbers which are the least stable/most unstable (closest to the real line), these are:

$$\begin{aligned} \alpha_1^c &= -0.764 - 1.08 \times 10^{-2}i \\ \alpha_2^c &= -8.58 \times 10^{-2} + 3.41 \times 10^{-5}i \\ \alpha_3^c &= 0.923 + 2.18 \times 10^{-3}i. \end{aligned} \quad (5.6)$$

The locations of these wavenumbers are shown on the complex α -plane in Figure 5.10 and these will be used to predict the wavenumbers arising from the DNS.

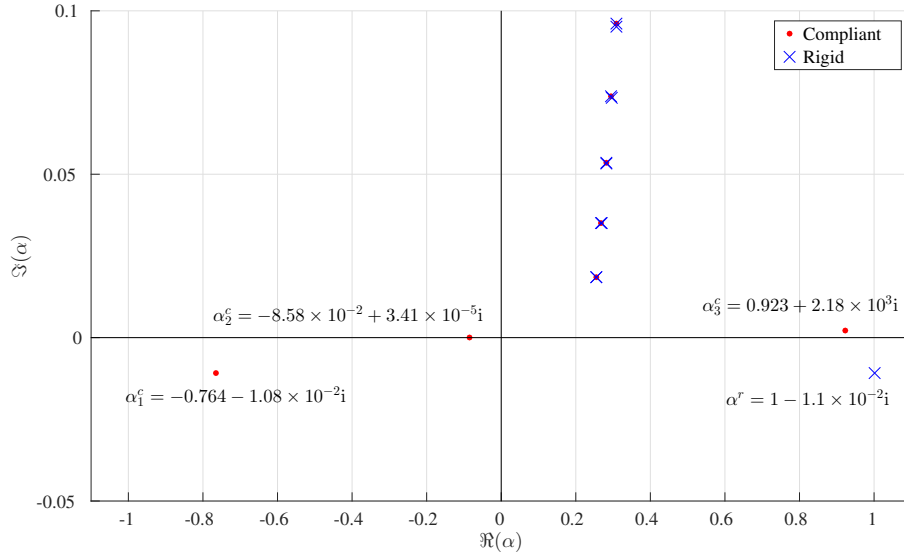


Figure 5.10: Locations of the rigid (blue \times) and compliant (red \bullet) wall eigenvalues obtained from the solutions of the Orr-Sommerfeld equation.

DNS

For this case, the flow configuration is a compliant wall extending from the streamwise locations $x = 100$ to $x = 900$ in a computational domain of non-dimensional length of 1000. Figure 5.11 shows the wall displacement obtained from the DNS, notice that the end effects are more prominent here compared to **TSM** and the fitted region was chosen in accordance with this (as denoted by the vertical dashed lines). It is clear that the wall displacement is a superposition of several modes, at least one of which is a long wavelength mode, this will now be investigated by decomposing the profile into its individual components.

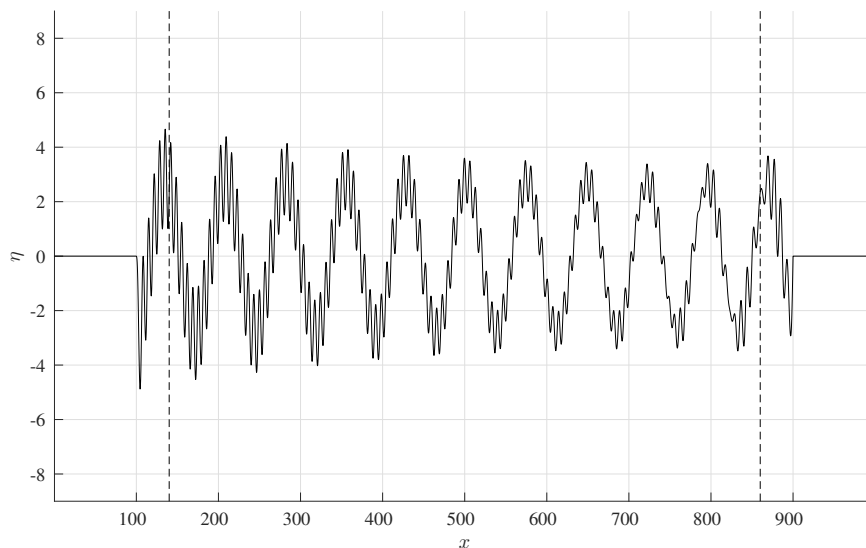


Figure 5.11: Wall displacement taken from the DNS. The fitting region is chosen in such a way that the end effects are not captured (and is indicated by the dashed lines).

Figure 5.12(a) shows the DNS wall displacement η within the region indicated by the dashed lines in Figure 5.11. Figure 5.12(b) shows both η (black) and its approximation $\tilde{\eta}$ (red) where once again, the approximation is quite accurate with an approximation error of 0.2%. The relative error between η and $\tilde{\eta}$ is shown in Figure 5.12(c) where the error is higher towards the down-

stream end but nonetheless, the approximation is still very good. This implies that the ends still have some effect on the wall displacement but these effects are still somewhat negligible compared to the rest of the compliant wall.

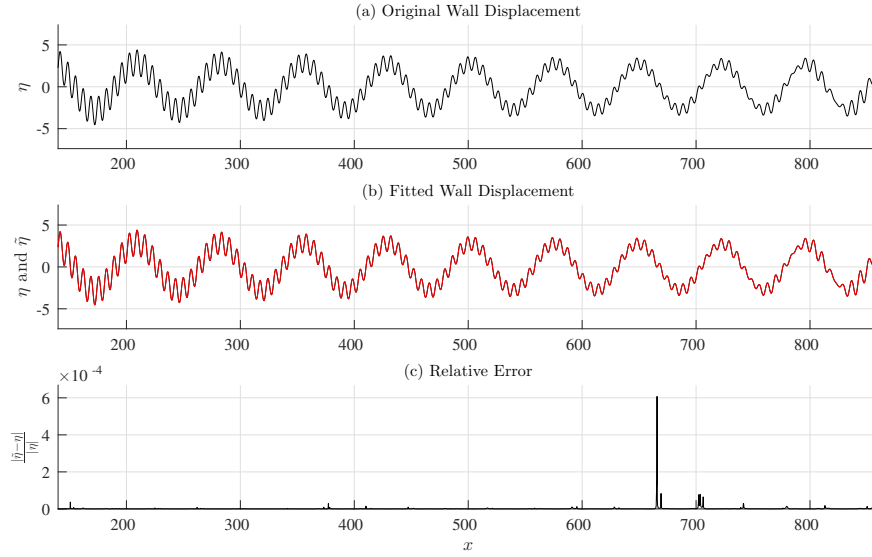


Figure 5.12: (a) DNS wall displacement η . (b) DNS wall displacement η (black) and the approximated wall displacement $\tilde{\eta}$ (red). (c) Relative error between η and $\tilde{\eta}$.

The wall displacement profile seen in Figure 5.11 consists of three wavenumbers:

$$\begin{aligned}\tilde{\alpha}_1^c &= -0.764 - 1.09 \times 10^{-2}i \\ \tilde{\alpha}_2^c &= -8.56 \times 10^{-2} + 8.3 \times 10^{-5}i \\ \tilde{\alpha}_3^c &= 0.931 + 2.03 \times 10^{-3}i.\end{aligned}\tag{5.7}$$

This gives an approximation $\tilde{\eta}$ for the DNS wall displacement η as

$$\hat{\eta}(x, t) = \tilde{\eta}(x)e^{i\beta t} = A_1e^{i(\tilde{\alpha}_1^c x - \beta t)} + A_2e^{i(\tilde{\alpha}_2^c x - \beta t)} + A_3e^{i(\tilde{\alpha}_3^c x - \beta t)} + \text{c.c.}\tag{5.8}$$

where $\beta = 0.2375$ (which is the inflow frequency). From this, it can be seen that the wavenumber predictions obtained from the solutions of the Orr-Sommerfeld

equation given in (5.6) are quite accurate. However the exact values of the amplitudes A_n is not important but what is significant is their relative sizes, this can either be seen from the values of the ratios between them or through the Fourier spectrum of the wave.

Figure 5.13 shows the Fourier decomposition of the wall displacement profile shown in Figure 5.11. The decomposition shows three peaks centred around the locations of the magnitudes of the wavenumbers given in (5.7). (Note that the Fourier decomposition cannot distinguish between upstream and downstream travelling modes, only their magnitudes.) Therefore, this implies that the mode $\tilde{\alpha}_2^c$ has the highest relative amplitude, this is followed by $\tilde{\alpha}_3^c$ then $\tilde{\alpha}_1^c$.

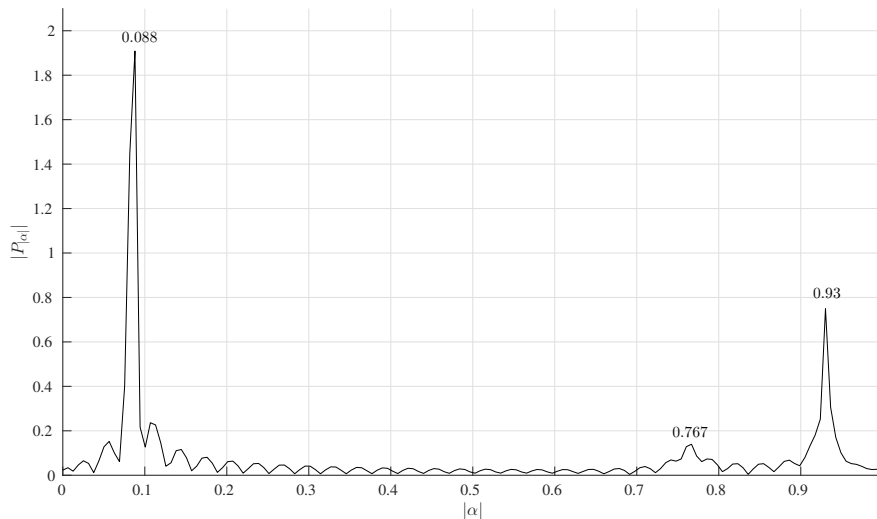


Figure 5.13: Fourier spectrum of the wall displacement profile shown in Figure 5.11. The three peaks that result are centred around the magnitudes of the approximated wavenumbers given in (5.7) and this gives an indication of their relative associated amplitudes.

5.4.2 Wall Displacement Decomposition

The wall displacement in Figure 5.11 is a superposition of three modes with the wavenumbers given in (5.7). Figure 5.14 shows these three individ-

ual wavenumbers plotted separately to illustrate the contribution of each to the wall displacement (note that these have been plotted across the whole compliant wall and not just the fitting region).

The wavenumber labelled $\tilde{\alpha}_3^c$ can be associated with the TS mode which is stabilised by the compliant wall and this can be verified by its location in complex α -plane shown in Figure 5.10 (this TS stabilisation will be explained further in the next subsection). Unlike in **TSM**, the TS mode is not the only mode present here. The mode $\tilde{\alpha}_2^c$ is a long wavelength wall-based mode that decays very slowly as it travels downstream and given its relatively small magnitude, this wavenumber can be associated with the divergence mode. Finally, $\tilde{\alpha}_1^c$ has a negative real part implying that its associated phase velocity travels *upstream*, therefore this particular mode originates from the downstream end of the compliant wall and decays as it travels upstream.

5.4.3 Tollmien-Schlichting Stabilisation

In order to further understand the TS stabilisation capabilities of the compliant wall, suppose that the flow domain consists of a rigid wall only, then given the location of the flow parameters on the β -Re plane, the flow has to be destabilised by the TS mode. Indeed, Figure 5.15 shows a plot of the wall vorticity when the whole domain ($x = 0$ to $x = 1000$) is bound by a rigid wall. The exponential growth rate of the wall vorticity is given by the rigid wall wavenumber α^r in (5.5) and is represented by the dashed lines surrounding the wave.

If the compliant wall section is inserted between $x = 100$ and 900 , the wall vorticity is stabilised across the compliant wall. Indeed, Figure 5.16 shows the vorticity across the flow domain when the compliant wall is inserted (and this

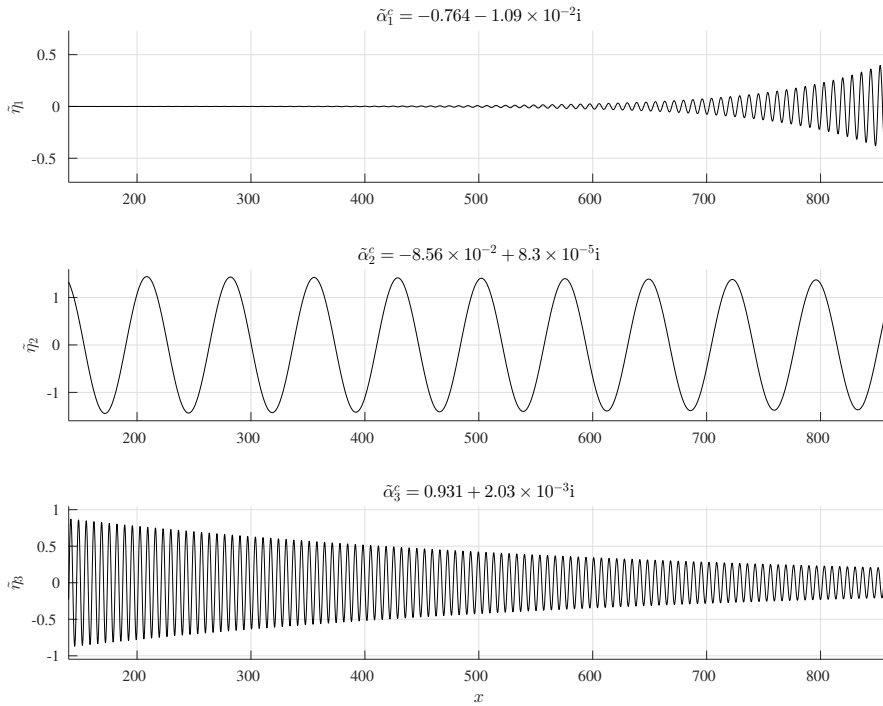


Figure 5.14: Wall displacement components for the wavenumbers given in (5.6). The superposition of these modes forms of the approximate wall displacement $\tilde{\eta}$ given in Figure 5.12(b).

is denoted by the vertical dotted lines). In the upstream rigid wall section $x \in [0, 100]$, the TS mode causes the vorticity to grow exponentially (as denoted by the black dashed lines). However over the compliant wall, the vorticity is stabilised and is associated with an exponential decay (denoted by the red dashed lines surrounding the wave in the region $x \in [100, 900]$). Finally after the flow exits the compliant wall section at $x = 900$, the TS mode starts to grow exponentially again (denoted by the dashed lines).

5.4.4 Remarks on TSS

In TSM, the TS mode and how the compliant wall can reduce its growth rate was investigated. Here, the TS mode has been *stabilised* by the compliant wall section as seen in Figures 5.15 and 5.16. If the compliant wall section

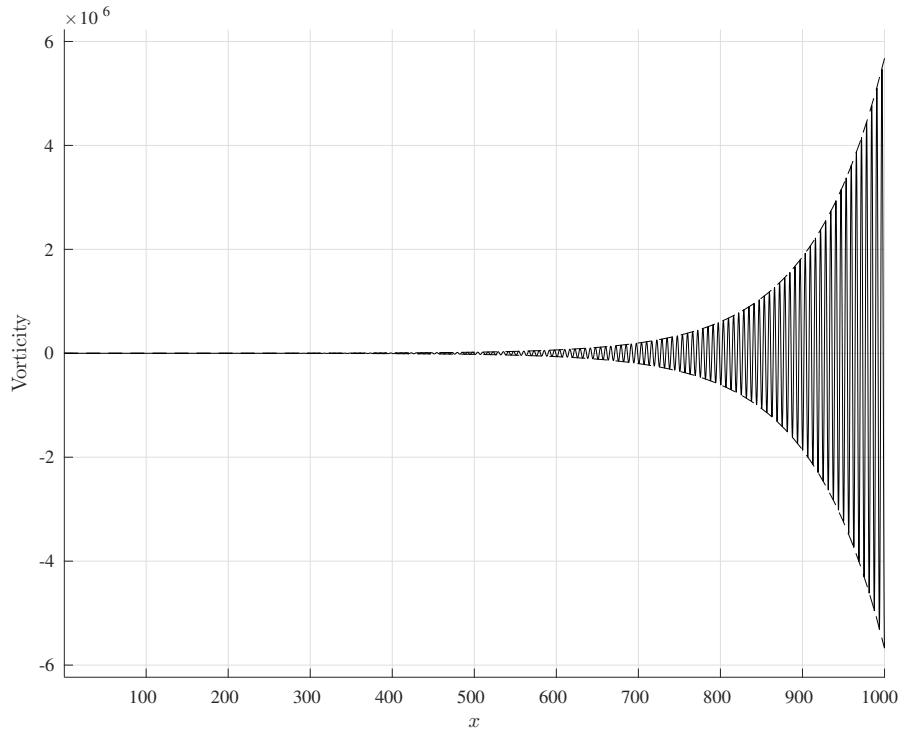


Figure 5.15: Vorticity across the flow domain if the wall is rigid throughout. The dashed lines denoted the exponential growth rate of the wave given by α^r given in (5.5).

was longer, then the TS instability will continue to decay even further and therefore, the compliant wall can be used as an effective means of controlling the growth of the flow-based TS instability.

In the two cases **TSM** and **TSS** shown so far, the TS mode and the effect of the compliant wall on its growth was investigated and were reproductions from earlier works. The DNS method described in Chapter 4 was initially intended to deal with these cases and the solution of the Orr-Sommerfeld equation predicted the wavenumbers quite accurately when the TS mode is present. In the two forthcoming sections **TWF** and **DivEnd**, the DNS method is pushed further to investigate the wall-based modes which have not been seen using the current method.

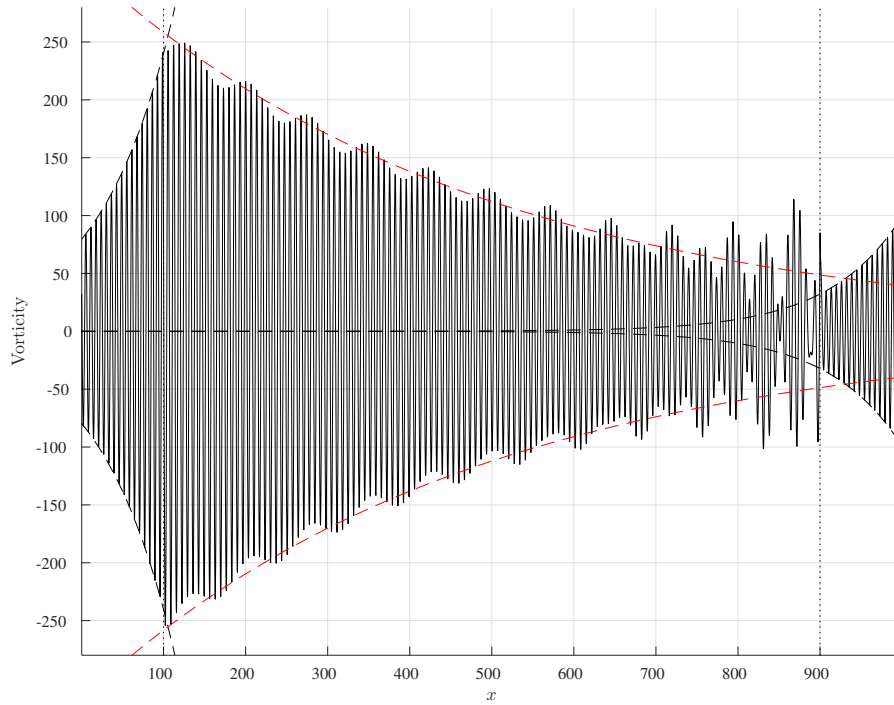


Figure 5.16: Vorticity across the wall with the compliant section between $x = 100$ and 900 (denoted by the vertical dotted lines). The dashed lines denote the exponential growth and decay rate of the vorticity over the rigid and compliant wall sections, respectively. Over the rigid walls, the growth is exponential (denoted by the black dashed lines) while over the compliant wall, the vorticity decays exponentially (denoted by the red dashed lines).

5.5 TWF: Travelling Wave Flutter

In the following case, a set of flow parameters is chosen in such a way that the TS mode is not excited, only the TWF mode. First of all, in order to avoid the TS mode, a relatively small value of the Reynolds number needs to be chosen. Second, in order to avoid exciting the divergence mode, the wall mass m has to be greater than one third^{IV}.

^{IV}Recall from Chapter 2 that the onset Reynolds numbers for divergence and TWF are

$$\text{Re}_d = \text{Re}_0 \sqrt{\frac{15}{8}} \quad \text{and} \quad \text{Re}_{TWF} = \text{Re}_0 \sqrt{\frac{5}{5m+1}}$$

respectively. Therefore if $m > \frac{1}{3}$, then $\text{Re}_d > \text{Re}_{TWF}$.

For **TWF**, the same wall parameters are used as in **TSM** and **TSS** with the exception of the wall mass which is increased to 10, therefore the set of wall parameters are

$$m = 10, \quad B = 8 \times 10^7, \quad T = 0, \quad K = 2 \times 10^7, \quad d = 0.$$

The onset Reynolds numbers for the divergence and TWF modes are

$$\text{Re}_d \approx 12247 \quad \text{and} \quad \text{Re}_{TWF} \approx 2800.$$

5.5.1 Flow Parameter Choices

Figures 5.17 and 5.18 show the neutral curves for this set of flow parameters on the α -Re and β -Re planes respectively, the contributions from the rigid and compliant walls have been labelled accordingly. In Figure 5.17, it can be seen that the curve associated with the TS mode has shrunk implying that the compliant has effectively stabilised by the TS instability but as a consequence, the FISI (being the TWF mode) has occupied a large portion of the α -Re plane. As for Figure 5.18, the TS mode has been assimilated into the compliant wall neutral curve forming a single curve that includes both the wall and flow-based modes.

For this case, the proliferation of the TWF mode is desired with no effects coming from either the divergence or TS modes. Therefore, the flow parameters can be chosen as

$$\text{Re} = 4000 \quad \text{and} \quad \beta = 0.6$$

as labelled in Figure 5.18. For this choice, the TS mode is far from being excited since the Reynolds number is far smaller than the TS onset.

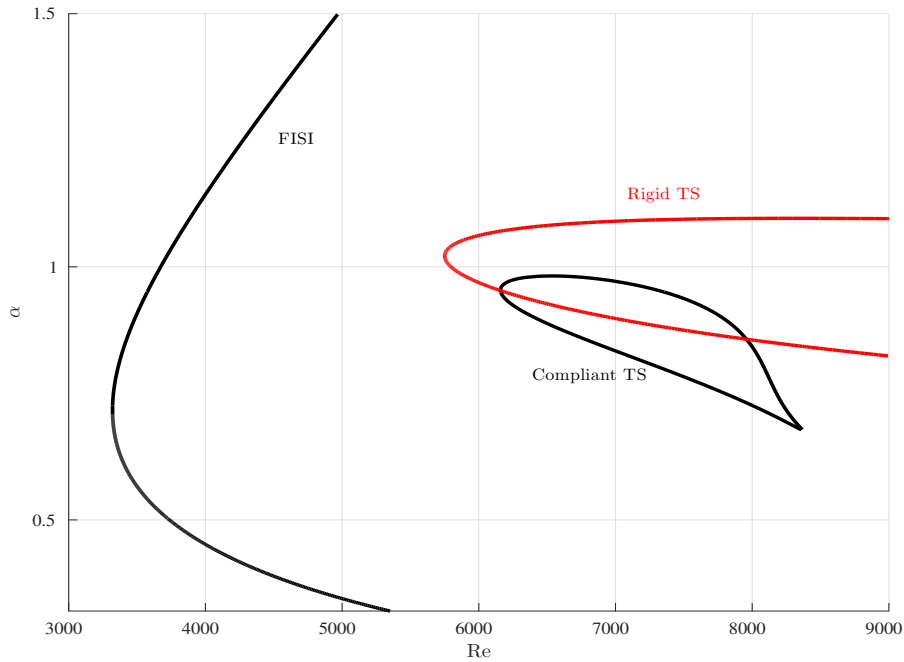


Figure 5.17: Neutral stability curves on the α -Re plane for the rigid (red) and compliant (black) wall with $m = 10$, $B = 8 \times 10^7$, $T = 0$, $K = 2 \times 10^7$, $d = 0$. The curves representing the FISI and the TS modes are labelled accordingly.

For this set of wall and flow parameters, there are two spatial eigenvalues that are the most unstable which are:

$$\begin{aligned} \alpha_1 &= -0.901 - 1.66 \times 10^{-3}i \\ \alpha_2 &= 0.834 - 1.11 \times 10^{-4}i. \end{aligned} \tag{5.9}$$

The locations of these wavenumbers are shown on the complex α -plane in Figure 5.19. Initially from these eigenvalues, it can be hypothesised that there should be two unstable modes travelling in opposite directions. These wavenumbers can be used as predictions for those arising from the DNS.

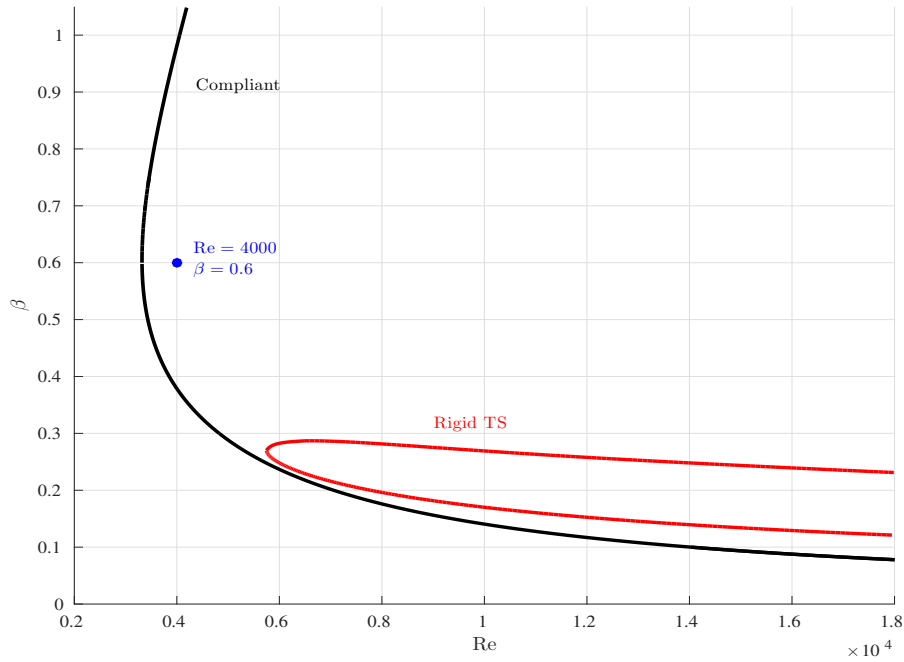


Figure 5.18: Neutral stability curves on the β - Re plane for the rigid (red) and compliant (black) wall with parameters $m = 10$, $B = 8 \times 10^7$, $T = 0$, $K = 2 \times 10^7$, $d = 0$. The dot represents the flow parameters chosen for the case **TWF**. The curve representing the flow-based mode has been assimilated into the compliant wall neutral curve.

5.5.2 DNS

A DNS is performed for the a compliant wall extending from $x = 50$ to 450 in a domain of length 500, the wall displacement, shown in Figure 5.20, takes the form of an *amplitude modulated wave*^V.

Figure 5.21(a) shows the DNS wall displacement η within the region indicated in Figure 5.20. Figure 5.21(b) shows the DNS wall displacement η (black) and its approximation $\tilde{\eta}$ (red), the fit is somewhat less accurate compared to the previous cases observed, this is seen in the relative error between η and $\tilde{\eta}$ as shown in Figure 5.21(c), the approximation error in this case is

^VIt should be noted that the vorticity time-histories were investigated beforehand and it seems that the wall displacement takes a significantly longer time to settle down to a time-periodic state compared to **TSM** and **TSS**, however the wave here was only approximated after such a time has been reached.

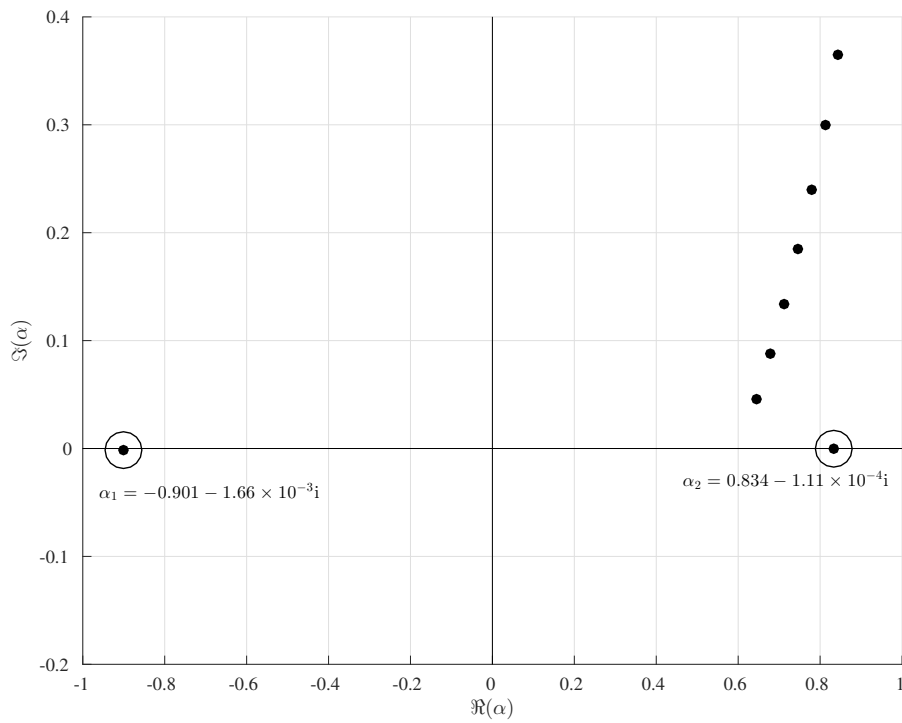


Figure 5.19: Location of the wavenumbers (5.9) which will be used as predictions for the DNS.

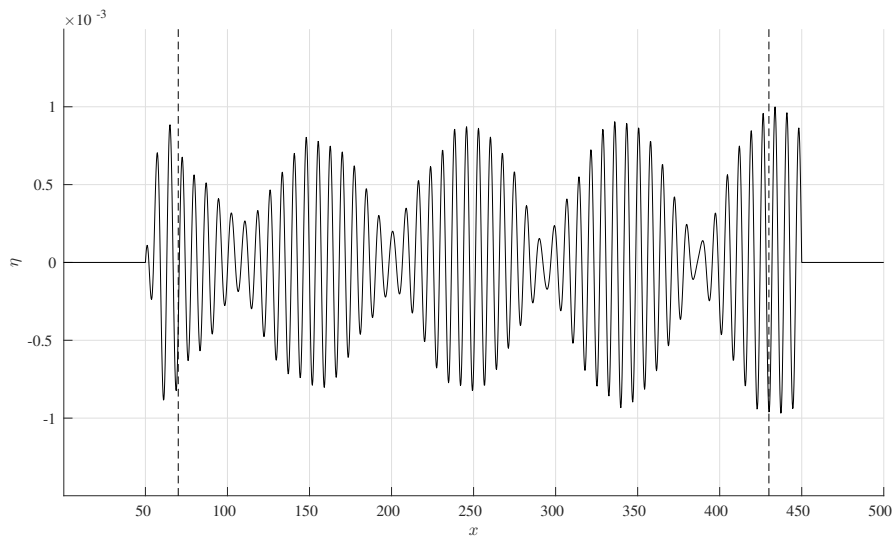


Figure 5.20: Wall displacement taken from the DNS. The fitting region is chosen in such a way that the end effects are not captured (and is denoted by the dashed lines)

6%. The approximation to the wall displacement is given by $\hat{\eta}$ which takes the

form

$$\hat{\eta}(x, t) = A_1 e^{i(\tilde{\alpha}_1 x - \beta t)} + A_2 e^{i(\tilde{\alpha}_2 x - \beta t)} + \text{c.c.}$$

$$\text{where } \tilde{\alpha}_1 = -0.904 - 1.72 \times 10^{-3}i \quad (5.10)$$

$$\tilde{\alpha}_2 = 0.836 - 8.7 \times 10^{-5}i. \quad (5.11)$$

For this case, the fit is not as good as the previous two cases but notwithstanding, the wavenumbers obtained from the solution of the Orr-Sommerfeld equation still provides a good approximation to those obtained from the DNS.

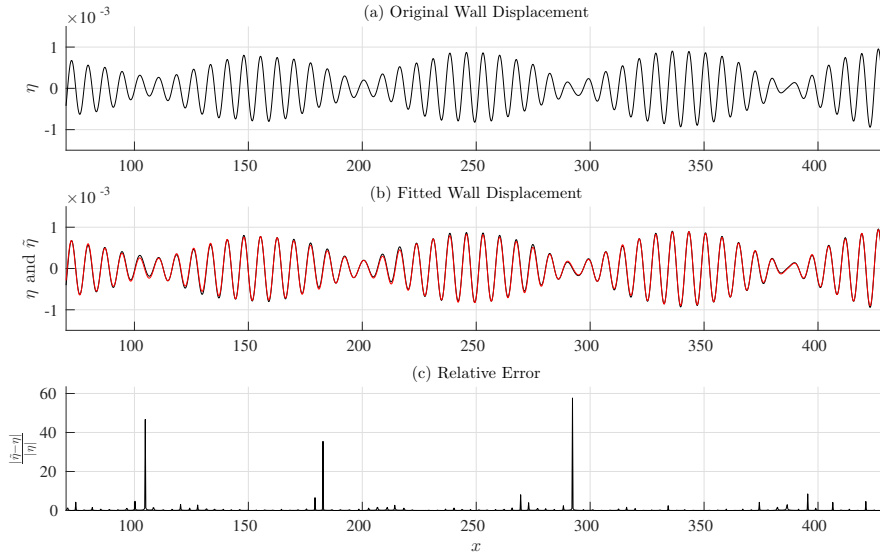


Figure 5.21: (a) DNS wall displacement η . (b) DNS wall displacement η (black) and the approximated wall displacement $\tilde{\eta}$ (red). (c) Relative error between η and $\tilde{\eta}$.

The relative sizes of the amplitudes for the two modes are represented in the form of the Fourier spectrum shown in Figure 5.22. The magnitudes of the amplitudes of the two waves are comparable unlike in **TSS** where one mode dominated the other two. This means that both modes play similar roles in predicting the wall displacement.

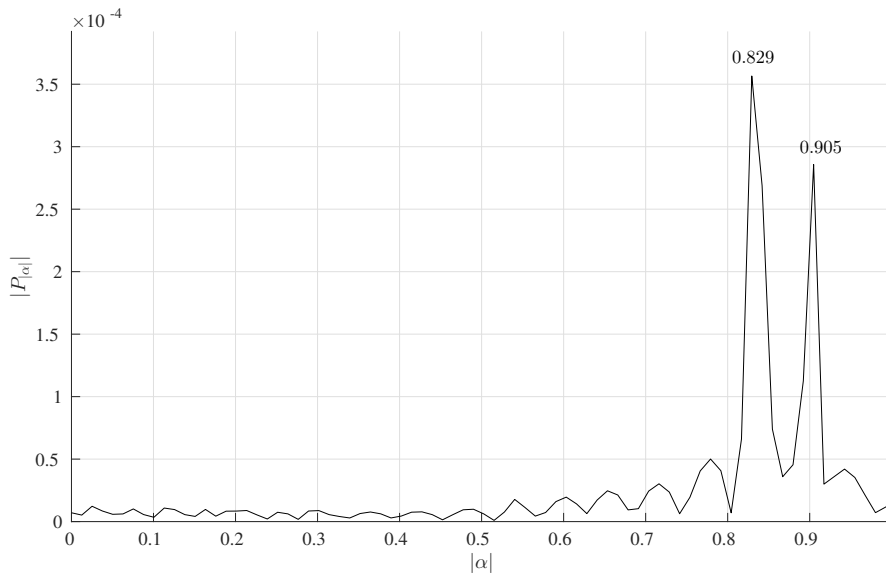


Figure 5.22: Fourier spectrum of the wall displacement profile shown in Figure 5.11. The two peaks are centred around the magnitudes of the approximated wavenumbers given in (5.10) and this gives an indication of their relative sizes.

5.5.3 Wall Displacement Decomposition

The wall displacement shown in Figure 5.20 is the superposition of the two modes dictated by the wavenumbers given in (5.10). These two constituent modes can be plotted separately as shown in Figure 5.23 (note that these have been plotted across the whole compliant wall and not just the fitting region). Both waves that arise are due to the TWF mode and according to the values of their real parts, these modes travel in opposite directions. Although these two waves have similar wavelengths (approximately 7.3), they are out of phase in such a way that they result in the modulated amplitude wave seen in Figure 5.20.

The relatively small value of the Reynolds number has avoided the excitation of the TS instability, however the stable TS wave at the inflow has acted as a source of excitation at the upstream boundary for the $\tilde{\alpha}_2$ mode to propagate over the compliant wall. Additionally, another mode arises due to

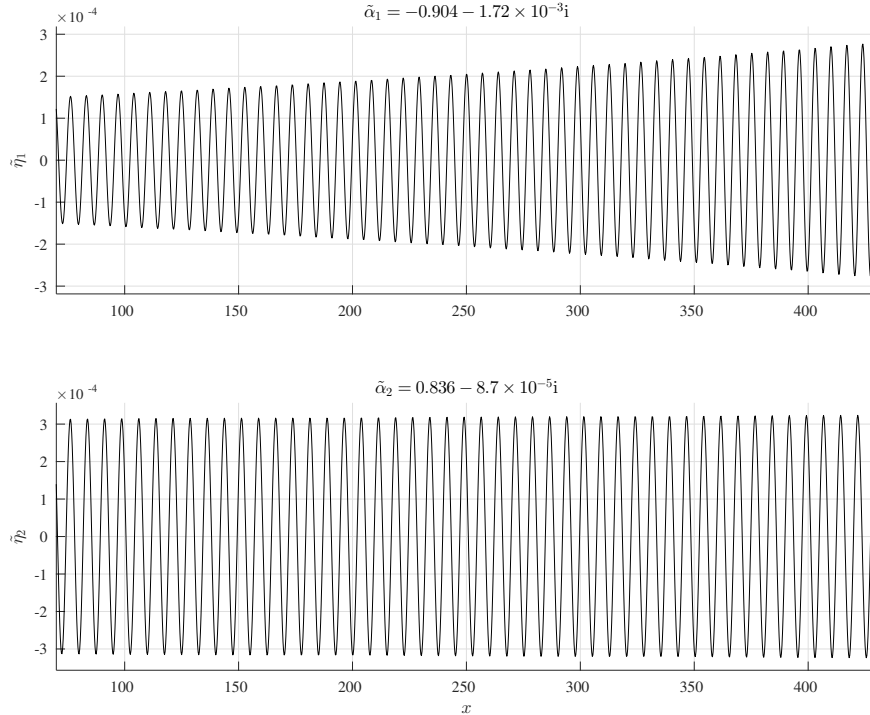


Figure 5.23: Wall displacement components for the wavenumbers given in (5.10). The superposition of these modes forms of the approximate wall displacement $\tilde{\eta}$ given in Figure 5.21(b).

a reflection from the downstream boundary (corresponding $\tilde{\alpha}_1$) causing it to travel upstream and decays as it does so.

This case is the first documented evidence of the TWF mode being provoked by using the present DNS method. Here, the TS mode plays no part but it does act as a source of excitation for the wall-based modes. The DNS method works well and the wavenumbers obtained can be predicted from the solutions of the Orr-Sommerfeld equation with reasonable accuracy.

5.6 DivEnd: Divergence & End Effects

In this final case, the effects of the divergence instability are investigated. One of the more interesting characteristics, which will become apparent, is the

fact that the solution of the Orr-Sommerfeld equation not only predicts the wavenumbers that approximate the wall displacement in the middle region, but also predicts the wavenumbers that dictate the end effects as well.

In order to choose the appropriate wall and flow parameters, several factors have to be taken into consideration. First of all, the Reynolds number of the flow has to be relatively small in order to excite the divergence mode without provoking the TS mode as well. Second, the wall mass m has to be less than $\frac{1}{3}$ in order to have an onset Reynolds number for the divergence mode to be less than that of TWF. To this end, a choice of wall parameters can be chosen as

$$m = 0.17, \quad B = 4.167 \times 10^7, \quad T = 0, \quad K = 6.67 \times 10^4, \quad d = 100.$$

The onset Reynolds numbers for the divergence and TWF modes in this case are

$$\text{Re}_d = 2500 \quad \text{and} \quad \text{Re}_{TWF} = 3001.$$

5.6.1 Choice of Flow Parameters

Figures 5.24 and 5.25 show the neutral stability curves on α -Re and β -Re planes respectively. In Figure 5.24, there are two curves for the compliant wall (black), the inner (dashed) curve represents TWF mode while the outer curve represents a merger between the divergence and TS modes. In fact, the TS mode has been stabilised and assimilated into the larger curve to take the form of a “hump” over the larger curve.

Figure 5.25 shows the two neutral curves on the β -Re plane, one representing the TS mode from the rigid wall (red) while the other represents the FISI from the compliant wall (black). The choice of flow parameters should

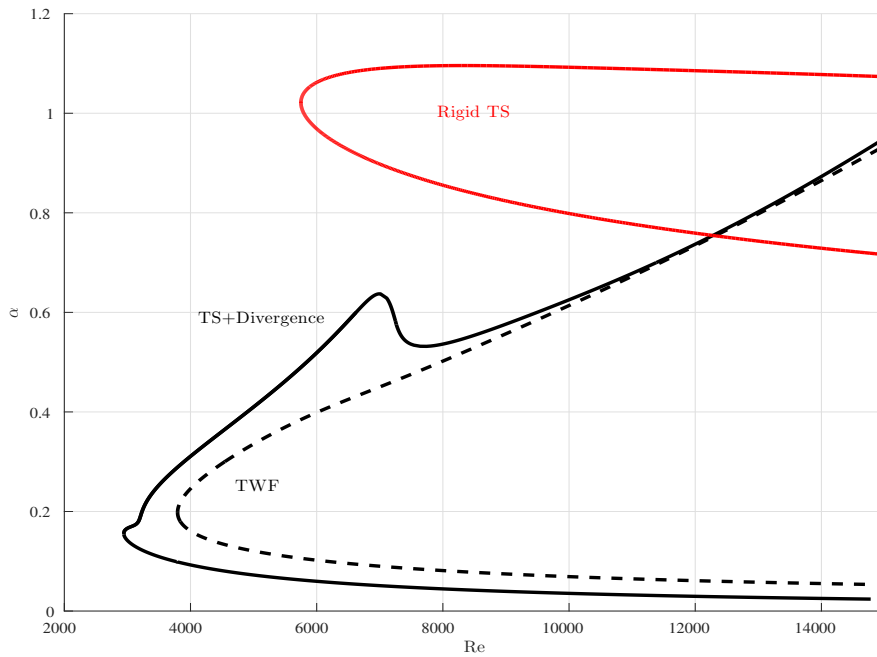


Figure 5.24: Neutral stability curves on the α -Re plane for the rigid (red) and compliant (black) wall with $m = 0.17$, $B = 4.167 \times 10^7$, $T = 0$, $K = 6.67 \times 10^4$, $d = 100$. The dashed black curve represents the TWF mode while the solid black curve represents the merger between the TS and divergence modes.

be such that the divergence mode is excited and not the others and having a small Reynolds number and frequency helps in achieving this. Therefore, the appropriate choice of flow parameters can

$$\text{Re} = 3000 \quad \text{and} \quad \beta = 0.01049$$

as labelled in Figure 5.25.

When the solution of the Orr-Sommerfeld equation is obtained for the compliant wall, there are *five* wavenumbers that the least stable/most unstable for the given parameter choices which are:

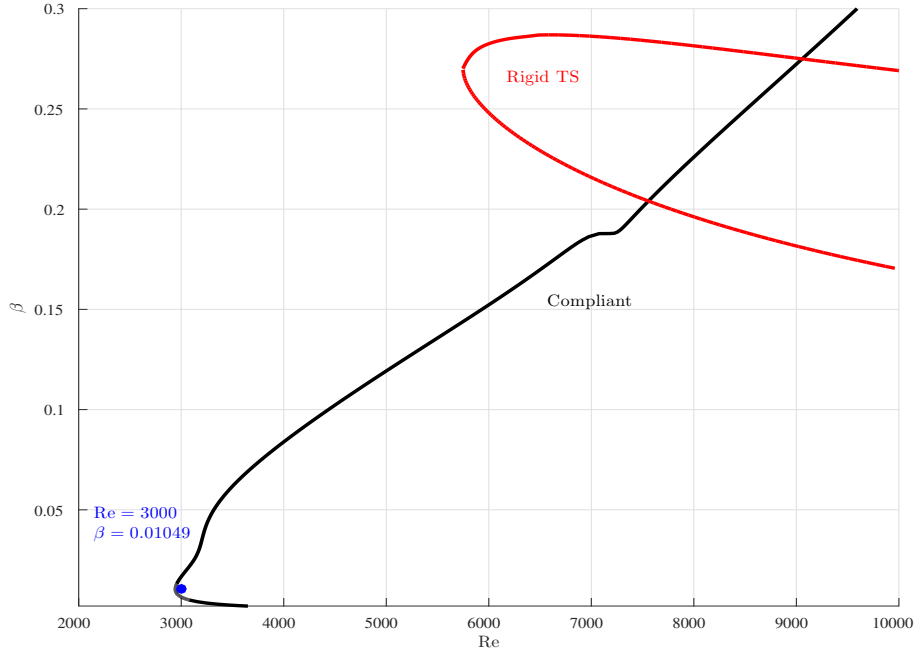


Figure 5.25: Neutral stability curves on the β -Re plane for the rigid (red) and compliant (black) walls with $m = 0.17$, $B = 4.167 \times 10^7$, $T = 0$, $K = 6.67 \times 10^4$, $d = 100$. The dot on the β -Re plane represents the flow parameters chosen for the case **DivEnd**.

$$\begin{aligned}
 \alpha_1 &= -0.301 - 1.26 \times 10^{-2}i \\
 \alpha_2 &= -0.111 + 3.88 \times 10^{-3}i \\
 \alpha_3 &= 1.79 \times 10^{-2} + 1.19 \times 10^{-2}i \\
 \alpha_4 &= 0.151 - 5.11 \times 10^{-4}i \\
 \alpha_5 &= 0.261 - 1.8 \times 10^{-2}i.
 \end{aligned} \tag{5.12}$$

The locations of these wavenumbers are indicated on the complex α -plane as shown in Figure 5.26.

5.6.2 DNS

For this case, the flow configuration consists of a relatively long compliant wall extending from $x = 100$ to $x = 900$ in a flow domain of length 1000. Since the divergence mode is expected to have a wavelength longer than either TS or

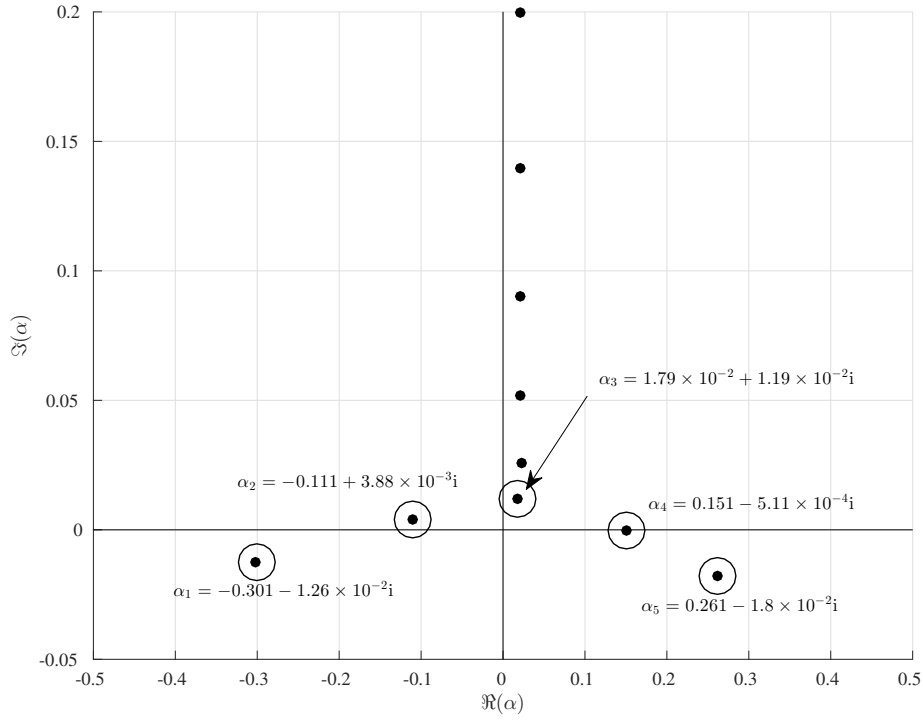


Figure 5.26: Locations of the wavenumbers obtained from the solutions of the Orr-Sommerfeld equation over the compliant wall as given in (5.12).

TWF, a longer wall is needed to observe the full extent of the mode's growth.

Figure 5.27 shows the wall displacement obtained from the DNS with two regions labelled \mathcal{L}_1 and \mathcal{L}_2 . It can be seen that the arising mode has a relatively large wavelength (compared to those of TS and TWF instabilities observed before). It is also apparent that the compliant wall ends have a considerable effect on the wall displacement, therefore in order to have a good approximate form for the wall displacement and avoid contamination from the wall end effects, the smaller fitting region \mathcal{L}_1 will be used for the approximation. Later when the end effects are investigated, the region \mathcal{L}_2 shall be used.

In order to see which modes are necessary to approximate wall displacement within \mathcal{L}_1 , a FFT can be used to determine which modes have the highest relative amplitudes, and hence are the most dominant (or at least, the most

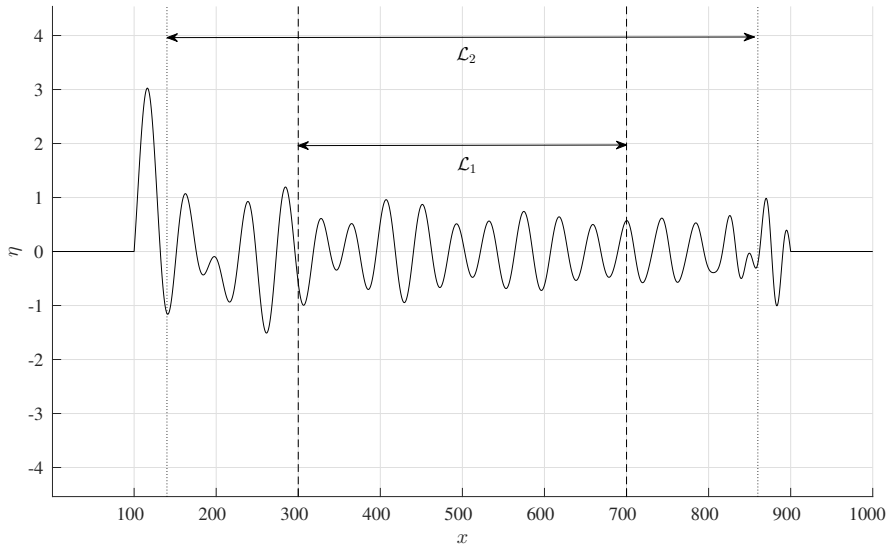


Figure 5.27: Wall displacement taken from the DNS. There are two different fitting regions labelled $\mathcal{L}_1 = [300, 700]$ and $\mathcal{L}_2 = [140, 860]$. The region \mathcal{L}_1 does not capture the contribution coming from the end effects but \mathcal{L}_2 does.

pertinent to the approximation). Figure 5.28 shows the FFT applied to the wall displacement across the entire compliant wall section, the spectrum shows three peaks centred at 0.151, 0.107 and 0.0251 as well as a range of values extending from 0.2 to 0.32. For now, suppose that the wavenumbers closest to the two highest peaks α_2 and α_4 are used to approximate the wall displacement η . The approximate form of the wall displacement $\tilde{\eta}$ within the region \mathcal{L}_1 can be obtained as

$$\tilde{\eta}(x, t) = A_2 e^{i(\tilde{\alpha}_2 x - \beta t)} + A_4 e^{i(\tilde{\alpha}_4 x - \beta t)} + \text{c.c.}$$

$$\text{where } \tilde{\alpha}_2 = -0.111 + 4.77 \times 10^{-3}i \quad (5.13)$$

$$\tilde{\alpha}_4 = 0.151 + 9.07 \times 10^{-4}i. \quad (5.14)$$

The predicted wavenumbers α_2 and α_4 from the Orr-Sommerfeld equation given in (5.12) provide excellent estimates for those arising from the DNS. Indeed, Figure 5.29(a) shows the DNS wall displacement η within the region labelled \mathcal{L}_1 , this is approximated by $\tilde{\eta}$ (red) mentioned above to give an approx-

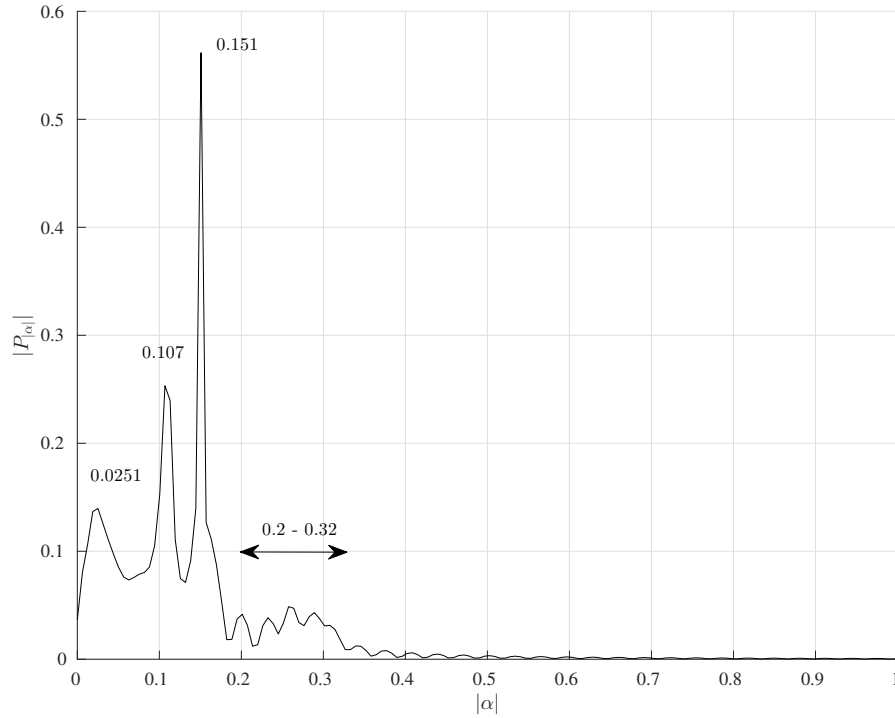


Figure 5.28: Fourier spectrum of the wall displacement profile shown in Figure 5.27 across the entire compliant wall section. The values at the peaks have been labelled accordingly.

imate form shown in Figure 5.29(b) (red) superimposed on η (black). From this, it can be seen that the approximated wall displacement $\tilde{\eta}$ corresponds quite well with that of the DNS. The relative error between the two waves is shown in Figure 5.29(c) with an approximation error of 4%.

The approximated wall displacement $\tilde{\eta}$ consists of two modes that correspond to $\tilde{\alpha}_2$ and $\tilde{\alpha}_4$, the contributions of each of these is shown in Figure 5.30. The two arising modes have a relatively large wavelength, $\tilde{\alpha}_4$ is almost neutrally stable (since its imaginary part is close to zero) while $\tilde{\alpha}_2$ decays downstream.

The mode $\tilde{\alpha}_4$ can be identified as the divergence instability given its growth rate, wavelength and very small phase speed. On the other hand, the mode $\tilde{\alpha}_2$ represents an upstream travelling growing mode which originates from the

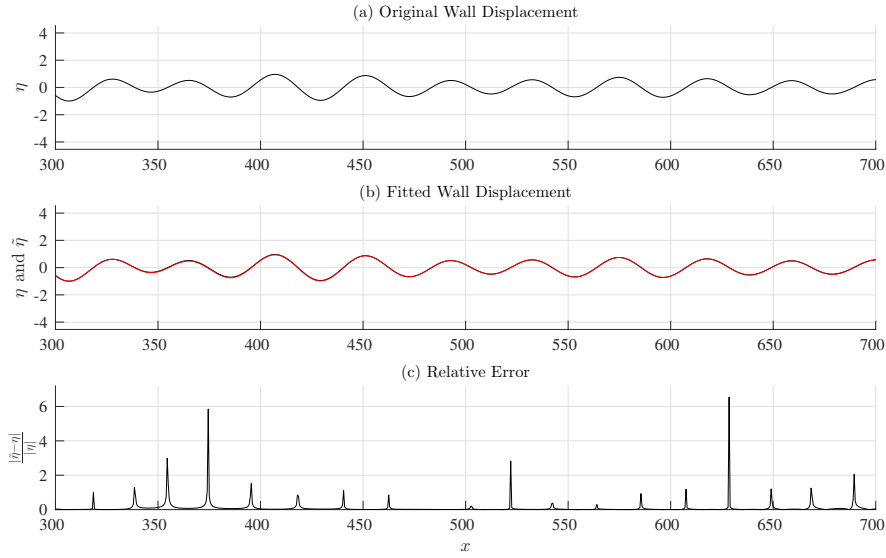


Figure 5.29: (a) DNS wall displacement η within \mathcal{L}_1 . (b) DNS wall displacement η (black) and the approximated wall displacement $\tilde{\eta}$ (red). (c) Relative error between η and $\tilde{\eta}$.

downstream boundary.

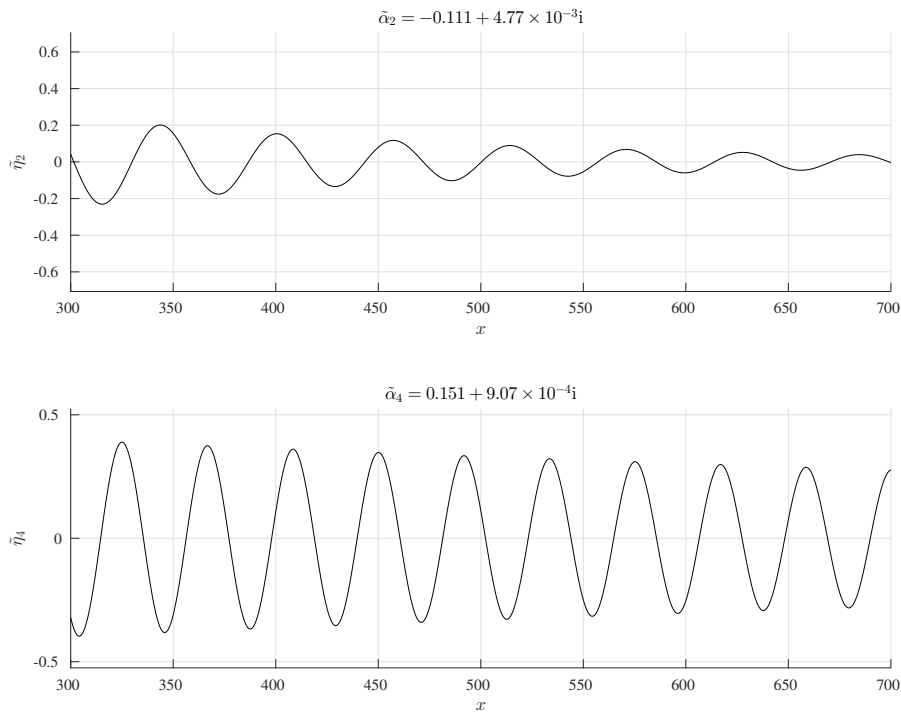


Figure 5.30: Wall displacement components for the wavenumbers $\tilde{\alpha}_2$ and $\tilde{\alpha}_4$ given in (5.13). The superposition of these two modes forms the approximate wall displacement $\tilde{\eta}$ given in Figure 5.29(b).

As yet, it can be seen that only the two most dominant modes $\tilde{\alpha}_2$ and $\tilde{\alpha}_4$ (from the point of view of their amplitudes as illustrated by the Fourier spectrum in Figure 5.28) are sufficient to approximate the wall displacement within a region where the end effects play an insignificant role, namely \mathcal{L}_1 . Therefore, it can be posited that the wavenumbers $\tilde{\alpha}_2$ and $\tilde{\alpha}_4$ are good predictors for the arising wavenumbers when no end effects are prevalent, specifically if the wall is infinitely long. But a question can be posed that asks how this approximation would fair if the end effects were included, this is investigated below where the role of the other wavenumbers $\tilde{\alpha}_1, \tilde{\alpha}_3$ and $\tilde{\alpha}_5$ come into play.

5.6.3 End Effects

Suppose, for the sake argument, that the two modes α_2 and α_4 (as earlier) are used to approximate the wall displacement within the larger region \mathcal{L}_2 shown in Figure 5.27. In this case, the wall ends distort the efficacy of the approximation near the wall ends, indeed, this approximation is shown in Figure 5.31(b). The error between η and $\tilde{\eta}$ (as in Figure 5.31(c)) becomes more apparent near the ends of the fitting region implying that the wall end effects start to play a more significant role and the approximation has to be modified since $\tilde{\alpha}_2$ and $\tilde{\alpha}_4$ can no longer be used as effective predictions for the wall displacement. (Note that this discrepancy only holds when the wall is finite.)

Suppose that now, the other wavenumbers α_1, α_3 and α_5 are used in modifying the wall displacement approximation^{VI}. These three wavenumbers will be used as predictions in different combinations in order to modify the wall

^{VI}Note that the modes α_2 and α_4 have to be included in the approximation since, first of all, they are the most dominant according to the Fourier spectrum and, second, they approximate the wall displacement in the middle region.

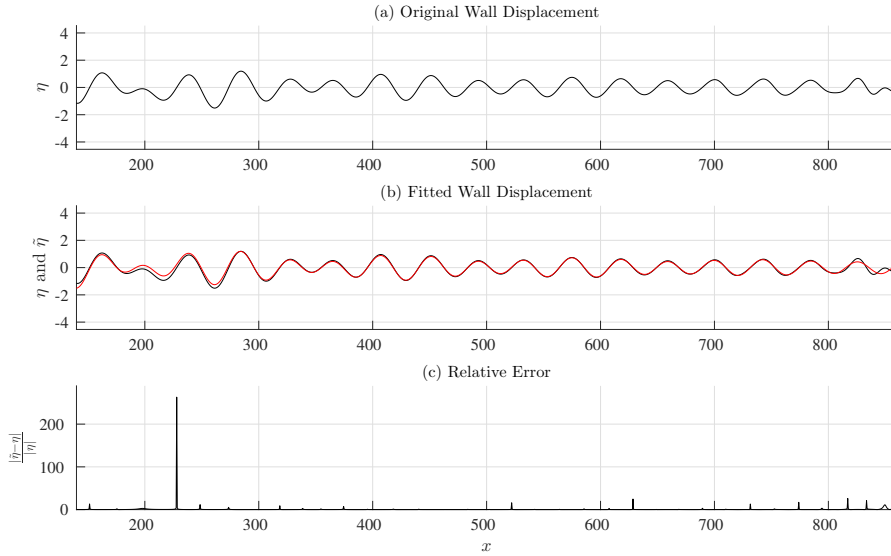


Figure 5.31: (a) DNS wall displacement η within \mathcal{L}_2 using α_2 and α_4 as estimates. (b) DNS wall displacement η (black) and the approximated wall displacement $\tilde{\eta}$ (red). (c) Relative error between η and $\tilde{\eta}$.

displacement.

Figure 5.32 shows the DNS wall displacement η (black) and the corresponding approximations $\tilde{\eta}$ (red) using different combination of the wavenumbers as follows:

- (a) Using α_2 and α_4 to approximate the wall displacement in \mathcal{L}_2
- (b) $\alpha_2, \alpha_3, \alpha_4$
- (c) $\alpha_1, \alpha_2, \alpha_4, \alpha_5$
- (d) $\alpha_1, \alpha_2, \alpha_3, \alpha_4, \alpha_5$.

Figure 5.33 shows the corresponding absolute errors between η and $\tilde{\eta}$ for the different approximations while Figure 5.34 shows the relative error. These can be interpreted as follows:

- (a) α_2, α_4 : This is simply a reproduction of Figure 5.31 and is included here to facilitate comparison with the next cases. The approximation works well in the middle bulk of the compliant wall but ceases to hold near the ends since end effects become more prominent.

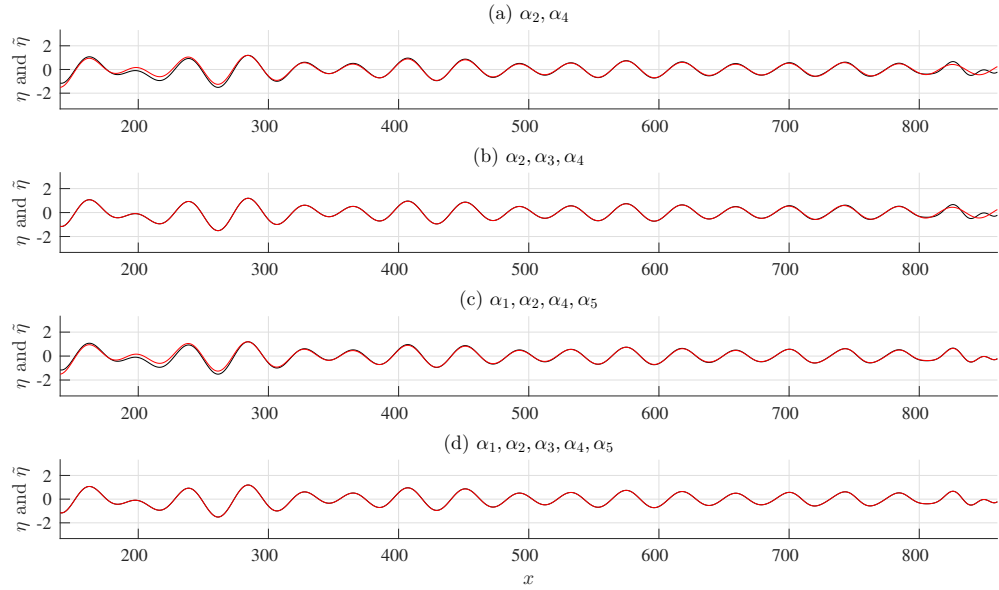


Figure 5.32: DNS wall displacement η (black) and the approximated wall displacement $\tilde{\eta}$ (red) for different modes used in the approximation. These are labelled accordingly.

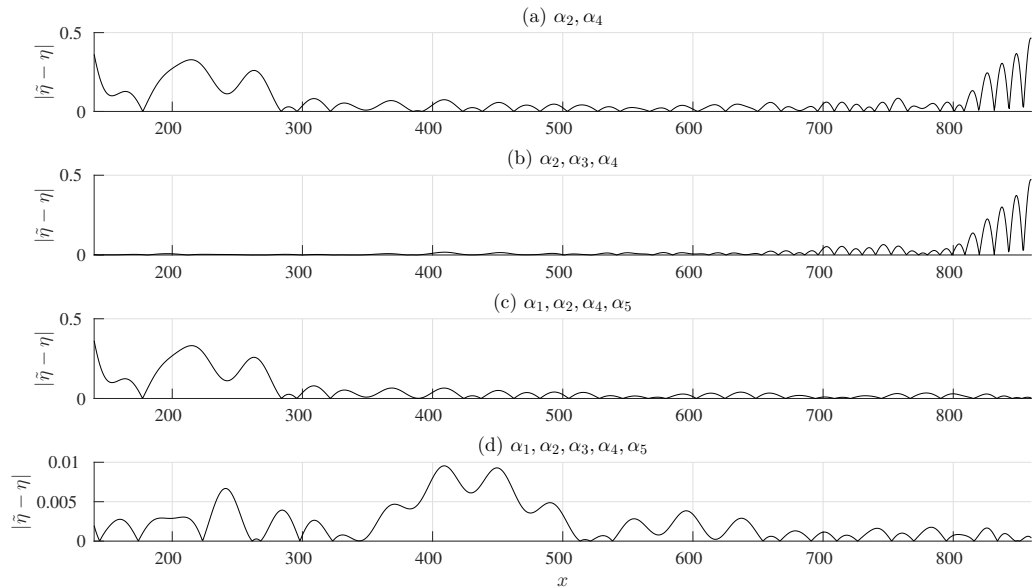


Figure 5.33: Absolute errors between η and $\tilde{\eta}$ from Figure 5.32.

(b) $\alpha_2, \alpha_3, \alpha_4$: Here, it can be seen that including the wavenumber α_3 in the approximation improves the fit at the upstream end of the compliant wall greatly, however the same cannot be said about the downstream end. This

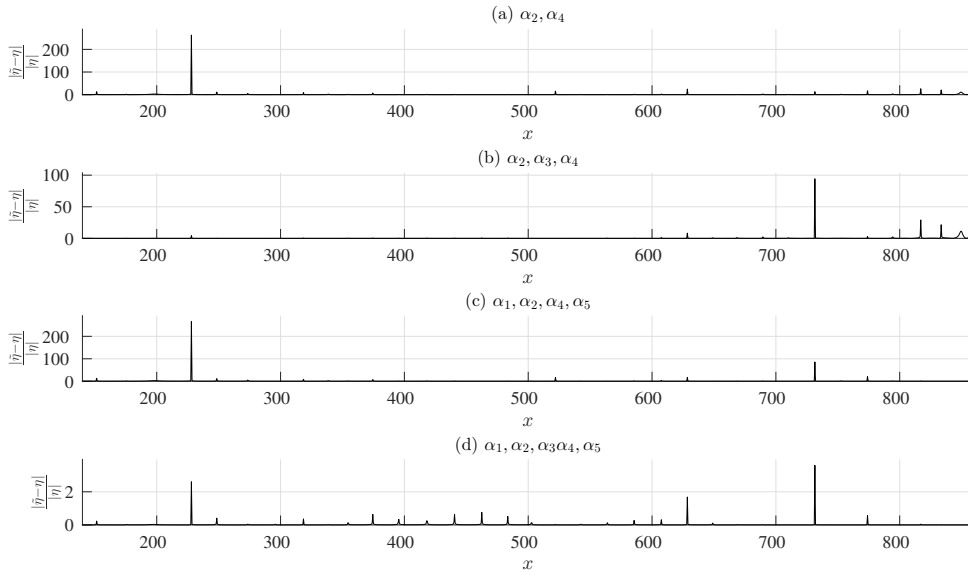


Figure 5.34: Relative errors between η and $\tilde{\eta}$ from Figure 5.32.

can also be seen from the error in Figure 5.33(b) where at the upstream end, the error becomes almost negligible but at the downstream end, the error is the same as in (a).

- (c) $\alpha_1, \alpha_2, \alpha_4, \alpha_5$: Now, the approximation includes the modes α_1 and α_5 as well as α_2 and α_4 . The result is the opposite of what happens in the case (b), namely, the *downstream* end is approximated well but the upstream end is still subjected to the discrepancy from the wall ends. It should be noted that including *either* α_1 *or* α_5 will not improve the approximation at the downstream end, they have to *both* be included in the approximation.
- (d) $\alpha_1, \alpha_2, \alpha_3, \alpha_4, \alpha_5$: From the previous two cases (b) and (c), including α_3 in the approximation improves the accuracy at the upstream end while including α_1 and α_5 does the same for the downstream end. Therefore, including all three modes α_1, α_3 and α_5 should improve the approximation at both ends and capture the wall end effects very effectively. Indeed, Figure 5.32(d) shows this very situation with the significantly minimised error in Figure 5.33(d).

Figure 5.34 shows the relative errors for the four cases mentioned above. It can be seen that when α_3 is included in the approximation, the relative error at the upstream boundary is substantially reduced while the downstream boundary is unaffected, similarly for the inclusion of α_1 and α_5 at the downstream end. But when all modes are included in the approximation, the relative error reduces from over 260 to less than 4 implying that all five modes play a role in approximating the wall displacement profile.

Therefore, it can be seen that each of the five modes in (5.12) play an important role in approximating the wall displacement as follows: α_2 and α_4 approximate the wall displacement in the middle region, α_3 approximates the effects from the upstream end while α_1 and α_5 approximate the effects from the downstream end. The full form of $\hat{\eta}$, in this case, is

$$\hat{\eta}(x, t) = \sum_{n=1}^5 A_n e^{i(\tilde{\alpha}_n x - \beta t)} + \text{c.c.}$$

The approximated wavenumbers in this case are given in Table 5.1 and are compared to those obtained from the solutions of the Orr-Sommerfeld equation.

DNS	Orr-Sommerfeld Solutions
$\tilde{\alpha}_1 = -0.301 - 1.33 \times 10^{-2}i$	$\alpha_1 = -0.301 - 1.26 \times 10^{-2}i$
$\tilde{\alpha}_2 = -0.111 + 4.6 \times 10^{-3}i$	$\alpha_2 = -0.111 + 3.88 \times 10^{-3}i$
$\tilde{\alpha}_3 = 2.11 \times 10^{-2} + 1.36 \times 10^{-2}i$	$\alpha_3 = 1.79 \times 10^{-2} + 1.19 \times 10^{-2}i$
$\tilde{\alpha}_4 = 0.151 + 8.66 \times 10^{-4}i$	$\alpha_4 = 0.151 - 5.11 \times 10^{-4}i$
$\tilde{\alpha}_5 = 0.261 - 1.92 \times 10^{-2}i$	$\alpha_5 = 0.261 - 1.8 \times 10^{-2}i$

Table 5.1: DNS wavenumbers compared to those obtained from the Orr-Sommerfeld solutions.

Note that for the mode $\tilde{\alpha}_4$, the imaginary part has a different sign compared to that of the Orr-Sommerfeld solution α_4 . One explanation of this would be the fact that the DNS surely has a slight discrepancy when the approximation is performed. All the other modes have imaginary parts that are slightly different compared to those obtained from the approximation but given the size of $\Im(\alpha_4)$ (which is $\mathcal{O}(10^{-4})$), a minuscule deviation managed to change its sign.

The separate modes that make up the wall displacement in Figure 5.32(d) are plotted in Figure 5.35. The values of $\tilde{\alpha}_2$ and $\tilde{\alpha}_4$ are slightly different to those obtained in the case when the fitting region was \mathcal{L}_1 but they still approximate the wall displacement well nonetheless. Here, $\tilde{\eta}_2$ and $\tilde{\eta}_4$ take the same forms as they did in Figure 5.35 allowing the middle portion of the wall to be approximated well. The mode $\tilde{\alpha}_3$ is a very long wave that decays very rapidly over the compliant wall and therefore alters the upstream end to such an extent that the approximation is improved but at the downstream end, there is little to no affect. Finally, the two modes $\tilde{\alpha}_1$ and $\tilde{\alpha}_5$ may seem to be the least significant (given their small relative amplitudes according to the Fourier spectrum given in Figure 5.28), however near the downstream end, both these modes start to grow in amplitude to such an extent that they compete with other three modes hence improving the approximation at the downstream end.

5.6.4 Remarks for DivEnd

This case has shown that the solutions of the Orr-Sommerfeld equation not only provide predictions to the wavenumbers arising from the DNS for the divergence case, but it also provides predictions for the wavenumbers that predict the end effects as well. A flow configuration where the divergence in-

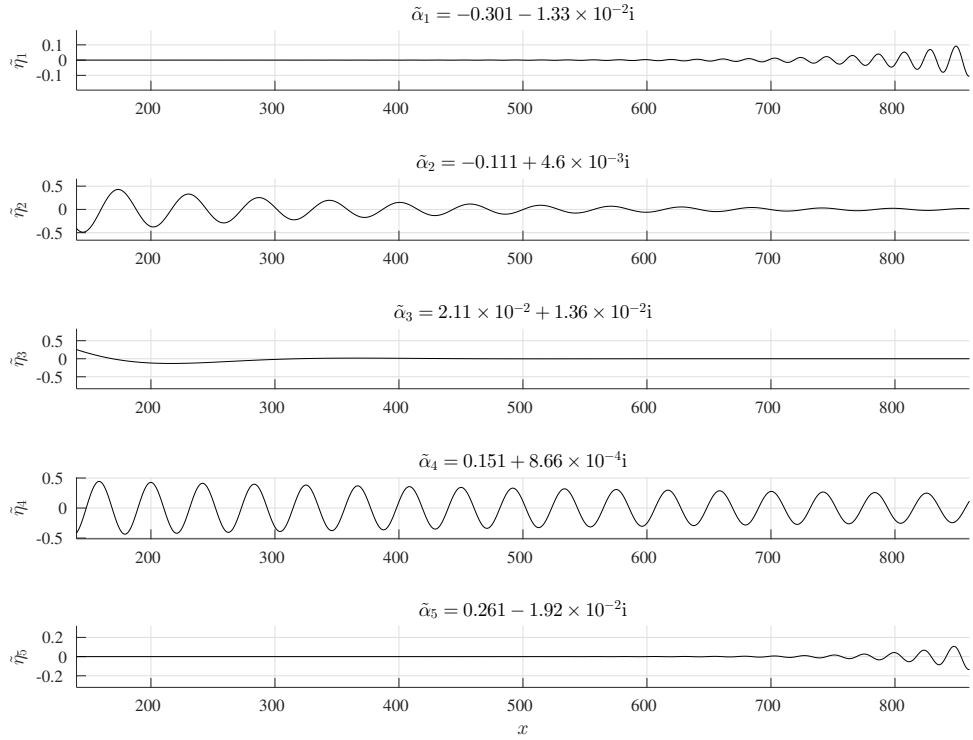


Figure 5.35: Wall displacement components for the all the wavenumbers in (5.12). The superposition of these modes gives the approximate wall displacement in Figure 5.32(d).

stability is observed using the current DNS method has not been documented and this is the first evidence of such a mode that is unaffected by other instabilities. Also, it is interesting to note that even though the method used to obtain solutions of the Orr-Sommerfeld equation described in Chapter 3 was designed for an infinite compliant wall, it still managed to obtain approximations to the wavenumbers that dictate the wall end effects arising from the DNS for a finite compliant wall section.

A similar case was performed using a different set of flow parameters that resulted in a decaying divergence mode and the conclusions were the same, i.e. there will be five modes that are unstable/least stable.

5.7 Summary

All the cases in this chapter considered flows with a spatial variation and the two new cases are those labelled **TWF** and **DivEnd**. In both cases, the flow parameters were chosen to avoid exciting the TS mode in order to observe the wall-based modes, TWF and divergence, unpolluted by the flow-based TS mode.

In **TWF**, the first wall-based was discussed from a DNS point of view and the wavenumbers arising in that case have been effectively predicted by the solutions of the Orr-Sommerfeld equation as per the method discussed in Chapter 3.

In the first three cases, the wall end effects did not affect the wall displacement near the ends drastically however the same cannot be said for the last case **DivEnd**. Here, the divergence instability played a role in affecting the wall displacement profile and the wall end effects played a huge role in affecting the displacement near the ends of the compliant wall. Even with this in mind, the solutions of the Orr-Sommerfeld equation managed to effectively predict the arising wavenumbers from the divergence instability as well as those that contribute to the end effects. There were five eigenvalues of greatest interest (those which are closest to the real line on the complex α plane), two of those approximated the contribution of the divergence instability, another two captured the downstream end effects and the last one captured the upstream end effects.

Chapter 6

Absolute Instability

6.1 Introduction

In this section, several cases are considered for which the flow exhibits a *global* or *absolute instability*. In Chapter 5, the spatial evolution of the TS, TWF and divergence modes was studied when the flow was subjected to a time-periodic forcing. The wall displacement profiles were a superposition of several modes which were predicted effectively by the solutions of the Orr-Sommerfeld equation. In some of the cases (particularly with a small Reynolds number and forcing frequency), the contribution from the end effects was also predicted effectively.

In this chapter, the disturbances generated by either a periodic forcing or a localised impulsive disturbance cause the wall displacement to take an *absolutely unstable* form; the wall heights grow everywhere causing the disturbance to grow in both the upstream and downstream directions. There are two different characteristic themes that will be presented here (and they will be labelled using bold letters). The first, labelled **STG**, is when the disturbance

results in an absolute instability that grows spatially and temporally while the second, labelled **TG**, is when the disturbance grows temporally only and takes the form of a static, non-oscillating wave.

In the first case **STG**, the solutions of the Orr-Sommerfeld equation and the curves of c against R and α are used to provide candidates for the flow parameters that are expected to result in absolute instability. Then, a DNS are preformed to see if the flow is indeed absolutely unstable, finally, the wall displacements obtained from the DNS will be corroborated using Briggs' method (which is discussed in Appendix H).

In the second case **TG** where the disturbance develops into a static temporally growing global instability, the results from the DNS are compared to two-dimensional global mode computations (which come courtesy of *Dr. M. J. Blount*). Several changes will also be made to the flow configuration to study the effects of changing, for instance, the compliant wall length, joint conditions, wall mass and damping. Finally, a brief account of the energy equations will be set up to study the energy transfer between the compliant wall and the flow.

6.1.1 Wall Parameters

For all the cases presented in this chapter, the following one-parameter family of wall parameters will be considered:

$$m = 2, \quad B = \frac{5.12 \times 10^9}{2^n}, \quad T = 0, \quad K = 78125 \times 2^n, \quad d = 200.$$

This family of wall parameters is chosen particularly since it shows the desired characteristics which are the subject of study in this chapter most clearly. Also,

the product of B and K is kept constant and therefore, the lengthscale of the system is also constant. Recall that the inherent lengthscale of the system is given by

$$R_0 = \sqrt{2\sqrt{BK} + T}.$$

Therefore keeping the product of B and K constant allows R_0 to take the approximate fixed value of 6325. The analytic approximations of the critical Reynolds numbers of divergence, TWF and the flutter-type instability depend on R_0 (see for example Chapter 2 and Davies & Carpenter [31]) and therefore, they will also remain constant and take the following values:

$$\begin{aligned} \text{Divergence: } R_d &= \sqrt{\frac{15}{8}} R_0 \approx 8660 \\ \text{TWF: } R_{TWF} &= \sqrt{\frac{5}{5m+1}} R_0 \approx 4264 \\ \text{Flutter-type: } R_f &= \frac{3}{2} \sqrt{\frac{5m+5}{6m+1}} R_0 \approx 10190. \end{aligned} \tag{6.1}$$

The product of K and B dictates the lengthscale of the system but their ratio dictates the critical wavenumber for the divergence instability. According to Davies & Carpenter [30] (and is indicated in Chapter 2), the analytic approximation for the critical wavenumber is

$$\alpha_c = \sqrt[4]{\frac{K}{B}} = 2^{\frac{n}{2}-4}. \tag{6.2}$$

The approximations given in (6.1) and (6.2), are valid under the long-wavelength approximation ($\alpha \sim 0$) but as the ratio $\alpha_c \rightarrow 1$, these approximations ceases to hold.

Table 6.1.1 shows the values of B and K for different values of n along with their corresponding critical wavenumbers α_c from (6.2). The table also shows

the numerically obtained critical Reynolds number R_c and temporal frequency ω_c at this fixed wavenumber (i.e. R_c is the value of the Reynolds number at which the flow becomes unstable for the fixed wavenumber α_c while ω_c is its corresponding frequency).

n	B	K	α_c	R_c	ω_c
0	5.12×10^9	78125	$\frac{1}{16}$	8869	10^{-3}
1	2.56×10^9	156250	$\frac{\sqrt{2}}{16}$	8924	1.67×10^{-3}
2	1.28×10^9	3.125×10^5	$\frac{1}{8}$	9913	1.71×10^{-2}
3	6.4×10^8	6.25×10^5	$\frac{\sqrt{2}}{8}$	9886	3.35×10^{-2}
4	3.2×10^8	1.25×10^6	$\frac{1}{4}$	9732	5.52×10^{-2}
5	1.6×10^8	2.5×10^6	$\frac{\sqrt{2}}{4}$	9454	8.58×10^{-2}
6	8×10^7	5×10^6	$\frac{1}{2}$	8902	0.126
7	4×10^7	10^7	$\frac{\sqrt{2}}{2}$	7555	0.181
8	2×10^7	2×10^7	1	7252	0.572

Table 6.1: Values of B and K for different n along with the analytic approximation for α_c from equation (6.2) and the numerical approximations for R_c and ω_c .

A Note on the Discretisation of Space & Time

In Chapter 5, the ratio between the temporal and spatial discretisations $\frac{\Delta t}{\Delta x}$ was taken to be $\frac{1}{2}$ ($\Delta x = 0.5$ and $\Delta t = 0.25$). This ratio served the purpose of resolving the instabilities accurately, smaller values were also tested but yielded the same results. In the cases shown in this chapter, the flow is set up to become absolutely unstable and therefore the ratio $\frac{\Delta t}{\Delta x}$ had to be made smaller in order to avoid numerical instabilities. To this end, $\frac{\Delta t}{\Delta x} = \frac{1}{10}$ ($\Delta x = 0.25$ and $\Delta t = 0.025$) was found to be the most appropriate choice

(smaller values were also taken but the results were the same).

6.2 STG: Spatio-Temporal Growth

In this section, the absolute instability that grows spatially and temporally is studied. This section is split into two subsections labelled **STG1** and **STG2** and these present the information under two different settings. In both **STG1** and **STG2**, the disturbance is excited in three ways: an inflow profile with high frequency, low frequency and a localised impulsive forcing. The different inflow frequencies are chosen to investigate how the absolute instability is affected by forcing frequencies at the inflow. On the other hand, the localised impulsive forcing is used to excite the disturbance to study the effect of a background impulse on the proliferation of the absolute instability. The results extracted from these three different cases are compared to one another and to the results obtained from Briggs' method.

6.2.1 STG1

For this first case, the set of wall parameters given by $n = 0$ is chosen and the neutral stability curve on the α -Re plane is shown in Figure 6.1. In order to find a suitable candidate for the Reynolds number of the flow that results in an absolute instability, the variation of the phase speed c against α and Re need to be studied. After the suitable value of Re is obtained, a DNS will then be performed for the given flow parameters then the wavenumbers and phase speeds for the absolute instability are extracted. Finally, Briggs' method will be used to interpret and corroborate these results and to confirm that the instability is in fact absolute.

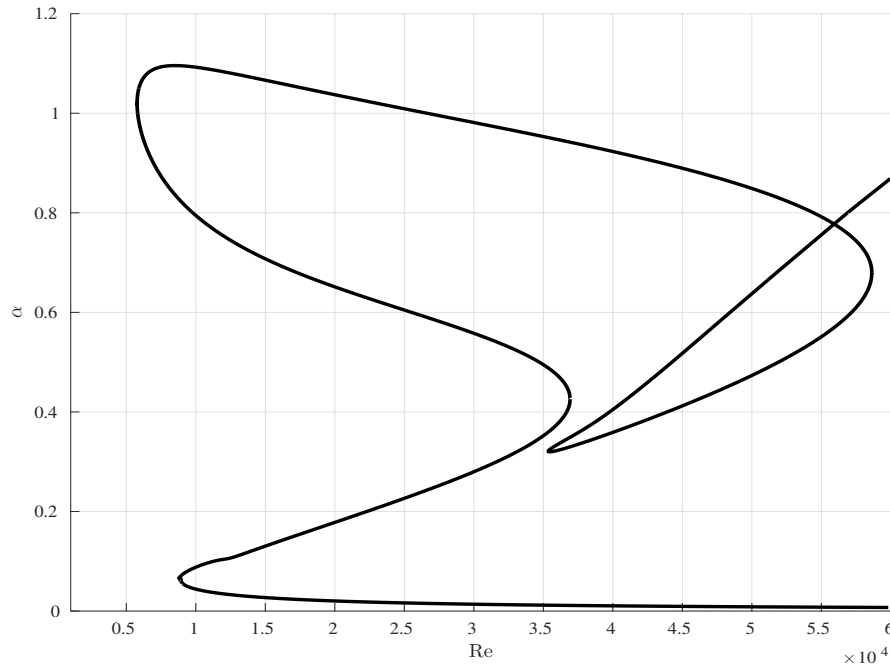


Figure 6.1: Neutral stability curve on the α -Re plane for the wall parameters $m = 2$, $B = 5.12 \times 10^9$, $T = 0$, $K = 78125$, $d = 200$.

c - α Curves

In order to obtain a candidate for the Reynolds number for an absolute instability, first consider the variation of the phase speed c against the wavenumber α for a fixed value of Re. Figures 6.2 and 6.3 show the variation of the real and imaginary parts of c plotted against α for fixed $\text{Re} = 13190$ and 13210 respectively.

Figure 6.2 shows three different modes: the modified flow-based/TS (blue), divergence (red) and TWF (green) modes (note that the vertical dashed lines denote the locations where any of the modes cross $\Im(c) = 0$). The TS mode is unstable for values of α in the interval $I_T = [0.734, 1.077]$ while divergence^I is unstable in $I_d = [0.0297, 0.1126]$. The TWF mode is stable throughout and plays no significant role here but is included for completeness.

^INotice that the divergence mode is stationary at onset (has zero phase speed at $\alpha = 0.0297$) and its maximum growth rate is at least 30 times greater than that of TS.

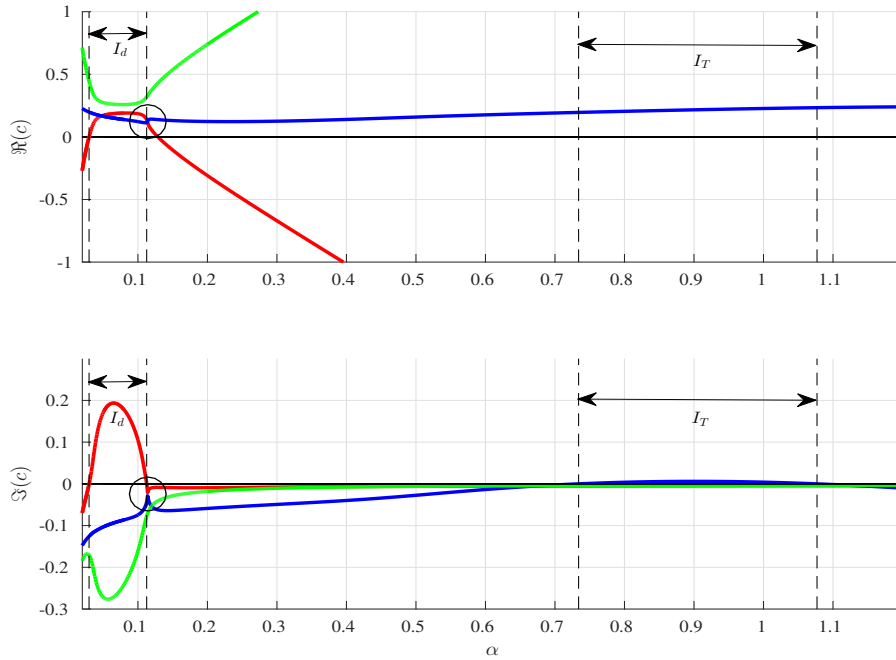


Figure 6.2: Components of c against α for a fixed $\text{Re} = 13190$. The three lines represent the TS (blue), divergence (red) and TWF (green) modes. The labelled wavenumber intervals show where TS and divergence destabilise the flow (I_T and I_d respectively). Around $\alpha = 0.1138$ (circled), the divergence and TS modes start to interact at $c = 0.121 - 0.025i$.

At $\alpha = 0.1138$ (represented by a circle), the lines representing the TS and divergence modes (blue and red respectively) start to “interact” at the phase speed $c = 0.121 - 0.025i$. Increasing the Reynolds number slightly to 13210 results in a distinct change in behaviour as seen in Figure 6.3. This interaction at $\alpha = 0.1138$ yields two new modes, one of them (blue) destabilises the flow at *two* separate wavenumber intervals $\tilde{I}_T = [0.734, 1.077]$ and $\tilde{I}_d = [0.0297, 0.1128]$ while the other mode (red) is stable throughout. This implies that a small increase in the Reynolds number has led to an instability that is the result of an interaction between the divergence and TS modes which destabilises the flow at two separate wavenumber intervals. This can be seen in a clearer setting in Figures 6.4 and 6.5 which are the same as 6.2 and 6.3 respectively but zoomed in at the regions of interest around $\alpha = 0.1138$.

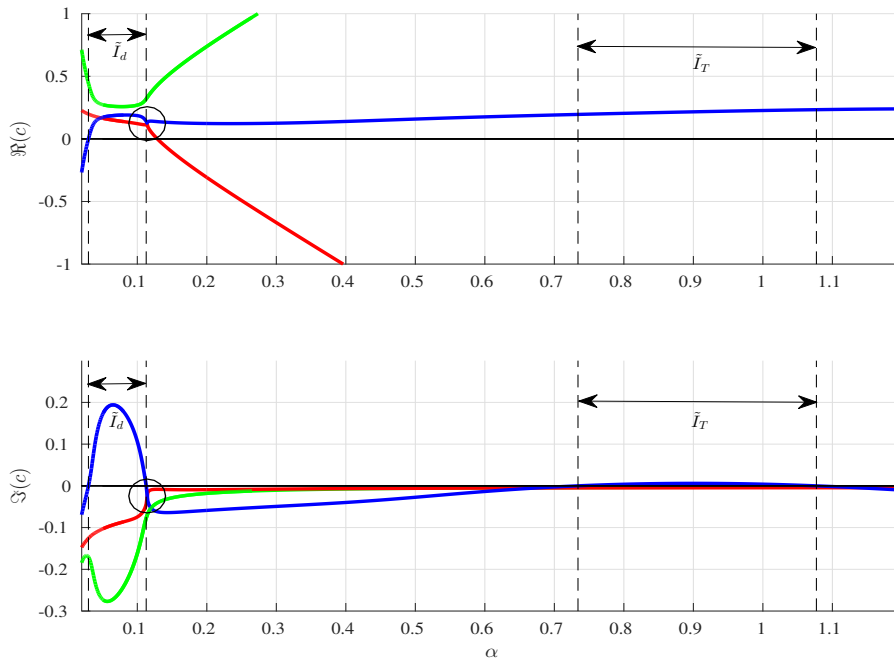


Figure 6.3: Similar to Figure 6.2 but for $Re = 13210$. The divergence and TS modes interact at $\alpha = 0.1138$ (circled) resulting in an instability (blue) that destabilises the flow at the two intervals labelled \tilde{I}_T and \tilde{I}_d .

From this, it can be deduced that the Reynolds number $Re = 13200$ can be a good candidate for absolute instability. In order to further verify this choice of flow parameters, the variation of c against Re for a fixed wavenumber α will be investigated.

***c-Re* Curves**

Figure 6.6 shows the variation of the phase speed components $\Re(c)$ and $\Im(c)$ with Re for a fixed wavenumber $\alpha = 0.1137$ (less than the proposed location of the interaction at $\alpha = 0.1138$). The two modes start interacting around the vicinity of $Re = 13200$ (circled) and a slight increase in the value of the wavenumber α to 0.114, as in Figure 6.7, causes the two modes to “interact” just as before.

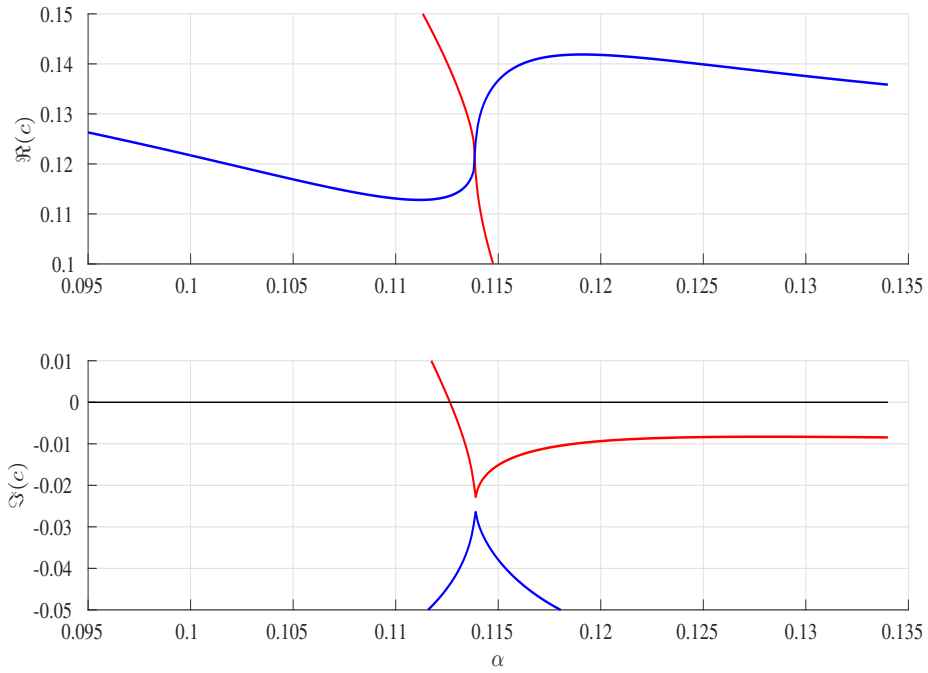


Figure 6.4: Just as in Figure 6.2 but zoomed in on the circled region. The line representing real part of the divergence mode (red) crosses over the TS mode while the imaginary parts form a pinch.

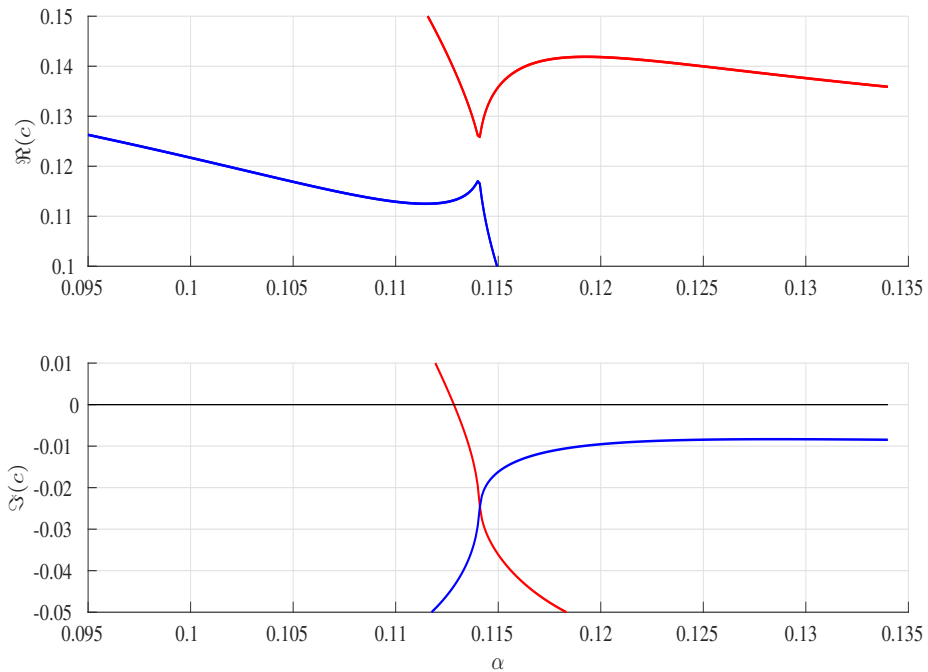


Figure 6.5: Just as in Figure 6.3 but zoomed in on the circled region. After the increase in the Reynolds number, the lines representing the real parts of the divergence mode form the pinch while the imaginary parts cross over.

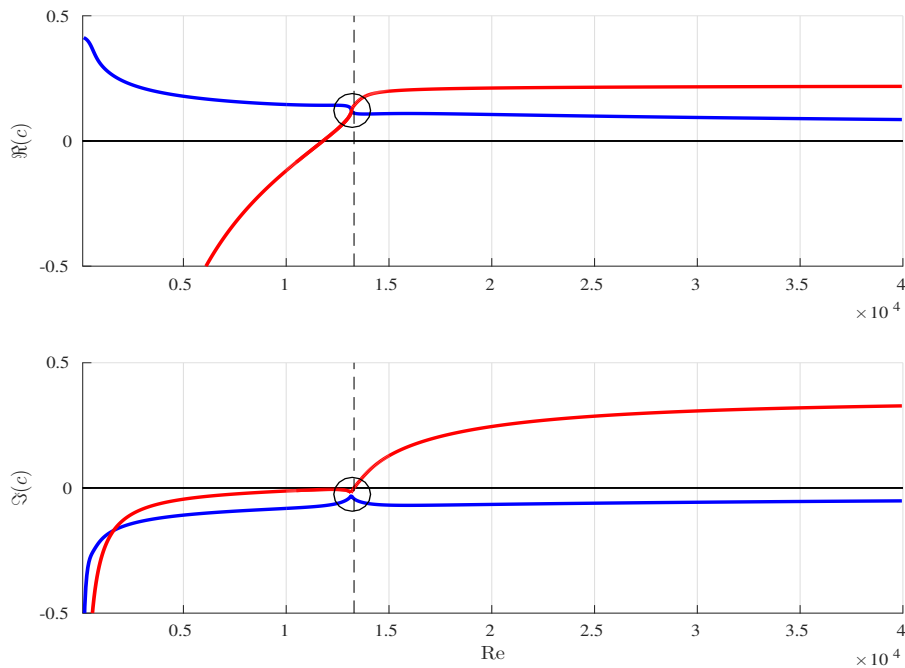


Figure 6.6: Components of c against Re for a fixed $\alpha = 0.1137$. The two lines represent different modes and the vertical dashed line denotes the location where any mode crosses $\Im(c) = 0$. Around $\text{Re} = 13200$ (circled), the two modes interact at $c = 0.121 - 0.025i$.

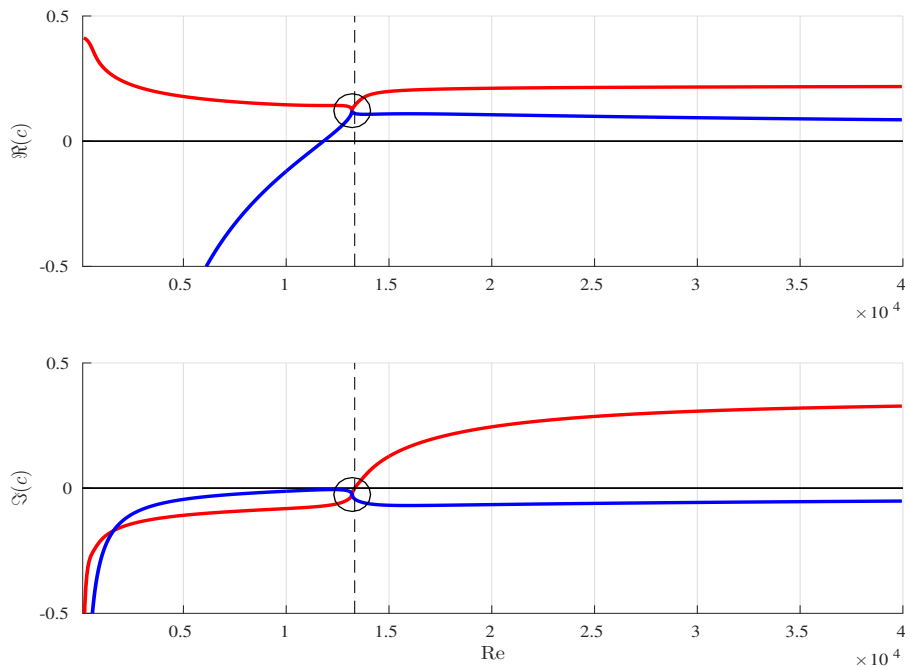


Figure 6.7: Similar to Figure 6.6 but for $\alpha = 0.114$. The two lines interact and switch over for values of Re less than 13200 (circled).

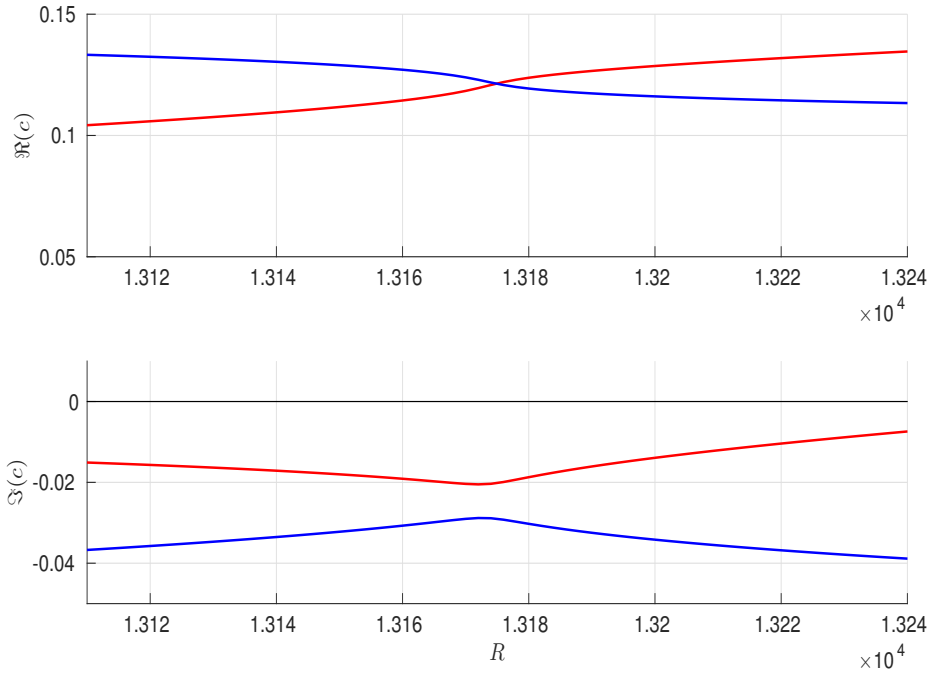


Figure 6.8: Just as in Figure 6.6 but zoomed in on the circled region. The line representing real part of the divergence mode (red) crosses over the TS mode while the imaginary parts form a pinch.

Figures 6.8 and 6.9 are the same as Figures 6.6 and 6.7, respectively, but zoomed in at the circled regions to show the interaction between the divergence and TS modes.

From Figures 6.2, 6.3, 6.6 and 6.7, it can be deduced that the interaction between the TS and divergence modes around $\text{Re} = 13200$ and $\alpha = 0.1138$ forms a new mode which destabilises the flow at two distinct wavenumber intervals and this interaction could result in a disturbance that grows absolutely. This claim shall now be verified by performing several simulations for this choice of flow parameters then confirmed by Briggs' method.

DNS

Three different flow simulations are performed here, two for an inflow profile with forcing frequencies $\beta = 0.12$ and 0.01137 and one with a localised

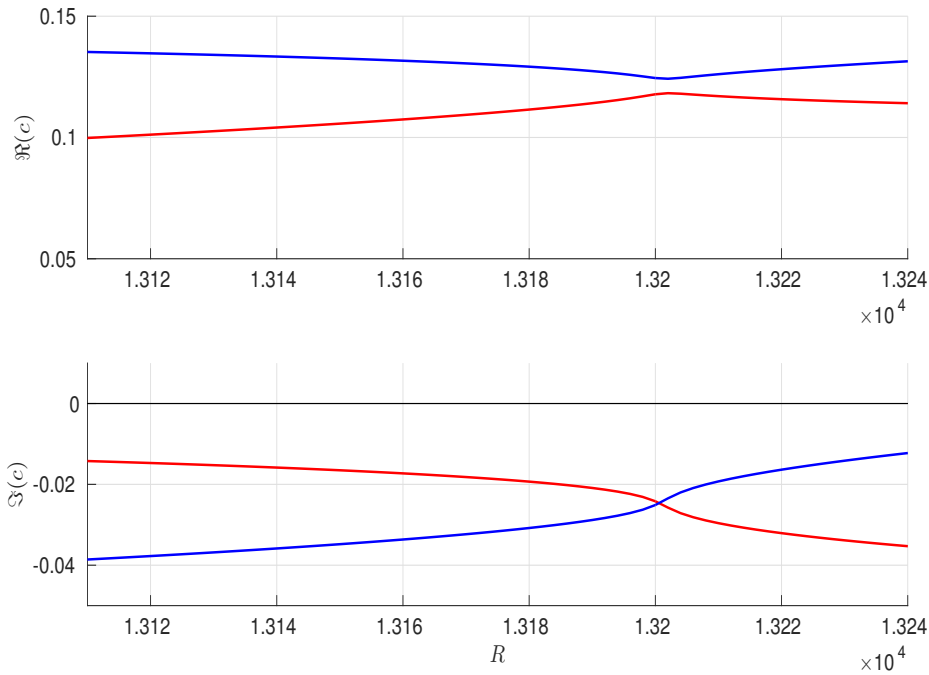


Figure 6.9: Just as in Figure 6.7 but zoomed in on the circled region. After the increase in the wavenumber, the lines representing the real parts of the divergence mode form the pinch while the imaginary parts cross over.

impulsive excitation. Disturbing the flow by means of a localised impulsive forcing will eliminate the need for introducing a forcing frequency β into the system. Additionally, since the flow is suspected to be unstable, any near-field effects due to the impulsive excitation are not going to affect the overall behaviour.

$\beta=0.12$

Consider a flow domain of length 500 with a compliant wall section extending from $x = 100$ to 450 in a flow with $Re = 13200$ (which is the value at which the modal interaction was observed earlier in the plots of the components of c against Re and α). The flow is excited by means of an inflow profile with a forcing frequency $\beta = 0.12$ and in this case, the disturbance will cause the wall displacement to take the general form shown in Figure 6.10. The instability has a phase speed 0.1736 (i.e. this is the non-dimensional speed at which the

crests/troughs travel down the length of the compliant wall). The instability also grows spatially *and* temporally everywhere hence implying that the instability grows absolutely (at least according to the DNS).

Note that in Figure 6.10, the wall displacement axis has not been labelled, this is because the waveform has an associated *geometric quasi-periodic time period* τ . This means that if the wall displacement takes the form $\eta(t)$ at some time t , for example, then $\eta(t + \tau)$ will be exactly the same as $\eta(t)$ but with an amplification factor, this is explained further below.

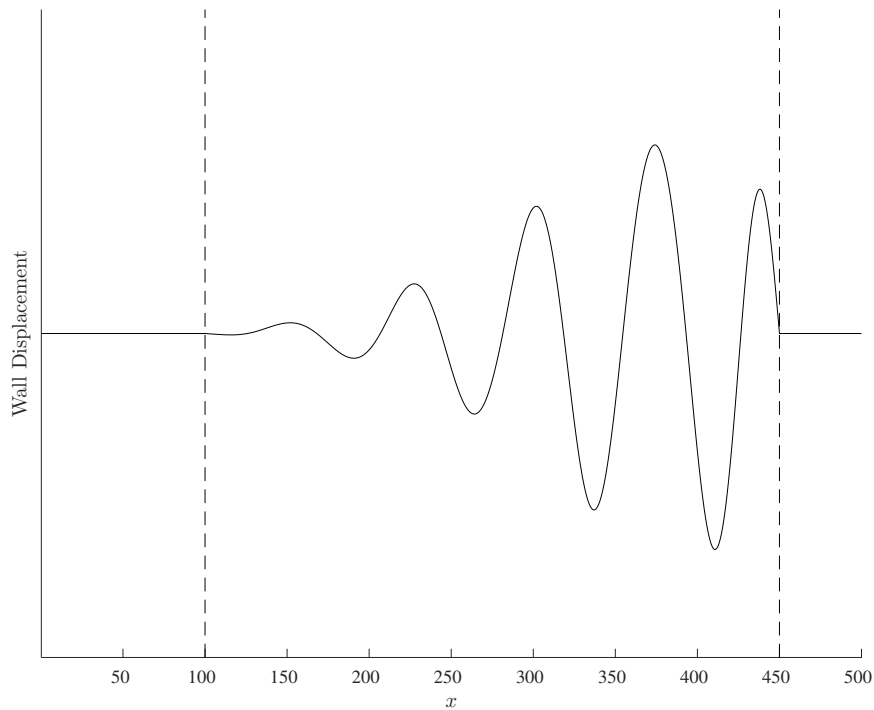


Figure 6.10: **STG1** with $\beta = 0.12$, the vertical dashed lines denote the start and end of the compliant wall section. The instability has a phase speed 0.1736 and an exponential growth rate 0.01257. The most dominant wavenumber is 0.08796 and the *gq*-period is 410.

The Geometric Quasi-Period τ

Suppose that the wall height at all the streamwise locations at some time t is given by the vector

$$\boldsymbol{\eta}(t) = (\eta(x_0, t), \eta(x_1, t), \dots, \eta(x_{n_e}, t))$$

where the streamwise positions within the compliant wall is given by the vector

$$\boldsymbol{x} = (x_0, x_1, \dots, x_{n_e}).$$

If the wall displacement profile is geometric quasi-periodic, then after a time τ (known as the *geometric quasi-period*), the wall takes the same form it did before but with a multiplicative factor, i.e.

$$\boldsymbol{\eta}(t_0 + \tau) = \tilde{A}\boldsymbol{\eta}(t_0) \tag{6.3}$$

where t_0 is any time after which the transients have subsided and \tilde{A} is an amplification factor. Therefore, this implies that the wall heights $\boldsymbol{\eta}$ will have to grow exponentially. The term “geometric quasi-period” is borrowed from mathematical analysis since it best describes the evolution of the waves observed in the DNS, this will be hereafter denoted as *gq-period*. For the particular case when $\beta = 0.12$, the gq-period τ is approximately 410. (It should be noted that the values of τ will be given to the nearest 10 since they have to be extracted manually from the DNS.)

Extracting Wavenumbers

In order to see which wavenumbers are the most dominant, a *Fast Fourier Transform* (FFT) can be applied on the wall displacements giving the most

dominant wavenumber as 0.08796^{II}.

Extracting Growth Rates

The profile that is observed in Figure 6.10 grows temporally everywhere and the growth rate can be determined using a relatively crude, yet effective method. First of all, the height at a fixed streamwise position $x = X$ will be denoted $\tilde{\eta}_X$ and is assumed to take the form

$$\tilde{\eta}_X(t) = Ae^{\lambda t} \quad (6.4)$$

which satisfies (6.3). The time t has to be greater than the time t_0 mentioned earlier and for the sake of convenience, t can be taken to be an integer multiple of τ . Taking the logarithm of (6.4) gives

$$\ln(\tilde{\eta}_X(t)) = C + \lambda t \quad \text{where} \quad C = \ln(A).$$

The DNS results provide values of t and $\tilde{\eta}_X(t)$ and therefore λ and A can be determined by means of a *linear regression*, an example of this is shown in Figure 6.11.

The figure shows the plot of $\ln(\tilde{\eta}_{347}(t))$ (the logarithm of the wall height at the fixed streamwise position $x = 347$) at different times separated by multiples of τ . The plot forms a straight line implying that the assumption of exponential growth is perfectly valid (which is not unexpected). The values of A and λ in this particular case are

$$A = 9.782 \times 10^{-7} \quad \text{and} \quad \lambda = 0.01253.$$

^{II}The term “most dominant wavenumber” here refers to the wavenumber that has the highest value in the Fourier spectrum.

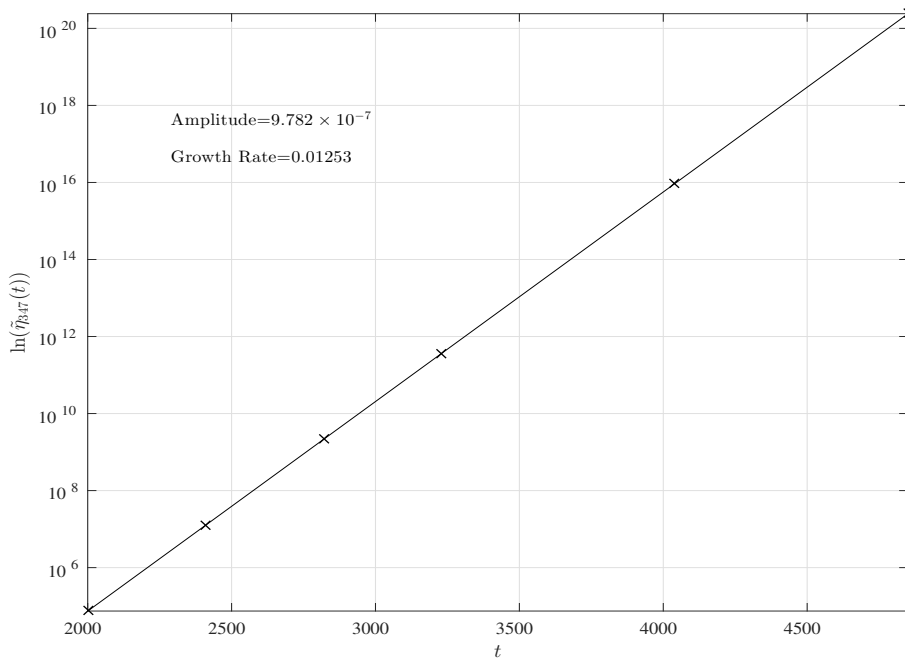


Figure 6.11: Logarithm of the wall height at the fixed streamwise location $x = 347$ plotted against time. The wall heights obtained from the DNS (\times) and the exponential curve of best fit ($—$) are plotted together to show that the growth is in fact exponential.

Note that the amplification factor A is not relevant, the important term is λ and the fact that it should be positive for exponential growth.

$\beta=0.01137$

Suppose now that the inflow disturbance frequency is reduced to $\beta = 0.01137$ and the compliant wall is shortened, in particular, it now extends from $x = 20$ to 200 in a domain of length 220. If the simulation is run for a long enough time, the wall displacement takes the general form shown in Figure 6.12. (Once again, the wall displacement axis has not been labelled since the wall takes this exact same form at different gq-periods as it grows exponentially.)

The instability in this case has a phase speed of 0.17 and grows temporally everywhere with an exponential growth rate 0.01156. The most dominant

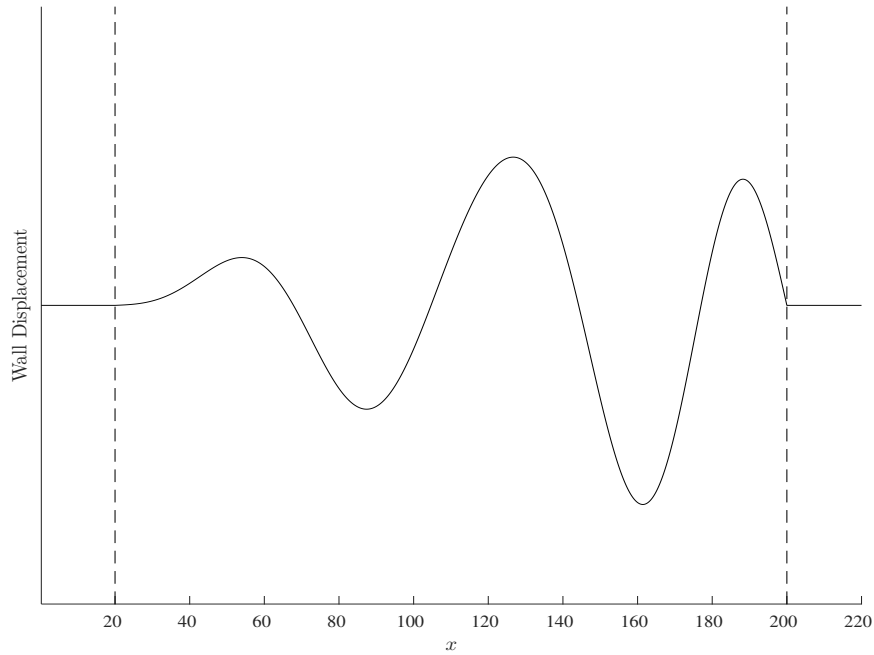


Figure 6.12: **STG1** with $\beta = 0.01137$, the vertical dashed lines denote the start and end of the compliant wall section. The instability has a phase speed 0.17 and an exponential growth rate 0.01156. The most dominant wavenumber is 0.08568 and the gq-period is 430.

wavenumber is 0.08568 and the gq-period τ is 430. All these results were extracted in exactly the same way as before. In this case, even though both the compliant length and the inflow frequency were reduced for the same wall parameters and the Reynolds number, similar values of the wavenumber, phase speed and growth rates were obtained.

Localised Impulsive Forcing

Consider the same flow configuration as when $\beta = 0.01137$ (a flow domain of length 220 with a compliant wall between $x = 20$ and 200) but is undisturbed at the inflow ($\varphi = 0$ at $x = 0$) and the excitation is triggered by a localised impulsive forcing. At the start of the simulation, the wall responds to the initial excitation but after some time, the wall displacement starts to take the general form shown in Figure 6.13.

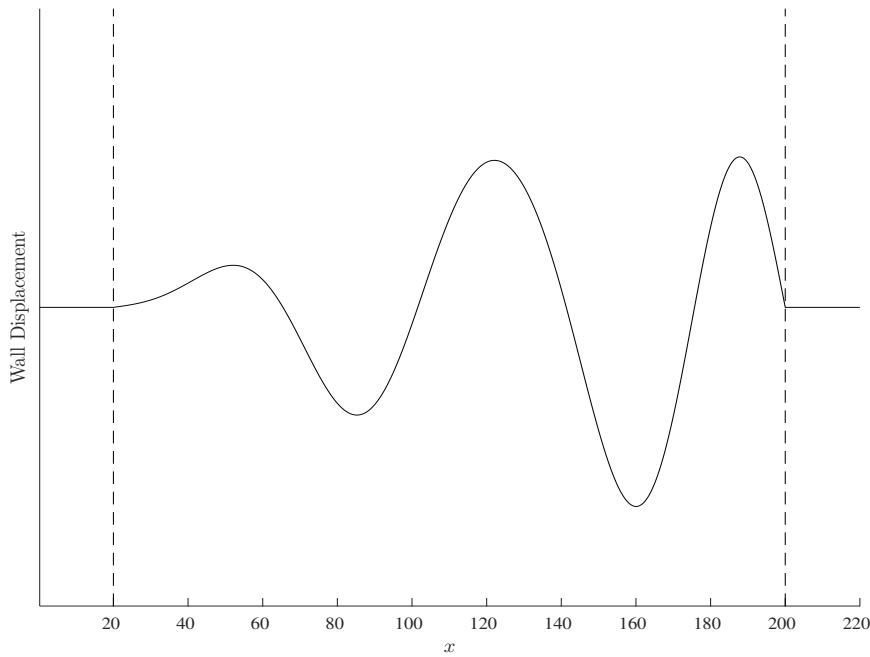


Figure 6.13: **STG1** with a localised impulse, the vertical dashed lines denote the start and end of the compliant wall section. The instability has a phase speed 0.1641 and an exponential growth rate 0.01155. The most dominant wavenumber is 0.08568 and the gq-period is 430.

The instability grows with an exponential growth rate 0.01155 and has a phase speed 0.1641, the most dominant wavenumber is 0.08568 and the gq-period τ is 430. Notice that the profile observed in Figure 6.13 appears to be strikingly similar to that in Figure 6.12 implying that the impulse and the inflow profile both act as triggers for the absolute instability.

Comparison Between the Different Simulations

Table 6.2 shows a summary of results extracted from the three different simulations. These include the magnitudes of the most dominant wavenumber $|\alpha_{DNS}|$, phase speed c_{DNS} , the exponential growth rate λ_{DNS} and the gq-period τ .

Method of Excitation	$ \alpha_{DNS} $	c_{DNS}	λ_{DNS}	τ
$\beta = 0.12$	0.08796	0.1736	0.01257	410
$\beta = 0.01137$	0.08568	0.17	0.01156	430
Impulse	0.08568	0.1641	0.01155	430

Table 6.2: Summary of results from the three different simulations.

Note that all the three simulations yield very similar results (the case when $\beta = 0.12$ is a little different due to the longer compliant wall length, but nevertheless, it is still quite reasonably close to the others). Therefore it seems that the chosen set of wall parameters, given by $n = 0$, and the Reynolds number $\text{Re} = 13200$ have a natural tendency to give an instability with a most dominant wavenumber $|\alpha| \approx 0.086$, a phase speed $c \approx 0.17$ which has an exponential temporal growth rate $\lambda \approx 0.119$. These results arise even when the wall length and the method of excitation are different. The growth of this particular disturbance is an indication of absolute instability due to an interaction between TS and divergence (as noted from the plots of the components of c against α and Re in Figures 6.2, 6.3, 6.6 and 6.7). Briggs' method will now be used to verify the fact that the instability is absolute.

Briggs' Method

Consider a fixed complex temporal frequency $\omega = \omega_r + i\omega_i$ ($\omega_r, \omega_i \in \mathbb{R}$). This corresponds to eigenvalues on the complex α -plane that are the result of solving the dispersion relation $\omega(\alpha) = 0$. Fixing ω_r and varying ω_i forms spatial branches on the complex α -plane and some of these branches form saddle points. If these branches originate from different half-spaces *and* the saddle point corresponds to a complex temporal frequency whose imaginary part is positive, then the instability is absolute.

Figure 6.14 shows the set of points that trace out two spatial branches formed by fixing $\omega_r = 0.0157$ (red) and 0.0158 (blue) while varying ω_i . A saddle point is formed at the wavenumber $\alpha = 0.0855 - 0.0121i$ (represented by a cross) which corresponds to a root of the dispersion relation $\omega = 0.01576 + 0.01301i$. This complex frequency has a positive imaginary part and the spatial branches originate from different half-spaces (as in Figure 6.14). Therefore according to Briggs' criterion, this implies that the disturbance grows to become an *absolute instability*. The results from Briggs' method are summarised thus (SP here denotes "saddle point"):

$$\begin{aligned}\alpha_{SP} &= 0.0855 - 0.0121i \\ \omega_{SP} &= 0.01576 + 0.01301i \\ c_{SP} &= \frac{\omega_{SP}}{\alpha_{SP}} = 0.1596 + 0.1747i.\end{aligned}\tag{6.5}$$

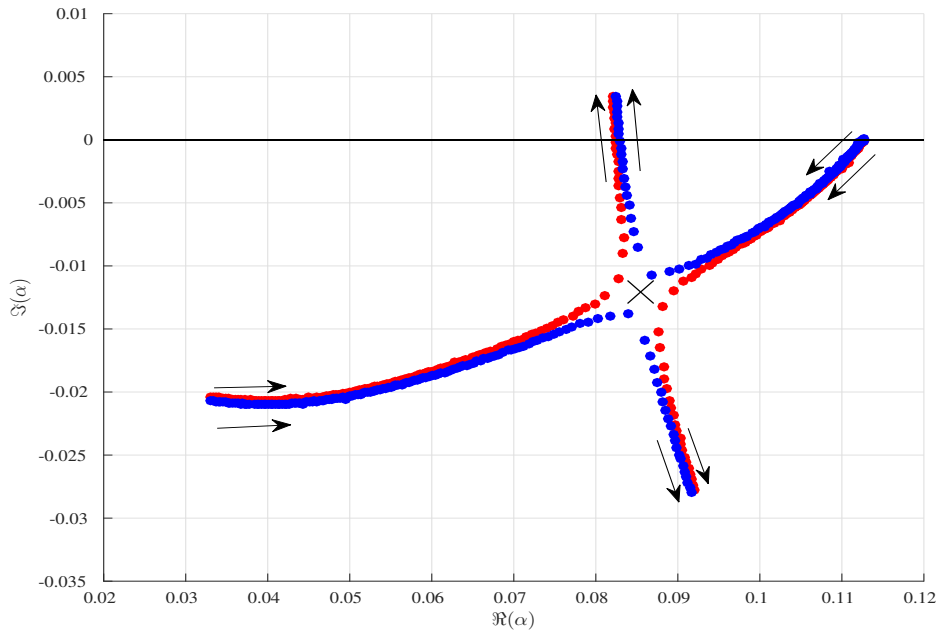


Figure 6.14: Saddle point formed at $\alpha = 0.0855 - 0.0121i$ (\times). These spatial branches are formed by varying $\Im(\omega)$ for fixed $\Re(\omega) = 0.0157$ (red) and 0.0158 (blue).

Comparison Between DNS & Briggs' Method

Table 6.3 shows a comparison between the results extracted from the three simulations and Briggs' method. These include the magnitude of the most dominant wavenumber $|\alpha|$, phase speed c and temporal growth rate λ (note that from the saddle point, the phase speed is $c = \Re(c_{SP})$ and the growth rate is $\lambda = \Im(\omega_{SP})$). From this table 6.3 it can be seen that Briggs' method can be used as a way to predict the wavenumbers, phase speeds and exponential growth rates of the absolute instability.

	$ \alpha $	c	λ
$\beta = 0.12$	0.08796	0.1736	0.01257
$\beta = 0.01137$	0.08568	0.17	0.01156
Impulse	0.08568	0.1641	0.01155
Briggs' method	0.08635	0.1596	0.01301

Table 6.3: Comparison between the results obtained from the three simulations of **STG1** and Briggs' method.

Another Saddle Point?

It is worth noting that this system has another saddle point but that does not mean it would manifest as an absolute instability. Indeed, Figure 6.15 shows a saddle point that is formed by taking the spatial branches for a fixed value of $\omega_r = 0.022299$ (blue) and 0.022301 (red) while varying ω_i . The saddle point is located at $\alpha = 0.1134 + 0.2381i$ which corresponds to a complex temporal frequency $\omega = 0.0223 + 0.004812i$. Even though the imaginary part of the frequency is positive, it does not correspond to an absolute instability since the two branches do *not* originate from different half-spaces. This explains why these parameters were not observed in any of the simulations.

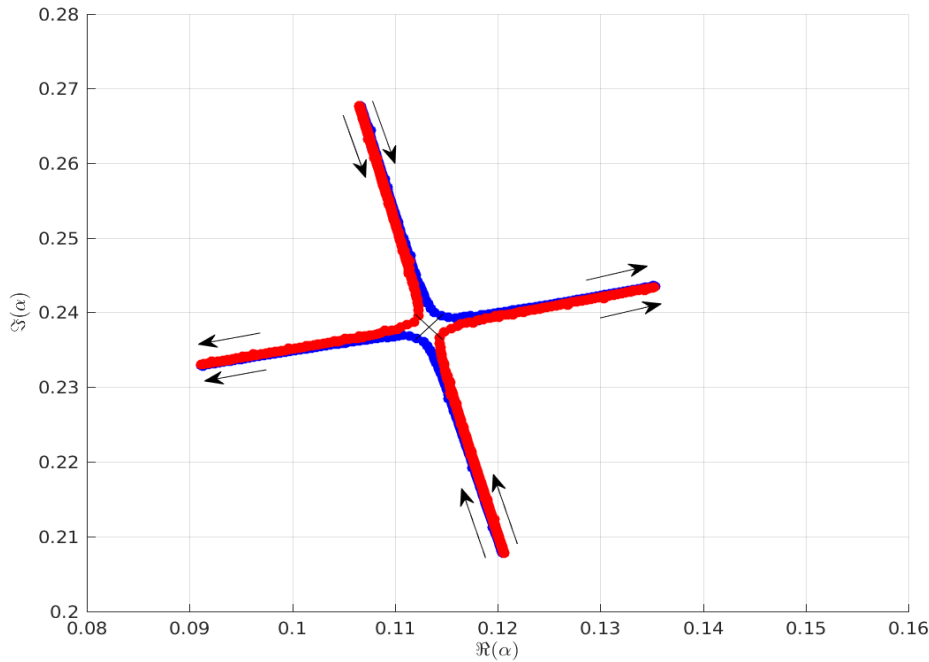


Figure 6.15: Saddle point formed at $\alpha = 0.1137 + 0.0238i$ (\times). These spatial branches are formed by varying $\Im(\omega)$ for fixed $\Re(\omega) = 0.022299$ (blue) and 0.022301 (red), however this saddle point does *not* correspond to an absolute instability since the branches do not originate from different half-spaces.

6.2.2 STG2

The fact that Briggs' method can be used to predict the wavenumbers, phase speeds and growth rates will now be exploited.

For this case, a different set of wall parameters is chosen, particularly the set given by $n = 1$. In order to obtain a potential candidate for the Reynolds number, the curves of c against α need to first be studied to find a location of interaction between the divergence and TS modes. Briggs' method can then be used to identify the saddle point that can be used to predict the parameters for the absolute instability. Finally, simulations are performed (similar to **STG1**) to confirm the predictions obtained from Briggs' method.

Candidate Reynolds Number for Absolute Instability

In order to obtain a value of the Reynolds number that leads to absolute instability for this set of wall parameters, consider the variation of c against α for fixed values of Re . Figures 6.16 and 6.17 show this variation for $Re = 10880$ and 10900 respectively.

In Figure 6.16, the two curves represent different instabilities: the divergence mode (red), which is unstable for values of α in $I_d = [0.054, 0.122]$, and the TS mode (blue), which is unstable in $I_T = [0.772, 1.087]$. These two modes interact at $\alpha = 0.1225$ to give a phase speed $c = 0.126 - 0.025i$ (circled). (Note that the TWF mode has not been shown here since it plays no part.)

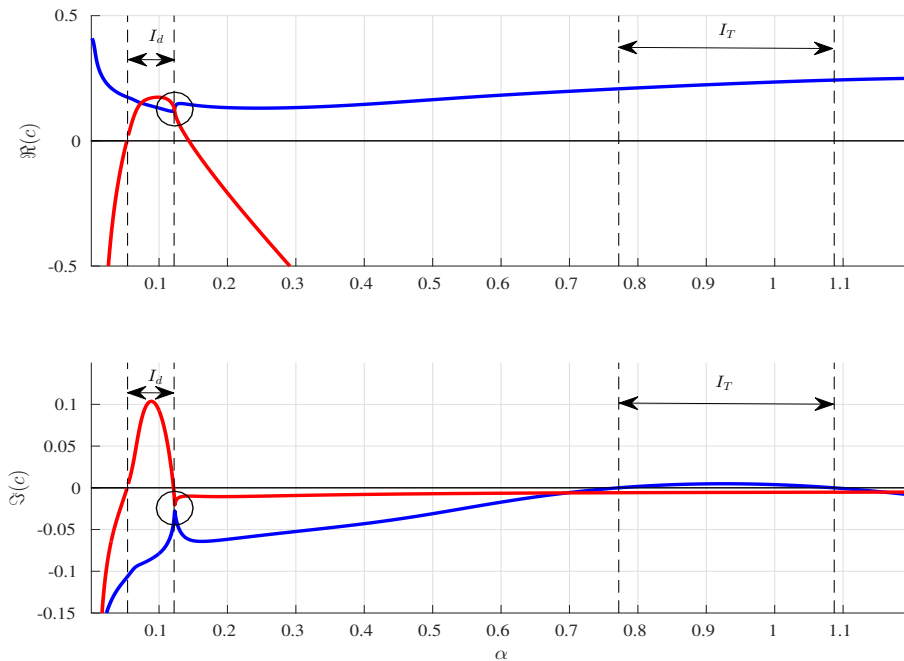


Figure 6.16: Components of c against α for a fixed $Re = 10880$. The two lines represent the TS (blue) and divergence (red) modes. The labelled wavenumber intervals show where TS and divergence are destabilised (I_T and I_d respectively). Around $\alpha = 0.1225$ (circled), the divergence and TS modes start to interact at $c = 0.126 - 0.025i$.

Increasing the Reynolds number to 10900, as in Figure 6.17, shows a distinct interaction between the two modes (the exact same phenomenon that

was observed in Figures 6.2 and 6.3 in **STG1**). This interaction between the divergence and TS modes results in a mode (red) that destabilises the flow for values of α in two separate wavenumber intervals $\tilde{I}_d = [0.053, 0.122]$ and $\tilde{I}_T = [0.772, 1.087]$ while the other mode (blue) is stable throughout. Therefore $Re = 10890$ can be a possible candidate for the Reynolds number that results in an absolute instability^{III}.

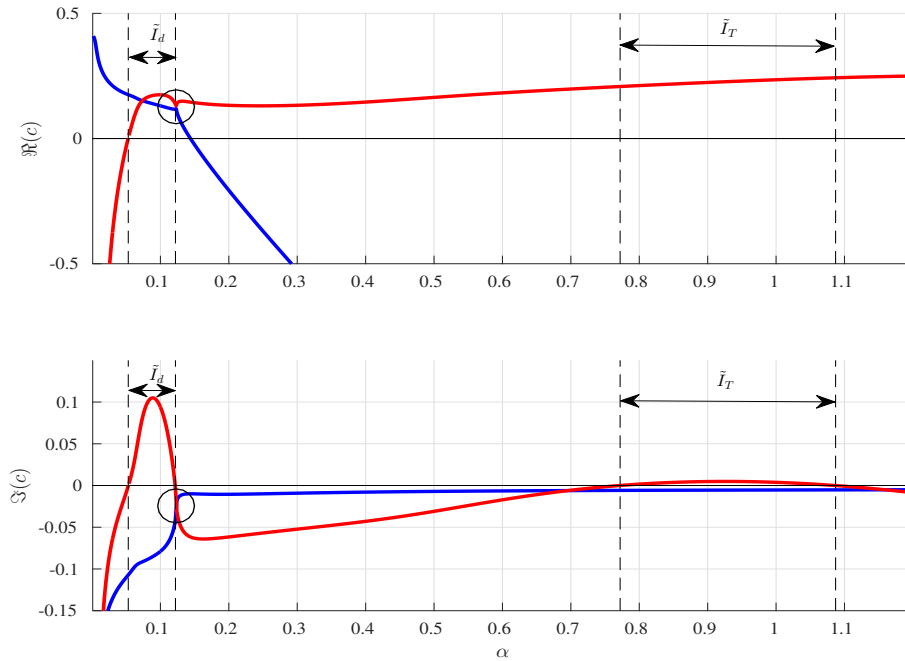


Figure 6.17: Similar to Figure 6.16 but for $Re = 10900$. The divergence and TS modes interact at $\alpha = 0.1225$ (circled) resulting in a mode (red) that destabilises the flow at the two intervals labelled \tilde{I}_T and \tilde{I}_d .

Prediction: Briggs' Method

Figure 6.18 shows the set of points that trace out two spatial branches on the complex α -plane obtained by fixing the real part of the complex frequency to 0.0167 (red) and 0.0169 (blue) and varying its imaginary part. These spatial branches originate from different half-spaces and form a saddle point at $\alpha = 0.099 - 0.01i$ (cross) which corresponds to a root of the dispersion relation

^{III}The variation of α against Re was also used to corroborate that this is indeed a suitable choice of Re .

$\omega = 0.01686 + 0.008644i$. Therefore Briggs' method gives the following results:

$$\alpha_{SP} = 0.099 - 0.01i$$

$$\omega_{SP} = 0.01686 + 0.008644i$$

$$c_{SP} = 0.1599 + 0.1035i.$$

Since $\Im(\omega)$ is positive and the branches originate from different half-spaces, this implies that the disturbance forms an absolute instability. If a DNS is performed, then Briggs' method can provide the following predictions for the most dominant wavenumber, phase speed and temporal growth rate as follows:

$$|\alpha| = 0.0995 \tag{6.6}$$

$$c = \Re(c_{SP}) = 0.1599 \tag{6.7}$$

$$\lambda = \Im(\omega_{SP}) = 0.008644. \tag{6.8}$$

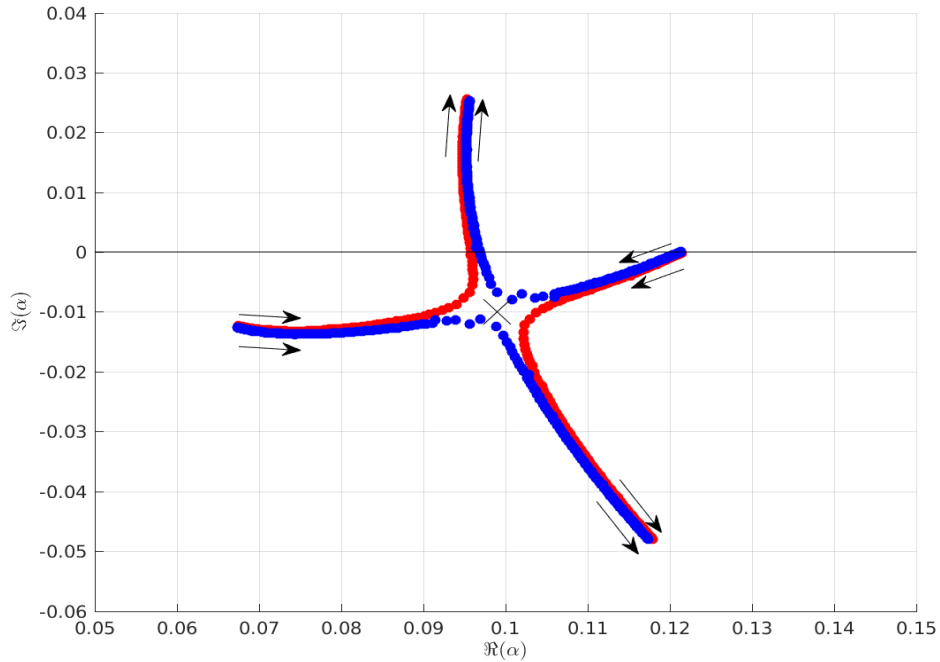


Figure 6.18: Saddle point formed at $\alpha = 0.099 - 0.01i$ (\times). These spatial branches are formed by varying $\Im(\omega)$ for fixed $\Re(\omega) = 0.0167$ (red) and 0.0169 (blue).

Verifying the Predication: DNS

Consider a domain of length 350 with a compliant wall between $x = 20$ and 320 in a flow with $\text{Re} = 10890$. Just as in **STG1**, three simulations are conducted which are excited in three different ways; an impulse excitation and two inflow profiles with $\beta = 0.12$ and $\beta = 0.01476$.

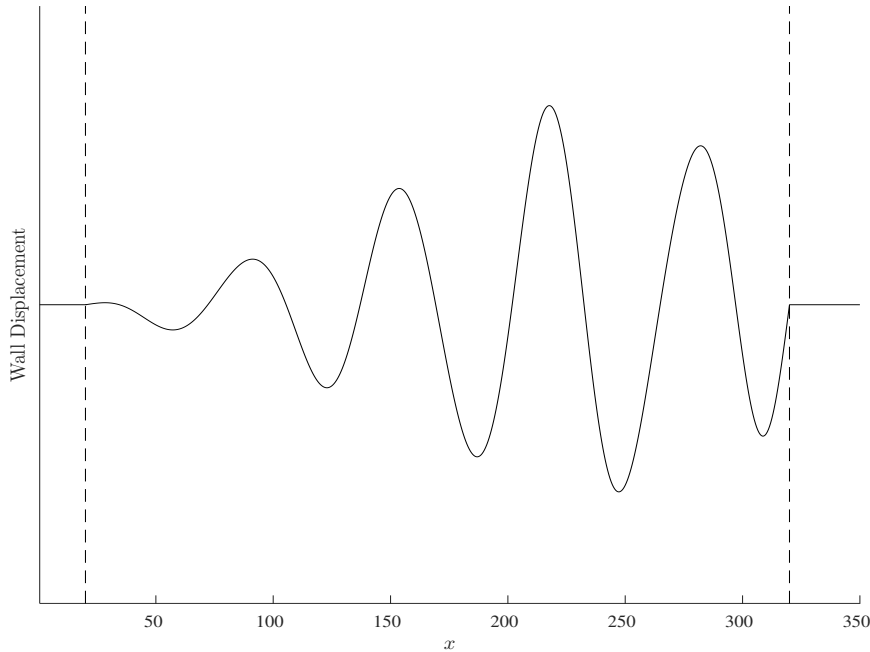


Figure 6.19: General form of **STG2** for $\beta = 0.12, 0.01476$ and the impulse excitation (the vertical dashed lines denote the start and end of the compliant wall section). The crests/troughs travel downstream with a speed c , the magnitude of the most dominant wavenumber is $|\alpha|$ and the instability grows with an exponential growth rate λ , all these are given in Table 6.4. The same general form is displayed for all three different excitations.

After enough time has passed -to allow the transients to subside- the wall displacement in all three cases takes the general form shown in Figure 6.19 (notice that the wall displacement axis has not been labelled since it has an associated gq-period τ just as in **STG1**). The resulting instability has a phase speed c and grows temporally everywhere with an exponential growth rate λ . The magnitude of the most dominant wavenumber α can be isolated by

applying a FFT on the wall displacements. All this information from the three simulations is shown in Table 6.4 along with the predictions made from Briggs' method.

	$ \alpha $	c	λ	τ
$\beta = 0.12$	0.09875	0.1649	0.00785	380
$\beta = 0.01476$	0.09873	0.1675	0.00786	380
Impulse	0.09873	0.1649	0.00785	380
Briggs' method	0.0995	0.1599	0.008644	-

Table 6.4: Comparison between the three **STG2** simulations along with the predictions made from Briggs' method given in (6.6).

From the DNS results, it can be seen that the choice of wall parameters and Reynolds number have a tendency to produce very similar phase speeds, wavenumbers and growth rates regardless of how the flow has been excited. The saddle point also gives very similar results to those obtained from the DNS suggesting that Briggs' method is a reliable way to predict the onset of an absolute instability which is a result of an interaction between the TS and divergence modes and gives parameters that are similar to those obtained from the DNS.

Notice that the in both **STG1** and **STG2**, there has been a slight discrepancy between the predicted values from the saddle point and those obtained from the DNS. This is because the eigenvalues on the complex α and ω -planes have been determined under the assumption that the compliant wall is infinitely long. Even with this hindrance, the predictions are still very good.

6.2.3 Summary of STG

Choice of Reynolds Number for Absolute Instability

Consider a fixed set of wall parameters and Reynolds number Re_0 . The choice of Re_0 should be such that if the components of the phase speed c are plotted against the wavenumber α for fixed Reynolds numbers $\text{Re} = \text{Re}_0 - \delta\text{Re}$ and $\text{Re}_0 + \delta\text{Re}$ (for some $\delta\text{Re} \ll \text{Re}_0$), then there will be an interaction between the TS and divergence modes for values of α close to the unstable region of the divergence mode. More precisely, if the components of c were to be plotted against α for $\text{Re}_0 - \delta\text{Re}$, then there should be two modes that destabilise the flow, divergence at a range of small wavenumbers I_d and TS at a range of higher wavenumbers I_T (for example, see Figures 6.2 and 6.16). The two modes interact at a location near the higher end of I_d (as denoted by the circles in Figures 6.2 and 6.16). When the Reynolds number is increased to $\text{Re}_0 + \delta\text{Re}$, the divergence and TS modes would interact to form two new modes, one of them is stable for all the values of Re while the other destabilises the flow at \tilde{I}_d and \tilde{I}_T (which are the modified intervals I_d and I_T respectively as seen in Figures 6.3 and 6.17). Denote the wavenumber at the location of the interaction by $\tilde{\alpha}$ and the phase speed by $\tilde{c} \in \mathbb{C}$ (i.e. the location of the circle in Figures 6.2, 6.3, 6.16 and 6.17).

Prediction of the Wavenumbers, Phase Speeds & Growth Rates

In order to use Briggs' method to obtain predictions for the absolute instability, consider the values of a complex temporal frequency near $\tilde{\omega} = \tilde{\alpha}\tilde{c}$. Fixing $\Re(\tilde{\omega})$ and varying $\Im(\tilde{\omega})$ traces out spatial branches on the complex α -plane to form a saddle point α^* (as denoted by the crosses on Figures 6.14 and 6.18). This point corresponds to a root of the dispersion relation located at

ω^* on the complex ω -plane. If $\Im(\omega^*) > 0$ and the spatial branches originate from different half-spaces, then the disturbance would grow to form an *absolute instability*. Therefore predictions for absolute instability from the saddle point are:

- * Most dominant wavenumber: $|\alpha^*|$
- * Exponential temporal growth rate: $\Im(\omega^*)$
- * Phase speed: $\Re(\frac{\omega^*}{\alpha^*})$.

DNS

For the DNS, a simulation can be performed for $\text{Re} = \text{Re}_0$ prescribed earlier and the disturbance can be excited by either an inflow profile or a localised impulsive forcing^{IV}.

The simulations have to be run for a long enough time in order to allow any transients to subside. The disturbance causes the wall displacement to take the form of a spatially growing instability with a positive phase speed, the wave has an associated gq-period and an exponential growth rate as well (just as in Figures 6.12, 6.10, 6.13 and 6.19). The following information can be extracted from the DNS:

- * Exponential growth rate: λ
- * Most dominant wavenumber: $|\hat{\alpha}|$
- * GQ-period: τ
- * Downstream speed: \hat{c} .

^{IV}From **STG1** and **STG2**, it was seen that the different methods of exciting the disturbance yielded similar results. To this end, an impulse excitation may be more appropriate in disturbing the flow since it is analogous to a background disturbance that triggers the absolute instability. Additionally, no inflow frequency has to be assigned. The near-field effects that arise due to this excitation will be irrelevant since they are overwhelmed by the absolute instability.

The predictions made from Briggs' method can be compared to the information extracted from the DNS as follows:

$$\begin{aligned}\lambda &\approx \Im(\omega^*) \\ \hat{c} &\approx \Re\left(\frac{\omega^*}{\alpha^*}\right) \\ |\hat{\alpha}| &\approx |\alpha^*| \subseteq \tilde{I}_d.\end{aligned}$$

Briggs' method has proved vital in predicting the onset of an absolute instability for **STG** when the divergence and TS modes interact.

6.3 TG: Temporal Growth

In this section, a more interesting phenomenon is presented with regards to the growth of *global* instabilities. In **STG**, the absolute instability evolved spatially and temporally with an associated gq-period and an exponential growth rate. In the cases to follow, the global instability takes the form of a *static* wave that grows temporally with an exponential growth rate (i.e. the wall displacement profile takes the form $e^{T(t)} \sin(X(x))$ for some functions T and X where t is the after which all transients have dissipated and x is the streamwise location in the compliant wall).

First, a set of wall and flow parameters is chosen and the variation of the phase speed c against α is investigated. Once a viable candidate for the Reynolds number is found, simulations are performed where the flow is excited by means of a localised impulsive force. Afterwards, modifications to the flow configuration are made in order to investigate their individual effects on the instability.

6.3.1 TG

Consider the set of wall parameters given by $n = 1$ in Table 6.1. The variation of $\Re(c)$ and $\Im(c)$ should first be used to locate possible interesting flow parameter choices and then simulations can be performed.

c - α Curves

Consider the components of the phase speed c against the wavenumber α for a fixed Reynolds number $\text{Re} = 10000$ as shown in Figure 6.20. The three lines indicate different modes: TS (blue), divergence (red) and TWF (green). The TS mode is unstable for values of α in the $I_T = [0.793, 1.091]$ while the divergence mode is unstable in $I_d = [0.06, 0.11]$ (the TWF mode is stable everywhere and does not play a role here).

At $\alpha = 0.093$ (indicated by a dotted vertical line), the real parts of the curves representing the TS and divergence modes “collide” to give a phase speed whose real part is 0.1235 (as denoted by the circle), the divergence growth rate (given by imaginary part) at that this particular value of α is 0.03129.

If the value of the Reynolds number is increased to 10500, the lines representing the real parts of the divergence and TS modes cross over but *do not* interact in the same way seen earlier in *STG* (see for example Figures 6.3 and 6.17). With this increase in the value of Re , the maximum growth rate of divergence more than doubles while that of TS remains relatively unchanged. In this case, the Reynolds $\text{Re} = 10000$ can be chosen as a candidate for the absolute instability.

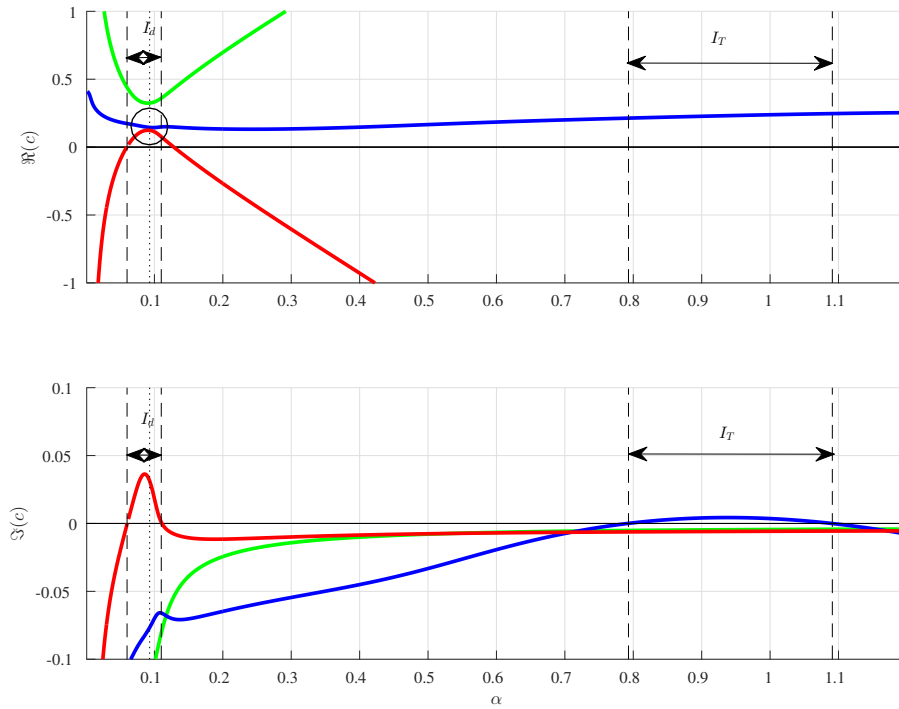


Figure 6.20: Components of c against α for a fixed $\text{Re} = 10000$. The three lines represent the TS (blue), divergence (red) and TWF (green) modes. The labelled wavenumber intervals show where TS and divergence are destabilised (I_T and I_d respectively). Around $\alpha = 0.093$ (denoted by the vertical dotted line), the divergence and TS modes start to “collide”.

DNS

Consider a flow domain of length 150 with the compliant wall section extending from $x = 44$ to 116 in a flow with $\text{Re} = 10000$. The flow is disturbed by means of a localised impulsive forcing in the middle of the compliant wall in order to eliminate the need for introducing an inflow disturbance frequency. At the start of the simulation, the wall will respond to the initial excitation but after the transients effects have subsided, the wall displacement starts to settle down and take the form of a static, non-oscillating wave that grows temporally everywhere. The general form of the wall displacement is given in Figure 6.22 and the wall takes this same form for *all* subsequent times *and* keeps growing temporally everywhere with *no* spatial oscillation. Therefore, the instability

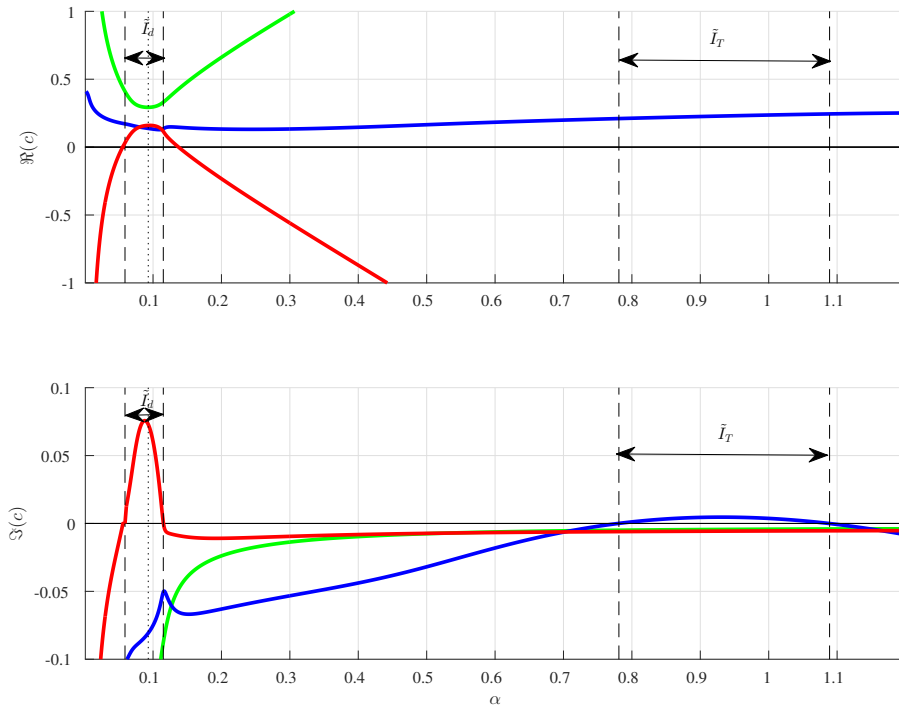


Figure 6.21: Similar to Figure 6.20 but with $\text{Re} = 10500$. The lines representing the real parts of TS and divergence have crossed over without displaying the same interaction behaviour seen in **STG**.

in this case has zero phase speed and zero group velocity. The wavenumber spectrum shows a range of values around a single peak as shown in Figure 6.23.

In order to visualise this better, the wall displacements at different times have been superimposed on top of one another in Figure 6.24. The wall heights are plotted from $t = 2500$ to 3140 in increments of 80 with the arrows showing the direction of growth. From this, it can be hypothesised that the instability's temporal growth rate is exponential (as expected).

Figure 6.25 shows the logarithm of the crest's height obtained from the DNS (located at $x = 74$ and is denoted by a series of crosses) plotted against time in order to determine the exponential growth rate which is denoted λ . From this, it can be deduced that the height of the crest grows exponentially

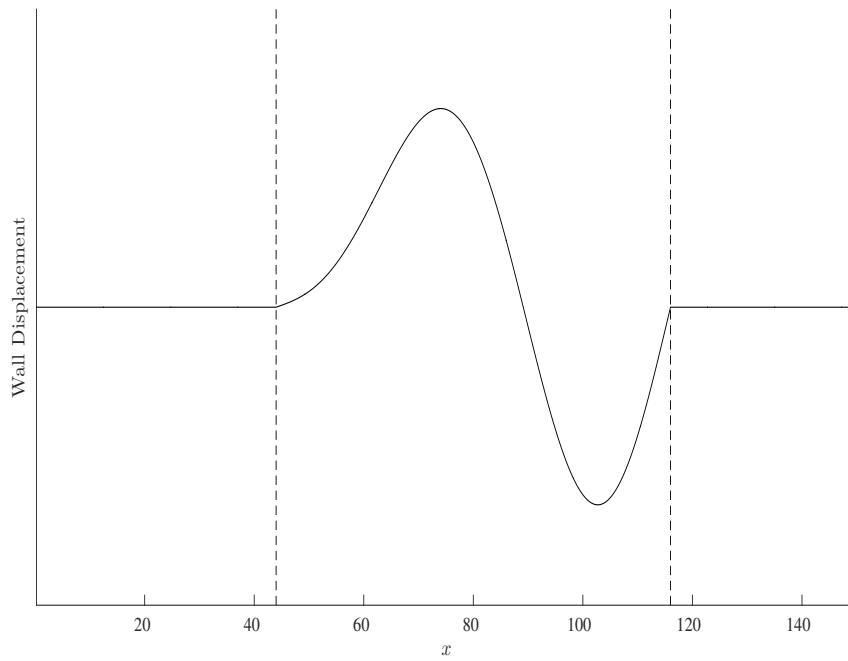


Figure 6.22: General form of the wall displacement for **TG**. The vertical dashed lines denote the start and end of the compliant wall section.

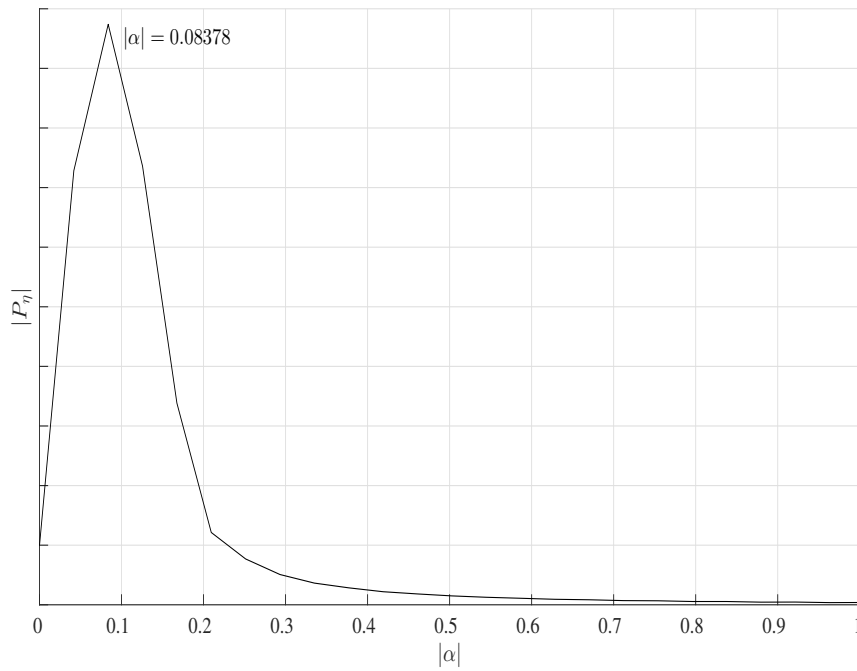


Figure 6.23: Fourier spectrum of the wall displacement shown in Figure 6.22. The spectrum shows range of values that peak at $|\alpha| = 0.08378$.

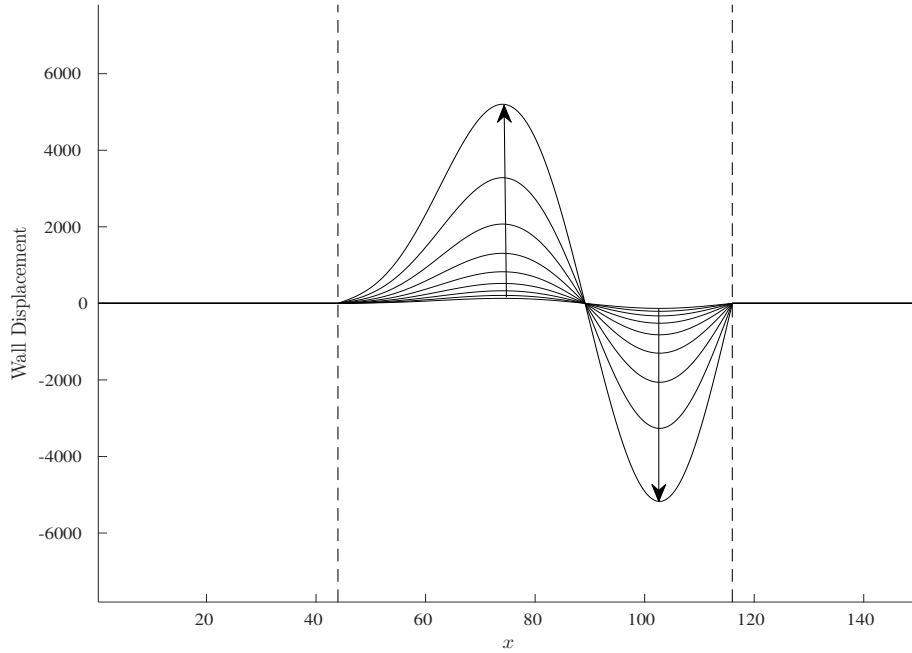


Figure 6.24: Plot of the wall displacements for the times $t = 2500$ to 3140 in increments of 80 . This is shown in order to illustrate the exponential growth rate of the instability as indicated by the arrows.

with time as $\sim e^{\lambda t}$ where $\lambda = 5.752 \times 10^{-3}$. The line $\tilde{\eta}_{74}(t)$ (which is the height of the wall at $x = 74$) given by

$$\tilde{\eta}_{74}(t) = Ae^{\lambda t}$$

$$\text{where } A = 7.443 \times 10^{-5} \quad \text{and} \quad \lambda = 5.752 \times 10^{-3}$$

which represents the approximated wall height at $x = 74$ (once again, the value of A is not relevant in this context, only λ). This is plotted in Figure 6.25 (line) and it fits all the data point obtained from the DNS.

In summary, it seems that this combination of the Reynolds number, wall length and end conditions have lead to a perfect balance to allow the disturbance to develop into a static, non-oscillating, temporally growing global instability with an exponential growth rate of 5.75×10^{-3} and a wavenum-

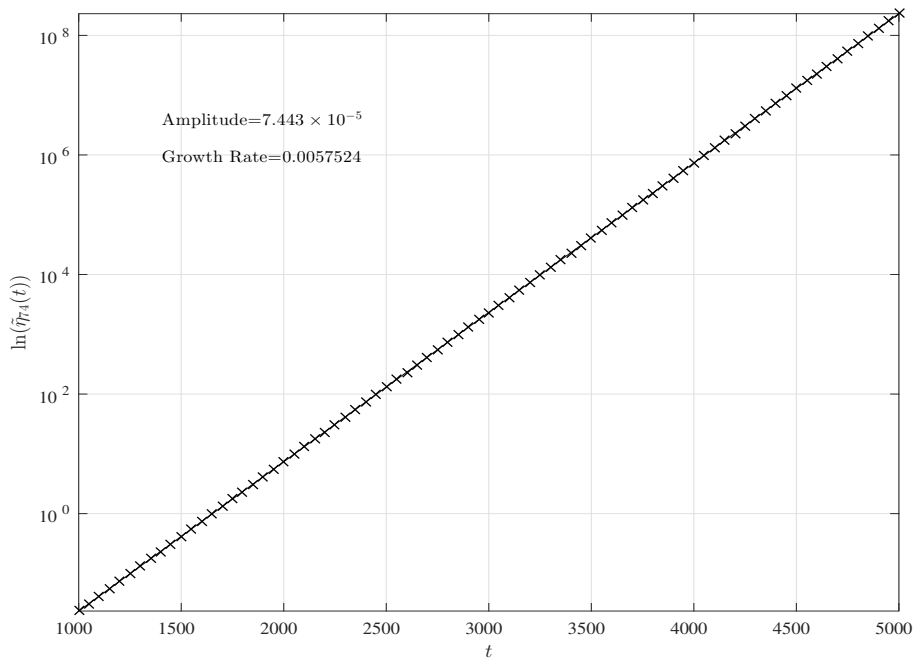


Figure 6.25: Logarithm of the crest’s height (at $x = 74$) plotted against time. The wall heights obtained from the DNS (\times) and the exponential curve of best fit ($—$) are plotted together to show that the growth is in fact exponential.

ber 0.08378. If any one of these factors is changed, then the same behaviour might not be observed. These characteristics suggest that the instability is reminiscent of the *divergence* mode at onset, this is because it takes the form of a long wavelength static wave forming “nodes” and “anti-nodes” as it grows temporally everywhere. It should be made very clear that the instability is *not* a typical standing wave since the peaks do not oscillate, they only keep growing temporally.

Briggs’ Method

In this subsection, Briggs’ method is used to see whether it can be used as a predictor for the growth rates, wavenumbers and phase speeds just as in **STG**. Pre-emptively, it may be hypothesised that Briggs’ method may not be the best way to make these predictions. This is because the static development of the global instability is sensitive to changes in wall length (as will become

apparent in §6.4.2) and this is not captured by Briggs' method since it is based on the procedure which does not take wall lengths into account.

Figure 6.26 shows two spatial branches on the complex α -plane that are formed by fixing the real part of the temporal frequency to 0.01115 (blue) and 0.01135 (red) and varying its imaginary part. These branches originate from different half-spaces and form a saddle point at $\alpha = 0.09304 - 0.004296i$ (cross) which corresponds to the root of the dispersion relation $\omega = 0.01128 + 2.762 \times 10^{-3}i$.

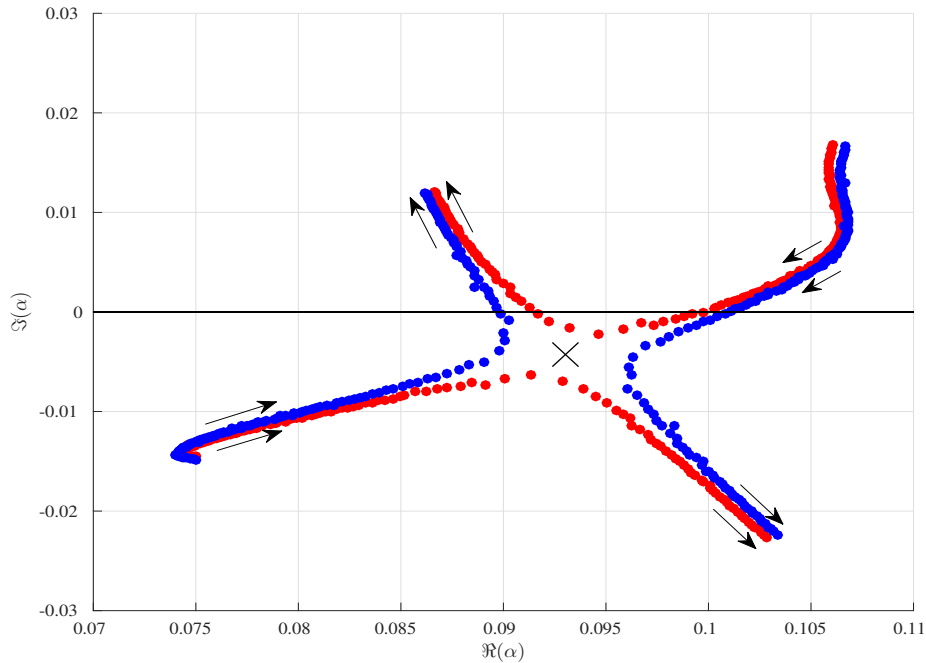


Figure 6.26: Saddle point formed around $\alpha = 0.09304 - 4.296 \times 10^{-3}i$ (\times). These spatial branches are formed by varying $\Im(\omega)$ for fixed $\Re(\omega) = 0.01115$ (blue) and 0.01135 (red).

Table 6.5 shows the relevant information extracted from the simulations and Briggs' method. The results from the DNS and the saddle point do not match and the main reason for that could be the fact that the procedure used for Briggs' method does not take wall lengths or edge effects into account. Notice that, $\Im(\omega)$ is *positive* and the branches originate from different half-

spaces implying that the instability is absolute which matches up with the findings of the DNS. However the error between the two is significantly greater than those seen in **STG**.

	DNS	Briggs' Method
Wavenumber $ \alpha $	0.08378	0.09314
Growth Rate λ or $\Im(\omega)$	5.75×10^{-3}	2.762×10^{-3}

Table 6.5: Comparison between the three **STG2** simulations along with the predictions made from Briggs' method given in (6.6).

This indicates that Briggs' method could predict the general behaviour of the instability (i.e. absolute) but not the parameters that make up the instability. Additionally, Briggs' method gives no indication that the wall displacement forms a static global instability (i.e. zero phase speed).

To this end, another approach has to be employed to verify the growth rates and can then be used as a method for predicting them, in this case, *two-dimensional global mode computations* are used. This method was devised by *Dr. M. J. Blount* and is used to corroborate growth rates for the statically growing global instabilities since it takes wall lengths into account. Before the two-dimensional global mode computations are conducted, some modifications to **TG** are first be made and this includes changing the compliant wall length, mass, damping coefficient and the Reynolds number. This is done in order to see what effects they have on the growth rates then later in §6.5, the DNS results are compared to the two-dimensional global mode computations.

6.4 Modifications to TG

In this section, the flow configuration in **TG** will be modified by changing one factor. These modifications will be labelled thusly:

- **TGE**: End conditions
- **TGL**: Length of the compliant wall section
- **TGR**: Reynolds number
- **TGC**: Combination of factors
- **TGM**: Mass of the compliant wall
- **TGD**: Damping coefficient.

The growth rates obtained from these different cases are then compared to the growth rates obtained from the two-dimensional global mode computations in §6.5.

6.4.1 TGE: End Conditions

Suppose that the compliant wall section is now *clamped* at the ends instead of being hinged while keeping all the other factors the same. After the initial excitation, the wall settles down to take the general form shown in Figure 6.27. The instability in this case has *negative* velocity and an associated gq-period of $\tau = 1270$. It is interesting to note that the instability *decays* temporally everywhere with an exponential decay rate of $\lambda = -1.279 \times 10^{-3}$ and has a velocity of -0.04356 (i.e. the crests/troughs of the wave travels backwards). This is shown in Figure 6.27 where the wall displacement is plotted at consecutive periods and the arrows denote the instability's exponential decay (the vertical dashed lines represent the positions of the start and end of the compliant wall section which are the same as in **TG**).

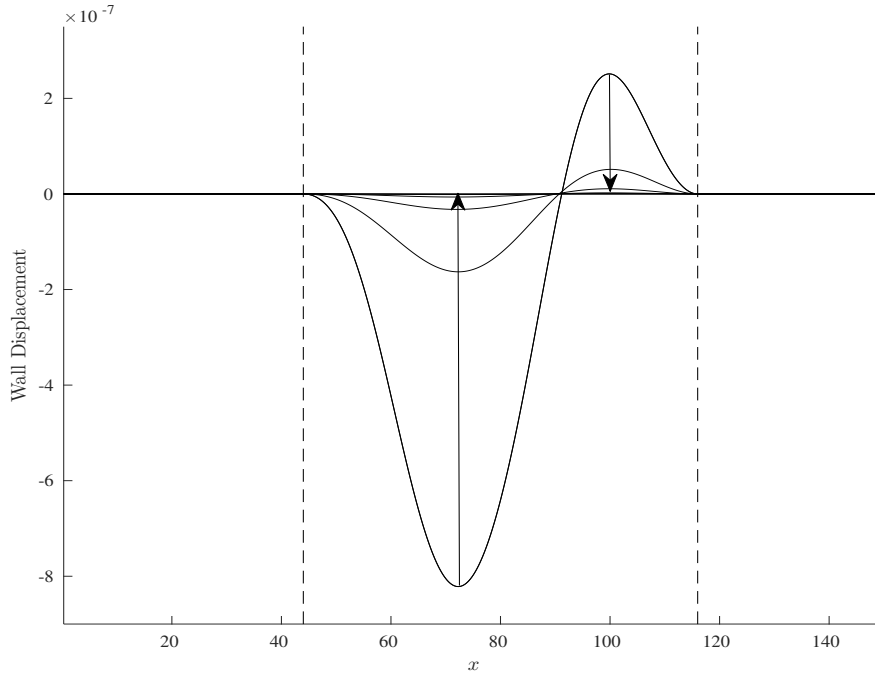


Figure 6.27: General form of the wall displacement when the wall is clamped at the ends, the wave is plotted at consecutive gq -periods and the arrows show the exponential decay. The vertical dashed lines represent the start and end of the compliant wall section.

Imposing the clamping condition makes the compliant wall effectively stiffer thus causing the delicate balance that gives rise to the static wave (as seen in **TG**) to break resulting in an instability that decays and has a non-zero group velocity. These claims can be difficult to corroborate using the solutions of the Orr-Sommerfeld equation since it was based on a compliant wall of infinite length. Nevertheless, it is still interesting to see the effect of changing only the end condition on the development of the instability.

6.4.2 TGL: Compliant Wall Length

In the cases presented earlier, **TG** and **TGE**, the compliant wall length L was fixed to be 72. If the length L is changed, then the wall displacement will behave differently.

$L > 72$

First, consider a compliant wall section of length $L = 144$ while all other factors are kept the same. Naïvely, it might be expected that the instability should take the form of two wavelengths (more particularly, the Fourier spectrum should show a range of values that peak at a single point just as in Figure 6.23). The wave would be expected to be a global instability that is static, non-oscillating and temporally growing everywhere since the wall is twice as long, but such is not the case. Instead, the instability that arises has a speed $c = 0.08965$ and grows exponentially with a temporal growth rate $\lambda = 2.819 \times 10^{-3}$ and has an associated gq-period of $\tau = 900$.

The simulation was also repeated for compliant walls of lengths greater than 72. In general, increasing the length of the wall section results in a global instability with a positive phase speed and an exponential growth rate which is less than that of **TG**. Some of these results are shown in Table 6.6.

 $L < 72$

Consider a compliant wall of length $L = 36$. In this case, the wall displacement takes the form of half a wavelength that is static and non-oscillating as shown in Figure 6.28. The instability grows temporally everywhere with an exponential growth rate $\lambda = 0.01013$ which is almost twice that of **TG**. Simulations were also performed for compliant walls of lengths less than 72 and in general, reducing the wall length increases the exponential growth rate while still retaining the static nature of the instability. However, reducing the wall length too much (below 33) causes the wall to respond to the initial excitation then decay completely.

Exponential growth rates and phase speeds from the DNS for different

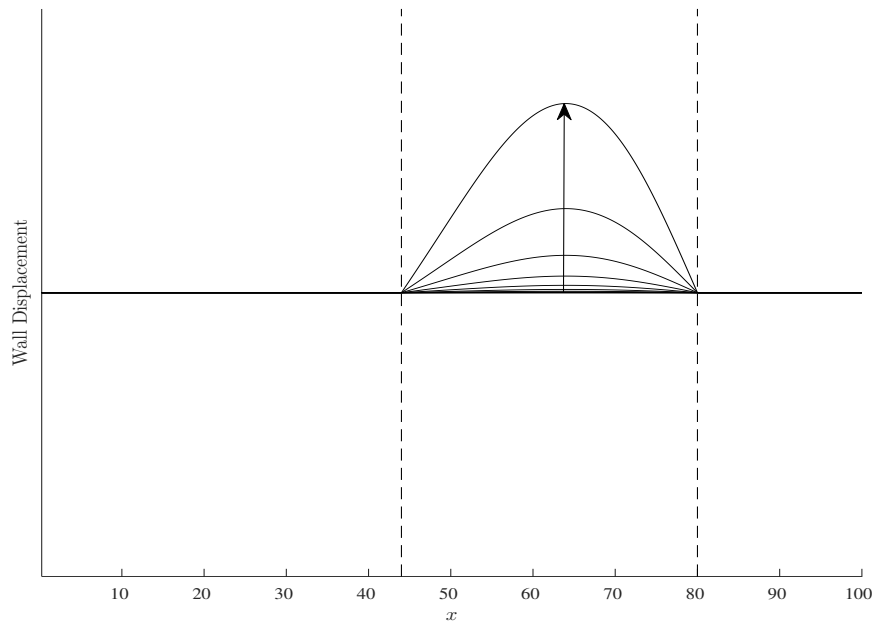


Figure 6.28: Wall displacement plotted at several times when the wall length 36.

compliant wall lengths are shown in Table 6.6. It seems that increasing the wall length significantly above 72 breaks the delicate balance that gives rise to the static wave and results in an instability with a positive group velocity and a reduced growth rate. However reducing the length of the compliant wall section can allow the instability to retain its static, non-oscillating nature while increasing its growth rate. The general effect of changing the wall length is investigated further by using the two-dimensional global mode computations later in §6.5.

L	λ	c
33	1.07×10^{-2}	0
36	1.013×10^{-2}	0
54	2.954×10^{-3}	0
72	5.752×10^{-3}	0
100	9.651×10^{-4}	0.03165
108	3.301×10^{-3}	0.06142
144	2.844×10^{-3}	0.08965

Table 6.6: Growth rates λ and phase speeds c for different wall lengths L .

From this table, it can be hypothesised that for long walls, the finite end effects play a major role in destabilising the flow but for shorter walls, the resonance effects are the most dominant suggesting that different destabilising mechanisms are at play.

6.4.3 TGR: Reynolds Number

Suppose that the Reynolds number is increased to $Re = 11000$ while keeping all other factors the same. The instability that results has a phase speed $c = 0.0848$ and grows with an exponential growth rate of $\lambda = 0.007926$. Increasing the Reynolds number can be thought of as effectively reducing the viscosity of the flow hence causing an increased growth rate but this also causes the instability to have a positive speed as well.

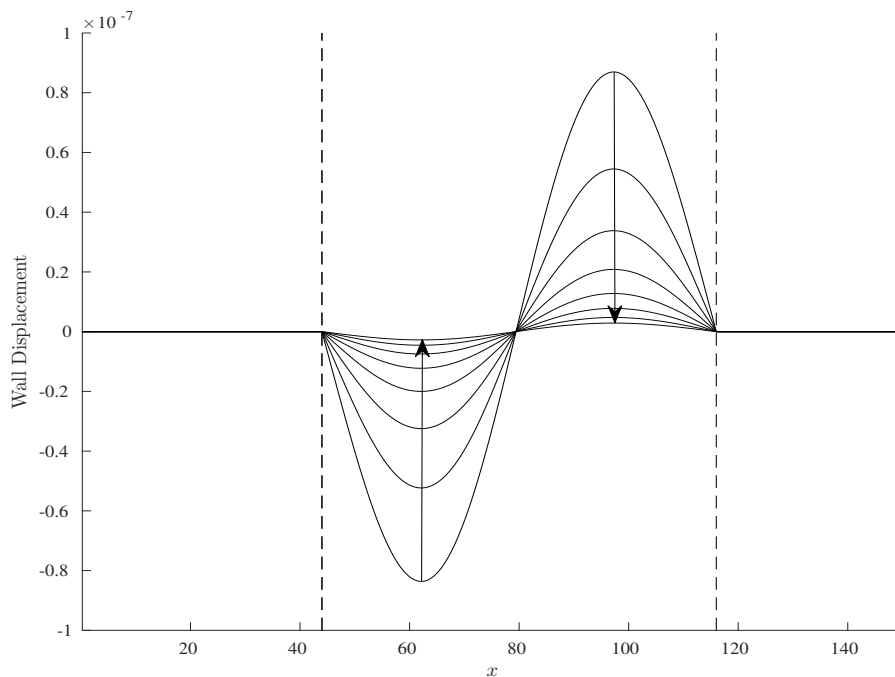


Figure 6.29: Wall displacement plotted at evenly spaced times for **TGR**, the arrows indicate the exponential decay.

On the other hand, reducing the Reynolds number down to $Re = 8900$ gives

a wall displacement that looks very similar to **TG** (as in Figure 6.22) but in this case, the wave takes the form of a static wave that *decays* temporally everywhere. Figure 6.29 shows the wall displacements plotted at different times to show the exponential rate of decay (depicted by the arrows) which is $\lambda = -0.001274$. Therefore, reducing the Reynolds number can be thought of as effectively increasing the fluid viscosity which has a stabilising effect on the development of the wall displacement.

6.4.4 TGC: A Combination of Factors

The cases presented in **TGL** and **TGR** show how delicate the static growth of the divergence instability at onset can be when the wall lengths and Reynolds numbers are changed. Changing any of these factors can cause the global instability to have a non-zero speed or result in temporal decay. With this in mind, it can be hypothesised that if several factors were changed appropriately, then the static temporally growing instability can be recovered. Indeed, suppose that the compliant wall section is made longer, extending from $x = 20$ to 200, and the Reynolds number is reduced to $\text{Re} = 8900$. In this case, the wall displacement takes the form shown in Figure 6.30.

The global instability forms a static, non-oscillating temporally growing wave with the exponential growth rate $\lambda = 6.086 \times 10^{-4}$ and consists of $2\frac{1}{2}$ wavelengths (in other words, the wave consists of 6 “nodes” and 5 “anti-nodes”). Therefore, this indicates that if several appropriate changes are made to the flow configuration, then the static exponentially growing global instability can be recovered even though the individual changes do not preserve this property.

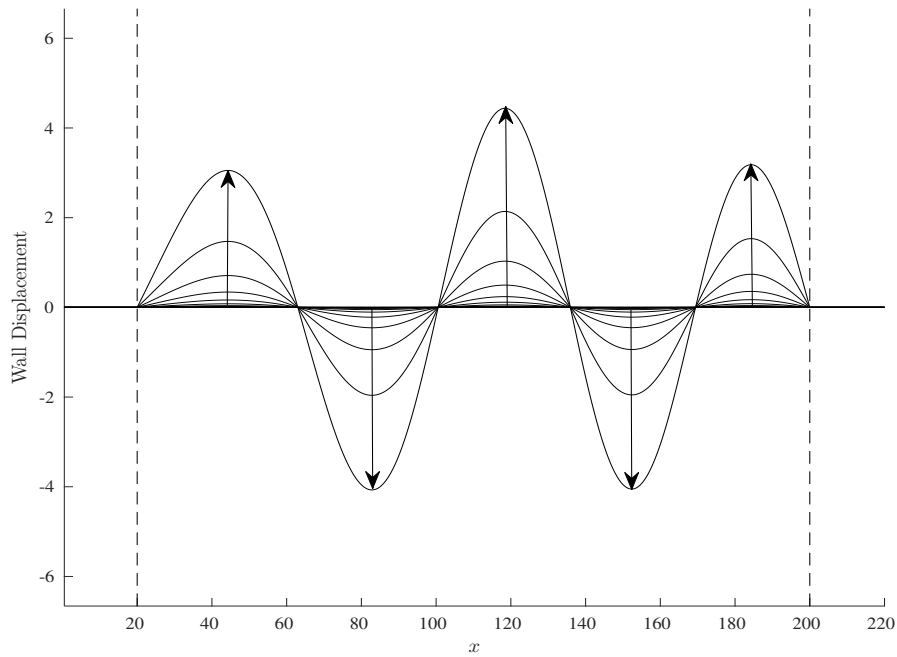


Figure 6.30: Wall displacement for **TGC** plotted at evenly spaced time intervals to show the exponential growth rate. The vertical dashed lines denote the start and end of the compliant wall section.

A very similar phenomenon has been observed in the swimming of dolphins as noted by Aleyev [2] where at high swimming speeds, the dolphin skin forms wave-like folds that are stationary with respect to the motion of the dolphin itself, this is shown in Figure 6.31 taken from Aleyev [2] (in fact, these experiments were also conducted on swimming humans as well). These folds look very similar to the static wave seen in Figure 6.30 which could suggest that the dolphin may be experiencing divergence instability at onset.

6.4.5 TGM: Wall Mass

The inherent lengthscale of the flow configuration is dictated by the product of B and K (since $T = 0$) therefore changing the other wall parameters should not affect the lengthscale of the system but can have an effect on the growth rate. First of all, consider the flow configuration given by **TG** ($\text{Re} = 10000$

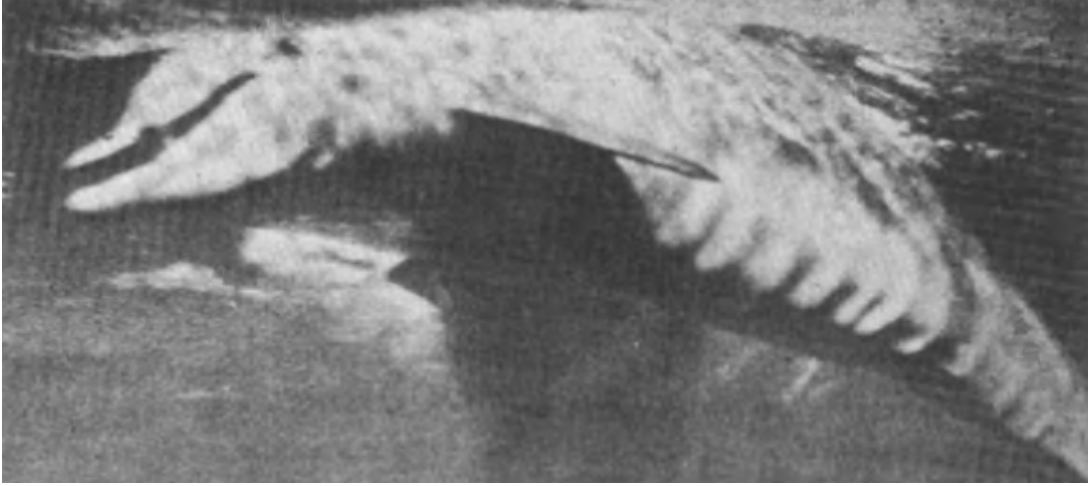


Figure 6.31: Wave-like folds on the dolphin skin which are stationary with respect to the motion of the dolphin, this is taken from Aleyev [2]

and $L = 72$) for different wall masses. The instability in this case takes exactly the same form as it did in Figure 6.24 but with different growth rates as in Table 6.7.

m	λ
0.2	5.82×10^{-3}
2	5.75×10^{-3}
20	4.51×10^{-3}
200	2.53×10^{-3}

Table 6.7: Growth rates of **TG** with different values of m .

Therefore increasing the wall mass reduces the growth rate of the instability hence effectively controlling its growth^V. This will be elaborated upon further in §6.5.

6.4.6 TGD: Damping Coefficient

It was seen that the wall mass acted as a control mechanism for the growth of the global instability. Another wall parameter that can be changed without

^VNote that regardless of the wall mass, the instability grows exponentially, this fits in well with the fact that the divergence onset is unaffected by the wall's mass (see for example Davies & Carpenter [30]). Even though the onset of divergence is not affected, its growth rate is.

affecting the inherent lengthscale is the damping coefficient d . For the sake of variety, the damping coefficient will be changed for the flow configuration given in **TGC** ($\text{Re} = 8900$ and $L = 180$). Once again, the instability takes exactly the same form as in Figure 6.30 but the growth rates are reduced and this information is shown in Table 6.8.

d	λ
0	6.47×10^{-4}
200	6.09×10^{-4}
1000	4.30×10^{-4}
2000	2.87×10^{-4}

Table 6.8: Growth rates of **TGC** with different values of d .

Just as in **TGM**, increasing the damping has reduced the exponential growth rate of the instability and therefore, it can be used a means of controlling the growth of the instability but not stabilise it. A brief investigation into the mechanism behind the growth of these instabilities for different values of m and d is conducted later in §6.6 by means of energy transfer.

All the results presented so far in **TG**, **TGL**, **TGM** and **TGD** have only included growth rates that are obtained from the DNS. These are now compared to two-dimensional global mode computations in order to corroborate the values of the growth rates and to see the general effect of changing the wall length, wall mass and damping.

6.5 Two-Dimensional Global Mode Computations

This section briefly outlines a numerical procedure developed by *Dr. M. J. Blount* that incorporates the compliant wall length into the solutions of

the Orr-Sommerfeld equation in order to obtain growth rates. This is used to verify the growth rates of the instability found in **TGL**, **TGM** and **TGD**.

The procedure takes full advantage of the fact that the basic velocity U , normal velocity v and disturbance profiles φ are all symmetric. A tridiagonal form of the matrix equations is used to form a block diagonal matrix form of the global eigenvalue problem which also takes into account the compliant wall length. Note that for this procedure, the end conditions are assumed to be hinged. The eigenvalues of the generalised eigenvalue problem are obtained by using an Arnoldi iteration subject to approximate starting values for the growth rates and an outflow wavenumber.

6.5.1 Compliant Wall Length

Figure 6.32 shows the growth rates observed in **TGL**. The line shows the exponential growth rates obtained from the global solver while the crosses are some sampled values obtained from the DNS as given in Table 6.6. From this, it can be seen that the global eigenvalues can predict the DNS results for different compliant wall lengths effectively.

Note that as the compliant wall length is increased, the growth rate keeps increasing to reach a maximum point then decreases again and continues to do so for all subsequent wall lengths. The growth rate for short compliant walls is greater than those for a longer wall and each part of the curve represents a different observed state, in other words, as the wall length increases, the wall displacement shifts between different states (some of the states represent an instability that is static while others can have positive group velocity).

As the length of the compliant wall is increased further, the fluctuations of

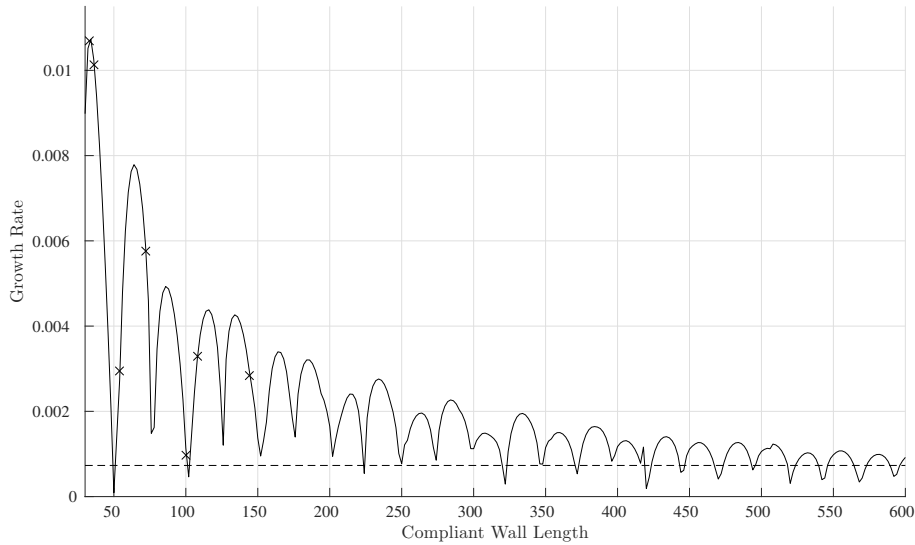


Figure 6.32: Comparison between the growth rates obtained from the two-dimensional global mode computations (—) and the DNS (\times) given in Table 6.6 for **TGL**. The horizontal dashed line is at the growth rate 7.307×10^{-4} which is the approximation to the average growth rate as the wall becomes longer.

the growth rate decreases to approach the positive growth rate of 7.307×10^{-4} (as denoted by the horizontal dashed line). This value is an approximation to the average growth rate that results if the wall was very long.

From this, it can be conjectured that in the limit of very long compliant walls, the growth of the instability arises from a modal interaction but for short panels, the growth rate can either be intensified or diminished due to resonance effects. These effects depend on how an unstable wave can be fitted between the ends of the compliant panel.

Very short compliant walls (particularly less than 33) have not been considered since in those cases, the wall is far too short to even support half a wavelength. Therefore when the impulsive excitation is introduced, the wall would respond to the impulse but then start to oscillate and decay.

6.5.2 Wall Mass & Damping

Figure 6.33 shows the change in the growth rate for different values of m for the flow configuration given in **TGM**, the global mode computations are compared to the DNS results given in Table 6.7. As the wall mass is increased, the compliant wall becomes effectively heavier therefore hindering the growth of the global instability. It is worth noting that for very large values of m , other factors may affect the growth rate, this could explain the relative disparity between the DNS results and the global modes for $m = 200$.

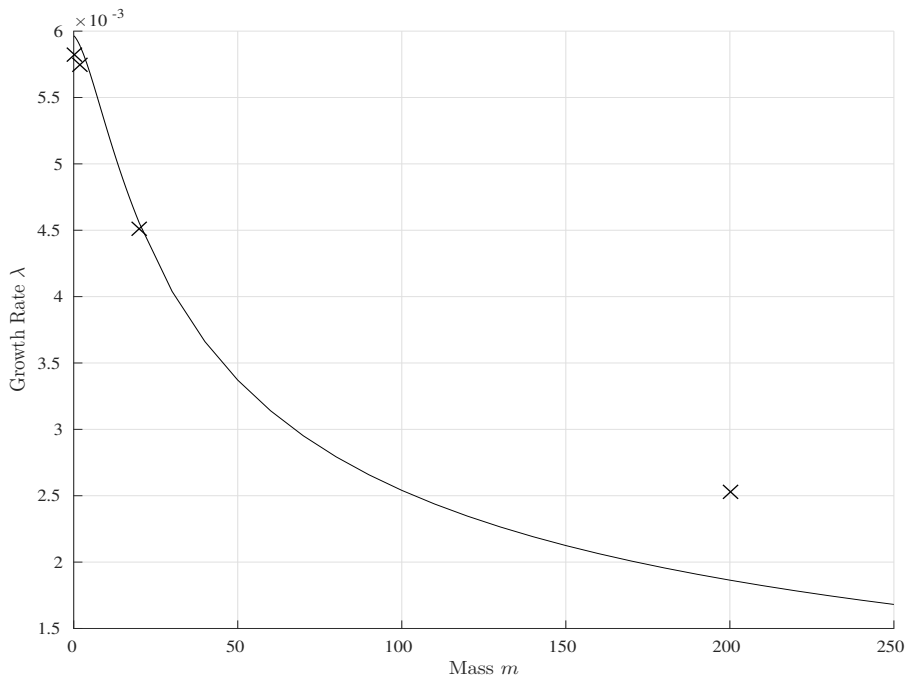


Figure 6.33: Comparison between the growth rates obtained from the two-dimensional global mode computations (—) and the DNS (\times) given in Table 6.7 for **TGM**.

Similarly, Figure 6.34 shows the change in the growth rate for different values of d for the flow configuration given in **TGD**. The global mode computations are compared to the DNS results given in Table 6.8. Increasing the wall damping can be thought of as effectively removing energy from the wall

and into the flow hence reducing the growth rate. This is characteristic of the Class A instabilities mentioned in Chapter 1 which is when a flow is *stabilised* by the irreversible energy transfer *into* the flow.

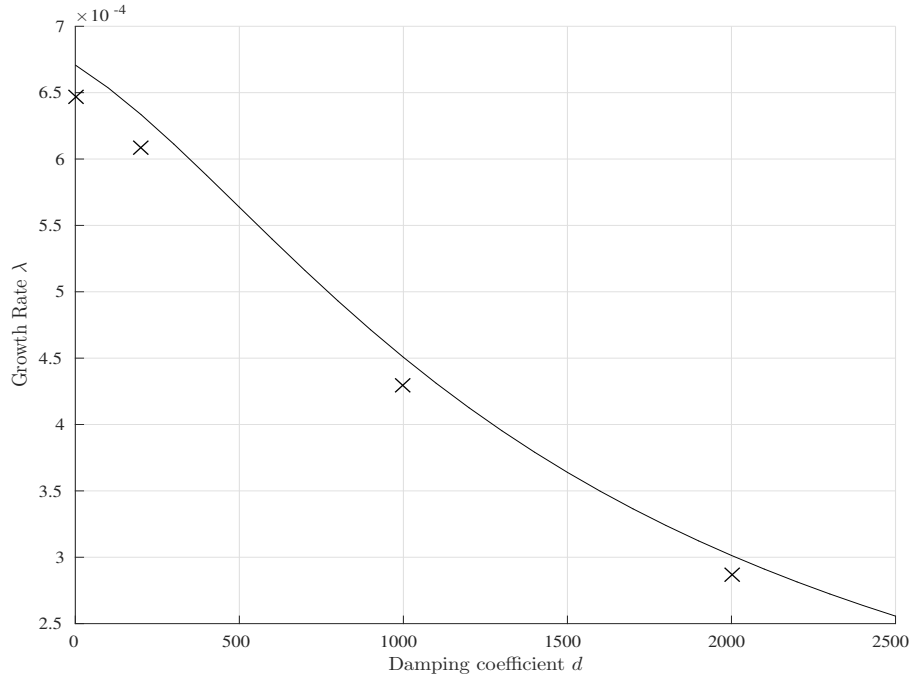


Figure 6.34: Comparison between the growth rates obtained from the two-dimensional global eigenvalues (—) and the DNS (\times) given in Table 6.8 for TGD.

6.5.3 Remarks on the Two-Dimensional Global Mode Computations

It should be noted that this two-dimensional global solver that includes the compliant wall length was developed by *Dr. M. J. Blount*, it was provided for the purposes of this thesis as a means for verifying the exponential growth rates obtained from the DNS. This only increases confidence that the simulation method presented in Chapter 4 can capture global instabilities that take the form of a static, non-oscillating, temporally growing wave and gives reasonably accurate predictions for the growth rates. The results obtained from the two-

dimensional global mode computations and the DNS have a few discrepancies (as observed in Figures 6.32, 6.33 and 6.32) but these differences are minuscule, usually of $\mathcal{O}(10^{-4})$ or less.

This method provides an excellent view of what happens when some of the factors are changed, for example, increasing the wall mass or damping coefficient reduces the growth rate without changing the inherent lengthscale of the system. Therefore, the parameters m and d can act as a means of controlling the growth of the instability but *not* as a means of stabilising it. Similarly for the compliant wall length, the solution of the Orr-Sommerfeld equation described in Chapter 3 only accommodates for an infinite compliant wall and cannot be used in this context. Therefore, using this global solver incorporates the wall lengths into the problem to obtain values for the growth rates.

6.6 Wall Energy Balances

It was seen that increasing the wall mass or damping can reduce the growth rate of the instability without affecting its qualitative behaviour. These changes can be attributed to an energy transfer from the wall into the flow hence causing the growth rate of the instability to decrease due to this energy removal. In order to investigate this energy exchange, the energy flux equations are set up (from previous literature) and then be applied to some of the examples seen earlier.

In order to obtain the energy flux equation, consider the governing equa-

tions as in Chapter 4:

$$x - \text{momentum equation: } \frac{\partial u}{\partial t} + U \frac{\partial u}{\partial x} + \frac{dU}{dy} v = -\frac{\partial p}{\partial x} + \frac{1}{R} \left(\frac{\partial^2 u}{\partial x^2} + \frac{\partial^2 u}{\partial y^2} \right) \quad (6.9a)$$

$$y - \text{momentum equation: } \frac{\partial v}{\partial t} + U \frac{\partial v}{\partial x} = -\frac{\partial p}{\partial y} + \frac{1}{R} \left(\frac{\partial^2 v}{\partial x^2} + \frac{\partial^2 v}{\partial y^2} \right) \quad (6.9b)$$

$$\text{Conservation of mass: } \frac{\partial u}{\partial x} + \frac{\partial v}{\partial y} = 0 \quad (6.9c)$$

$$\text{Vorticity: } \frac{\partial u}{\partial y} - \frac{\partial v}{\partial x} = \omega. \quad (6.9d)$$

Multiplying (6.9a) by u and adding it to (6.9b) multiplied by v gives

$$u \frac{\partial u}{\partial t} + v \frac{\partial v}{\partial t} + Uu \frac{\partial u}{\partial x} + Uv \frac{\partial v}{\partial x} + \frac{dU}{dy} uv = - \left\{ \frac{\partial p}{\partial x} u + \frac{\partial p}{\partial y} v \right\} + \frac{1}{R} \left[u \frac{\partial^2 u}{\partial x^2} + u \frac{\partial^2 u}{\partial y^2} + v \frac{\partial^2 v}{\partial x^2} + v \frac{\partial^2 v}{\partial y^2} \right]. \quad (6.10)$$

The terms on the left hand side can be simplified to

$$\frac{1}{2} \frac{\partial}{\partial t} (u^2 + v^2) + \frac{1}{2} \frac{\partial}{\partial x} [U (u^2 + v^2)] + \frac{dU}{dy} uv.$$

The pressure terms on the right hand side ($\{\square\}$) can be written as

$$\{\square\} = \frac{\partial}{\partial x} (pu) + \frac{\partial}{\partial y} (pv) \quad \text{by using } (6.9c).$$

Finally, the Reynolds number terms ($[\square]$) can be written as

$$[\square] = \frac{\partial}{\partial y} (u\omega) - \frac{\partial}{\partial x} (v\omega) - \omega^2 \quad \text{by using } (6.9c) \quad \text{and } (6.9d).$$

Therefore, equation (6.10) becomes

$$\begin{aligned} \frac{1}{2} \frac{\partial}{\partial t} (u^2 + v^2) + \frac{1}{2} \frac{\partial}{\partial x} [U(u^2 + v^2)] + \frac{dU}{dy} uv + \left\{ \frac{\partial}{\partial x} (pu) + \frac{\partial}{\partial y} (pv) \right\} \\ = \frac{1}{R} \left[\frac{\partial}{\partial y} (u\omega) - \frac{\partial}{\partial x} (v\omega) - \omega^2 \right]. \end{aligned} \quad (6.11)$$

Integrating with respect to y across the channel half-width $y \in [0, 1]$ gives

$$\begin{aligned} \frac{1}{2} \frac{\partial}{\partial t} \int_0^1 (u^2 + v^2) dy + \frac{1}{2} \frac{\partial}{\partial x} \int_0^1 U(u^2 + v^2) dy + \int_0^1 \frac{dU}{dy} uv dy + \frac{\partial}{\partial x} \int_0^1 pu dy + [pv]_0^1 \\ = \frac{1}{R} \left[[u\omega]_0^1 - \frac{\partial}{\partial x} \int_0^1 v\omega dy - \int_0^1 \omega^2 dy \right]. \end{aligned} \quad (6.12)$$

This expression can be simplified by using the fact that the pressure p and the streamwise disturbance velocity u were both assumed to be odd, therefore $u(x, 0, t) = p(x, 0, t) = 0$.

Two of the terms in the energy equation (6.12) are of special interest, the first term is a disturbance energy term which is expressed in terms of the flow speed $|\mathbf{u}|^2 = u^2 + v^2$ as

$$\mathcal{K} = \mathcal{K}(x, t) = \frac{1}{2} \int_0^1 (u^2 + v^2) dy.$$

The second is with regards to the dissipation effects related to the kinetic energy and is known as the *enstrophy* \mathcal{E} , this is given by

$$\mathcal{E} = \mathcal{E}(x, t) = \frac{1}{2} \int_0^1 \omega^2 dy.$$

Equation (6.12) can now be rewritten as a function in x and t only as

$$\begin{aligned} \frac{\partial}{\partial t} \mathcal{K} + \frac{\partial}{\partial x} \left[\frac{1}{2} \int_0^1 U(u^2 + v^2) dy + \int_0^1 up dy + \frac{1}{R} \int_0^1 v\omega dy \right] \\ + \int_0^1 \frac{dU}{dy} uv dy + \frac{2}{R} \mathcal{E} = -p_w v_w + \frac{1}{R} u_w \omega_w. \end{aligned} \quad (6.13)$$

The terms with a subscript w (\square_w) denote quantities evaluated at the wall, i.e.

$$f_w = f_w(x, t) = f(x, 1, t).$$

In order to obtain the energy flux equation, (6.13) would have to be averaged in time but there are three qualitatively different cases to consider:

- ① Time periodic case (as in Chapter 5)
- ② GQ-periodic case (**STG**)
- ③ Divergence case (**TG**).

① Time-Periodic Case

In Chapter 5, the flow variables displayed a time-periodic behaviour, i.e. the flow variables, denoted f (be they the wall displacement, velocity components, etc.) take the form

$$f(x, y, t + \tau) = f(x, y, t)$$

where τ is the time period. It is crucial to note that the flow variables take this form *after* the transients have subsided and any reflections have died out, this time will be denoted T_0 here. All the flow simulations shown with this property were disturbed by an inflow profile with a built-in frequency β .

To the normal mode approximation implies that the arbitrary function f has to take the form

$$f(x, y, t) = \Re (F(x, y)e^{-i\tilde{\omega}t}) \quad \text{for } t > T_0 \quad (6.14)$$

where the function F is complex in general and the frequency $\tilde{\omega}$ is real, in fact, it has to be equal to the inflow frequency $\beta \in \mathbb{R}$. With this form in mind, the function f can be rewritten as

$$f = \frac{1}{2} (Fe^{-i\beta t} + \bar{F}e^{i\beta t})$$

where the single bar ($\bar{\square}$) denotes the complex conjugate. From this, it can be deduced that the time period τ takes the form

$$\tau = \frac{2\pi}{\beta\Delta t} \quad (6.15)$$

and therefore, τ satisfies the integral

$$\frac{1}{\tau} \int_0^{\tau} e^{\pm i\beta t} dt = 0.$$

Notice that in equation (6.13), all the flow terms appear as products of pairs, therefore another function g needs to be introduced which takes the same form as f in (6.14), i.e.

$$g(x, y, t) = \Re (G(x, y)e^{-i\beta t}).$$

The products fg and f^2 are given by:

$$fg = \frac{1}{4} [FGe^{-2i\beta t} + \bar{F}\bar{G}e^{2i\beta t} + F\bar{G} + \bar{F}G] \quad (6.16a)$$

$$f^2 = \frac{1}{4} [F^2e^{-2i\beta t} + \bar{F}^2e^{2i\beta t} + 2F\bar{F}] \quad (6.16b)$$

The term fg represents the product of pairs of u, v, p or ω while f^2 represents u^2 and v^2 . Since the time derivative of u^2 and v^2 is taken in $\frac{\partial}{\partial t}\mathcal{K}$, then an expression for the time derivative of f^2 is needed which is

$$\frac{\partial}{\partial t}f^2 = -\frac{i\beta}{2} [F^2e^{-2i\beta t} - \bar{F}^2e^{2i\beta t}] \quad (6.17)$$

Denote the two-term average over a time period τ by two bars ($\overline{\overline{\quad}}$), i.e.

$$\overline{\overline{fg}} = \overline{\overline{fg}}(x, y) = \frac{1}{\tau} \int_0^\tau f(x, y, t)g(x, y, t) dt. \quad (6.18)$$

Taking the time-average of equations (6.16a), (6.16b) and (6.17) eliminate the oscillatory terms (those with $e^{\pm 2i\beta t}$) and therefore

$$\overline{\overline{fg}} = \frac{1}{4} (F\bar{G} + \bar{F}G) \quad (6.19a)$$

$$\overline{\overline{f^2}} = \frac{1}{2} F\bar{F} \quad (6.19b)$$

$$\overline{\overline{\frac{\partial}{\partial t}f^2}} = 0. \quad (6.19c)$$

Taking the two-term average of equation (6.13) over the time-period τ eliminates the oscillatory terms to give an equation in terms of the streamwise

direction x only as

$$\begin{aligned}
 \frac{d}{dx} \left[\overbrace{\frac{1}{2} \int_0^1 U(\overline{u^2} + \overline{v^2}) dy}^{(I)} + \overbrace{\int_0^1 \overline{u\bar{p}} dy}^{(IIi)} + \overbrace{\frac{1}{R} \int_0^1 \overline{v\bar{\omega}} dy}^{(IIii)} \right] \\
 + \underbrace{\int_0^1 \frac{dU}{dy} \overline{uv} dy}_{(III)} + \underbrace{\frac{2}{R} \bar{\mathcal{E}}}_{(IV)} = - \underbrace{\overline{p_w v_w}}_{(V)} + \underbrace{\frac{1}{R} \overline{\omega_w u_w}}_{(VI)} \quad (6.20)
 \end{aligned}$$

$$\text{where } \bar{\mathcal{E}} = \bar{\mathcal{E}}(x) = \frac{1}{2} \int_0^1 \overline{\omega^2} dy.$$

(Note that in this case, averaging over a single-time period is equivalent to averaging over the whole simulation time.)

In this arrangement, the energy terms that arise due to the fluid flow are on the left hand side while those arising from the wall flexibility are on the right. The terms labelled with Roman numerals are interpreted as follows:

- (I) *Disturbance energy* arising due to the fluid motion of the basic flow past a given streamwise location.
- (II) *Work done* as a result of disturbance and *perturbation stresses* (note that in practice, the term labelled (IIii) is usually quite small).
- (III) Energy production due to the *Reynolds stress*.
- (IV) Enstrophy representing *viscous dissipation*.

The terms on the right hand side can be expressed differently using the linearised boundary conditions, namely

$$u_w = u(x, 1, t) = -U'(1)\eta(x, t) = 2\eta(x, t) \quad \text{and} \quad v_w = v(x, 1, t) = \frac{\partial \eta}{\partial t}(x, t).$$

These terms can be interpreted as follows:

(VI) $-p_w v_w = -p_w \frac{\partial \eta}{\partial t}$: the *irreversible* work done by the *disturbance pressure* on the compliant wall.

(VII) $\frac{1}{R} u_w \omega_w = \frac{2}{R} \omega_w \eta$: the energy removal which is equivalent to an *additional viscous dissipation* (according to Carpenter [14]).

This now establishes the energy flux equation for the case when the flow is time-periodic and will now be applied to the **TSS** case shown in Chapter 5 (this has been documented before in Davies & Carpenter [30])^{VI}.

Energy Equation for TSS

In the **TSS** case shown in Chapter 5, the TS mode has been stabilised by the presence of the compliant wall and this is seen in Figures 6.35 and 6.36. First, Figure 6.35 shows the streamwise variation of the disturbance energy (which was labelled (I) in equation (6.20)). Over the upstream rigid wall section, the energy increases exponentially but as soon as it enters the compliant wall, there is a drastic jump followed by exponential decay. This decay continues until the end of the compliant wall is reached after which point the energy starts to grow again over the downstream rigid section. If the compliant wall is long enough, then the disturbance energy will keep decaying hence effectively stabilising the TS instability.

Figure 6.36 shows the streamwise variation of the enstrophy term \mathcal{E} . Once again, there is exponential growth over the rigid sections but the compliant wall has effectively stabilised the disturbance resulting in exponential decay.

This energy equation can be used for all cases where the flow is time-

^{VI}Note that not all the terms in the energy equation will be presented, only the relevant ones. The other energy terms are presented in order to establish the energy equations.

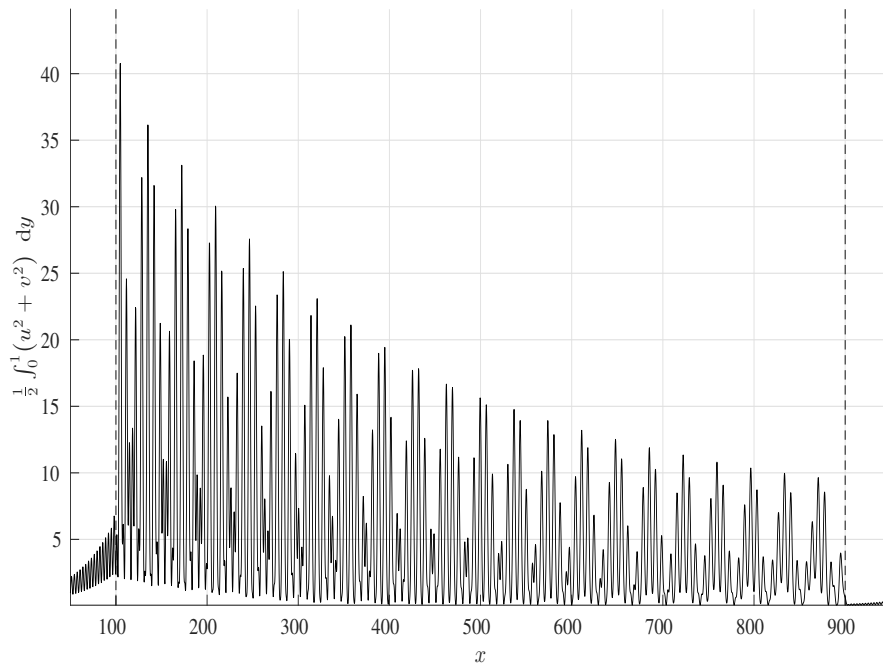


Figure 6.35: Streamwise variation (labelled (I) in equation (6.20)) of the disturbance energy for **TSS**. The vertical dashed lines indicate the start and end of the compliant wall section.

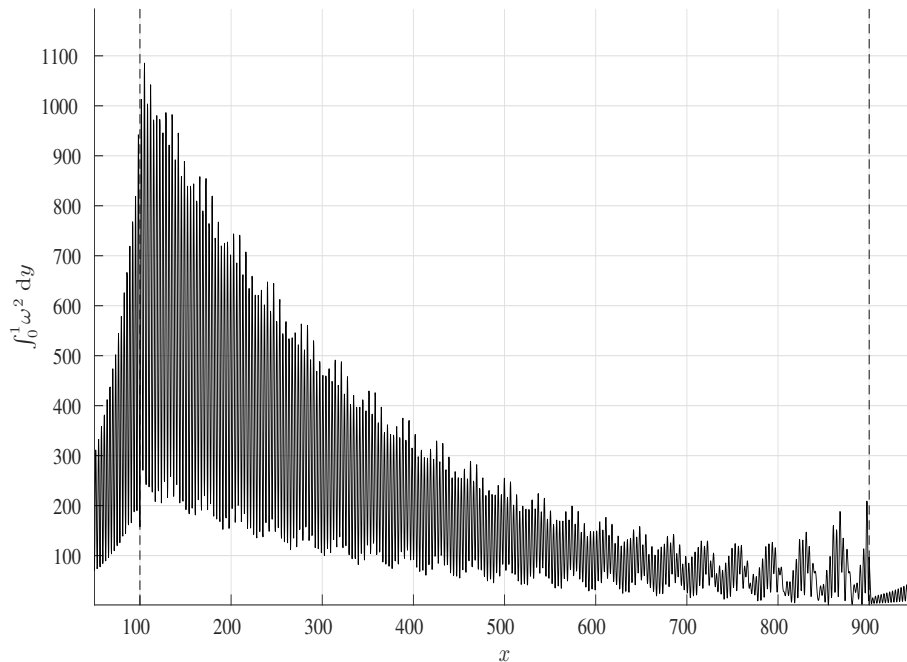


Figure 6.36: Streamwise variation of the enstrophy for **TSS**. The vertical dashed lines indicate the start and end of the compliant wall section.

periodic, for example **TSM**, **TWF** and **DivEnd**, but these will not be presented here since they do not provide interesting insight into the energy exchange. For example, in **TSM**, the results are similar to those observed with the wall heights, in other words, the compliant wall serves the purpose of reducing the TS growth rate but *not* stabilise it. However in **TWF** and **DivEnd**, the wall energy plummets shortly after entering the flow domain since over the rigid wall section, the TS mode is highly stabilised particularly due to the low Reynolds number and so it does not manifest in the flow at all.

② GQ-Periodic Case

When the disturbance develops into an absolute instability that grows with a gq-period as in **STG**, the time-averaging obtained earlier does not hold any more since the flow variables have an associated exponential growth rate as well as an oscillatory component. However the way in which the energy equations are obtained is somewhat similar.

Suppose that the flow variables evolve gq-periodically with a gq-period τ as in **STG**. In this case, the flow variables take the form

$$f(x, y, t) = \Re (F(x, y)e^{-i\tilde{\omega}t}) \quad (6.21)$$

where the frequency $\tilde{\omega}$ is complex in this case, i.e. $\tilde{\omega} = \omega_r + i\omega_i$ ($\omega_r, \omega_i \in \mathbb{R}$). Therefore, the arbitrary function f can be written as

$$f = \frac{1}{2} (Fe^{-i\omega_r t} + \bar{F}e^{i\omega_r t}) e^{\omega_i t}. \quad (6.22)$$

With these expressions in mind, the products fg and f^2 (where g takes

the form (6.21)) are the same as in equations (6.16) but with an additional exponential term $e^{2\omega_i t}$, i.e. :

$$fg = \frac{1}{4} [FGe^{-2i\omega_r t} + \bar{F}\bar{G}e^{2i\omega_r t} + F\bar{G} + \bar{F}G] e^{2\omega_i t} \quad (6.23a)$$

$$f^2 = \frac{1}{4} [F^2e^{-2i\omega_r t} + \bar{F}^2e^{2i\omega_r t} + 2F\bar{F}] e^{2\omega_i t}. \quad (6.23b)$$

Taking the time derivative of the f^2 term results in additional terms (compared to (6.17))

$$\begin{aligned} \frac{\partial}{\partial t} f^2 = -\frac{i\omega_r}{2} [F^2e^{-2i\omega_r t} - \bar{F}^2e^{2i\omega_r t}] e^{2\omega_i t} \\ + \frac{\omega_i}{2} [F^2e^{-2i\omega_r t} + \bar{F}^2e^{2i\omega_r t} + 2F\bar{F}] e^{2\omega_i t} \end{aligned} \quad (6.24)$$

(Note that if $\omega_r = \beta$ and $\omega_i = 0$, then equations (6.16) and (6.17) for the periodic evolution will be recovered.)

The extra term $e^{2\omega_i t}$ is the exponentially growing contribution compared to (6.16), this can be divided out before taking a time-average, let this be denoted by a double tilde ($\widetilde{\widetilde{\square}}$), i.e.

$$\widetilde{\widetilde{fg}} = \widetilde{\widetilde{fg}}(x, y) = \frac{1}{\tau} \int_0^\tau \frac{1}{e^{2\omega_i t}} f(x, y, t) g(x, y, t) dt \quad (6.25)$$

Dividing the expressions in (6.23) and (6.24) by $e^{2\omega_i t}$ then taking the time-average eliminates the oscillatory terms $e^{\pm 2i\omega_r t}$ to give

$$\widetilde{\widetilde{fg}} = \frac{1}{4} (F\bar{G} + \bar{F}G) \quad (6.26a)$$

$$\widetilde{\widetilde{f^2}} = \frac{1}{2} F\bar{F} \quad (6.26b)$$

$$\frac{\partial}{\partial t} \widetilde{\widetilde{f^2}} = \omega_i F\bar{F}. \quad (6.26c)$$

Notice that equations (6.26a) and (6.26b) are the same as (6.19a) and (6.19b), so

$$\widetilde{\widetilde{fg}} = \overline{\overline{fg}} \quad \text{and} \quad \widetilde{\widetilde{f^2}} = \overline{\overline{f^2}}.$$

However, the average of the time derivative in (6.26c) is no longer zero;

$$\frac{\partial}{\partial t} \widetilde{\widetilde{(u^2 + v^2)}} = \frac{\partial}{\partial t} \widetilde{\widetilde{u^2}} + \frac{\partial}{\partial t} \widetilde{\widetilde{v^2}} = \omega_i \hat{u} \bar{\bar{u}} + \omega_i \hat{v} \bar{\bar{v}} = \omega_i (|\hat{u}|^2 + |\hat{v}|^2). \quad (6.27)$$

The functions \hat{u} and \hat{v} are the equivalent of F in relation to u and v , i.e.

$$u = \Re(\hat{u}e^{-i\bar{\omega}t}) \quad \text{and} \quad v = \Re(\hat{v}e^{-i\bar{\omega}t}).$$

Equation (6.27) is not zero as in (6.19c) and therefore, this adds an extra contribution to the energy equation. In summary, dividing equation (6.13) by $e^{2\omega_i t}$ then taking the two term average will give equation (6.20) with an extra term coming from the disturbance energy:

$$\begin{aligned} & \overbrace{\omega_i \int_0^1 |\hat{u}|^2 + |\hat{v}|^2 dy}^{(X)} + \frac{d}{dx} \left[\overbrace{\frac{1}{2} \int_0^1 U(\overline{\overline{u^2}} + \overline{\overline{v^2}}) dy}^{(I)} + \overbrace{\int_0^1 \overline{\overline{u\bar{p}}} dy + \frac{1}{R} \int_0^1 \overline{\overline{v\bar{\omega}}} dy}^{(II)} \right] \\ & \quad + \underbrace{\int_0^1 \frac{dU}{dy} \overline{\overline{u\bar{v}}} dy}_{(III)} + \underbrace{\frac{2}{R} \overline{\overline{\mathcal{E}}}}_{(IV)} = - \underbrace{\overline{\overline{p_w v_w}}}_{(V)} + \underbrace{\frac{1}{R} \overline{\overline{\omega_w u_w}}}_{(VI)} \quad (6.28) \end{aligned}$$

$$\text{where } \overline{\overline{\mathcal{E}}} = \overline{\overline{\mathcal{E}}}(x) = \frac{1}{2} \int_0^1 \overline{\overline{\omega^2}} dy.$$

In the gq-periodic case as in **STG**, there is an extra term (labelled (X)) proportional to the growth rate ω_i contributing to the disturbance energy compared to equation (6.20).

Energy Equation for STG2

Figures 6.37 and 6.38 show the streamwise variation of the enstrophy and the disturbance energy, respectively. It can be seen that these values grow to large magnitudes compared to **TSS** seen earlier and this is expected since the instability grows absolutely.

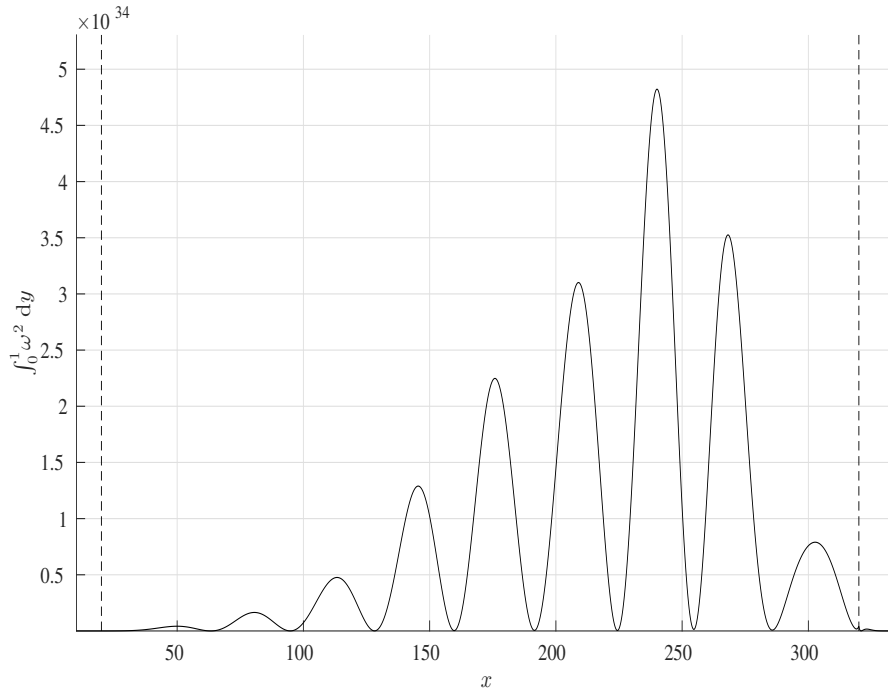


Figure 6.37: Streamwise variation of the enstrophy for **STG2**. The vertical dashed lines indicate the start and end of the compliant wall section.

Figure 6.39 shows the streamwise variation of the production and dissipation terms ((IV) and (V) in equation (6.28) respectively) and it is clear that the energy production far surpasses the energy dissipation and this can be the reason behind the growth of the wall displacement.

The **STG** cases show that the extra term (X) in (6.28) proportional to the growth rate ω_i causes the absolute growth. This term arises due to the fact that the flow variables grow gq -periodically with an associated exponential growth rate.

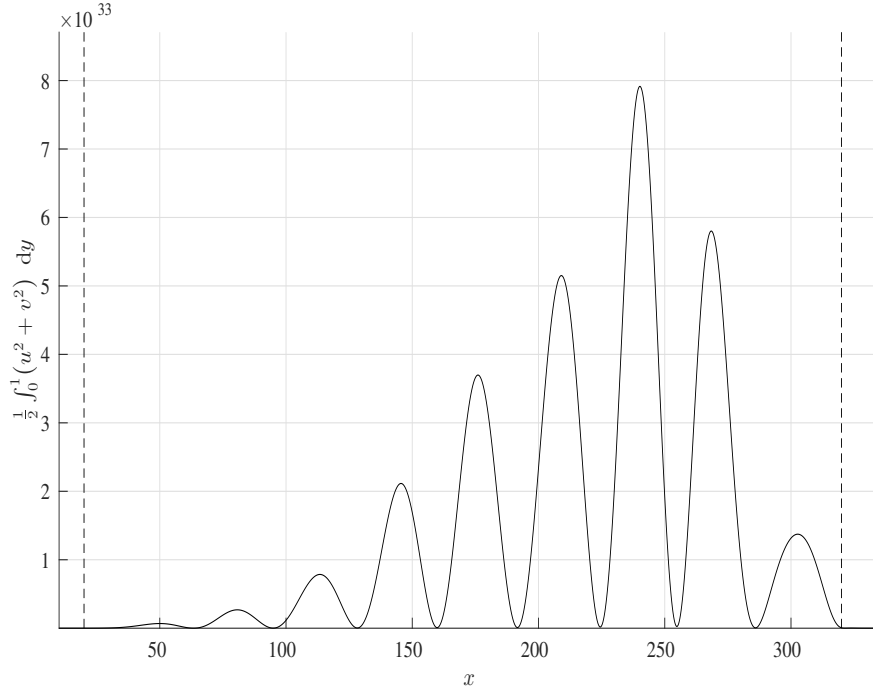


Figure 6.38: Streamwise variation of the disturbance energy (labelled (I)) for **STG2**. The vertical dashed lines indicate the start and end of the compliant wall section.

③ Divergence Case

For the final case, the energy flux with regards to the exponential growth attributed to the global instability due to the onset of the divergence instability (as shown in the **TG** cases) is investigated. In this case, there is no time period associated with the growth, in fact, the flow variables grow exponentially, as

$$f(x, y, t) = \Re(F(x, y)e^{-i\tilde{\omega}t}) \quad (6.29)$$

where the frequency $\tilde{\omega}$ is purely imaginary. The factor $\tilde{\omega}$ can therefore be written as $\tilde{\omega} = i\lambda$ where λ is the growth rate. Therefore f can be written as

$$f = \Re(F)e^{\lambda t} = \frac{1}{2}(F + \bar{F})e^{\lambda t}. \quad (6.30)$$

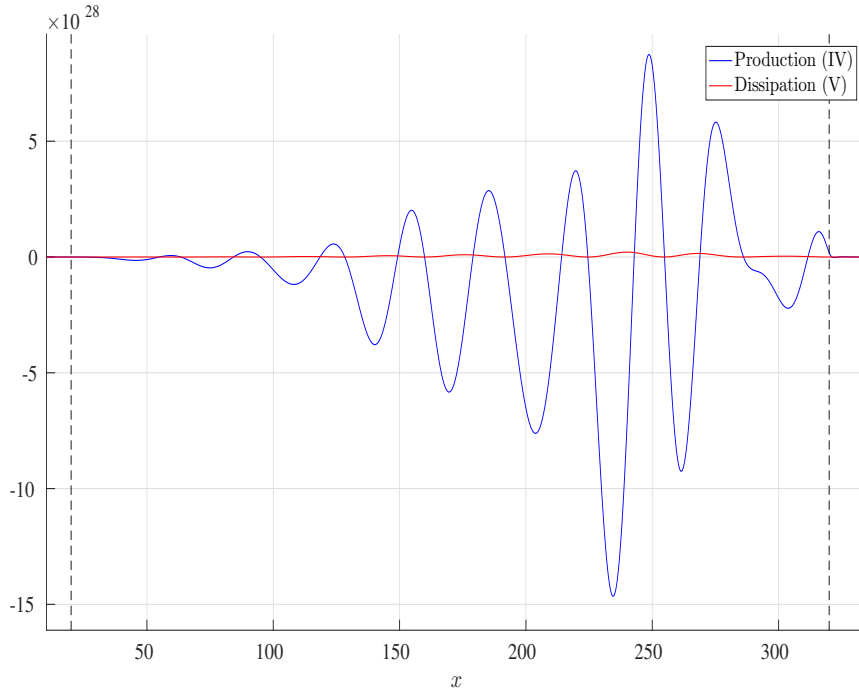


Figure 6.39: Streamwise variation of the energy production and dissipation terms for **STG2** (which are labelled accordingly). The vertical dashed lines indicate the start and end of the compliant wall section.

The products fg and f^2 (where g takes the form (6.29)) will be:

$$fg = \Re(F)\Re(G)e^{2\lambda t} \quad (6.31a)$$

$$f^2 = \Re(F)^2 e^{2\lambda t}. \quad (6.31b)$$

Taking the time derivative of f^2 gives

$$\frac{\partial}{\partial t} f^2 = 2\lambda \Re(F)^2 e^{2\lambda t}. \quad (6.32)$$

(Note that if $\omega_r = 0$ and $\omega_i = \lambda$ in equations (6.23) and (6.24), then (6.31) and (6.32) can be recovered.)

For the growth of the global instability, there is no time-period associated with the growth. Therefore simply dividing the terms in (6.31) and (6.32) by

$e^{2\lambda t}$ eliminates the time dependence completely^{VII}.

The functions u, v, p and ω in (6.13) can be represented as

$$u(x, y, t) = \Re(\hat{u}e^{-i\tilde{\omega}t}) = \Re(\check{u})e^{\lambda t} \quad \text{etc. .}$$

For the sake of simplicity, denote real part of \hat{u} by \check{u} (similarly for the rest), therefore dividing equation (6.13) by $e^{2\lambda t}$ gives

$$2\lambda \int_0^1 \check{u}^2 + \check{v}^2 \, dy + \frac{d}{dx} \left[\frac{1}{2} \int_0^1 U(\check{u}^2 + \check{v}^2) \, dy + \int_0^1 \check{u}\check{p} \, dy + \frac{1}{R} \int_0^1 \check{v}\check{\omega} \, dy \right] + \int_0^1 \frac{dU}{dy} \check{u}\check{v} \, dy + \frac{2}{R} \check{\mathcal{E}} = -\check{p}_w \check{v}_w + \frac{1}{R} \check{\omega}_w \check{u}_w. \quad (6.33)$$

$$\text{where } \check{\mathcal{E}} = \check{\mathcal{E}}(x) = \frac{1}{2} \int_0^1 \check{\omega}^2 \, dy.$$

This energy equation is qualitatively different to those obtained in equations (6.20) and (6.28) earlier since there is no period associated with the growth. The time averaging only yields the real parts for the functions in question.

Energy Equation for TGC

Figures 6.40 and 6.41 show the disturbance energy and the enstrophy while Figure 6.42 shows the energy production and dissipation. Just as before, the production term is far greater than the dissipation term and dominates to destabilise the flow absolutely.

The purpose of obtaining the energy flux equations for the divergence case

^{VII}Since the flow is not periodic in any way, setting $\omega_r = 0$ and $\omega_i = \lambda$ in (6.26) does not recover the expressions for the divergence case.

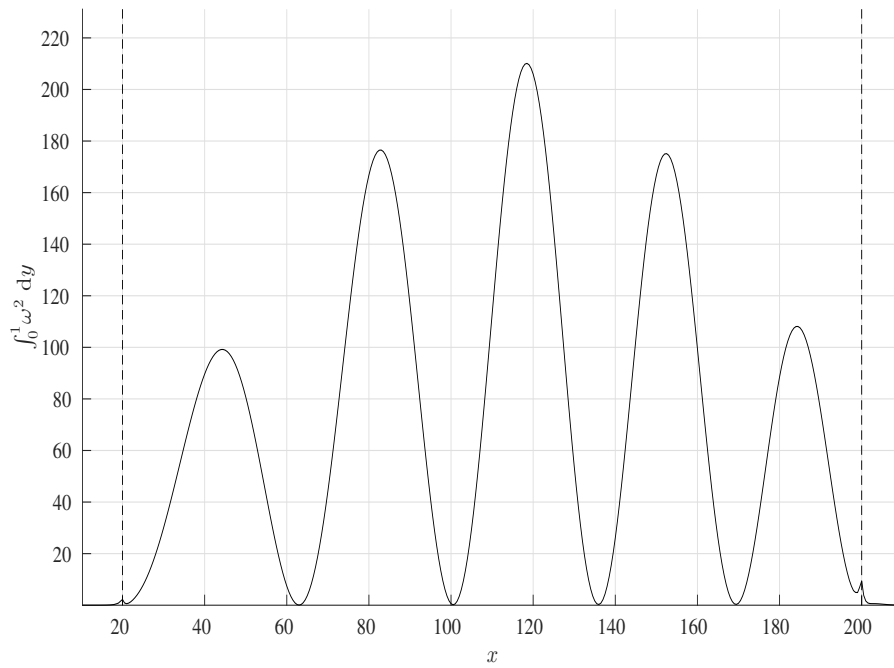


Figure 6.40: Streamwise variation of the enstrophy for **TGC**. The vertical dashed lines indicate the start and end of the compliant wall section.

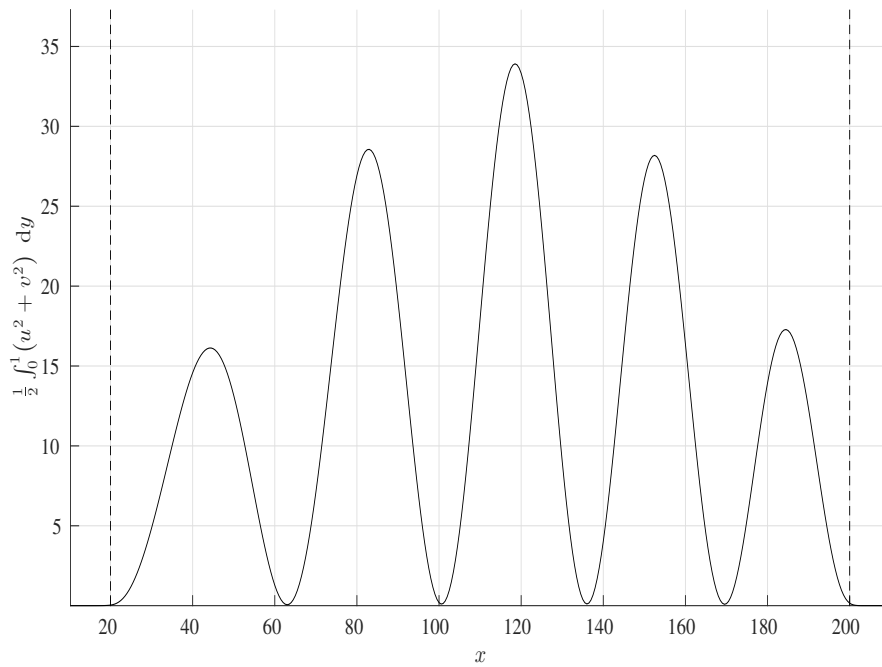


Figure 6.41: Streamwise variation of the enstrophy for **TGC**. The vertical dashed lines indicate the start and end of the compliant wall section.

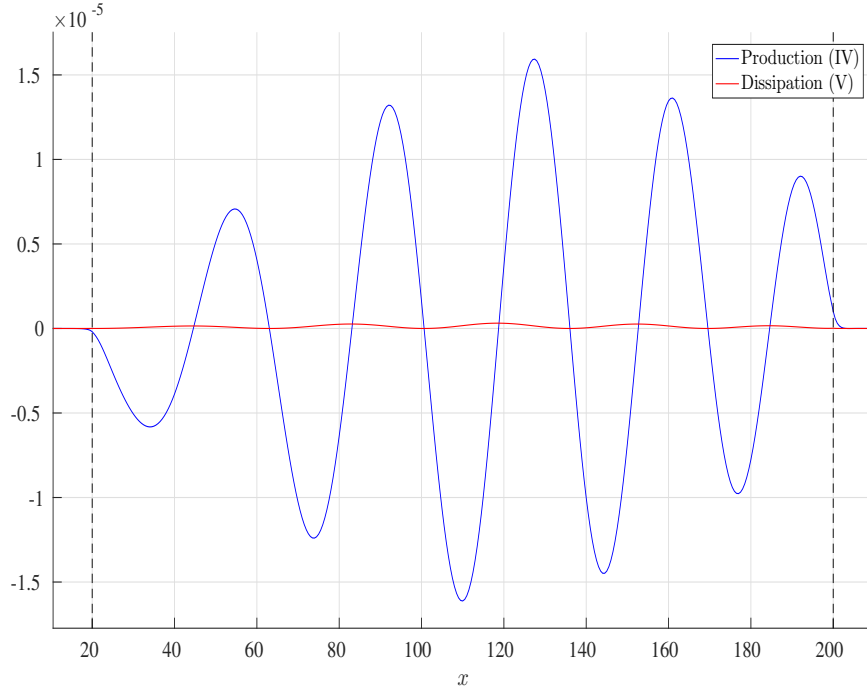


Figure 6.42: Streamwise variation of the energy production and dissipation terms for **TGC** (which are labelled accordingly). The vertical dashed lines indicate the start and end of the compliant wall section.

TG was to study the energy exchange for the different wall parameters, particularly m and d in **TGM** and **TGD**. It was seen that increasing the wall mass or damping can reduce the growth rate of the global instability but not stabilise it.

Energy Equation for TGD

If these energy plots were considered for the different values of damping (as in **TGD**), then the way in which the damping affects the energy exchange can be investigated. For example, Figure 6.43 shows the disturbance energy for two of the cases seen in **TGC** where $d = 1000$ (denoted by $--$) and $d = 2000$ ($---$). Increasing the value of d caused the growth of the energy to be hindered and judging from the growth rates seen earlier, this observation is expected^{VIII}.

^{VIII}The energy plots for the other values of the damping are not plotted here since their growth rates are far higher than those of $d = 1000$ and 2000 making it very difficult to distinguish between the different cases.

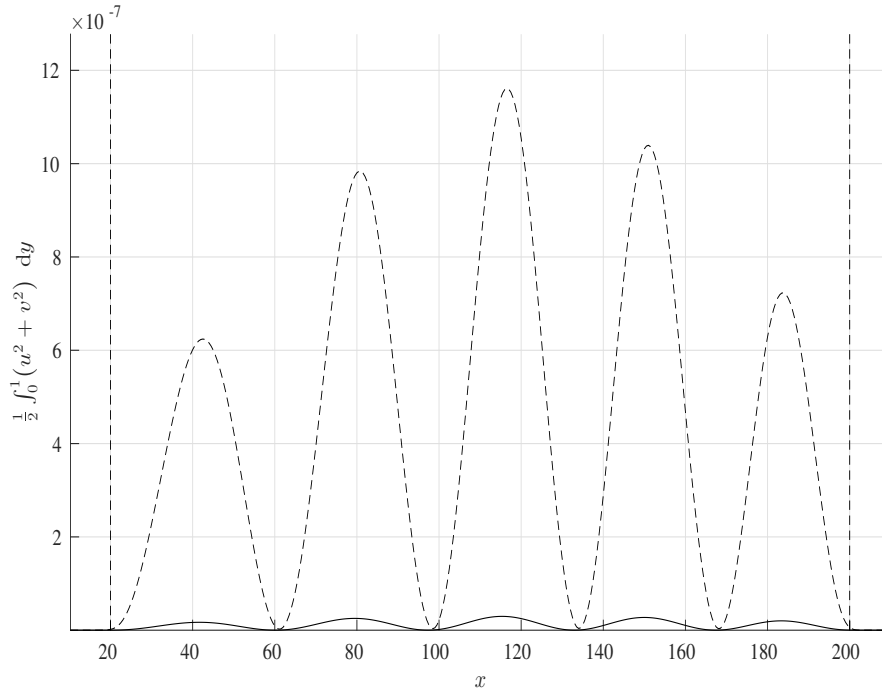


Figure 6.43: Streamwise variation of the disturbance energy for **TGC** with $d = 1000$ (---) and $d = 2000$ (—). The vertical dashed lines indicate the start and end of the compliant wall section.

Energy Equation for TGM

One final modification would be the change in mass as in **TGM**. Figure 6.44 shows the streamwise variation of the disturbance energy when the mass is $m = 0.2$ (---) and $m = 2$ (—). Therefore as the mass of the compliant wall increases, the rate of growth of the energy decreases, this corresponds to an global instability whose growth rate is reduced by an increase in the wall mass.

Remarks on the Energy Equations

From the first example **TSS** where the flow variables are time-periodic, the presence of the compliant wall section caused the energy from the TS mode to dissipate as the disturbance travels over the compliant wall section implying that the TS mode has been effectively stabilised. As for the two cases of absolute and global instability **STG2** and **TGC**, the energy equations

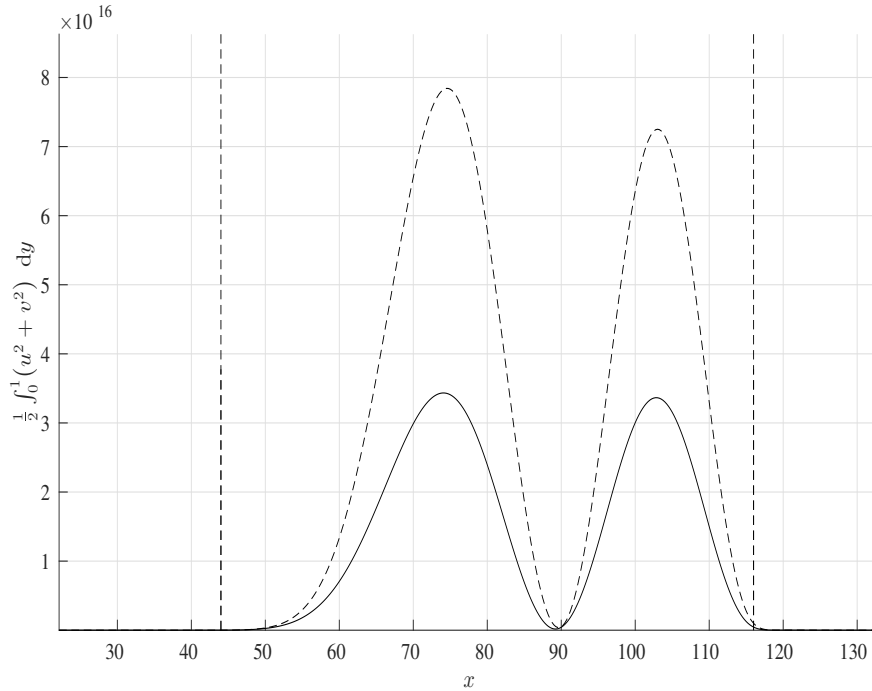


Figure 6.44: Streamwise variation of the disturbance energy for **TG** with $m = 0.2$ (---) and $m = 2$ (—). The vertical dashed lines indicate the start and end of the compliant wall section.

resulted in an extra term that is proportional to the growth rate which is the main culprit for causing the instability grow absolutely/globally.

The account for the energies has not been made extensive here mainly due to time restrictions. However, these result further support the fact that the compliant wall is an excellent way of stabilising the TS mode (as documented before extensively), the absolute/global instability, on the other hand, causes the disturbance energy to grow exponentially. Changing the wall mass and damping can effectively control the growth of the global instability; changing these can alter the exponential growth rate without changing the inherent characteristics or lengthscale of the flow as a whole.

6.7 Summary

In this chapter, the growth of absolute and global instabilities was studied. The first case **STG** showed an absolute instability that grew spatially and temporally with a gq-period and an amplification factor. This absolute instability was a result of an interaction between the TS and divergence modes and was excited by an impulsive forcing or an inflow profile associated with the TS mode. In either case, the DNS produced similar results for a given set of wall and flow parameters implying that the absolute instability was an inherent feature for this choice of parameters. The wavenumbers, phase speeds and growth rates of this form of instability were predicted effectively by using the solution of the Orr-Sommerfeld equation, the curves of c against R and α as well as Briggs' method.

In the second case **TG**, the global instability took the form of a static, non-oscillating temporally growing wave which was a result of exciting the divergence mode at onset. The growth rates from the DNS were compared to those obtained from the two-dimensional global mode computations and the results were comparable. The effect of changing some of the factors in the flow configuration was studied, this included changing the end effects, compliant wall length, Reynolds number, wall mass and damping.

Finally, the energy flux equations for the cases when the flow variables are periodic, gq-periodic and globally growing were set up. This was mainly to study the effect of changing the wall parameters m and d on the growth of the divergence mode at onset.

Chapter 7

Conclusions

7.1 Conclusion of the Thesis

In this thesis, we have documented the onset of the wall-based TWF and divergence instabilities from a numerical point of view. In the past, these modes have not been systematically studied using the current DNS method since a majority of the work focussed on TS suppression. It was found that the solutions of the Orr-Sommerfeld equation managed to obtain very good predictions for the wavenumbers arising from the DNS for the wall-based modes even though these solutions are only strictly valid for an infinitely extended compliant wall. Moreover, when the end effects were quite prominent and affected the wall displacement near the ends more drastically (just as in the case of the divergence instability), the solutions of the Orr-Sommerfeld equation still managed to predict the contributing wavenumbers from the end effects as well as the divergence mode itself.

A numerical investigation into the onset of absolute and global instabilities was also carried out where the disturbances grew to such an extent that

they destabilised the flow. First, an absolute instability that developed both spatially and temporally was investigated. In this case, the variation of the real and imaginary parts of the phase speed against the wavenumber and Reynolds number were used as a means for obtaining candidates for appropriate flow parameters. The simulations were performed by using different means of excitation, particularly, two different excitation frequencies and a localised impulsive forcing. The results obtained from the three simulations were then compared to Briggs' method which was used to predict the growth rates, phase speeds and wavenumbers and the results were comparable.

Finally, the growth of a global instability which took the form of a static, non-oscillating temporally growing wave were studied. This was quite intriguing part since this shows the manifestation of the divergence instability at onset (since the instability has zero phase speed). The wave that forms the wall displacement does not oscillate in time but does continue to grow exponentially with a fixed form of spatial variation.

This final case was then modified by changing several factors such as the compliant wall length, mass and damping. It seems that this particular behaviour (global growth of the instability in a static fashion) is quite sensitive to changes in the compliant wall length and therefore, the originally developed Orr-Sommerfeld solutions and Briggs' method were not capable of capturing all the interesting characteristics. However, a global eigenvalue solver with the wall length built in proved helpful in corroborating the results obtained from the DNS. Increasing the wall mass and damping, on the other hand, acted as control mechanisms for the growth of this global instability, in other words, the instability will still grow globally but with a reduced growth rate which is inversely proportional to the mass or damping.

7.2 Future Work

An investigation into the energy balances that result in absolute and global instabilities (as described in Chapter 6) can be carried out in order to investigate the mechanisms that lead to the instability. Moreover, the effects of changing the wall mass and damping on the energy transfer can be studied in more depth.

The two-dimensional global mode computations can be modified in order to obtain phase speeds as well as the growth rates. An investigation into these can help identify a range of wall lengths that support the static temporally growing waves and their associated growth rates.

Appendix A

Inviscid Solutions

This part of the appendix gives a brief description of the solutions of the Rayleigh equation obtained by Heisenberg [70].

Consider the Rayleigh equation

$$(U - c)(\varphi'' - \alpha^2\varphi) - U''\varphi = 0. \quad (\text{A.1})$$

This is a second order differential equation and therefore, it has to have two linearly independent solutions. Heisenberg solved the Rayleigh equation by expanding φ analytically in terms of α^2 (where he assumed that $\alpha^2 \sim 0$) as

$$\varphi(y) = \sum_{n=0}^{\infty} \alpha^{2n} \varphi_n(y).$$

Replacing φ into (A.1) gives an $\mathcal{O}(1)$ equation

$$(U - c)\varphi_0'' - U''\varphi_0 = 0$$

which has a general solution

$$\varphi_0(y) = k_0(U - c) + k_1(U - c) \int_{y_0}^y (U - c)^{-2} dy$$

where y_0 is an arbitrary constant and k_i are constants of integration. The constant y_0 can be fixed to any desired value, the only consequence is a resulting multiplicative factor, but here, $y_0 = 0$ denoting the channel centreline.

The terms of $\mathcal{O}(\alpha^{2n})$ for $n \in \mathbb{N}$ are

$$(U - c)\varphi_n'' - U''\varphi_n = (U - c)\varphi_{n-1}$$

with a solution that can be recursively defined as

$$\varphi_n(y) = (U - c) \int_0^y (U - c)^{-2} \int_0^{y_1} (U - c)\varphi_{n-1} dy_2 dy_1. \quad (\text{A.2})$$

For example,

$$\begin{aligned} \varphi_1(y) &= k_0(U - c) \int_0^y (U - c)^{-2} \int_0^{y_1} (U - c)^2 dy_2 dy_1 \\ &+ k_1(U - c) \int_0^y (U - c)^{-2} \int_0^{y_1} (U - c)^2 \int_0^{y_2} (U - c)^{-2} dy_3 dy_2 dy_1. \end{aligned}$$

Notice that φ_0 and φ_1 have even and odd parts and therefore φ can be written in a different form as

$$\varphi(y) = k_0\varphi^e(y) + k_1\varphi^o(y).$$

Here, φ has been decoupled into its even and odd parts represented by φ^e and

φ^o respectively. These individual components are:

$$\varphi^e(y) = (U - c) \left[1 + \alpha^2 \int_0^y (U - c)^{-2} \int_0^{y_1} (U - c)^2 dy_2 dy_1 + \mathcal{O}(\alpha^4) \right]$$

$$\varphi^o(y) = (U - c) \int_0^y (U - c)^{-2} \left[1 + \alpha^2 \int_0^{y_1} (U - c)^2 \int_0^{y_2} (U - c)^{-2} dy_3 dy_2 + \mathcal{O}(\alpha^4) \right] dy_1.$$

Therefore in general, the Heisenberg solution can be written as

$$\varphi_j(y) = k_j (U - c) \sum_{n=0}^{\infty} \alpha^{2n} q_{j,n}(y) \quad \text{for } j = 0, 1$$

$$\text{where } q_{0,0}(y) = 1, \quad q_{1,0}(y) = \int_{y_0}^y (U - c)^{-1} dy$$

$$q_{j,n+1}(y) = \int_{y_0}^y (U - c)^{-2} \int_{y_0}^y (U - c)^2 q_{j,n}(y) dy dy \quad \forall n \in \mathbb{N}_0. \quad (\text{A.3})$$

The case when $j = 0$ corresponds to the even solution while $j = 1$ corresponds to the odd solution. These expressions are uniformly convergent for bounded values for α and a fixed value of $y \neq 0$.

Appendix B

Chebyshev Polynomials

This part of the appendix lists some properties of Chebyshev polynomials, along with useful formulae for their derivatives and integrals. These are used extensively in order to discretise flow variables in the y -direction in Chapters 3 and 4.

Definition

- For any $n \in \mathbb{N}_0$, the n^{th} Chebyshev polynomial of the first kind is defined as:

$$T_n(y) := \cos(n \cos^{-1}(y)) \quad \forall y \in [-1, 1].$$

- The Chebyshev polynomial $T_n(y)$ is one of the two linearly independent solutions of the Chebyshev differential equation of degree $n \in \mathbb{N}_0$

$$(1 - y^2)u(y)'' - yu(y)' + n^2u(y) = 0 \quad \text{for } y \in [-1, 1].$$

The other solution (also known as the Chebyshev polynomial of the second kind and denoted $U_n(y)$) will not be discussed.

- The Chebyshev polynomials are orthogonal with the weighting $(1-y^2)^{-\frac{1}{2}}$, in other words:

$$\int_{-1}^1 \frac{T_n(y)T_m(y)}{\sqrt{1-y^2}} dy = \begin{cases} 0 & n \neq m \\ \pi & n = m = 0 \\ \frac{\pi}{2} & n = m \neq 0. \end{cases}$$

- The Chebyshev polynomials can be defined recursively for $y \in [-1, 1]$ as:

$$T_n(y) = \begin{cases} 1 & n = 0 \\ y & n = 1 \\ 2yT_{n-1}(y) - T_{n-2}(y) & n \geq 2 \end{cases}$$

- These recursive relations can be used to prove the following:

$$\begin{aligned} * \quad T_m(y)T_n(y) &= \frac{1}{2} (T_{m+n}(y) + T_{|m-n|}(y)) \quad \forall m, n \in \mathbb{N}_0 \\ * \quad T_n(\pm 1) &= (\pm 1)^n \quad \forall n \in \mathbb{N}_0. \end{aligned}$$

Differentiation Formulae

- At $y = \pm 1$, the p^{th} derivative of $T_n(y)$ is given by:

$$\left. \frac{d^p T_n}{dy^p} \right|_{y=\pm 1} = (\pm 1)^{n+p} \prod_{k=0}^{p-1} \frac{n^2 - k^2}{2k + 1} \quad \text{for } 1 \leq p \leq n.$$

- The Chebyshev polynomial $T_n(y)$ has:

* Extrema at the *Gauss-Lobatto points*:

$$y_j = \cos\left(\frac{j}{n}\pi\right) \quad \text{for } j = 0, 1, \dots, n.$$

* Roots at the *Chebyshev nodes*:

$$\tilde{y}_j = \cos\left(\frac{2j-1}{n}\pi\right) \quad \text{for } j = 0, 1, \dots, n.$$

- The k^{th} derivative of the n^{th} Chebyshev polynomial T_n evaluated at the Gauss-Lobatto points is given by:

$$T_n^{(k)}(y_j) = \begin{cases} 0 & n = 0 \\ T_0^{(k-1)}(y_j) & n = 1 \\ 4T_1^{(k-1)}(y_j) & n = 2 \\ 2nT_{n-1}^{(k-1)}(y_j) + \frac{n}{n-1}T_{n-1}^{(k)}(y_j) & n = 3, 4, \dots, N \end{cases}$$

Integration Formulae

For a function $Y = Y(y)$ and $n \in \mathbb{N}_0$, the following integration recipes will prove useful in Chapter 5:

$$* \int_0^y T_n(y_1) dy_1 = \begin{cases} T_1 & n = 0 \\ \frac{1}{4}(T_2 + T_0) & n = 1 \\ \frac{1}{2}\left(\frac{1}{n+1}T_{n+1} - \frac{1}{n-1}T_{n-1}\right) & n \geq 2 \end{cases}$$

$$* \int_0^y \int_0^{y_1} T_n(y_2) \, dy_2 \, dy_1 = \begin{cases} \frac{1}{4} (T_2 + T_0) & n = 0 \\ \frac{1}{24} (T_3 + 3T_1) & n = 1 \\ \frac{1}{48} (T_4 - 8T_2 - 9T_0) & n = 2 \\ \frac{1}{4} \left(\frac{1}{(n+1)(n+2)} T_{n+2} - \frac{2}{(n+1)(n-1)} T_n + \frac{1}{(n-1)(n-2)} T_{n-2} \right) - c_n T_0 & n \geq 3 \end{cases}$$

$$\text{where } c_n = \begin{cases} 0 & \text{if } n \text{ is odd} \\ \frac{(-1)^{\frac{n}{2}}}{n^2 - 4} & \text{if } n \text{ is even} \end{cases}$$

$$* \int_{-1}^1 T_n(y) \, dy = \begin{cases} 0 & n = 1 \\ \frac{(-1)^{n+1}}{1-n^2} & \text{otherwise} \end{cases}$$

$$* \int_0^1 T_{2n}(y) \, dy = -\frac{1}{4n^2 - 1}.$$

Appendix C

Plotting Eigenfunctions

This part of the appendix describes the way in which the eigenfunctions φ can be plotted.

Suppose that an eigenvalue problem (given in (3.16)) has been solved in order to obtain an eigenvalue be it α, c or ω and its eigenvector \mathbf{a} . The corresponding eigenfunction φ can be written as a vector

$$\varphi(\mathbf{y}) \equiv (\varphi_0, \varphi_1, \varphi_2, \dots, \varphi_N)$$

$$\text{where } \varphi_n = \varphi(y_n) \quad \text{and} \quad y_n = \cos\left(\frac{\pi n}{N+1}\right)$$

where N is the highest degree of the Chebyshev polynomial taken in the ap-

proximation. The values of φ_n can be determined from the matrix equation

$$\begin{pmatrix} \varphi_0 \\ \varphi_1 \\ \varphi_2 \\ \vdots \\ \varphi_N \end{pmatrix} = \begin{pmatrix} T_0(y_0) & T_2(y_0) & T_4(y_0) & \dots & T_M(y_0) \\ T_0(y_1) & T_2(y_1) & T_4(y_1) & \dots & T_M(y_1) \\ T_0(y_2) & T_2(y_2) & T_4(y_2) & \dots & T_M(y_2) \\ \vdots & \vdots & \vdots & \ddots & \vdots \\ T_0(y_N) & T_2(y_N) & T_4(y_N) & \dots & T_M(y_N) \end{pmatrix} \begin{pmatrix} a_0 \\ a_2 \\ a_4 \\ \vdots \\ a_M \end{pmatrix}.$$

This provides an expression for φ in terms of its components and can therefore be used to plot the eigenfunctions which correspond to a given eigenvalue.

Appendix D

Reformulation of the Discretisation in Terms of α & ω

In this part of the appendix, the generalised eigenvalue problems in α and c are reformulated in order to have ω as the eigenvalue rather than c . The method in which this is performed is the same as the original derivation in Chapter 3. The boundary conditions are also reformulated accordingly and are incorporated into the last two rows of the matrices in question.

The generalised eigenvalue problems in α and c can be rewritten in terms of α and ω instead as:

$$(Z_4\alpha^4 + Z_3\alpha^3 + Z_2\alpha_2 + Z_1\alpha + Z_0)\mathbf{a} = \mathbf{0} \quad \text{and} \quad (\tilde{A}_2\omega^2 + \tilde{A}_1\omega + \tilde{A}_0)\mathbf{a} = \mathbf{0}.$$

The matrices of the system are:

$$\tilde{A}_0 = \begin{pmatrix} & & \left[\left[\frac{1}{iR} D_4 - \left(\frac{2\alpha^2}{iR} + \alpha U \right) D_2 \right] \right. \\ & & \left. + \left(\frac{1}{iR} \alpha^4 + U \alpha^3 - 2\alpha \right) D_0 \right] \\ -\alpha & -\alpha & -\alpha & \dots & -\alpha \\ \frac{B\alpha^4 + T\alpha^2 + K}{R^2} & \frac{B\alpha^4 + T\alpha^2 + K}{R^2} & \frac{B\alpha^4 + T\alpha^2 + K}{R^2} & \dots & \frac{B\alpha^4 + T\alpha^2 + K}{R^2} \end{pmatrix}$$

$$\tilde{A}_1 = \begin{pmatrix} & & & & [[D_2 - \alpha^2 D_0]] \\ 0 & 2 & 8 & \dots & 2M^2 \\ \frac{2}{3}\alpha - \frac{id}{R} & -\frac{2}{5}\alpha - \frac{id}{R} & \frac{2}{35}\alpha - \frac{id}{R} & \dots & \frac{6\alpha}{(4M^2-1)(4M^2-9)} - \frac{id}{R} \end{pmatrix}$$

$$\tilde{A}_2 = \begin{pmatrix} & & & & \left[\begin{array}{l} \text{Zero matrix of size} \\ (M-1) \times (M+1) \end{array} \right] \\ 0 & 0 & 0 & \dots & 0 \\ -1 - m & \frac{1}{3} - m & \frac{1}{15} - m & \dots & \frac{1}{4M^2-1} - m \end{pmatrix}$$

$$Z_0 = \begin{pmatrix} & & & & [[\frac{1}{iR} D_4 + \omega D_2]] \\ 0 & 2\omega & 8\omega & \dots & 2M^2\omega \\ (-1 - m)\omega^2 & (\frac{1}{3} - m)\omega^2 & (\frac{1}{15} - m)\omega^2 & \dots & (\frac{1}{4M^2-1} - m)\omega^2 \\ -\frac{id\omega}{R} + \frac{K}{R^2} & -\frac{id\omega}{R} + \frac{K}{R^2} & -\frac{id\omega}{R} + \frac{K}{R^2} & \dots & -\frac{id\omega}{R} + \frac{K}{R^2} \end{pmatrix}$$

$$Z_1 = \begin{pmatrix} & & & & [[-UD_2 - 2D_0]] \\ -1 & -1 & -1 & \dots & -1 \\ \frac{2}{3}\omega & -\frac{2}{5}\omega & \frac{2}{35}\omega & \dots & \frac{6\omega}{(4M^2-1)(4M^2-9)} \end{pmatrix}$$

$$Z_2 = \begin{pmatrix} & & [[-\frac{2}{iR}D_2 - \omega D_0]] & & \\ 0 & 0 & 0 & \dots & 0 \\ \frac{T}{R^2} & \frac{T}{R^2} & \frac{T}{R^2} & \dots & \frac{T}{R^2} \end{pmatrix}$$

$$Z_3 = \begin{pmatrix} & & [[UD_0]] & & \\ 0 & 0 & 0 & \dots & 0 \\ 0 & 0 & 0 & \dots & 0 \end{pmatrix}$$

$$Z_4 = \begin{pmatrix} & & [[\frac{1}{iR}D_0]] & & \\ 0 & 0 & 0 & \dots & 0 \\ \frac{B}{R^2} & \frac{B}{R^2} & \frac{B}{R^2} & \dots & \frac{B}{R^2} \end{pmatrix}.$$

The terms in the double square brackets ($[[\square]]$) are block matrices of size $(M - 1) \times (M + 1)$. These are determined from their respective forms in Appendix B (where the rows and columns of the matrices are labelled from 0 to N), the odd rows and columns are then eliminated and the last two rows removed in order to incorporate the boundary conditions.

Appendix E

Full Forms of M_3 & M_5

In §4.5 Chapter 4, the matrices M_3 and M_5 were introduced as the discretised forms of $\iint f$ and $\iint Uf$. The first rows of said matrices are eliminated in order to incorporate the boundary conditions while the last row of M_3 and the last two rows of M_5 are dispensed with as a consequence of the Tau method (due to Lanczos [80]).

Consider the Chebyshev expansion of the function f , namely

$$f(x, y, t) = \frac{1}{2}f_1(x, t)T_0(y) + \sum_{k=2}^N f_k(x, t)T_{2(k-1)}(y).$$

The full form of $\iint f$ is given as by

$$\begin{aligned} \iint f = & \left[\frac{f_1}{8} - \frac{3f_2}{16} + \sum_{k=3}^N f_k c_{2(k-1)} \right] T_0 \\ & + \sum_{k=2}^{N-1} \left([a_{23}^k f_{k-1} - 2a_{13}^k f_k + a_{12}^k f_{k+1}] T_{2(k-1)} \right) \\ & + [a_{23}^N f_{N-1} - 2a_{13}^N f_N] T_{2(N-1)} + a_{23}^{N+1} T_{2N} \quad (\text{E.1}) \end{aligned}$$

$$\text{where } a_{mn}^k = \frac{1}{4(2k-m)(2k-n)} \quad \text{and} \quad c_{2k} = \frac{(-1)^k}{4(k^2-1)}.$$

The c_k terms arise due to the indefinite integration but these terms are irrelevant since they are replaced by the boundary conditions. The corresponding matrix form M_3 will be

$$M_3 = \begin{pmatrix} \frac{1}{8} & -\frac{3}{16} & c_4 & c_6 & \cdots & c_{2(N-3)} & c_{2(N-2)} & c_{2(N-1)} \\ a_{23}^2 & -2a_{13}^2 & a_{12}^2 & & & & & \\ & a_{23}^3 & -2a_{13}^3 & a_{12}^3 & & & & \\ & & a_{23}^4 & -2a_{13}^4 & a_{12}^4 & & & \\ & & & \ddots & \ddots & \ddots & & \\ & & & & a_{23}^{N-2} & -2a_{13}^{N-2} & a_{12}^{N-2} & \\ & & & & & a_{23}^{N-1} & -2a_{13}^{N-1} & a_{12}^{N-1} \\ & & & & & & a_{23}^N & -2a_{13}^N \\ & & & & & & & a_{23}^{N+1} \end{pmatrix}.$$

Once again, the full form is not necessary since the last row is eliminated and the first row is replaced with one of the boundary conditions.

As for $\iint Uf$, the y -discretisation takes a far more complicated form:

$$\begin{aligned} \iint Uf &= \left[\frac{7}{64}f_1 - \frac{5}{32}f_2 + \frac{3}{64}f_3 + \frac{1}{4} \sum_{k=3}^{N-1} \left((f_{k-1} - 2f_k + f_{k+1}) c_{2k-2} \right) \right. \\ &+ \frac{1}{4} (f_{N-1} - 2f_N) c_{2N-2} + \left. \frac{1}{4} f_N c_{2N} \right] T_0 + [B_3^2 f_1 - 6b_{13}^2 f_2 + B_5^2 f_3 - b_{12}^2 f_4] T_2 \\ &+ \sum_{k=4}^{N-2} \left([-b_{23}^3 f_{k-2} + B_3^3 f_{k-1} - 6b_{13}^3 f_k + B_5^3 f_{k+1} - b_{12}^3 f_{k+2}] T_{2(k-1)} \right) \\ &+ [-b_{23}^{N-1} f_{N-3} + B_3^{N-1} f_{N-2} - 6b_{13}^{N-1} f_{N-1} + B_5^{N-1} f_N] T_{2N-4} \\ &+ [-b_{23}^N f_{N-2} + B_3^N f_{N-1} - 6b_{13}^N f_N] T_{2N-2} \\ &+ [-b_{23}^{N+1} f_{N-1} + B_3^{N+1} f_N] T_{2N} - b_{23}^{N+2} f_N T_{2N+2} \quad (\text{E.2}) \end{aligned}$$

where $b_{mn}^k = \frac{1}{16(2k-m)(2k-n)}$, $B_n^k = \frac{4k-n}{8(2k-1)(2k-2)(2k-3)}$

and $c_{2k} = \frac{(-1)^k}{4(k^2-1)}$.

The corresponding matrix representation M_5 is:

$$M_5 = \begin{pmatrix} \frac{7}{64} & \frac{-5+8c_4}{32} & \frac{3-32c_4+16c_6}{64} & C_6 & C_8 & \dots & C_{2(N-3)} & C_{2(N-2)} & C_{2(N-1)} \\ B_3^2 & -6b_{13}^2 & B_5^2 & -b_{12}^2 & & & & & \\ -b_{23}^3 & B_3^3 & -6b_{13}^3 & B_5^3 & -b_{12}^3 & & & & \\ & -b_{23}^4 & B_3^4 & -6b_{13}^4 & B_5^4 & -b_{12}^4 & & & \\ & & \ddots & \ddots & \ddots & \ddots & \ddots & & \\ & & & -b_{23}^{N-3} & B_3^{N-3} & -6b_{13}^{N-3} & B_5^{N-3} & -b_{12}^{N-3} & \\ & & & & -b_{23}^{N-2} & B_3^{N-2} & -6b_{13}^{N-2} & B_5^{N-2} & -b_{12}^{N-2} \\ & & & & & -b_{23}^{N-1} & B_3^{N-1} & -6b_{13}^{N-1} & B_5^{N-1} \\ & & & & & & -b_{23}^N & B_3^N & -6b_{13}^N \\ & & & & & & & -b_{23}^{N+1} & B_3^{N+1} \\ & & & & & & & & -b_{23}^{N+2} \end{pmatrix}$$

where $C_k = \frac{1}{4}(c_{k-2} - 2c_k + c_{k+2})$.

Appendix F

The Tau Method

This part of the appendix briefly describes the Tau method due to Lanczos [80]. This method is discussed by means of an example, in particular, the Airy differential equation

$$\frac{d^2y}{dx^2} - xy = 0 \quad x \in \mathbb{R}.$$

This differential equation has two linearly independent solutions represented as $\text{Ai}(x)$ and $\text{Bi}(x)$ for all $x \in \mathbb{R}$ but in order to demonstrate the Tau method, consider a power series expansion for y as

$$y(x) = \sum_{n=0}^{\infty} a_n x^n$$

for some coefficients a_n to be determined. Replacing the expansion into the Airy equation gives

$$2a_2 + \sum_{n=1}^{\infty} ([a_{n+2}(n+1)(n+2) - a_{n-1}] x^n) = 0.$$

The coefficients a_n can be determined by using the recursive relation

$$a_2 = 0, \quad a_{n+2} = \frac{1}{(n+1)(n+2)} a_{n-1} \quad \forall n \in \mathbb{N}$$

where the coefficients a_0 and a_1 can be determined from appropriate initial/boundary conditions, if so, all the coefficients can then be determined uniquely. Here, an infinite expansion is assumed and there is the distinct possibility that it may not converge in some cases. However if it does converge, then the range of convergence may or may not be finite and this issue needs to be addressed separately.

Suppose now that the power series expansion for y is truncated at some N , in other words, y takes the form

$$y(x) = \sum_{n=0}^N a_n x^n.$$

In this case, establishing a recurrence relation is not valid since it would require a non-zero a_{N+1} term. Replacing into the Airy differential equation gives

$$2a_2 + \sum_{n=1}^{N-2} \left(\left[a_{n+2}(n+1)(n+2) - a_{n-1} \right] x^n \right) - a_{N-2} x^{N-1} - a_{N-1} x^N - a_N x^{N+1} = 0.$$

This forms a set of $N+2$ equations (equating the coefficients of $x^0, x^1, x^2, \dots, x^{N+1}$) in $N+1$ unknowns (a_0, a_1, \dots, a_N) making the system overdetermined.

In order to deal with the overdetermination, some terms can be introduced to the right hand side of the Airy equation. These terms can be regarded as error terms which are introduced intentionally in order to solve the equation by means of a finite power series. In the case of the Airy differential equation,

a function that takes the form

$$\rho(x) = \tau_1 x^N + \tau_2 x^{N+1}.$$

can be introduced to the right hand side where τ_1 and τ_2 are *a priori* unknown constants. The resulting equation equates the highest powers of x with the τ terms and since they are regarded as error terms, they can then be dispensed with at a later point.

In general, the overdetermination can be removed by a having a right hand side term of the form

$$\rho(x) = \tau p_n(x)$$

for some polynomial p_n . This error term allows a truncated series expansion which is quite small near $x = 0$. The differential equation is hence, satisfied accurately in the neighbourhood of $x = 0$ but the error increases rapidly near $x = 1$. In practice, one τ term usually suffices and more than two terms are almost never required.

This is of course a very brief account of the Tau method by means of a relatively simplistic example. For further details, refer to Lanczos [80].

Appendix G

Thomas Algorithm (TDMA)

In this part of the appendix, the Thomas algorithm (otherwise known as the **Tri-Diagonal Matrix Algorithm**) and its modified form are described.

The Thomas algorithm is equivalent to Gaussian elimination and is used to solve banded systems of equations. In general, the Thomas algorithm is not always stable but it can be in some cases, say if the matrix is diagonally dominant. First, the Thomas algorithm is described for tridiagonal and pentadiagonal systems of equations, then the modified form is discussed which is when the matrix is banded and has a full first row.

Tridiagonal

Consider the tridiagonal system of equations

$$\begin{pmatrix} b_1 & c_1 & & & \\ a_2 & b_2 & c_2 & & \\ & \ddots & \ddots & \ddots & \\ & & a_{N-1} & b_{N-1} & c_{N-1} \\ & & & a_N & b_N \end{pmatrix} \begin{pmatrix} y_1 \\ y_2 \\ \vdots \\ y_{N-1} \\ y_N \end{pmatrix} = \begin{pmatrix} f_1 \\ f_2 \\ \vdots \\ f_{N-1} \\ f_N \end{pmatrix}.$$

where the a, b, c and f terms are known while the y terms are to be determined.

First, the a -diagonal can be eliminated using a forward sweep as follows:

$$b'_1 = b_1, \quad c'_1 = c_1, \quad f'_1 = f_1$$

$$b'_n = b_{n-1} - \frac{a_n c'_{n-1}}{b'_{n-1}}, \quad c'_n = c_n, \quad f'_n = f_n - \frac{a_n f'_{n-1}}{b'_{n-1}} \quad \forall n = 2, 3, \dots, N.$$

This eliminates the a -diagonal to give an upper diagonal system of equations:

$$\begin{pmatrix} b'_1 & c'_1 & & & \\ & b'_2 & c'_2 & & \\ & & \ddots & \ddots & \\ & & & b'_{N-1} & c'_{N-1} \\ & & & & b'_N \end{pmatrix} \begin{pmatrix} y_1 \\ y_2 \\ \vdots \\ y_{N-1} \\ y_N \end{pmatrix} = \begin{pmatrix} f'_1 \\ f'_2 \\ \vdots \\ f'_{N-1} \\ f'_N \end{pmatrix}.$$

This can then be solved by backward substitution using

$$y_N = \frac{f'_N}{b'_N} \quad \text{and} \quad y_n = \frac{f'_n - c'_n y_{n+1}}{b'_n} \quad \forall n = 1, 2, \dots, N-1.$$

Similarly, the same can be done to eliminate the superdiagonals first rather than the subdiagonals, giving a lower diagonal matrix (with two subdiagonals) which can be solved by forward substitution.

Modified Thomas Algorithm

For a tridiagonal matrix with a full first row, the Thomas algorithm needs to be modified slightly. During the backwards sweep, terms from the first row can be removed successively to give a lower/upper diagonal matrix. For the standard TDMA presented earlier, the matrix was converted to an upper diagonal matrix but for the sake of variety, the lower diagonal matrix is shown here.

Consider the system of equations

$$\begin{pmatrix} d_1 & d_1 & d_3 & d_4 & \dots & d_{N-1} & d_N \\ a_2 & b_2 & c_2 & & & & \\ & a_3 & b_3 & c_3 & & & \\ & & \ddots & \ddots & \ddots & & \\ & & & a_{N-2} & b_{N-2} & c_{N-2} & \\ & & & & a_{N-1} & b_{N-1} & c_{N-1} \\ & & & & & a_N & b_N \end{pmatrix} \begin{pmatrix} y_1 \\ y_2 \\ y_3 \\ \vdots \\ y_{N-2} \\ y_{N-1} \\ y_N \end{pmatrix} = \begin{pmatrix} f_1 \\ f_2 \\ f_3 \\ \vdots \\ f_{N-2} \\ f_{N-1} \\ f_N \end{pmatrix}.$$

A procedure similar to the standard tridiagonal form of the Thomas algorithm is used to eliminate the c -diagonal first by using the transformations:

$$a'_N = a_N, \quad b'_N = b_N, \quad f'_N = f_N$$

$$a'_n = a_n, \quad b'_n = b_n - \frac{a_{n+1}c_n}{b'_{n+1}}, \quad f'_n = f_n - \frac{f_{n+1}c_n}{b'_{n+1}} \quad \forall n = 2, 3, \dots, N-1.$$

This reduces the system of equations to a lower diagonal matrix with a full first row as:

$$\begin{pmatrix} d_1 & d_1 & d_3 & d_4 & \dots & d_{N-1} & d_N \\ a'_2 & b'_2 & & & & & \\ & a'_3 & b'_3 & & & & \\ & & \ddots & \ddots & & & \\ & & & a'_{N-2} & b'_{N-2} & & \\ & & & & a'_{N-1} & b'_{N-1} & \\ & & & & & a'_N & b'_N \end{pmatrix} \begin{pmatrix} y_1 \\ y_2 \\ y_3 \\ \vdots \\ y_{N-2} \\ y_{N-1} \\ y_N \end{pmatrix} = \begin{pmatrix} f_1 \\ f'_2 \\ f'_3 \\ \vdots \\ f'_{N-2} \\ f'_{N-1} \\ f'_N \end{pmatrix} .$$

During the backward substitution, terms from the first row can be eliminated successively. The first row gives the equation

$$d_1 y_1 + d_2 y_2 + \dots + d_{N-1} y_{N-1} + d_N y_N = f_1$$

and after eliminating $N - n$ terms (for some $n \in \{1, 2, \dots, N\}$), this equation reduces to

$$d_1 y_1 + d_2 y_2 + \dots + d_{n-1} y_{n-1} + d'_n y_n = f_1^{(n)}$$

$$\text{where } d'_N = d_N, \quad f_1^{(N)} = f_1,$$

$$d'_n = d_n - \frac{a_{n+1} d'_{n+1}}{b'_{n+1}}, \quad f_1^{(n)} = f_1^{(n+1)} - \frac{f'_{n+1} d'_{n+1}}{b'_{n+1}} \quad \forall n = 1, 2, \dots, N - 1.$$

Repeating this elimination procedure for the elements of the first row leaves one term at the start, reducing the system of equations to a lower diagonal

Appendix H

Identification of Absolute Instabilities via Briggs' Method

Briggs' method for identifying absolute instabilities will be discussed here briefly. This procedure was initially developed by Briggs [11] in his work on plasma physics (the description provided here is taken from Schmid & Henningson [115]). An earlier mention of this method can be found in a 10 volume Course on Theoretical Physics written by Landau & Lifchitz in 1953. This procedure is similar to the steepest descent method however Briggs' method can distinguish between branches originating in different half-spaces and this criterion is imperative for identifying absolute instabilities.

Suppose that for fixed Reynolds number and wall parameters, the Orr-Sommerfeld equation and its boundary conditions give the dispersion relation

$$\mathcal{D}(\alpha, \omega; R) = 0.$$

If the wavenumber α is real and the temporal frequency ω is complex then the problem is in its *temporal form*, on the other hand, if ω is real and α is

complex then the problem is in its *spatial form*. If both α and ω are complex then the problem is termed *spatio-temporal*.

In the context of hydrodynamic stability theory, the spatio-temporal form of the Orr-Sommerfeld equation was studied by Betchov & Criminale [8] for inviscid fluid flows. Briggs [11] then proposed a proof for deriving the general criterion for absolute instabilities, he was then attributed with the method which now bears his name and has become a standards in the field.

In the years that followed, Gaster [54] investigated the eigenvalues of the Orr-Sommerfeld equation with non-negligible viscosity and found that the singularities obtained by Betchov & Criminale [8] still persisted for finite Reynolds numbers. These singularities must occur on the complex c -plane when

$$\frac{dc}{d\alpha} = 0$$

while the singularities on the complex ω -plane correspond to locations where

$$\frac{d\omega}{d\alpha} = 0.$$

Hence, this implies that the disturbance wavepacket has a zero group velocity. Briggs' method was employed in order to investigate absolute instabilities in other flow configurations such as a finite compliant wall sections in a semi-infinite flow by Wiplier & Ehrenstein [131] and the rotating disc by Lingwood [85] [86].

Briggs' method focusses on the dispersion relation in the form $\omega(\alpha) = 0$ and the branch point singularities ω^* which lie on the complex ω -plane that satisfy

$$\frac{\partial\omega^*}{\partial\alpha} = 0 \quad \text{for some } \omega^* \in \mathbb{C}.$$

The type of instability that arises is dictated by the positions of ω^* on the complex ω -plane. If *all* these branch point singularities ω^* lie on the bottom half-space (i.e. $\Im(\omega^*) < 0$), then the instability is *convective*. If at least one is in the upper half-space, then the instability is *absolute*.

In order to find the branch point singularities, a fixed value of $\omega \in \mathbb{C}$ is chosen, this frequency corresponds to eigenvalues on the complex α -plane which are a result of solving the dispersion relation. The real and imaginary parts of ω can then be varied and the corresponding roots on the complex α -plane are traced. If a *saddle point* is formed which corresponds to a complex frequency whose imaginary part is positive, then the instability is absolute *provided* that the branches forming the saddle point originate from different half-spaces, this is what is known as *Briggs' criterion* and is best described diagrammatically below.

Figure H.1 shows a generic example of how Briggs' method works. The left figure shows a grid of horizontal and vertical lines on the complex ω -plane; the horizontal lines represent choices of ω where $\Im(\omega)$ is fixed and $\Re(\omega)$ is varied while the vertical lines represent the opposite. Each line corresponds to a curve traced out by the eigenvalues in the wavenumber space which form a saddle point (marked by the red dot on the complex α -plane). In turn, this saddle point corresponds to a complex frequency (given by the red dot) which is the determining factor as to whether or not the flow is absolutely unstable. The two conditions that have to be satisfied for absolute instability are:

- *Unstable temporal frequency*: The saddle point corresponds to a complex temporal frequency ω whose imaginary part is positive.
- *Briggs' criterion*: The branches that form the saddle point on the complex α -plane originate from different half-spaces.

For the generic example in Figure H.1, the saddle point corresponds to a value on the complex ω -plane whose imaginary part is positive *but* the branches do not originate from different half-spaces, therefore the instability is *not* absolute in this case. This example is merely a demonstration of the workings of Briggs' method.

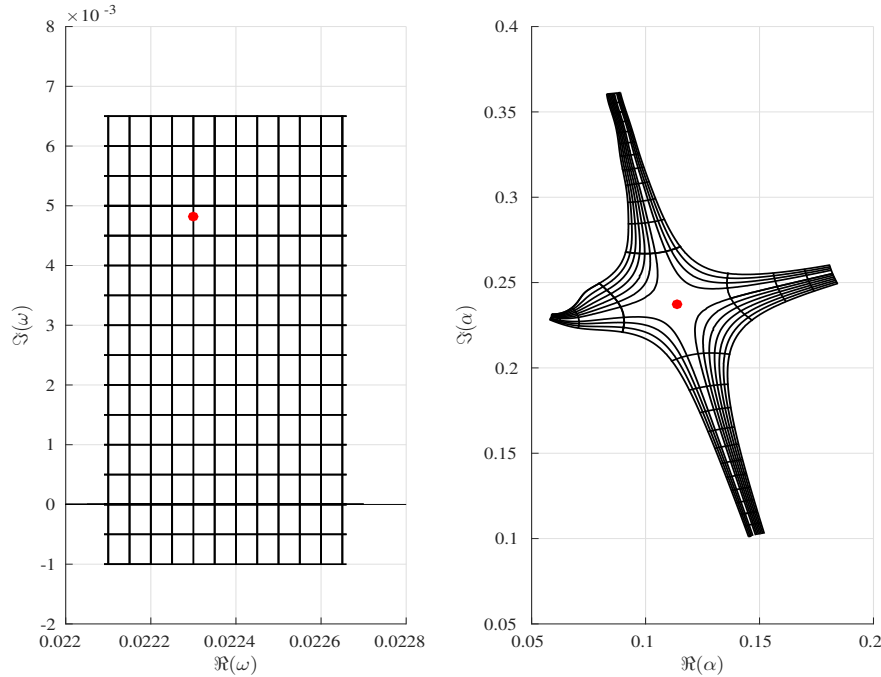


Figure H.1: Generic demonstration of Briggs' method.

An alternative approach was developed by Triantafyllou *et al.* [123] which considered the reverse problem. Suppose a wavenumber $\alpha \in \mathbb{C}$ is chosen, this gives roots of the dispersion relation as eigenvalues on the complex ω -plane. If the real and imaginary parts of α are varied (in the same grid fashion as in Figure H.1), then the temporal contours trace out a cusp on the complex ω -plane instead of a saddle point to indicate whether the instability is absolute. In the literature, this method is usually referred to as Bers' method

Bibliography

- [1] <http://uk.mathworks.com/help/matlab/ref/polyeig.html>.
- [2] Y. G. Aleyev. Nekton, Dr. W. *Junk, The Hague, 435pp*, 1977.
- [3] G. Angelidis and A. Semlyen. Improved Methodologies for the Calculation of Critical Eigenvalues in Small Signal Stability Analysis. *IEEE Transactions on Power Systems*, 11(3):1209–1217, 1996.
- [4] R. Bale, M. Hao, A. P. S. Bhalla, N. Patel, and N. a. Patankar. Gray’s paradox: A fluid mechanical perspective. *Scientific reports*, 4:5904, 2014.
- [5] T. B. Benjamin. Effects of a flexible boundary on hydrodynamic stability. *Journal of Fluid Mechanics*, 9(4):513–532, 1960.
- [6] T. B. Benjamin. The threefold classification of unstable disturbances in flexible surfaces bounding inviscid flows. *Journal of Fluid Mechanics*, 16(03):436, 1963.
- [7] T. B. Benjamin. Fluid flow with flexible boundaries. In *Applied Mechanics*, pages 109–128. Springer Berlin Heidelberg, 1966.
- [8] R. Betchov and W. O. Criminale. Stability of Parallel Flows. *Applied Mathematics and Mechanics Series*, 10, 1967.

-
- [9] D. Bourne. Hydrodynamic stability, the Chebyshev tau method and spurious eigenvalues. *Continuum Mechanics and Thermodynamics*, 15:571–579, 2003.
- [10] T. J. Bridges and P. J. Morris. Differential eigenvalue problems in which the parameter appears nonlinearly. *Journal of Computational Physics*, 55(3):437–460, 1984.
- [11] R. J. Briggs. Electron-stream interaction with plasmas. *Electron-stream interaction with plasmas*, 1964.
- [12] M. A. Burke, A. D. Lucey, R. M. Howell, and N. S. Elliott. Stability of a flexible insert in one wall of an inviscid channel flow. *Journal of Fluids and Structures*, 48:435–450, 2014.
- [13] W. B. Bush and F. E. Fendell. Asymptotic analysis of turbulent channel and boundary-layer flow. *Journal of Fluid Mechanics*, 56(04):657–681, 1972.
- [14] P. W. Carpenter. Status of Transition Delay using Compliant Walls. *Viscous Drag Reduction in Boundary Layers*, 123:79–113, 1990.
- [15] P. W. Carpenter. Optimization of multiple-panel compliant walls for delay of laminar-turbulent transition. *AIAA journal*, 31(7):1187–1188, 1993.
- [16] P. W. Carpenter. Can Boundary-Layer Turbulence be Eliminated Without the Use of Auxilliary Power? *Proceedings of Flow Acoustics: A Technology Audit, Ecole Centrale de Lyon, France*, pages 84–86, 1994.
- [17] P. W. Carpenter. Current status of the use of wall compliance for laminar-flow control. *Experimental Thermal and Fluid Science*, 16(12):133–140, 1998.

- [18] P. W. Carpenter. *Propagation of waves across junctions between rigid and compliant walls*. Kluwer Academic Publishers, 2003.
- [19] P. W. Carpenter, C. Davies, and A. D. Lucey. Hydrodynamics and compliant walls: Does the dolphin have a secret? *Current Science*, 79(6):758–765, 2000.
- [20] P. W. Carpenter and J. S. B. Gajjar. A general theory for two- and three-dimensional wall-mode instabilities in boundary layers over isotropic and anisotropic compliant walls. *Theoretical and Computational Fluid Dynamics*, 1(6):349–378, 1990.
- [21] P. W. Carpenter and A. D. Garrad. The hydrodynamic stability of flow over Kramer-type compliant surfaces. Part 1. Tollmien-Schlichting instabilities. *Journal of Fluid Mechanics*, 155:465–510, 1985.
- [22] P. W. Carpenter and A. D. Garrad. The hydrodynamic stability of flow over Kramer-type compliant surfaces. Part 2. Flow-induced surface instabilities. *Journal of Fluid Mechanics*, 170:199–232, 1986.
- [23] P. W. Carpenter and P. J. Morris. The effect of anisotropic wall compliance on boundary-layer stability and transition. *Journal of Fluid Mechanics*, 218:171–223, 1990.
- [24] F. Charru. *Hydrodynamic Instabilities, Vol. 37*. Cambridge University Press, first edition, 2011.
- [25] S. J. Cowley and X. Wu. Asymptotic Approaches to Transition Modelling. *Agard, Special Course on Progress in Transition Modelling*, 1:1–38, 1994.
- [26] D. Crighton and J. Oswell. Fluid loading with mean flow. I. Response of an elastic plate to localized excitation. *Philosophical Transactions of the*

-
- Royal Society of London. Series A: Physical and Engineering Sciences*, 335(1639):557–592, 1991.
- [27] G. Danabasoglu, S. Biringen, and C. L. Streett. Spatial simulation of instability control by periodic suction blowing. *Physics of Fluids A: Fluid Dynamics*, 3(9):2138–2147, 1991.
- [28] C. Davies. *Evolution of Tollmien-Schlichting waves over a compliant panel*. PhD thesis, 1995.
- [29] C. Davies. Convective and absolute instabilities of flow over compliant walls. *Flow Past Highly Compliant Boundaries and in Collapsible Tubes: Proceedings of the IUTAM Symposium held at the University of Warwick, United Kingdom, 2630 March 2001*, 2:69–93, 2003.
- [30] C. Davies and P. W. Carpenter. Instabilities in a plane channel flow between compliant walls. *Journal of Fluid Mechanics*, 352:205–243, 1997.
- [31] C. Davies and P. W. Carpenter. Numerical simulation of the evolution of Tollmien-Schlichting waves over finite compliant panels. *Journal of Fluid Mechanics*, 335:361–392, 1997.
- [32] C. Davies and P. W. Carpenter. A Novel Velocity-Vorticity Formulation of the Navier-Stokes Equations with Applications to Boundary Layer Disturbance Evolution. *Journal of Computational Physics*, 172(1):119–165, 2001.
- [33] J. A. Domaradzki and R. W. Metcalfe. Stabilization of laminar boundary layers by compliant membranes. *Physics of Fluids*, 30(3):695, 1987.
- [34] T. Driscoll and N. Hale. Rectangular spectral collocation. *IMA Journal of Numerical Analysis*, pages 1–25, 2015.

- [35] D. Empfield. More to the Story on Wetsuits to be Worn in the Olympics
<http://www.slowtwitch.com/mainheadings/features/ituwetsuits.html>,
1999.
- [36] H. F. Fasel. Investigation of the stability of boundary layers by a finite-difference model of the NavierStokes equations. *Journal of Fluid Mechanics*, 78:355–383, 1976.
- [37] H. F. Fasel. Recent developments in the numerical solution of the Navier-Stokes equations and hydrodynamic stability problems. *Computational fluid dynamics.(A80-37230 15-34) Washington, DC, Hemisphere Publishing Corp.*, 1:167–279, 1980.
- [38] H. F. Fasel and U. W. E. Konzelmann. Non-parallel stability of a flat-plate boundary layer using the complete Navier-Stokes equations. *J. Fluid Mech.*, 221:311–347, 1990.
- [39] H. F. Fasel, U. Rist, and U. W. E. Konzelmann. Numerical investigation of the three-dimensional development in boundary-layer transition. *AIAA Journal*, 28:29–37, 1990.
- [40] F. E. Fish. Comparative Kinematics and Hydrodynamics of Odontocete Cetaceans : Morphological and Ecological Correlates With Swimming Performance. 2877:2867–2877, 1998.
- [41] F. E. Fish. Review of Dolphin Hydrodynamics and Swimming Performance. *Review of Dolphin*, page 193, 1999.
- [42] F. E. Fish. Review of Dolphin Hydrodynamics and Swimming Performance. *Review of Dolphin*, page 193, 1999.
- [43] F. E. Fish. A porpoise for power. *Journal of Experimental Biology* 208(6):977-978. 2005., page 2, 2005.

-
- [44] F. E. Fish and C. A. Hui. Dolphin swimming—a review. *Mammal Review*, 21(4):181–195, 1991.
- [45] F. E. Fish and J. J. Rohr. Review of dolphin hydrodynamics and swimming performance. *No. SPAWAR/CA-TR-1801. Space and naval warfare systems command San Diego CA*, 1999.
- [46] M. Gad-el Hak. Flow Control. *Applied Mechanics Reviews*, 42(10):261–293, 1989.
- [47] M. Gad-el Hak. Compliant Coatings: A Decade of Progress. *Applied Mechanics Reviews*, 49(10S):S147, 1996.
- [48] M. Gad-El-Hak. Compliant coatings: the simpler alternative. *Experimental Thermal and Fluid Science*, 16(1-2):141–156, 1998.
- [49] M. Gad-el hak. Drag Reduction Using Compliant Walls. In *Flow Past Highly Compliant Boundaries and in Collapsible Tubes: Proceedings of the IUTAM Symposium held at the University of Warwick, United Kingdom, 2630 March 2001*, chapter 9, pages 191–229. Kluwer Academic Publishers, 2003.
- [50] J. S. B. Gajjar and P. Sibanda. The hydrodynamic stability of channel flow with compliant boundaries. *Theoretical and Computational Fluid Dynamics*, 8(2):105–129, 1996.
- [51] J. S. B. Gajjar and F. T. Smith. On the global instability of free disturbances with a time-dependent nonlinear viscous critical layer. *Journal of Fluid Mechanics*, 157(-1):53, 1985.
- [52] S. J. Garrett and N. Peake. The absolute instability of the boundary layer on a rotating cone. *European Journal of Mechanics, B/Fluids*, 26(3):344–353, 2007.

- [53] M. Gaster. A note on the relation between temporally-increasing and spatially-increasing disturbances in hydrodynamic stability. *Journal of Fluid Mechanics*, 14(02):222, 1962.
- [54] M. Gaster. Growth of Disturbances in Both Space and Time. *Physics of Fluids*, 11(4):723, 1968.
- [55] M. Gaster. Is the dolphin a red herring? *Turbulence management and relaminarisation*, pages 285–304, 1987.
- [56] T. B. Gatski. Review of incompressible fluid flow computations using the vorticity-velocity formulation. *Applied Numerical Mathematics*, 7(3):227–239, mar 1991.
- [57] N. Gavriely, T. R. Shee, D. W. Cugell, and J. B. Grotberg. Flutter in flow-limited collapsible tubes: a mechanism for generation of wheezes, 1989.
- [58] J. Gray. Studies In Animal Locomotion VI. The propulsive powers of the dolphin. *The Journal of Experimental Biology*, 13:192–199, 1936.
- [59] C. H. Green and C. H. Ellen. The stability of plane poiseuille flow between flexible walls. *Journal of Fluid Mechanics*, 51(2):403–416, 1972.
- [60] J. B. Grotberg. Fluid-dynamic flapping of a collapsible channel: sound generation and flow limitation. *Journal of Biomechanics*, 13(1975):219–230, 1980.
- [61] J. B. Grotberg. Pulmonary flow and transport phenomena. *Annual Review of Fluid Mechanics*, 26:529–571, 1994.
- [62] J. B. Grotberg and O. E. Jensen. Biofluid Mechanics in Flexible Tubes. *Annual Review of Fluid Mechanics*, 36:121–147, 2004.

-
- [63] J. B. Grotberg and T. R. Shee. Compressible-Flow Channel Flutter. *Journal of Fluid Mechanics*, 159:175–193, 1985.
- [64] A. Goussis and A. Bottaro. Instabilities of the flow in a curved channel with compliant walls. *Proceedings of the Royal Society A: Mathematical, Physical and Engineering Sciences*, 463(2085):2201–2222, 2007.
- [65] P. Hall. The Linear Stability of Flat Stokes Layers. *Proceedings of the Royal Society A: Mathematical, Physical and Engineering Sciences*, 359(1697):151–166, 1978.
- [66] P. Hall. An asymptotic investigation of the stationary modes of instability of the boundary layer on a rotating disc. *Proceedings of the Royal Society A: Mathematical, Physical and Engineering Sciences*, 406(1830):93–106, 1986.
- [67] P. Hall. On the instability of Stokes layers at high Reynolds numbers. *Journal of Fluid Mechanics*, 482:1–15, 2003.
- [68] J. J. Healey. On the neutral curve of the flat-plate boundary layer: comparison between experiment, OrrSommerfeld theory and asymptotic theory. *Journal of Fluid Mechanics*, 288:59, 1995.
- [69] C. Heaney. The numerical simulation of wavepackets in a transitional boundary layer. (May), 2007.
- [70] W. Heisenberg. Uber Stabilitat und Turbulenz von Flussigkeitsstromen. *Annalen der Physik*, 74(15):577–627, 1924.
- [71] P. Huerre and P. A. Monkewitz. Local and Global Instabilities in Spatially Developing Flows. *Annual Review of Fluid Mechanics*, 22:473–537, 1990.

- [72] M. P. Juniper, A. Hanifi, and V. Theofilis. Modal Stability Theory. *Applied Mechanics Reviews*, 66(2):021004, 2014.
- [73] K. W. Morton and D. F. Mayers. *Numerical Solution of Partial Differential Equations*. Cambridge University Press, 2005.
- [74] E. Kim and H. Choi. Spacetime characteristics of a compliant wall in a turbulent channel flow. *Journal of Fluid Mechanics*, 756:30–53, 2014.
- [75] M. O. Kramer. Boundary Layer Stabilization by Disturbed Damping. *Journal of the American Society for Naval Engineers*, 72(1):25–34, 1960.
- [76] M. O. Kramer. The Dolphin’s Secret. *Jouranl of the American Society for Naval Engineers*, 73(1):103–108, 1961.
- [77] M. O. Kramer. Hydrodynamics of the Dolphin. *Advances in Hydro-science*, 2:111–130, 1965.
- [78] M. O. Kramer. Boundary Layer Control. *Naval Engineers Journal*, 89(5):41–45, 1977.
- [79] P. Lancaster. *Lambda-Matrices and Vibrating Systems*. Courier Corporation, 2011.
- [80] C. Lanczos. *Applied Analysis*. Courier Corporation, 1988.
- [81] M. T. Landahl. On the stability of a laminar incompressible boundary layer over a flexible surface. *Journal of Fluid Mechanics*, 13(04):609–632, 1962.
- [82] T. Lee, M. Fisher, and W. H. Schwarz. Investigation of the effects of a compliant surface on boundary-layer stability. *Journal of Fluid Mechanics*, 288(-1):37, 1995.

-
- [83] S. K. Lele. Compact finite difference schemes with spectral-like resolution. *Journal of Computational Physics*, 103:16–42, 1992.
- [84] J. Lerner and E. Knobloch. The Long-Wave Instability of a Defect in a Uniform Parallel Shear. *Journal of Fluid Mechanics*, 189(1):117–134, 1988.
- [85] R. J. Lingwood. Absolute instability of the rotating-disk boundary layer. *Laminar-Turbulent Transition: IUTAM Symposium, Sendai/Japan, September 59, 1994*, pages 389–396, 1995.
- [86] R. J. Lingwood. Absolute instability of the Ekman layer and related rotating flows. *Journal of Fluid Mechanics*, 331:405–428, 1997.
- [87] A. D. Lucey. The excitation of waves on a flexible panel in a uniform flow. *Philosophical Transactions of the Royal Society A: Mathematical, Physical and Engineering Sciences*, 356(1749):2999–3039, 1998.
- [88] A. D. Lucey. Wave excitation on flexible walls in the presence of a fluid flow. *Flow Past Highly Compliant Boundaries and in Collapsible Tubes: Proceedings of the IUTAM Symposium held at the University of Warwick, United Kingdom, 2630 March 2001*, pages 119–145, 2003.
- [89] A. D. Lucey and P. W. Carpenter. A numerical simulation of the interaction of a compliant wall and inviscid flow. *Journal of Fluid Mechanics*, 234:121–146, 1992.
- [90] A. D. Lucey and P. W. Carpenter. On the difference between the hydroelastic instability of infinite and very long compliant panels, 1993.
- [91] A. D. Lucey and P. W. Carpenter. Boundary layer instability over compliant walls: Comparison between theory and experiment. *Physics of Fluids*, 7(10):2355, 1995.

- [92] M. Luhar, A. S. Sharma, and B. J. McKeon. A framework for studying the effect of compliant surfaces on wall turbulence. *Journal of Fluid Mechanics*, 768(Benjamin 1963):415–441, 2015.
- [93] J. Luo and X. Wu. On the linear instability of a finite Stokes layer: Instantaneous versus Floquet modes. *Physics of Fluids*, 22(5):054106, 2010.
- [94] X. Y. Luo and T. J. Pedley. A numerical simulation of unsteady flow in a two- dimensional collapsible channel. *Journal of Fluid Mechanics*, 314:191–225, 1996.
- [95] X. Y. Luo and T. J. Pedley. The effects of wall inertia on flow in a two- dimensional collapsible channel. *Journal of Fluid Mechanics*, 363:253–280, 1998.
- [96] X. Y. Luo and T. J. Pedley. Multiple solutions and flow limitation in collapsible channel flows. *Journal of Fluid Mechanics*, 420:301–324, 2000.
- [97] J. Maple. Single and Multiple Boundary Layer Phenomena - Examples. *Dynamics at the Horsetooth*, 2A, 2010.
- [98] A. Marathe and R. Govindarajan. Nonlinear Dynamical Systems, Their Stability, and Chaos. *Applied Mechanics Reviews*, 66(2):021002, 2014.
- [99] G. D. McBain, T. H. Chubb, and S. W. Armfield. Numerical solution of the Orr-Sommerfeld equation using the viscous Green function and split-Gaussian quadrature. *Journal of Computational and Applied Mathematics*, 224(1):397–404, 2009.
- [100] S. A. Metcalfe, R. W., Battistoni, F., Ekeroot, J., & Orszag. Evolution of boundary layer flow over a compliant wall during transition to turbulence. *Boundary Layer Transition and Control*, 1:36, 1991.

-
- [101] J. A. Moriarty and J. B. Grotberg. Flow-induced instabilities of a mucous-serous bilayer. *Journal Of Fluid Mechanics*, 397:1–22, 1999.
- [102] K. W. Morton and D. F. Mayers. Numerical Solution of Partial Differential Equations. *Computers and Mathematics with Applications*, 62:1–28, 2005.
- [103] A. Nayfeh. Triple-deck structure. *Computers & fluids*, 20(3):269–292, 1991.
- [104] S. A. Orszag. Accurate solution of the OrrSommerfeld stability equation. *Journal of Fluid Mechanics*, 50(04):689, 1971.
- [105] S. A. Orszag. Numerical simulation of incompressible flows within simple boundaries: I. Galerkin (spectral) representations. *Studies in Applied Mathematics*, 50(4):293–327, 1971.
- [106] V. V. Pavlov. Dolphin skin as a natural anisotropic compliant wall. *Bioinspiration & biomimetics*, 1(2):31–40, 2006.
- [107] T. Pedley and X. Luo. Modelling flow and oscillations in collapsible tubes. *Theoretical and computational fluid dynamics*, 10(1):277–294, 1998.
- [108] R. Peyret. *Spectral Methods for Incompressible Viscous Flow, Vol. 148*. Springer Science & Buisness Media, 2013.
- [109] S. C. Reddy, P. J. Schmid, and D. S. Henningson. The pseudo-spectra of the Orr-Sommerfeld operator. *SIAM Journal of Applied Mathematics*, 53(1):15–47, 1992.

- [110] S. H. Ridgway and D. A. Carder. Features of dolphin skin with potential hydrodynamic importance. *IEEE Engineering in Medicine and Biology Magazine*, 12(3):83–88, 1993.
- [111] J. J. Riley, M. Gad-el Hak, and N. Dame. Compliant Coatings. *Annual Review of Fluid Mechanics*, 20:393–420, 1988.
- [112] A. P. Rothmayer and F. T. Smith. Incompressible triple-deck theory. In *The Handbook of Fluid Dynamics*, pages 23.1–23.24. 1998.
- [113] H. Schlichting and K. Gersten. *Boundary Layer Theory*. Springer, 8 edition, 1999.
- [114] P. J. Schmid and L. Brandt. Analysis of Fluid Systems: Stability, Receptivity, Sensitivity Lecture notes from the FLOW-NORDITA Summer School on Advanced Instability Methods for Complex Flows, Stockholm, Sweden, 2013. *Applied Mechanics Reviews*, 66(2):021003, 2014.
- [115] P. J. Schmid and D. S. Henningson. *Stability and Transition in Shear Flows, Vol. 142*. Springer Science & Buisness Media, 2012.
- [116] P. K. Sen and D. S. Arora. On the stability of laminar boundary-layer flow over a flat plate with a compliant surface. *Journal of Fluid Mechanics*, 197:201–240, 1988.
- [117] P. K. Sen, P. W. Carpenter, S. Hegde, and C. Davies. A wave driver theory for vortical waves propagating across junctions with application to those between rigid and compliant walls. *Journal of Fluid Mechanics*, 625:1–46, 2009.
- [118] V. N. Shtern and F. Hussain. Azimuthal instability of divergent flows. *Journal of Fluid Mechanics*, 256:535–560, 1993.

-
- [119] P. S. Stewart, S. L. Waters, and O. E. Jensen. Local and global instabilities of flow in a flexible-walled channel. *European Journal of Mechanics, B/Fluids*, 28(4):541–557, 2009.
- [120] J. T. Stuart. On the non-linear mechanics of wave disturbances in stable and unstable parallel flows Part 1. The basic behaviour in plane Poiseuille flow. *Journal of Fluid Mechanics*, 9(03):371, 1960.
- [121] R. Telgarsky. Dominant Frequency Extraction. *arXiv preprint*, 2013.
- [122] M. Togneri. *A High-Order Finite Difference Investigation of Boundary Layer Perturbations*. PhD thesis, 2011.
- [123] G. S. Triantafyllou, K. Kupfer, and A. Bers. Absolute instabilities and self-sustained oscillations in the wake of circular cylinders. *Physical Review Letters*, 59(17):1914–1917, 1987.
- [124] L. Tuckerman and D. Barkley. Bifurcation analysis for timesteppers. *Numerical Methods for Bifurcation Problems and Large Scale Dynamical Systems*, pages 1–13, 2000.
- [125] M. Van Dyke. *Perturbation methods in fluid mechanics, Vol. 964*. Academic Press, 1964.
- [126] E. Vignaga, D. M. Sloan, X. Luo, H. Haynes, V. R. Phoenix, and W. T. Sloan. Erosion of biofilm-bound fluvial sediments. *Nature Geoscience*, 6(9):770–774, 2013.
- [127] Z. Wang, K. S. Yeo, and B. C. Khoo. On two-dimensional linear waves in Blasius boundary layer over viscoelastic layers. *European Journal of Mechanics B/Fluids*, 25(1):33–58, 2006.

- [128] J. Watson. On the non-linear mechanics of wave disturbances in stable and unstable parallel flows Part 2. The development of a solution for plane Poiseuille flow and for plane Couette flow. *Journal of Fluid Mechanics*, 9(03):371–389, 1960.
- [129] J. Watson. On spatially-growing finite disturbances in plane Poiseuille flow. *Journal of Fluid Mechanics*, 14(April):211–221, 1962.
- [130] X. Wen and V. Ajarapu. Application of a Novel Eigenvalue Trajectory Tracing Method to Identify Both Oscillatory Stability Margin and Damping Margin. *IEEE Transactions on Power Systems*, 21(2):817–824, 2006.
- [131] O. Wiplier and U. Ehrenstein. On the absolute instability in a boundary-layer flow with compliant coatings. *European Journal of Mechanics, B/Fluids*, 20(1):127–144, 2001.
- [132] K. S. Yeo, B. C. Khoo, and H. Z. Zhao. The Convective and Absolute Instability of Fluid Flow Over Viscoelastic Compliant Layers. *Journal of Sound and Vibration*, 223(3):379–398, 1999.
- [133] K. S. Yeo, H. Z. Zhao, and B. C. Khoo. Turbulent boundary layer over a compliant surface: absolute and convective instabilities. *Journal of Fluid Mechanics*, 449:141, 2001.